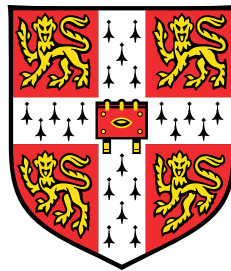


Photodetection and Spectrometry at the Nanoscale



Tom Albrow-Owen

University of Cambridge

This thesis is submitted for the degree of
Doctor of Philosophy

Queens' College

September 2019

Ymroddir tuag at fy mamgu, Laura Diana Owen (1925 - 2017)

Declaration

I hereby declare that except where specific reference is made to the work of others, the contents of this dissertation are original and have not been submitted in whole or in part for consideration for any other degree or qualification in this, or any other university. This dissertation is my own work and contains nothing which is the outcome of work done in collaboration with others, except as specified in the text and Acknowledgements. The main text of this dissertation is under the prescribed word and figure limit.

Tom Albrow-Owen
September 2019

Acknowledgements

First and foremost, I would like to express my gratitude to my supervisor, and the head of the Hybrid Nanomaterials Engineering (HNE) group, Dr Tawfique Hasan. I have come to appreciate that Tawfique is somewhat of a rarity in our departmental division: a supervisor and academic who is highly driven but who also possesses a keen social and emotional awareness; a group leader that knows when is right to push his students and when to offer words of encouragement. He has overseen and advised my research without micromanaging, whilst making sure to organise collaborations which have ensured a far healthier publication record than I could have ever achieved individually. With sincerity I can say that the commitment and dedication that he has shown toward building and organising an effective research team has been a genuine inspiration, with a lasting impact on my attitude toward my own career.

Secondly, to my research teammate Dr Zongyin Yang. At the beginning of this PhD, I admit that I thought his excitable approach toward research would be at odds with my own. However, amongst the practical help he gave me at the start of my PhD, adopting some of his willingness to simply experiment and explore more expansive ideas has been one of the lasting lessons of the last four years. Over time, we have formed an effective team in which our respective qualities have complemented each other to enable a truly collaborative effort which has achieved far more than we could have ever done alone. There is no better evidence of this than the publication of ‘Single-Nanowire Spectrometers’, fittingly in the same week as the submission of this thesis. Zongyin is one of the most talented engineers that I have worked with and I have no doubt that his capacity for conjuring big ideas will lead him onto great things in the future.

I must also thank the rest of the HNE group for their support. In particular Guohua Hu, who was the driving force behind the collaboration on solution-phase processing of Black Phosphorus, Tien-Chun Wu who has always been willing to share his talents for data processing to support others, and Leonard Ng, whose optimism and upbeat attitude has been a breath of fresh air for the group.

A thank you as well to Calum Williams, Henri Jussila, Richard and Sarwat Howe and Anna Ott for many useful discussions and practical advice. Furthermore, to Jack Alexander-

Webber and also Hannah Joyce - their input on my nanowire-related work was as enjoyable as it was invaluable, sparking a desire to return to my roots in fundamental physics.

To the friends and fellow sufferers in the 2014 CDT cohort, David Purdie, Tian Carey, Philippa Hooper, Yang Li, Simon Engelke and Zenas van Veldhoven, in particular regard to our collective toil in a ‘challenging’ MRes year; without their advice, support and lunch-time ranting sessions the experience would have been vastly more trying. To Tahmida Huq, Jakob Muench, Hannah Watson, Dylan Maxwell and Shahaab Akhavan, whose presence has always lightened times inside the CGC.

To all those who have provided me with my fondest memories throughout my PhD. Firstly to George Sedikides; it all wouldn’t have been close to the same without him. To Catherine Walker, who has very much lived and endured the write-up alongside me. To Mari Niemi, for all the happiest first year memories. And to Alma Popescu, Andy Russell, Jordan Burgess, Liz Chant, Lizzie Gaunt, Mark Mawdsley, Sameer Khan and Keval Patel, who have all supported me through the PhD in their own ways.

Finally, to my parents. In many ways, none of this would have been possible without them, but more specifically, without their encouragement in my final year of undergraduate study, I would almost certainly not even have applied to do a PhD in the first place. I’m still not sure they really understand what a photon is, though.

Abstract

Over the past fifteen years, one- and two-dimensional nanostructures have drawn intense attention across a range of scientific fields. For optoelectronic device applications these nanomaterials are particularly attractive due to their fundamental physical properties, such as dramatic environmental or photo-sensitivity, and effects arising from their sub-wavelength dimensions. Furthermore, their physical size alone presents an opportunity for their use as nanoscale components within miniaturised or flexible systems. In this thesis, optoelectronic device platforms based around two such nanomaterial systems – compositionally-engineered nanowires and layered black phosphorus – are developed and studied.

An ultra-miniaturised microspectrometer device platform is demonstrated, based on individual compositionally-engineered nanowires. Representing the most compact microspectrometer design to date, by over two orders of magnitude, this strategy is independent of the complex optical components, cavities or CCDs that constrain further miniaturisation of current systems. It is demonstrated that incident spectra can be computationally reconstructed from the different spectral response functions and measured photocurrents along these nanowires. This platform is highly versatile; operation can straightforwardly be expanded across the infrared to ultraviolet range. Despite their simplicity, these devices are capable of accurate monochromatic and broadband light reconstruction, as well as spectral imaging from centimetre-scale image planes down to lensless, single-cell-scale in-situ mapping. This could open new opportunities for almost any miniaturised spectroscopic application, including lab-on-a-chip systems, smartphones, drones, implants, and wearable devices.

Further to this, the first scalable strategy for depositing solution-processed black phosphorus films with viable device performance and stability is demonstrated. High concentration black phosphorus dispersions are produced by liquid-phase-exfoliation. Optimisation of a solvent-exchange method facilitates conversion of these dispersions into inks, which can be reliably inkjet printed to produce highly uniform black phosphorus films without significant flake degradation. Parylene-C encapsulation of these films ensures their long-term stability (> 30 days) when incorporated into photodetectors and lasers, operating under intense irradiation without any observed drop in performance over time.

Publications

(in chronological order)

1. G. Hu, **T. Albrow-Owen**, X. Jin, A. Ali, Y. Hu, R. C. T. Howe, K. Shehzad, Z. Yang, X. Zhu, R. I. Woodward, T.-C. Wu, H. Jussila, J.-B. Wu, P. Peng, P.-H. Tan, Z. Sun, E. J. R. Kelleher, M. Zhang, Y. Xu and T. Hasan. *Black phosphorus ink formulation for inkjet printing of optoelectronics and photonics*. Nat. Commun. **8**, 278 (2017).
2. J. Wang, S. Lin, X. Liang, M. Wang, P. Yan, G. Hu, **T. Albrow-Owen**, S. Ruan, Z. Sun and T. Hasan. *High-energy and efficient Raman soliton generation tunable from 1.98 to 2.29 μm in an all-silica-fiber thulium laser system*. Opt. Lett. **42**, 3518–3521 (2017).
3. H. Jussila, **T. Albrow-Owen**, H. Yang, G. Hu, S. Aksimsek, N. Granqvist, H. Lipsanen, R. C. T. Howe, Z. Sun and T. Hasan. *New approach for thickness determination of solution-deposited graphene thin films*. ACS Omega **2**, 2630–2638 (2017).
4. X. Jin, G. Hu, M. Zhang, Y. Hu, **T. Albrow-Owen**, R. C. T. Howe, T.-C. Wu, Q. Wu, Z. Zheng and T. Hasan. *102 fs pulse generation from a long-term locked fiber laser*. Opt. Express **26**, 12506–12513 (2018).
5. T. Juntunen, H. Jussila, M. Ruoho, S. Liu, G. Hu, **T. Albrow-Owen**, L. W. T. Ng, R. C. T. Howe, T. Hasan, Z. Sun and I. Tittonen. *Inkjet Printed Large-Area Flexible Few-Layer Graphene Thermoelectrics*. Adv. Funct. Mater. **28** (2018).
6. D. Li, H. Jussila, Y. Wang, G. Hu, **T. Albrow-Owen**, R. C. T. Howe, Z. Ren, J. Bai, T. Hasan and Z. Sun. *Wavelength and pulse duration tunable ultrafast fiber laser mode-locked with carbon nanotubes*. Sci. Rep. **8**, 2738 (2018).
7. R. I. Woodward, M. R. Majewski, N. Macadam, G. Hu, **T. Albrow-Owen**, T. Hasan, and S. D. Jackson. *Q-switched Dy:ZBLAN fiber lasers beyond 3 μm : comparison of pulse generation using acousto-optic modulation and inkjet-printed black phosphorus*. Opt. Express **27**, 15032–15045 (2019).
8. Z. Yang[†], **T. Albrow-Owen**[†], H. Cui, J. Alexander-Webber, F. Gu, X. Wang, T.-C. Wu, M. Zhuge, C. Williams, P. Wang, A. V. Zayats, W. Cai, L. Dai, S. Hofmann, M. Overend, L. Tong, Q. Yang, Z. Sun, and T. Hasan. *Single nanowire spectrometers*. Science, **365**, 1017–1020 (2019).

[†] denotes authors with equal contribution

-
9. T.-C. Wu, A. De Luca, Q. Zhong, X. Zhu, O. Ogbeide, D.-S. Um, G. Hu, **T. Albrow-Owen**, F. Udrea, and T. Hasan. *Inkjet-printed CMOS-integrated graphene-metal oxide sensors for breath analysis*. *npj 2D Mater. Appl.* **3** (2019).
 10. G. Hu, L. Yang, Z. Yang, Y. Wang, X. Jin, J. Dai, Q. Wu, S. Liu, X. Zhu, X. Wang, T.-C. Wu, R. C. T. Howe, **T. Albrow-Owen**, L. W. T. Ng, Q. Yang, L. G. Occhipinti, R. I. Woodward, E. J. R. Kelleher, Z. Sun, X. Huang, M. Zhang, C. D. Bain, T. Hasan. *A general ink formulation of 2d crystals for wafer-scale inkjet printing* (under review).

Posters and presentations

1. ‘Scalable liquid-phase production and characterisation of two-dimensional materials for photonic applications’, *Graphene NOWNANO Summer Conference*, poster presentation, Chester, UK, 27th - 30th June 2016.
2. ‘Black phosphorus ink formulation for inkjet printing of optoelectronics and photonics’, poster presentation, *International Winterschool on the Electronic Properties of Novel Materials*, Kirchberg in Tirol, Austria, 4th - 11th March 2017.
3. ‘Inkjet printing of Black Phosphorus’, conference talk, *CDT Summer Conference on the Science of Graphene and Related Materials*, Cambridge, UK, 12th - 15th June 2017.
4. ‘Inkjet printing of Black Phosphorus’, conference talk, *TMD-UK*, Sheffield, UK, 13th July 2017.

Patent applications

1. ‘Photodetector array’, British Patent Application no. 1911736.5, filed in August 2019, co-inventors: Zongyin Yang, **Tom Albrow-Owen** and Tawfique Hasan.

Table of contents

List of figures and abbreviations	xvii
1 Introduction	1
1.1 Motivation	1
1.2 Project outline	2
1.3 Thesis structure	5
2 Two-dimensional materials	9
2.1 Fundamental properties	10
2.1.1 Graphene	10
2.1.2 Black phosphorus	13
2.2 Production techniques	16
2.2.1 Mechanical exfoliation	16
2.2.2 Chemical vapour deposition	17
2.2.3 Liquid-phase exfoliation	18
2.3 Material characterisation	21
2.3.1 Atomic force microscopy	21
2.3.2 Raman spectroscopy	23
3 Solution-processing of black phosphorus for optoelectronics	27
3.1 Background: solution-phase techniques for deposition of two-dimensional materials	28
3.2 Black phosphorus dispersions	32
3.2.1 Production and characterisation of dispersions	32
3.2.2 Raman spectroscopy of black phosphorus films	35
3.2.3 Black phosphorus stability over time	39
3.3 Black phosphorus inks and their application in optoelectronics	44
3.3.1 Conversion of dispersions to inks	44

3.3.2	Printing optimisation and characterisation	46
3.3.3	Optoelectronic and photonic devices	49
4	Semiconductor Nanowires	55
4.1	Synthesis and properties	56
4.1.1	Growth techniques	56
4.1.2	The VLS mechanism	58
4.1.3	Geometry-dependent properties	61
4.2	Characterisation	65
4.2.1	Electron-mediated techniques	65
4.2.2	Photoluminescence spectroscopy	66
4.3	Bandgap-gradient nanowires in focus	67
4.3.1	Adapted growth strategies	67
4.3.2	Physical and optoelectronic properties	72
5	Nanomaterial optoelectronic devices	81
5.1	Nanofabrication techniques	83
5.1.1	Two- and one-dimensional material transfer	83
5.1.2	Photolithography	86
5.1.3	Electron-beam lithography	87
5.1.4	Electrode deposition	88
5.1.5	Passivating one- and two-dimensional devices	90
5.2	Nanowire-based photodetection	92
5.2.1	Photoconductors	92
5.2.2	Schottky barrier nanowire contacts	97
5.3	Miniaturised spectroscopy	100
5.3.1	Conventional systems	100
5.3.2	Filter array spectrometers	103
5.3.3	Wavelength-selective nanowire-based optoelectronic devices	108
6	Process development: nanowire transfer, characterisation and contact deposition	113
6.1	Nanowire deposition and characterisation	114
6.1.1	Transfer from growth substrates	114
6.1.2	Morphological and photoluminescence analysis	120
6.2	Depositing nanowire contacts	126
6.2.1	Challenges surrounding electrode deposition	126

6.2.2	Developing a process for nanowire embedding	130
6.2.3	Embedding alumina-encased nanowires	135
7	Nanowire-based devices	139
7.1	Graphene-nanowire hybrid devices	140
7.1.1	Graphene transfer, optimisation and characterisation	140
7.1.2	Graphene-top-coated embedded nanowires	144
7.2	Multi-electrode CdS _x Se _{1-x} nanowire device design and development	147
7.2.1	Device architecture and lithography dose testing	147
7.2.2	Preliminary device measurements	151
7.2.3	Optoelectronic characterisation	157
8	Prototyping a single nanowire spectrometer and spectral imaging system	167
8.1	Spectrometer operation and performance	168
8.1.1	Principles behind spectral reconstruction	168
8.1.2	Characterisation of spectral reconstruction	172
8.1.3	Further enhancing the reconstruction accuracy	177
8.2	Spectral imaging	182
9	Conclusion	187
9.1	Avenues for further research	187
9.1.1	Liquid-phase-exfoliated black phosphorus	187
9.1.2	Advancing the single nanowire spectrometer	187
9.1.3	Devices based on bandgap-gradient nanowires	190
9.2	Concluding summary	192
	References	195

List of figures and abbreviations

2.1	Fundamental properties of graphene	11
2.2	Fundamental properties of black phosphorus	14
2.3	Black phosphorus' polarisation-dependence and environmental instability .	15
2.4	Growth of graphene by chemical vapour deposition	18
2.5	Production of 2d materials by liquid-phase exfoliation	19
2.6	Atomic force microscopy of 2d materials	22
2.7	Raman spectroscopic analysis of graphene	23
2.8	Raman spectra of n-layered black phosphorus	24
3.1	Inkjet printing as a 2d material deposition technique.	29
3.2	Imaging of 2d material inkjet printing	31
3.3	Dispersion of black phosphorus in different solvents	33
3.4	Morphological characterisation of liquid-phase-exfoliated black phosphorus flakes	34
3.5	Black phosphorus degradation as analysed by Raman spectroscopy	36
3.6	Raman characterisation of dropcast black phosphorus dispersions	37
3.7	Assessing degradation of liquid-phase-exfoliated black phosphorus through Raman spectroscopic mapping	39
3.8	Black phosphorus flake degradation over time	41
3.9	Variation in BP flake degradation rate	43
3.10	Inkjet printing of black phosphorus inks	45
3.11	Inkjet printing and characterisation of patterned features	47
3.12	Characterisation of printed black phosphorus films	48
3.13	Demonstration of a hybrid photodetector based on a graphene-silicon junc- tion sensitised by a printed BP film	50
3.14	Demonstration of an ultra-fast laser based around a black-phosphorus printed film saturable absorber	52

4.1	Growth of nanowires by the vapour liquid solid method	59
4.2	Nanowire growth modes	60
4.3	Nanowire properties	63
4.4	Tuning bandgaps through semiconductor alloying.	68
4.5	Compositional-grading for semiconductor nanostructures	69
4.6	Apparatus for engineering on-nanowire compositional gradients	71
4.7	Imaging $\text{CdS}_x\text{Se}_{1-x}$ nanowires	73
4.8	Spatially resolved compositional analysis of $\text{CdS}_x\text{Se}_{1-x}$ nanowires	74
4.9	Photoluminescence mapping of a $\text{CdS}_x\text{Se}_{1-x}$ nanowire	75
4.10	Photoconductive properties of $\text{CdS}_x\text{Se}_{1-x}$ -graded compositional system	77
4.11	Directionally-dependent waveguiding in compositionally graded semiconductor nanowires	79
5.1	Wet-etch-based transfer techniques for 2d materials	84
5.2	Contact-based transfer of nanowires	85
5.3	Photolithography for device fabrication	87
5.4	Embedded nanowire devices	89
5.5	Passivation of nanowire and 2d material devices	92
5.6	A nanowire photoconductor	94
5.7	Properties of nanowire photoconductors	96
5.8	Schottky barriers at the nanowire-electrode interface	99
5.9	Microspectrometers based on miniaturised conventional systems	101
5.10	Interferometric microspectrometer designs	102
5.11	Filter array spectrometers	104
5.12	A colloidal quantum dot spectrometer	105
5.13	Different spectrometer strategies	106
5.14	Computational reconstruction of an incident spectrum by a filter-detector array	107
5.15	$\text{CdS}_x\text{Se}_{1-x}$ nanowire photodetectors	110
5.16	Wavelength-dependent nanowire photodetectors using $\text{CdS}_x\text{Se}_{1-x}$	111
6.1	Contact transfer of nanowires from growth to intermediary substrates	115
6.2	Mapping the intermediary substrate	117
6.3	Optical fibre probe-based nanowire transfer method	119
6.4	Morphological characterisation of $\text{CdS}_x\text{Se}_{1-x}$ nanowires	121
6.5	Morphology distribution across nanowire samples	122
6.6	Photoluminescence measurements of $\text{CdS}_x\text{Se}_{1-x}$ nanowires	124

6.7	Spatially-resolved transmission electron microscope imaging of a $\text{CdS}_x\text{Se}_{1-x}$ nanowire	125
6.8	The electrode deposition process	127
6.9	Characterisation of, and challenges for, metallisation and lift-off	129
6.10	Unsuitability of parylene-C for nanowire embedding	131
6.11	Nanowire embedding using SU-8 part i)	132
6.12	Nanowire embedding using SU-8 part ii)	133
6.13	Embedded nanowire devices	134
6.14	Embedded, alumina-encased nanowires	136
7.1	Transferred CVD graphene characterisation	142
7.2	Raman spectroscopy of transferred CVD graphene	143
7.3	Toward a graphene-nanowire hybrid device platform	145
7.4	Multielectrode device layout and fabrication stages	148
7.5	EBL dose testing for the electrode array	151
7.6	Varying the conditions at the contact interface	153
7.7	FET transport characteristics along the length of a $\text{CdS}_x\text{Se}_{1-x}$ nanowire	154
7.8	Al_2O_3 passivation of $\text{CdS}_x\text{Se}_{1-x}$ nanowire devices	155
7.9	Effect of ALD passivation and bias on measurement stability	157
7.10	Multi-electrode optoelectronic characterisation setup	158
7.11	Photodetector power and time response under different contact conditions.	160
7.12	Backgated optoelectronic characterisation.	161
7.13	Spectral response calibration	162
8.1	Principles of spectral reconstruction using a nanowire spectrometer	169
8.2	The reconstruction algorithm	171
8.3	Demonstration of spectral reconstruction by nanowire spectrometer	173
8.4	Device-to-device reproducibility	174
8.5	Stability of spectral reconstruction with unit failure and over time	176
8.6	Comparing the effects of measurement errors on non-iterative method- and adaptive regularization-based reconstructions	180
8.7	Simulated device performance with increased unit numbers	182
8.8	Macroscale spectral imaging	183
8.9	Spectral imaging at the micrometre scale	184
9.1	Potential design for a nanowire-array-based snapshot spectral imaging device	190

Abbreviations and symbols

Note: Symbols within equations are defined alongside in the main text.

0d	zero-dimensional
1d	one-dimensional
2d	two-dimensional
Ag	Silver
AFM	Atomic force microscopy
Al	Aluminium
ALD	Atomic layer deposition
Al ₂ O ₃	Aluminium oxide
APS	Ammonium persulfate
Ar	Argon
Au	Gold
BP	Black phosphorus
CAD	Computer-aided design
CCD	Charge-coupled device
Cd	Cadmium
CdS	Cadmium sulfide
CdSe	Cadmium selenide
CdS _x Se _{1-x}	Alloyed cadmium sulfur - cadmium selenide (where 0 < x < 1)
CH ₄	Methane
CHP	N-cyclohexyl-2-pyrrolidone
CMOS	Complementary metal-oxide-semiconductor
CNT	Carbon nanotube
Cr	Chromium
Cu	Copper
CuSO ₄	Copper sulfate
CV	Coefficient of variation
CVD	Chemical vapour deposition
DFT	Density functional theory
DI	De-ionised water
DMF	N,N-dimethylformamide
<i>e</i>	Elementary charge
<i>E_F</i>	Fermi energy
<i>E_g</i>	Bandgap energy

EBL	Electron-beam lithography
EDX	Energy-dispersive X-ray spectroscopy
EELS	Electron energy-loss spectroscopy
FET	Field effect transistor
FSR	Free spectral range
FWHM	Full-width at half-maximum
GaAs	Gallium arsenide
GaN	Gallium nitride
GaSb	Gallium antimonide
GCV	Generalised Cross Validation
Ge	Germanium
h	Planck's constant
\hbar	Reduced Planck's constant
h -BN	Hexagonal boron nitride
H ₂	Hydrogen
HAADF	High-angle annular dark-field
HCl	Hydrochloric acid
HMDS	Hexamethyldisilazane
H ₂ O	Water
H ₂ O ₂	Hydrogen peroxide
I_{On}/I_{Off}	On- / off-current ratio
In	Indium
In _x Ga _{1-x} N	Alloyed indium nitride - gallium nitride, (where $0 < x < 1$)
InAs	Indium arsenide
InP	Indium phosphide
IPA	Isopropanol
I_{PC}	Photocurrent
IR	Infrared
ITO	Indium tin oxide
k_B	Boltzmann constant
KPFM	Kelvin-probe force microscopy
λ	Wavelength
LED	Light emitting diode
LPE	Liquid-phase exfoliation
MBE	Molecular beam epitaxy
MEMS	Microelectromechanical systems

MoS ₂	Molybdenum disulfide
N ₂	Nitrogen
(NH ₄) ₂ S _x	Ammonium sulfide
(NH ₄) ₂ S ₂ O ₈	Ammonium persulfate
Ni	Nickel
NMP	1-methyl-2-pyrrolidone
O ₂	Oxygen
OPTP	Optical-pump terahertz-probe
PC	poly(bisphenol A carbonate)
PCB	Printed circuit board
PDMS	poly(dimethylsiloxane)
PET	Polyethylene terephthalate
PL	Photoluminescence
PMMA	Poly(methyl methacrylate)
P _x O _y	Phosphoric acid
QD	Quantum dot
RIE	Reactive ion etching
SAED	Selected-area electron diffraction
SAM	Self-assembled monolayer
SEM	Scanning electron microscopy
Si	Silicon
Si _x Ge _{1-x}	Alloyed silicon - germanium, (where 0 < x < 1)
Si ₃ N ₄	Silicon nitride
SiO ₂	Silicon dioxide
SNR	Signal to noise ratio
SPCM	Scanning photocurrent microscopy
SPM	Scanning probe microscopy
TCE	Transparent conductive electrode
TEM	Transmission electron microscopy
Ti	Titanium
TLM	Transmission line method
TMA	Trimethylaluminium
TMAH	Tetramethylammonium hydroxide
TMDs	Transition metal dichalcogenides
UV	Ultraviolet
VLS	Vapour-liquid-solid

W	Tungsten
Xe	Xenon
$Zn_{1-x}Cd_xS_{1-y}Se_y$	Alloyed zinc sulphide - cadmium selenide (where $0 < x, y < 1$)
ZnO	Zinc oxide
ZnS	Zinc sulphide

Chapter 1

Introduction

1.1 Motivation

Throughout the 20th and 21st centuries, one of the predominant themes of technological advance has been the miniaturisation of electronic devices. This is perhaps most strikingly illustrated by Gordon Moore's eponymous 'law', proposed in 1965, which has held roughly true up to the present day: that the spatial density of transistors that can be produced on an integrated circuit chip doubles roughly every two years. The driving force behind this progress has been the advancement of complementary metal-oxide-semiconductor (CMOS)-based manufacturing processes, to allow reliable mass-production of smaller and smaller semiconductor device features. These techniques are part of a so-called 'top-down' class of nano-manufacturing - that is, they centre on the sequential removal of material from bulk sections, mediated by lithographic patterning, in order to create increasingly complex nanoscale features.

In the last four to five decades, a complementary 'bottom-up' paradigm has emerged, based around zero-dimensional (quantum dots), one-dimensional (nanowires) and two-dimensional (layered crystals) nanomaterials, which can be 'grown' by the additive combination of precursor materials. These growth processes can allow a remarkable degree of control over the size, geometry and fundamental physical properties of the resultant structures. Nanomaterial systems continue to attract increasingly intense attention for the development of potential device platforms. In some cases this is simply by virtue of their size alone, in functioning as ultra-compact components, but in many others this is through novel functionality, such as based around quantum mechanical phenomena, or ultra-sensitivity to their environment. In particular, many nanomaterials are highly suited to optoelectronic applications; this is due to a variety of factors, including dramatic photosensitivity, as well as resonance-based effects that arise from their length-scales being similar to the wavelength of

ultraviolet and visible-range light. An extensive family of two-dimensional layered crystals has been rapidly uncovered over the last decade, with each material system posing different challenges for their use in this respect. Graphene, for instance, with its myriad superlative properties, does not possess a bandgap to allow for significant absorption of light. Meanwhile, black phosphorus has recently emerged as a two-dimensional material with a layer-dependent, direct bandgap. However, its extreme environmental instability make it a highly challenging structure to produce or deposit in a scalable manner, let alone with which to produce viable devices. Solution-phase processing has been demonstrated as a potential avenue to achieve this, however, thus far, no method has been developed to integrate liquid-phase black phosphorus dispersions into devices.

Under the umbrella of optical applications, spectrometers, which characterise the different components of light signals, are essential, ubiquitous analytical tools across industry and almost all fields of scientific research. They can tell us about the chemical processes occurring in galactic nebulae, millions of light-years away, down to the structural characteristics of protein molecules. However, the fundamental working principle behind the vast majority of spectrometers today in fact remains largely unchanged from that which Isaac Newton demonstrated with a prism in the 1600's - dispersing light, spatially separating its different component wavelengths. Due to inherent constraints on the distances which light must travel in these systems, one drawback of spectrometers based around them is that they are usually bulky and complex; it is near impossible to shrink them to sizes below the centimetre length-scale without significant reduction in performance.

The use of compositionally-engineered nanomaterials, with a range of light-sensitive materials incorporated into their structure, may provide a solution that allows extreme miniaturisation of spectrometer systems. Such ultra-compact spectrometers could have the potential to send powerful analytical technology from the lab-bench directly to a commercial, hand-held platform - such as smartphones - for the first time. This could, for instance, provide a user with the capability to assess the ripeness of fruit, the quality of pharmaceuticals, or even to identify counterfeit goods, from the palm of their hand. Beyond commercial technology, there is a vast range of applications across industry and research where a spectrometer with minimised footprint and weight would prove highly advantageous, from satellites and drone-based agricultural monitoring, down to lab-on-a-chip systems and cellular imaging.

1.2 Project outline

At the outset, the initial aim of this project was broad: to create wavelength-dependent optoelectronic devices based around hybrid structures of compositionally-graded $\text{CdS}_x\text{Se}_{1-x}$

nanowires and graphene. However, after initial experimental work, as well as through a detailed review of the literature surrounding a recently emerging class of ‘filter array’ microspectrometers, it was hypothesized that a photodetector array fabricated onto an individual $\text{CdS}_x\text{Se}_{1-x}$ nanowire may be able to function in a manner analogous to these ‘filter array’ devices. It became apparent from my preliminary results that this should be achievable using a simpler approach than that involving graphene-nanowire hybrid structures; that I could use established techniques for metal deposition to produce a device out of a $\text{CdS}_x\text{Se}_{1-x}$ nanowire alone, *a single-nanowire spectrometer*, with a footprint 2 - 3 orders of magnitude smaller than the most notable other microspectrometers at that time. Thus my primary objective became to prototype this device and which was divided into sub-objectives as follows:

Prototyping a nanowire spectrometer:

1. Develop processes and techniques to reliably fabricate multi-electrode $\text{CdS}_x\text{Se}_{1-x}$ nanowire devices.
 - (a) Establish a method to transfer nanowires from their growth substrate and onto a device substrate, with control over final positioning.
 - (b) Characterise the physical properties of the nanowires, using non-contact techniques, to inform device fabrication.
 - (c) Investigate different ways to form stable electronic contact to the nanowires, with preferably ohmic, consistent properties along the length of the structure.
 - (d) Optimise the electrode deposition such that an array of electrodes can be reliably formed on one nanowire at high resolution, to allow spatially-resolved optoelectronic characterisation with as many measurement points as possible.
2. Study the behaviour of these devices, and make corresponding optimisations.
 - (a) Carry out spatially resolved optoelectronic characterisation along the length of these nanowires using the electrode array, in particular including measurement of the wavelength-dependent photoresponse.
 - (b) Assess the stability of performance of these devices and investigate forms of passivation, surface treatments, or methods to reduce the contact resistance if necessary.
3. Demonstrate the capability of these devices to function as a spectrometer.

- (a) Informed by similar works in the literature, develop an algorithm that can use data measured from different points along the nanowire to computationally reconstruct an unknown, incident spectrum.
- (b) Characterise the performance of this reconstruction with respect to different monochromatic and broadband spectra, at a range of wavelengths.
- (c) Identify ways to further improve the accuracies of these reconstructions.
- (d) Using a scanning stage setup, assess whether the device can be used for spectral imaging, and at what resolutions.

In brief, it is the successful realisation of these three overarching objectives that collectively represent the central and most significant finding of this thesis and indeed, my main, novel contribution to the field: the engineering, experimental analysis, and working demonstration of a proof-of-concept, single-nanowire spectrometer.

Further to this, two significant secondary projects emerged during the PhD, involving two-dimensional materials. The first surrounded collaborative work toward the production of liquid-phase exfoliated black phosphorus ink, in doing so demonstrating the first controlled, scalable method of depositing this unstable material without degradation of its optoelectronic properties. My contributions to this project centred on carrying out experimental work to successfully produce and characterise these black phosphorus inks, as well as enacting the first systematic study of the degradation of liquid phase exfoliated black phosphorus flakes, using Raman spectroscopy and atomic force microscopy. The second was tangential to my work on the main project; a re-visitation of the original project goal - to create graphene-nanowire hybrid structures - as a result of new fabrication capabilities developed for the nanowire spectrometer.

Formulation of a black phosphorus ‘ink’:

1. Produce liquid-phase exfoliated black phosphorus dispersions.
2. Characterise the physical properties of the flakes in these films and investigate ways of assessing their degradation, relative to mechanically-exfoliated black phosphorus flakes.
3. Convert these dispersions to a black phosphorus ink that can be inkjet printed, and characterise the properties of the resultant films.
4. Collaborate with other groups to evaluate the operational stability of these films in devices, under intense irradiation.

Development of a hybrid graphene-nanowire optoelectronic platform:

1. Optimise a process for the transfer of chemical-vapour-deposition-grown graphene to arbitrary substrates, informed by non-contact characterisation of the graphene films.
2. Investigate a means of coating a $\text{CdS}_x\text{Se}_{1-x}$ nanowire with graphene, or vice-versa, without either material being damaged.
3. Fabricate graphene channels that are in contact with the nanowires and investigate photogating characteristics.
4. Develop an all-transparent, wavelength-dependent graphene-nanowire hybrid device, aiming to maximise the photosensitivity of each unit.
5. Test whether this could also function as a nanowire spectrometer, and compare its performance relative to that with metallic electrodes.

Further to these objectives, numerous parallel projects were pursued, as a result of collaborations or otherwise, that will not be fully detailed in this thesis in the interests of keeping the scope more focused on the main work; many were published and are as such listed in the 'Publications' section.

1.3 Thesis structure

The bulk of this thesis is contained within the middle seven chapters, bookended by this introductory chapter and a concluding summary chapter which also contains potential avenues for future investigation. These seven chapters can be broadly divided into two components; **Chapters 2 and 3** concern layered nanomaterials and my experimental work on black phosphorus, whilst **Chapters 4 - 8** provide background on, and detail the development of, the single-nanowire spectrometer platform. **Chapters 2, 4 and 5** are literature reviews, while **chapters 3, 6, 7 and 8** detail my experimental work and discussion of its results. In these chapters, where experimental work has been done in collaboration with others, notably Guohua Hu and Zongyin Yang, their contributions have been listed within the overview of each chapter.

Chapter 2 will address two-dimensional materials, beginning with a summary of the fundamental properties of the two materials featured in this thesis - graphene and black phosphorus - which have seen them garner such intense attention across a range of fields. Beyond this, the different methods used to produce these materials for my research shall

be introduced, before a brief overview of the two main techniques I utilised for their characterisation: Raman spectroscopy and atomic force microscopy. In **chapter 3** my work on developing a black phosphorus ink formulation, in collaboration with Guohua Hu of the Hybrid Nanomaterials Engineering (HNE) group and others is presented, based on item number 1 in the ‘Publications’ section. This will begin with some brief contextual background to inkjet printing of two-dimensional materials before covering my production of liquid-phase-exfoliated black phosphorus dispersions, how they were altered to produce printable formulations, before demonstration of their stable operation in devices. Throughout this section I will discuss how the instability of black phosphorus presents challenges for ink and device production, and how I studied and mitigated this.

In **chapter 4**, I will introduce semiconductor nanowires as a nanomaterial platform, covering how they can be grown and some of the defining fundamental properties that arise from their size and geometry. The techniques used in the field, and in my research, to characterise these properties are also presented here. The last subsection of this chapter will provide a comprehensive review of the limited literature available on the particular nanomaterial platform used for developing the spectrometers in my thesis: compositionally-graded $\text{CdS}_x\text{Se}_{1-x}$ nanowires. Finally, in **chapter 5** I will lay out how optoelectronic device platforms can be developed from these nanomaterials. This will first cover background on the practical techniques I have used to fabricate devices and the particular challenges involved. The physical concepts behind nanowire photodetection will be introduced from first principles. Lastly, I will summarise recent developments in microspectrometers, in particular devices that make use of computational reconstruction, detailing their operation and limitations, before presenting how a $\text{CdS}_x\text{Se}_{1-x}$ nanowire based device may fit into this field.

Moving onto my experimental work surrounding compositionally-engineered nanowires, **chapter 6** covers the processes and methodologies that were developed to fabricate devices during my research. The first aspect addressed here is the transfer of nanowires from the growth substrate as well as the characterisation of their morphological and photoluminescent properties, which in turn introduces the significant challenges that these nanowires present from a fabrication standpoint. The specific lithography and contact deposition processes used are summarised, presenting limitations in their application to the $\text{CdS}_x\text{Se}_{1-x}$ nanowires available. Here, I introduce a nanowire embedding process developed to address these issues, demonstrating how it can enable far more reliable fabrication of high resolution device features. In **chapter 7**, I will move on to discuss the specific multi-electrode array nanowire devices that are proposed for use as spectrometers, in particular their design, how they were fabricated using the techniques devised in chapter 5 and their characterisation and

consequent optimisation. Further to this I will cover work carried out toward developing a hybrid graphene-nanowire device platform, which also built upon the lithographic and embedding processes that I engineered. **Chapter 8** will encompass the demonstration of these devices as nanowire spectrometers, heavily based on item number 8 in the ‘Publications’ section, an equal-contribution collaborative work by myself and Zongyin Yang of the HNE group. It details the algorithm used to reconstruct spectra from the information gathered from the electrode arrays, before experimentally demonstrating monochromatic and broadband light reconstructions, as well as spectral imaging by a point scanning strategy. Here, I will also elaborate on how the performance of this spectrometer, and the spectral imaging system, has potential to be readily and significantly improved beyond our work thus far. Finally, in **chapter 9**, I shall present some avenues that could be pursued as a continuation of the investigations in this thesis. The three main focal points here are: studying the stability of black phosphorus inks, expanding the nanowire spectrometer system and producing devices based on graphene-nanowire hybrid structures. Then follows a brief, concluding summary of this thesis.

Chapter 2

Two-dimensional materials

Overview

The properties of graphene, a single layer of carbon atoms arranged into a hexagonal lattice, were first studied and predicted theoretically over 60 years ago. However, in practicality, it was predicted to be unstable with respect to the formation of lower dimensional allotropes of carbon, such as zero-dimensional (0d) fullerenes and one-dimensional (1d) carbon nanotubes (CNTs)^[1,2]. This was dramatically disproven in 2004 when it was first isolated from graphite by Andre Geim and Konstantin Novoselov^[3], in what turned out to be the catalyst for an extraordinary global research effort^[4,5].

Since then, a vast family of layered nanomaterials - typically broadly referred to as two-dimensional (2d) materials - has been identified and in many cases studied experimentally. 2d materials are primarily characterised by their stratified structures, with vertical stacks of repeating, atomically-thin crystalline layers. These layered crystals possess strong in-plane bonding *within* the lattice of each layer, but weak attractive forces *between* layers. Most importantly (and as suggested by their '2d' description) these materials can be 'exfoliated' to isolate few- or mono-layer crystal sheets. Here, electronic and optical properties are in many cases strongly thickness (that is, layer number) dependent, as carriers become confined, perpendicularly to the lattice planes, toward a quasi-2d space^[5].

Whilst graphene has attracted the most attention for application due to its diverse range of exotic, and in many cases superlative properties, attempting to design novel devices around a single 2d material can prove a limited approach. For instance, despite possessing ultrahigh carrier mobility, monolayer graphene lacks a bandgap to make use of this for ultrafast digital processing^[6]. Likewise, while it exhibits broadband optical response due to its band structure, photodetection is limited by an absorbance of only 2.3%^[7]. Here, other related 2d crystals, such as semiconducting transition metal dichalcogenides (TMDs),

or insulating hexagonal-boron nitride (*h*-BN), can provide complementary characteristics to those of semi-metallic graphene. One such layered nanomaterial to emerge in the last 5 years is black phosphorus (BP), of significant interest for optoelectronic devices due to its thickness-dependent bandgap and anisotropic response^[8]. However, it too presents its own challenges for both research and application, due to its poor environmental stability; degradation during its production and deposition remains arguably the main obstacle to the realisation of its potential^[9].

This chapter will focus on providing background to the two layered nanomaterials studied and utilised in my research, graphene and BP, through a review of the literature, as well as the experimental processes I have used to produce and characterise them. The first section shall address their properties in turn, centering on those that are most relevant to the experimental work and device fabrication detailed in this thesis. I briefly summarise the literature on graphene, providing context to the remarkable interest that it has generated and detailing in particular the characteristics which make it attractive for its primary role in my experimental work, as a transparent conductive electrode. Turning then to BP, reflecting its role in my thesis, the review will focus mainly on properties that make it suited as an active material in optoelectronic devices, before addressing its instability and the mechanisms involved. The second section will detail the three most commonly used methods of production for 2d materials, all of which are employed in my thesis - mechanical exfoliation, chemical vapour deposition and liquid-phase exfoliation - with reference to their relative strengths and weaknesses. Finally, in the third section, I describe the techniques used to characterise the properties of nanoscale crystals, detailing and discussing two of the primary tools used in my research, atomic force microscopy (AFM), and Raman spectroscopy, with a particular focus on how the latter may be used to analyse the degradation of BP.

2.1 Fundamental properties

2.1.1 Graphene

Graphene possesses many remarkable electronic, optical and physical properties that have caused it to attract intense attention in both academia and industry. Its structure, shown in Figs. 2.1a-c, is that of a single sheet of carbon atoms bonded through hybridized sp^2 orbitals to form a hexagonal lattice. Charge carriers in graphene behave as massless Dirac fermions and can be described by a linear dispersion relation (kinetic energy, E , as a function of wave number k):

$$E = \hbar v_F k, \quad (2.1)$$

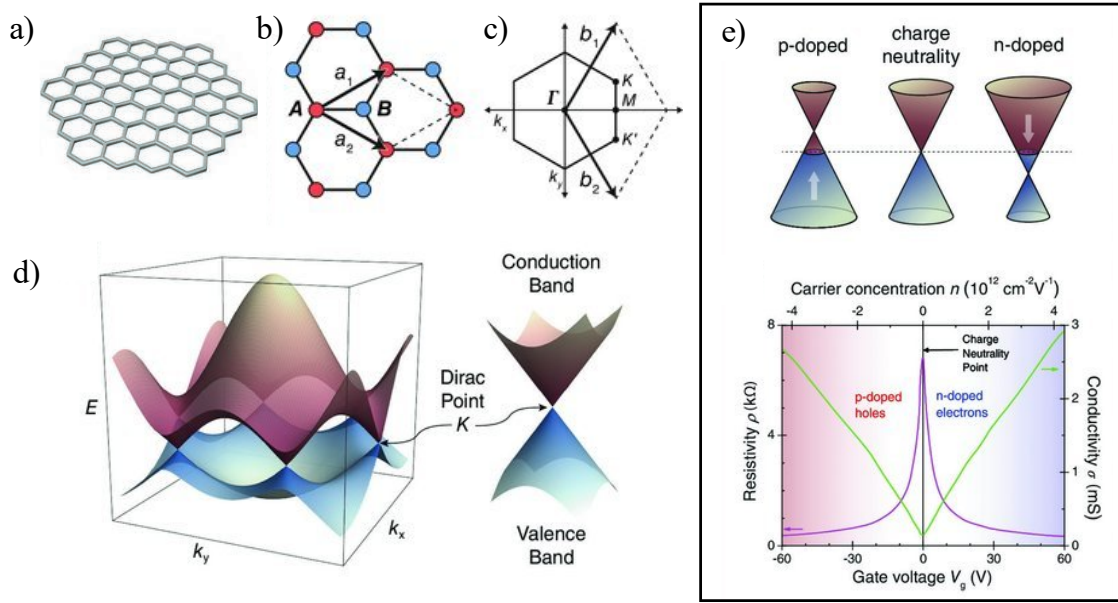


Fig. 2.1 **Fundamental properties of graphene.** (a) Schematic of a single monolayer of graphene. Adapted from ref. 10. (b) Arrangement of the graphene lattice, showing the two inequivalent points A and B of the unit cell and the lattice parameters a_1 and a_2 . (c) Reciprocal lattice for graphene, showing reciprocal lattice parameters b_1 and b_2 , as well as the Brillouin zone (central hexagon), with points K and K' - the Dirac points - at the corners, M at the edge mid-point, and Γ at the zone center. (d) Band structure of graphene, showing Dirac cones in the zoomed section, where conduction band (top) and valence band (bottom) meet at the Dirac point, with $E_k = 0$. (e) Typical trans-characteristics for an intrinsic graphene channel, showing the resistivity (purple) and conductivity (green) as a function of gate voltage. Band diagram illustrations above the plot show the shift in the density of states corresponding to variations in the gate voltage below, at, and above the charge neutrality (Dirac) point. b-d) adapted from ref. 11, e) adapted from ref. 1, as redrawn by ref. 10.

where v_F represents the fermi velocity of around 10^6 ms^{-1} , (the group velocity at the Fermi surface) at which electrons or holes can be thought to move across the lattice^[11,12]. Near-ballistic room temperature transport is observed in graphene, with carrier mobilities of around $2 \times 10^5 \text{ cm}^2\text{V}^{-1}\text{s}^{-1}$ observed in room temperature samples under ambient conditions^[5], while low temperature measurements of graphene nanoribbons and flakes encapsulated in *h*-BN have even been measured at up to $6 \times 10^6 \text{ cm}^2\text{V}^{-1}\text{s}^{-1}$ ^[13] and $1.8 \times 10^6 \text{ cm}^2\text{V}^{-1}\text{s}^{-1}$ ^[14] respectively. As can be seen in Figs. 2.1d and e, its electronic structure is that of a semi-metal, with two band edges meeting at a so-called Dirac point, giving rise to ambipolarity in its field response with continuous tunability between hole- and electron-mediated charge transport^[1]. Such an energy spectrum, with zero bandgap, means that it also demonstrates wavelength independent optical response^[15,16]. Optically, it absorbs $\sim 2.3\%$ of visible light, despite only being a single atom thick^[7,15], and exhibits ultra-fast carrier dynamics^[17,18].

Exceptional electronic conductivity is matched by record thermal conductivity, κ , of up to $\sim 5300 \text{ Wm}^{-1}\text{K}^{-1}$ [19]. Strong covalent inter-layer bonding results in notably robust mechanical properties, with high Young's modulus (1 TPa) and maximal strength (130 GPa) [20], however its monatomic thickness means it is also highly flexible [4].

These fundamental properties mean graphene has huge potential across an unprecedented range of applications. Whilst the absence of a bandgap presents a hurdle for its use in digital electronics, graphene is an ideal prospect for ultra-high frequency analogue electronics [21], with potential operation speeds exceeding 1 THz [22,23]. Long coherence and spin-relaxation times have seen it touted for the emerging field of spintronics [5,10,24], whilst existing at the very limit of nanoscale thickness gives it potential for energy storage [25–29], and as an ultra-thin membrane in a variety of applications ranging from microelectromechanical systems (MEMS) [30] to DNA sequencing [31].

In photonics and optoelectronics, it has shown great promise in a diverse range of photodetection mechanisms [32] and plasmonic structures [33–35], as well as in ultra-fast lasers, where it is utilized for its saturable absorption [36–38]. Its high flexibility and transparency also make it an ideal transparent conductive electrode (TCE) for use in wearable, stretchable electronics, and flexible display technology; in this respect it has an advantage over brittle indium tin oxide (ITO), the current industry-standard TCE [39–41].

Of most relevance to this project, is graphene's potential to act as an ultra-sensitive active channel. Graphene and other 2d material monolayers are unique in that the surface and bulk of the material are one and the same, and as a result of this, the behaviour of charge transport across a graphene layer is extremely responsive to any electrostatic perturbations at its surface, from external species or otherwise [5,32]. As a result, graphene's electronic properties are highly sensitive to the substrate on which it rests (mobilities in suspended samples are for instance over an order of magnitude higher than those on a substrate) [42], as well as physisorbed contamination, such as from polymers used in lithographic patterning processes, or even molecules, such as water, adsorbed to its surface under ambient conditions [43]. Such scenarios often have undesirable effects with respect to the intended application, acting to reduce the free path of carriers by providing extrinsic scattering centers, or to electrostatically dope the graphene layer [43].

However, this characteristic has made it of great use in ultra-sensitive chemical and biological species detection, as well as in-vivo devices, often through the functionalisation of graphene sheets to provide binding sites preferential to a particular analyte [44–47]. With respect to this thesis, this sensitivity can also be exploited in hybrid photodetector devices [48]. Whilst graphene's optical absorption is impressive relative to its thickness, in absolute terms its photoresponse is far below that ideally required of the active photosensitive medium

in a conventional detector^[5]. Hybrid schemes can bypass this challenge and exhibit ultra-high photoresponsivity, through attachment of semiconducting nano-structures, such as 0d quantum dots or 1d nanowires, on the graphene surface to act as the light-absorbing media. Optical excitation of carriers in these semiconductors will ‘photogate’ the graphene channel below, shifting its Dirac point through capacitive coupling or charge transfer^[48].

2.1.2 Black phosphorus

As the most stable form of elemental phosphorus, BP’s chemistry has been well established for many decades^[49]. However, in 2014 it emerged as a semiconducting layered material with significant potential for nanoscale devices when mechanical exfoliation and electronic characterisation of few-layer flakes was demonstrated by Li *et al.*^[50]. Figures 2.2a and b illustrate the orthorhombic crystal structure of bulk BP, with each layer a puckered lattice of covalently bonded phosphorus atoms, divisible into two sub-layers, as can be seen from the side-on view^[49]. Notable from the top-view in Fig. 2.2c, is the anisotropy of its structure, defined by two directional in-plane bonding arrangements: zigzag and armchair.

In terms of optoelectronic properties, as with most TMDs, the bandgap in BP is highly thickness-dependent, as illustrated by the band diagrams and theoretical calculations in Figs. 2.2d and e^[50,53,55,56]. However, unlike in TMDs, where the bandgap transitions from indirect to direct on exfoliation, in BP, it maintains its direct nature at any thickness^[54]. Whilst bulk BP has a direct bandgap of ~ 0.3 eV, when exfoliating down from few-layer to monolayer ‘phosphorene’, quantum confinement-related effects result in the bandgap widening to between ~ 0.6 eV (5-layer) and ~ 2.0 eV (monolayer), though the exact value of the latter is debated^[49,53,57]. Crucially, this positions BP across a broad and unique energy window in the family of 2d materials, between the bandgaps of patterned graphene (~ 200 meV) and TMDs (>1 eV), affording it potential for near-infrared optical telecommunications and mid-infrared optoelectronics^[6,8,56,58]. The first BP field-effect transistors have already shown I_{ON}/I_{OFF} ratios of 10^5 , exceeding the 10^4 required for competitive digital logic gates, though still far below the $\sim 10^8$ achieved with MoS₂ transistors^[6,50,59]. However, carrier mobilities in monolayer BP have been demonstrated up to $1000 \text{ cm}^2\text{V}^{-1}\text{s}^{-1}$ and are currently around an order of magnitude higher than those observed for TMDs^[50].

Arguably the most notable facet of its properties, due to its structure, BP exhibits strongly anisotropic in-plane electronic, optical and phononic characteristics, with effective carrier masses around an order of magnitude lighter in the armchair direction (x-direction)^[54,57]. Carrier mobilities and optical conductivity are therefore far higher along the armchair direction, whilst optical dichromism has been demonstrated, with suppressed absorption of light polarised along the zigzag (y-) direction, as evidenced in the plots in Fig. 2.3a, and excitonic

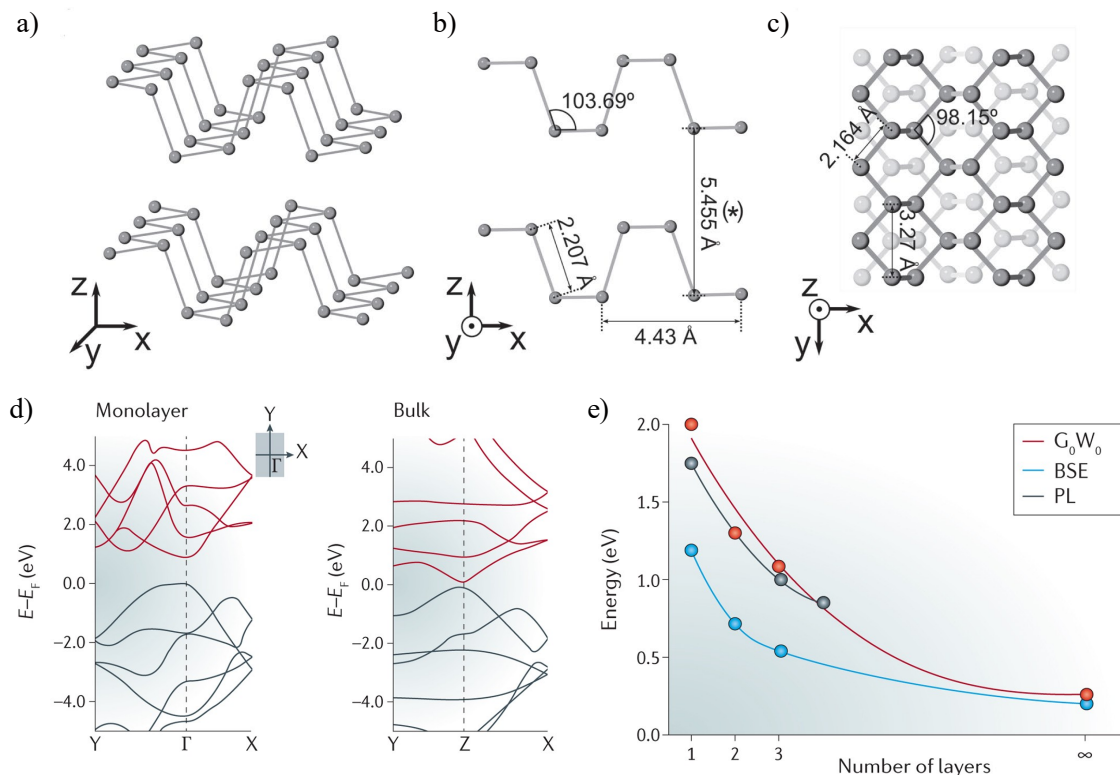


Fig. 2.2 **Fundamental properties of black phosphorus.** (a) Schematic showing a three dimensional perspective of stacked, puckered layers of bulk black phosphorus (BP). (b) and c) Side-on and top views of the BP crystal structure respectively, with bond angles and lengths as calculated by density functional theory (DFT) in ref. 51. (d) Band structure for monolayer and bulk BP, with dashed line indicating the Brillouin zone center, as calculated by DFT using the PBEsol functional. (e) Variation in bandgap with BP flake thickness, as calculated theoretically (G_0W_0 and Bethe-Salpeter equation (BSE)) and obtained through photoluminescence measurements (PL). Solid lines show power law fitting curves. a)-c) adapted from ref. 51. Data for d) and e) produced by refs. 52 and 53 respectively, displayed as redrawn by ref. 54.

emission that is linearly polarised along the x-direction^[60,61]. This makes BP an interesting candidate for polarisation-sensitive photodetectors and other optoelectronic applications, but also allows straightforward optical characterisation of the crystallographic orientation for a particular sample (discussed further in section 2.3.2)^[54,60]. Another significant potential application here are thermoelectrics, where a competitively high figure of merit for BP films is predicted, owing to the orthogonality between the preferred directions for heat and charge transfer^[62]. As with graphene, BP also exhibits robust mechanical flexibility, with stable electronic properties observed in encapsulated BP FETs over 5000 bending cycles^[63].

Whilst many proof of concept devices have been fabricated to study the behaviour of mechanically exfoliated BP, a major challenge for scalable applications is its environmental instability. As can be seen in Figs. 2.3b-d, when un-passivated BP is left under ambient

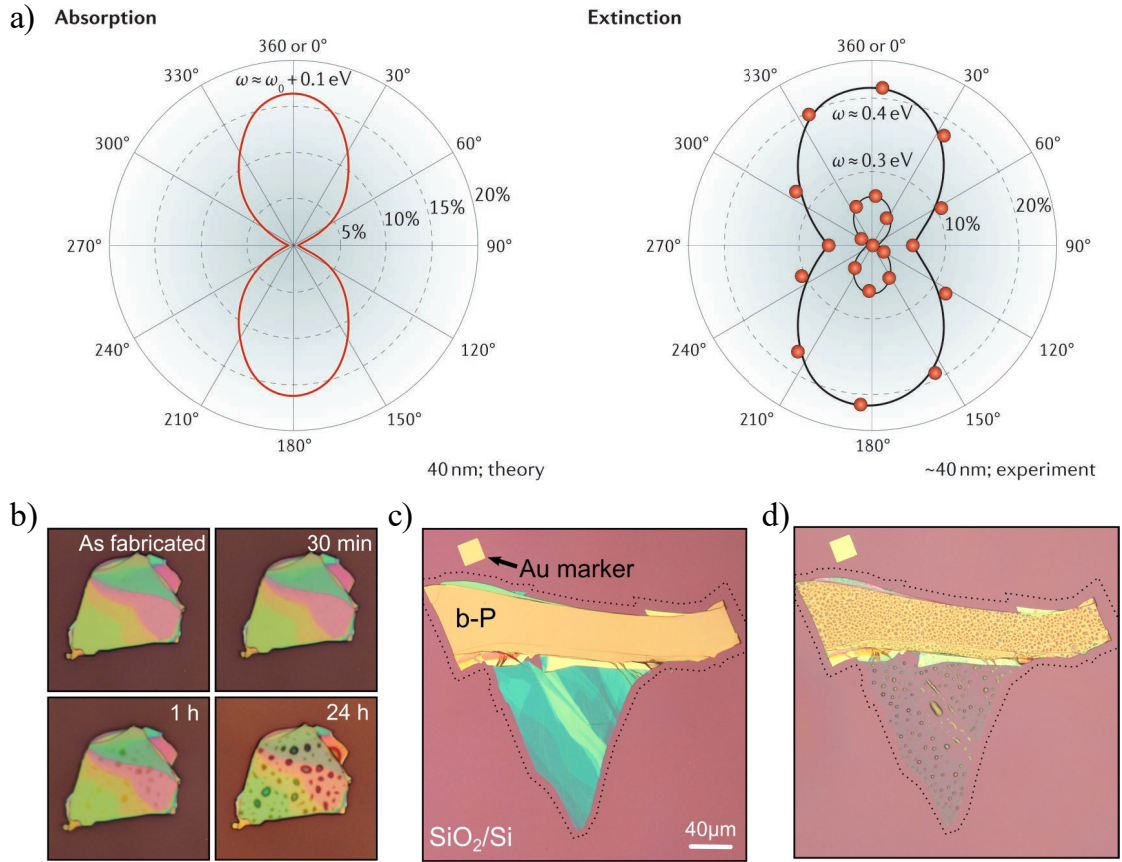


Fig. 2.3 Black phosphorus' polarisation-dependence and environmental instability. (a) (left) Polar plot of the theoretically calculated absorption coefficient for normal-incident light polarised at varying angles, on a 40 nm thick BP flake, at excitation energy, ω , 0.1 eV greater than the bandgap, ω_0 . Polar extinction spectra for a $\sim 40 \text{ nm}$ thick BP flake as measured experimentally (red dots) at excitation energies, ω , using Fourier transform infrared spectroscopy. Solid lines show an $a\sin^2\theta + b\cos^2\theta$ fit. Adapted from ref. 52. (b) Time-lapse optical images of a thick "bulk" BP flake under ambient conditions, degrading *via* the formation and growth of droplets of phosphoric acid on the flake surface. (c) and (d) The same BP flake, with bulk (top, yellow) and few-layer (bottom, blue) sections, freshly exfoliated, and after a week in ambient conditions respectively, showing complete degradation of the thinner sections. Parts b)-d) produced by ref. 51.

conditions, rapid photooxidation occurs, decomposing the exposed layers and nucleating droplets of phosphoric acid which grow as the reaction progresses^[51]. Favron *et al.* produced the first study of this degradation in exfoliated samples *via* Raman spectroscopic analysis (discussed further in section 3.2.2), demonstrating that the three key components were light, water vapour and oxygen, and furthermore that the reaction rate is linearly related to the concentration of oxygen and intensity of light^[9]. During the reaction, photo-induced charge transfer at the BP surface produces O_2^- , which further dissociates to form P_xO_y . The

formation of hydrogen bonds between adsorbed water and the bonded oxygen then facilitates the removal of P atoms from the surface lattice.

Crucially, Favron *et al.* also demonstrated that this photooxidation is strongly dependent on the thickness, that is, the number of layers, of the BP flakes, with their analysis suggesting that the rate of oxidation for an n -layer flake, $\frac{d\theta}{dt}$, increases linearly with respect to n ^[9]. Further to this, they also revealed that the rate of degradation was related to the bandgap of an n -layer flake, $E_{g,n}$ according to:

$$\frac{d\theta}{dt} \propto e^{-E_{g,n}^2}. \quad (2.2)$$

Here, the increase in bandgap from few to monolayer flakes - arising from quantum confinement - results in greater overlap of the edge of the BP conduction band and that of the O₂ acceptor states, leading to faster charge transfer between the two and thus, a higher degradation rate.

For few-layer flakes, after a short (few minutes) nucleation step, significant degradation of the optical properties can usually be seen under ambient conditions on a timescale of 1-2 hours, whilst complete decomposition to phosphoric acid can occur after only a matter of days^[9,64]. Use of a capping layer, such as parylene-C or PMMA, atomic layer deposition of AlO_x, or encapsulation in h -BN, can reliably prevent water vapour from interacting with the BP surface and is so far the most effective method for maintaining long-term stability of BP's electronic and optical properties^[65-68].

2.2 Production techniques

2.2.1 Mechanical exfoliation

The original technique first used by Geim and Novoselov to isolate graphene is known as micro-mechanical exfoliation, sometimes dubbed 'the scotch tape method'^[3]. Here, fragments of a bulk layered material are pressed between two sections of adhesive tape, which are then pulled apart, cleaving sections of layered material from the bulk due to the weak inter-layer bonding. This procedure is repeated to leave successively thinner flakes of material attached to the tape, before finally pressing one of the tape pieces to a desired substrate and peeling away, leaving behind deposited flakes. Depending on the material being exfoliated, pre-treatment of the substrate, such as with oxygen plasma, is often required to alter the surface energy such as to promote sufficient flake adhesion.

The process as a whole is labour intensive and near inherently un-scalable, with low monolayer yields and no control on flake dimensions. However it still remains the method of choice for proof-of-concept devices requiring the deposition of high-quality, pristine 2d material flakes^[69]. Furthermore, it serves as an entirely "dry" transfer technique that bypasses any solvent-based steps liable to create surface contamination. Considering the unstable chemistry of BP, where exposure to air or moisture must be minimised, mechanical exfoliation in a glove-box under inert conditions is to date the only reliable way to obtain monolayer flakes of sufficient size for electronic characterisation or device fabrication^[66]. The degradation of mechanically exfoliated BP flakes is studied in my experimental work in the next chapter.

2.2.2 Chemical vapour deposition

Chemical vapour deposition (CVD) has been used for decades in the semiconductor industry as a bottom-up technique to grow thin films on a variety of substrates^[70] and in recent years it has emerged as arguably the most promising candidate for the production of large-area, continuous monolayer graphene films, on an industrially scalable basis^[4,69]. Whilst growth of TMDs and *h*-BN is now also routinely achieved, the chemistry of BP has thus far prevented any reliable production of mono- or few-layer crystals *via* CVD methods^[5,66]. CVD-grown graphene is used within this thesis to serve as a sensing electrode in graphene-BP and -nanowire hybrid devices.

A typical graphene CVD process involves passing of a gaseous hydrocarbon over a transition metal substrate, under high temperature conditions of ~ 1000 °C^[4,69]. The metal surface acts as a catalyst to facilitate decomposition of the precursor material, allowing for nucleation of carbon adatoms at the surface and initiating development of a graphene lattice^[71]. The thickness of the film produced is primarily dependent on the properties of the transition metal used. Early methods of graphene production *via* CVD used Ni, which allows for majority few-layer film growth due to the relatively high solubility of carbon in the metal (~ 0.9 at 900 °C)^[72,73]. Here, during the growth process, carbon atoms dissolve into the Ni bulk at high temperatures, before precipitating out with subsequent cooling^[74]. For monolayer growth however, the most widely used metal is Cu, for which the solubility of carbon is negligible^[75,76]. This results in a self-limiting process whereby the catalytic action of the surface is blocked for areas where a graphene film has already formed, thus preventing the thickness growing beyond a single layer^[71].

While the scale of growth is essentially limited only by the dimensions of the substrate^[77], it is important to note that such CVD films are inherently polycrystalline^[78]. This is due to the nature of a typical CVD growth process, whereby graphene grains spread from

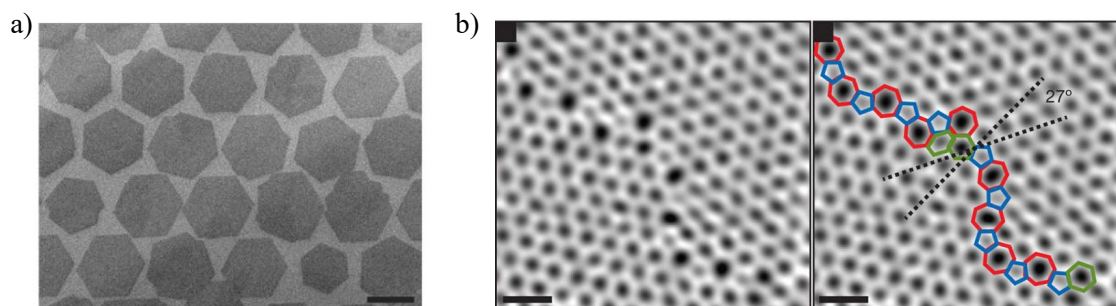


Fig. 2.4 **Growth of graphene by chemical vapour deposition.** (a) SEM image showing the CVD growth of monolayer graphene islands on a Cu foil, with regularly-spaced, suppressed nucleation as mediated by a pre-patterned seed crystal array. Scale bar is 10 μm . Taken by ref. 82. (b) Annular dark-field scanning transmission electron microscopy of a graphene grain boundary, produced by ref. 79, showing the ‘patchwork quilt’ nature of CVD graphene films, as well as the potential for lattice misalignment at grain boundaries, showing a 27° difference in lattice orientation (right-hand panel). Scale bars are 5 \AA .

multiple nucleation sites on the surface (see Fig. 2.4a), before joining up with each-other to form a continuous sheet^[79,80]. Due to the random orientation of nucleation and growth, lattice mismatch occurs at grain boundaries as illustrated in Fig. 2.4b, with a corresponding disruption of charge transport across these features^[78,81]. The size of grains, and thus the carrier mobility of the film, can be increased by suppression of the nucleation density (also illustrated in Fig. 2.4a), which can be controlled by a number of growth conditions, such as the pressure, temperature and the recipe of gases used, as well as by the creation of ‘seeding’ sites on the metal surface^[82].

No high-yield method currently exists for growth on insulating substrates and as such, another significant drawback of CVD is that any subsequent device fabrication requires the transfer of graphene off of the metal surface^[5]. As will be discussed in more detail in chapter 5, this is most commonly achieved via wet transfer based methods, whereby the graphene layer is coated in a polymer scaffold, before being floated onto an etchant solution to remove the metal substrate^[77,83]. The graphene-polymer layer can then be ‘fished’ from the solution onto a desired substrate and the scaffold removed with a suitable solvent. While versatile in their compatibility with a range of substrates, such wet transfer methods have been shown to induce significant strain, and corresponding transport disruption, in the resultant lattice^[84], as well as often leaving behind wrinkles, cracks and residual polymer^[85,86].

2.2.3 Liquid-phase exfoliation

Another widely used method for 2d material production is liquid-phase exfoliation (LPE), which is studied extensively in this thesis with regard to scalable production of BP. Typical

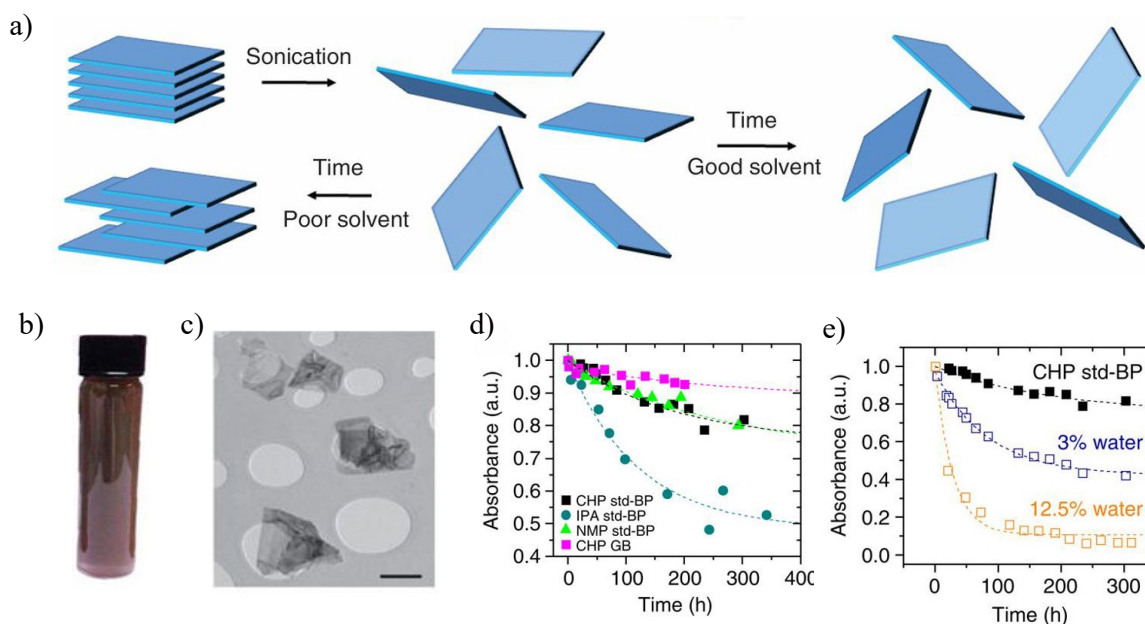


Fig. 2.5 Production of 2d materials by liquid-phase exfoliation. (a) Schematic illustrating ultrasonication-assisted liquid-phase exfoliation in a suitable solvent, producing a stable dispersion of single-layer flakes, and an unsuitable solvent, with reaggregation of monolayers to bulk, stacked crystals over time. Adapted from ref. 87. (b) Bottled dispersion of few-layer BP flakes exfoliated via ultrasonication in a CHP host solvent. (c) TEM imaging of few-layer flakes extracted from the dispersion in (b). Scale bar is 500 nm. (d) Stability comparison of four different BP dispersions, exfoliated in CHP, NMP and IPA under ambient conditions (std-BP) and CHP in glove box (GB), as demonstrated through the changes in their relative measured absorbance over time (at 465 nm). (e) The effect of water on the optical stability of BP dispersions, shown through comparison of the time-resolved absorbance (465 nm) of flakes exfoliated in a CHP host solvent, and the same dispersion with 3% and 12% water added. Parts b)-e) adapted from ref. 88.

LPE processes involve the submersion of bulk layered materials in a solvent, followed by the application of ultrasonic energy, to create highly localized pressure variations^[69,89,90]. Cavitation is induced within the liquid, and the subsequent collapse of inter-layer bubbles creates forces large enough to separate sheets of material from the bulk^[87]. Similar results can also be achieved through a variety of other methods, such as subjecting the mixture to high shear forces via processes such as microfluidisation. Chemical-based solution approaches can also achieve separation of 2d material sheets from the bulk - often through oxidation and subsequent reduction - though usually are detrimental to the properties of the nanomaterial flakes^[91,92]. After exfoliation, high speed centrifugation is usually employed to sediment unexfoliated material and thicker flakes, isolating dispersions with high yields of monolayer and few-layer flakes^[93]. The majority of LPE work has been focused on solution-processing of graphene and TMDs^[5], but more recently BP dispersions have also been produced^[94],

examples of which (including images of resultant, few-layer BP flakes), can be seen in Figs. 2.5b and c.

Host solvents or surfactant mixtures must be carefully chosen so as to maximise exfoliated flake yield and prevent re-aggregation of flakes post-exfoliation (as illustrated schematically in Fig. 2.5a), ensuring the stability of the dispersion over time with minimal sedimentation. The yield and stability can be assessed for different solvents by looking at the initial mixture concentrations and flake thickness distributions, and the change in optical properties (usually absorbance) over time, respectively. Here, consideration of the solution thermodynamics, through a solubility parameter analysis, is often made to predict which solvents may be suitable for a particular material^[95–97]. In the case of 2d flakes, the Hansen solubility parameter framework has proved the most reliable route, whereby the enthalpy of mixing per volume of mixture, $\Delta H_{Mix}/V$, can be expressed as:

$$\frac{\Delta H_{Mix}}{V} \approx \phi [(\delta_{D,S} - \delta_{D,N})^2 + \frac{1}{4}(\delta_{P,S} - \delta_{P,N})^2 + \frac{1}{4}(\delta_{H,S} - \delta_{H,N})^2] \quad (2.3)$$

where ϕ is the solute (flake) volume fraction and δ_D , δ_P and δ_H are Hansen solubility parameters relating to dispersive, polar and hydrogen-bond interactions respectively, with the second letter of the subscript denoting parameters of the solvent (S) or solute (N)^[95]. It can be seen that to minimise the enthalpy of mixing, and to promote a mixture that is stable against sedimentation, $\delta_{x,S} = \delta_{x,N}$, that is, the parameter for the solvent should match as closely as possible that of the flakes, for each of the three interactions considered.

For graphene, a variety of high boiling point solvents prove well matched, such as DMF (N,N-dimethylformamide), Benzyl benzoate and NMP (1-methyl-2-pyrrolidone), the latter of which has been most commonly used to produce the highest yields of mono- to few-layer flakes (for instance up to 97% 1-5 layer flakes in ref. 95)^[89,95,98]. However, the toxicity of these substances, and the high temperatures required to remove them post-exfoliation, mean that in some applications a compromise on yield must be made to use alternative, low boiling point solvents such as acetone, isopropanol or chloroform^[5].

In the case of BP, considering its sensitivity to moisture, light and oxygen, LPE methods provide a viable route to scalable production, as they can be carried out using anhydrous solvents, in the dark, under inert atmosphere. As with graphene, high boiling point solvents are the most well matched in terms of minimising interfacial tension with BP flakes, with DMF, NMP and CHP (N-cyclohexyl-2-pyrrolidone) shown to produce the most stable, well-exfoliated and highest concentration dispersions (shown in stability plot in Fig. 2.5d)^[88,94,99,100]. As can be seen in Fig. 2.5e, Hanlon *et al.* demonstrated the importance of using anhydrous solvents, showing rapid degradation of dispersions after addition of

water^[88]. BP flakes produced by LPE typically range from 3-15 nm in thickness, though Brent *et al.* showed evidence of mono and bi-layer crystals of far smaller relative lateral dimensions^[88,94,99,100].

LPE techniques hold a number of significant advantages, especially with respect to industrial-scale production. The equipment and materials used to produce them are low-cost and the techniques involved can easily be scaled for high-throughput processes^[69]. On top of this, as highlighted earlier, they can be applied to almost any known layered material, through appropriate tailoring of the solvents or surfactant-based solutions used^[96,101]. Perhaps most importantly, as will be covered in the next chapter, dispersions can be modified to create functional, 2d material inks, allowing for their deposition on almost any substrate through a variety of established methods, such as inkjet, gravure and flexographic printing, which have pre-existing industrial infrastructure^[5,69,98,102]. However, here it should be noted that films deposited in these ways are disordered in nature, formed of a network of interconnected flakes^[93]. As such, whilst individual flakes can retain high quality^[103], the electronic properties of the film as a whole are significantly compromised^[98].

2.3 Material characterisation

2.3.1 Atomic force microscopy

Atomic force microscopy (AFM) - more generally scanning probe microscopy (SPM) - is a powerful measurement technique for probing the surface topography of a material, routinely capable of sub-nanometer vertical resolution, lateral resolutions down to ~ 10 nm and is one of the central techniques for assessing the physical characteristics of 2d materials and nanowires within this thesis. More recently the technique has been expanded to afford analysis of a wide range of different properties including frictional forces, magnetic domains, electrostatic fields and surface work functions, tunnelling currents, as well as dopant types and densities.

Typical AFM operation involves a flexible micro-cantilever carrying a sharp tip, typically of radius 5 - 15 nm, scanning across the surface of the analyte in a raster pattern, controlled by a piezoelectric actuator capable of sub-Angstrom precision. An example of an AFM cantilever with tip is shown in Fig. 2.6a. A laser is shone onto the end of the cantilever and reflected onto a photodiode detector, where changes in the deflection of the probe are monitored as it interacts with the surface. ‘Tapping mode’ is the most contemporary technique for imaging, whereby the cantilever is driven to oscillate at a constant frequency (usually at or near resonance) and amplitude. The tip is brought close to, but not in contact

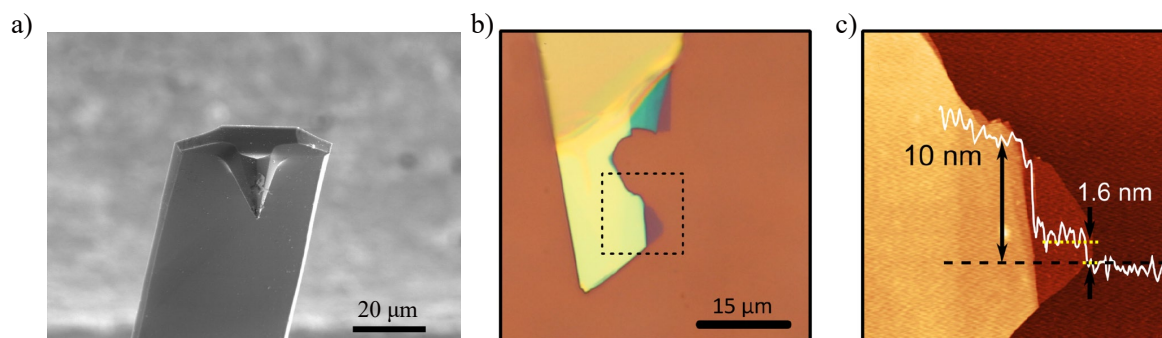


Fig. 2.6 **Atomic force microscopy of 2d materials.** (a) AFM cantilever with tip, as imaged *via* SEM after use, demonstrating the attachment of particulates from the environment over time. Scale bar is 20 μm . Adapted from en.wikipedia.org. (b) and (c) Optical and AFM image respectively of a mechanically exfoliated BP flake. Blacked dashed line in (b) indicates the area scanned via AFM, whilst the annotations on (c) show the topographic profile (white line) and step heights (arrows), as measured scanning across the black dashed line, of the thinner and thicker sections of the flake relative to the silicon substrate. b) and c) adapted from ref. 51.

with, the surface, where distance-dependent forces such as Van-der-Waal and dipole-dipole interactions act upon it. The resulting changes in oscillation amplitude serve as the input to a feedback loop, which correspondingly varies the height of the cantilever so as to maintain constant oscillation behaviour, in turn constructing a z-plane map as it is scanned along the surface. Figures 2.6b and c exemplify typical AFM imaging of a mechanically exfoliated 2d material flake, with corresponding height profile and optical image.

AFM is not without its limitations; lateral scan dimensions are restrained to around 100 - 150 μm , while high resolution imaging can take many hours to complete. Additionally, though horizontal control of the cantilever is extremely precise, actual resolution in the x-y plane is ultimately determined by the tip sharpness, and certain features, such as extreme pits or holes, are often challenging to measure accurately. Furthermore, AFM tips are liable to rapid wear and the blunting or damaging of these probes, or the attachment of loose particulates from the sample (as can be seen on the tip in Fig. 2.6a), can significantly reduce resolution as well as introduce artefacts into the image.

Probably the most common usage of AFM for 2d material characterisation is to determine flake thickness and number of layers. Here it is worth noting that in practice the measured or ‘apparent’ height of a monolayer is usually far greater than the theoretically predicted layer thickness, possibly due to the adsorbed moisture layer or other complexities relating to the tip-surface interaction. For instance in ref. 88, the step change between layers in BP flakes is measured as ~ 2.1 nm compared with a calculated crystal spacing of ~ 0.5 - 0.7 nm. AFM is also often employed to assess physical contamination or wrinkles at the flake surface, as well as to image LPE films for statistical analysis of thickness and lateral flake size distributions.

2.3.2 Raman spectroscopy

Raman spectroscopy is an all-optical characterization technique that has recently come to the fore as a highly effective tool for the analysis of graphene and other 2d materials, due to its speed, simplicity and its non-destructive, non-contact nature^[106–108]. Fundamentally, the measurement involves the illumination of a sample by an intense laser light source, of selected wavelength, and detection of the scattered photons by a charge coupled device (CCD). Spectra of light collected at the detector will contain a strong peak at the frequency of the laser due to lossless, elastic (Rayleigh) scattering of photons, along with weaker peaks

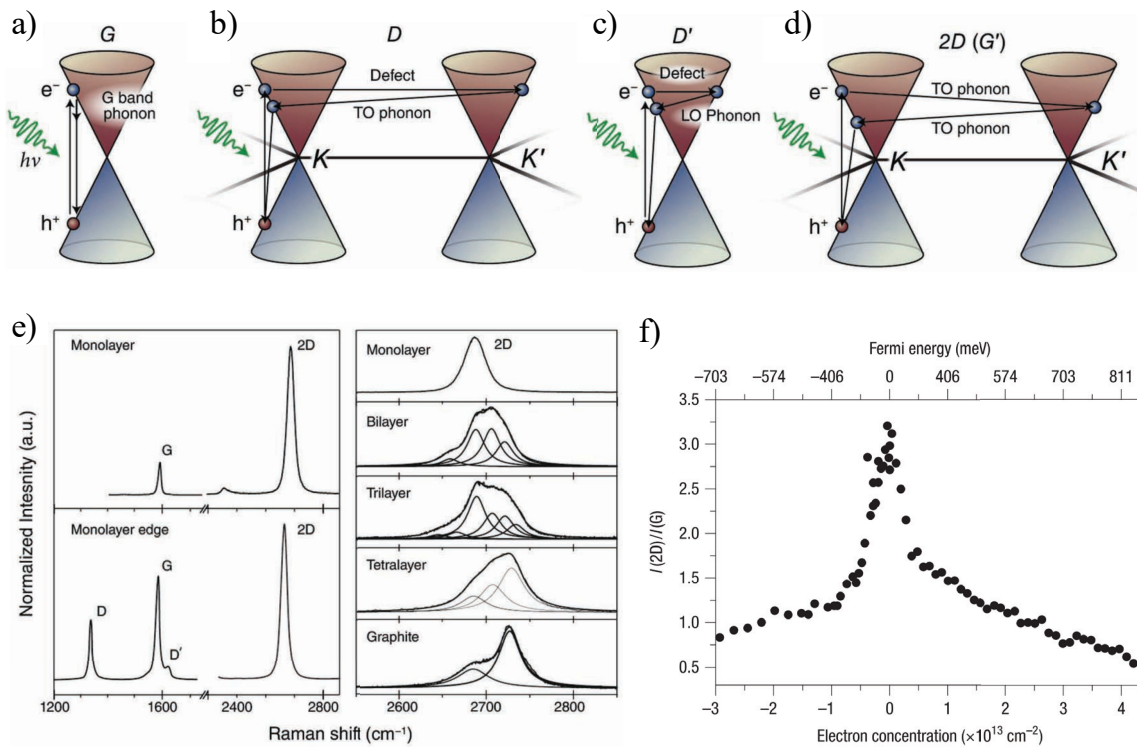


Fig. 2.7 Raman spectroscopic analysis of graphene. (a)-(d) Band diagram illustrations demonstrating mechanisms for a selection of Raman processes in graphene, showing (a) first-order Raman scattering corresponding to the G-band, (b) second order *inter-valley* scattering involving a defect and a *transverse* optic phonon corresponding to the D band, (c) second order *intra-valley* scattering involving a defect and a *longitudinal* optic phonon corresponding to the D' band and (d) second-order double resonance scattering from two transverse optic phonon modes, corresponding to the 2D (or G') band. (e) Characteristic Raman spectra taken from the center (top) and edge (bottom) of a graphene monolayer showing peaks associated with the processes detailed in a)-d). Parts a)-e) produced by refs. 104 and 10. (f) The intensity ratio, $I(2D)/I(G)$, between the 2D and G Raman peaks, under varying electrostatic doping, in an electrochemically top-gated graphene FET channel, as measured in ref. 105.

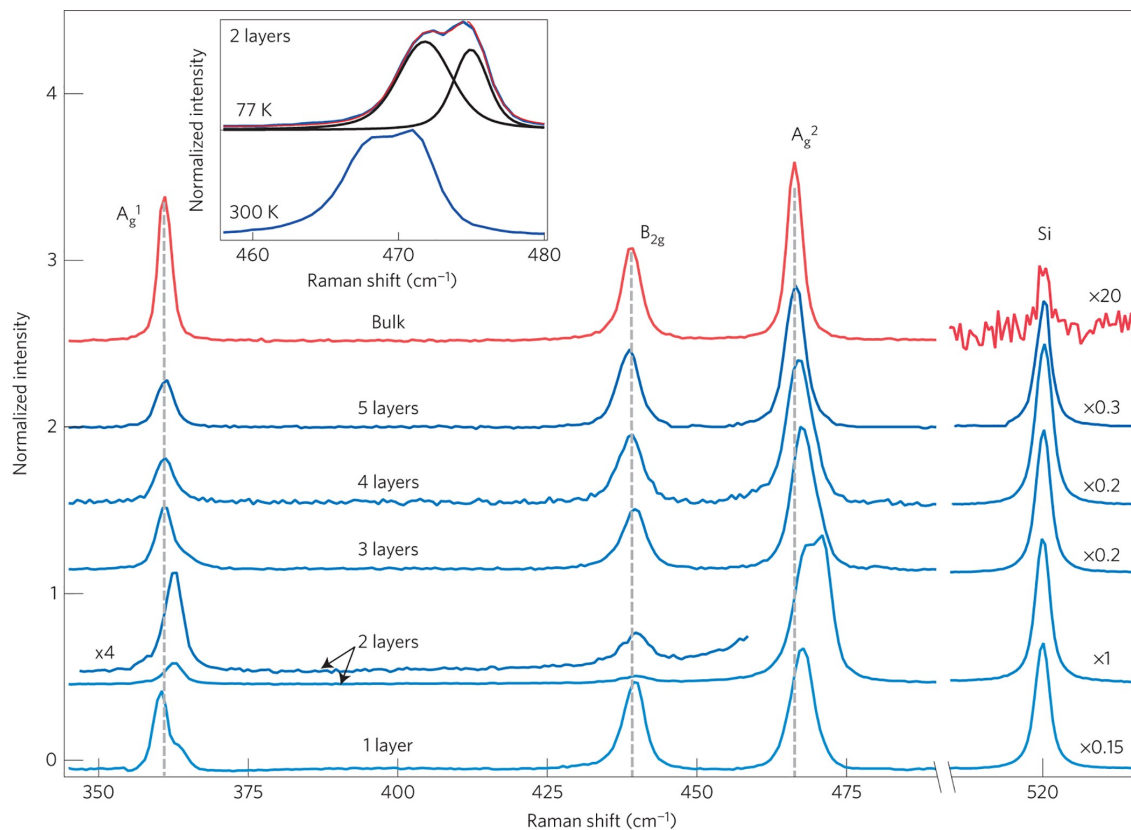


Fig. 2.8 **Raman spectra of n-layered black phosphorus.** Evolution of the characteristic BP Raman spectra from bulk to n-layer flakes, measured using a 532 nm wavelength laser at 300 K. Inset shows the exceptional case of the A_g² peak in bilayer BP, measured at low and room temperature. Figure adapted from ref. 9.

shifted at specific frequencies away from the excitation frequency^[106]. These shifts result from inelastic scattering of incident photons by phonons in the target material lattice, and can be at frequencies either above or below that of the laser, named anti-Stokes and Stokes shifts respectively^[109]. Using graphene as an example, band diagrams illustrating some of the Raman scattering processes that contribute to its most prominent resonance pathways are seen in Figs. 2.7a-d, whilst their corresponding peaks can be seen in the characteristic spectra in Fig. 2.7e.

Photon-phonon interactions are highly dependent on electron movement, interference and scattering within a lattice^[108]. As such, analysis of the position and relative intensity of Raman peaks can be used to probe a wide range of 2d material properties. In graphene these include the number of layers, doping, strain, structural defects, as well as being able to identify contamination, chemical modifications or the addition of functional groups that may have arisen in any previous processing stages^[105,110,111]. Furthermore, Raman spectroscopy is an especially useful analytical technique for graphene in particular, given that

all wavelengths of incident radiation are resonant due to its gapless band structure^[107,108,110]. The effect of electrostatic doping on the Raman peak in a graphene FET channel is plotted in Fig. 2.7f, exemplifying one way in which Raman spectroscopy can be used to probe the electronic properties of 2d materials.

The Raman spectrum of bulk BP, shown in Fig. 2.8, contains three characteristic peaks, corresponding to one out-of-plane phonon mode, A_g^1 , centered at 361 cm^{-1} , and two in-plane modes, B_{2g} and A_g^2 , centered at 438 cm^{-1} and 466 cm^{-1} respectively^[112]. As can also be seen in Fig. 2.8, with decreasing layer number, n , (aside from the exceptional case of bilayer BP) peak positions and shapes remain largely unchanged, aside from a modest shift of the A_g^2 center frequency, reaching $\sim 469\text{ cm}^{-1}$ at monolayer^[9]. As with many of its properties, BP's structural anisotropy means that these features are highly polarisation sensitive. Rotation of a BP flake with respect to the Raman laser polarisation (or vice versa) results in significant variation in the intensities of all three Raman modes, though for the A_g^1 and A_g^2 modes the extent and shape of these effects are also wavelength- and thickness-dependent^[113,114]. For my research, Raman spectroscopy is largely used for characterising the progression of BP flake degradation, as was pioneered in an extensive study by Favron *et al.* in ref. 9 and which shall be introduced in more detail in the next chapter.

Summary

In this chapter I have reviewed the literature on the 2d materials of concern to my thesis, graphene and BP. Considering graphene in the field of optoelectronics, its high flexibility and conductivity, as well as its robust physical properties and low absorption, make it ideal for use as a transparent electrode. Whilst its gapless band structure limits capabilities for detection, its uniquely sensitive transport properties offer an avenue toward high photoresponsivity, when, for instance, electrostatically coupled with a highly absorbing material. In the case of BP, it has been shown that its thickness dependent, *direct* bandgap, from 0.3 - 2.0 eV, makes it thus far the best suited 2d material for infrared detection. However, its unstable chemistry, with rapid degradation in ambient conditions, presents a significant challenge for device fabrication and the realisation of any scalable applications.

Further, I have provided background on the techniques used for production and characterisation of these materials in this thesis. Due to its chemistry and instability, LPE is of particular importance to BP in providing arguably the only viable route for its scalable production to date and the investigation of solution-processed BP flakes and films forms the majority of my work on 2d materials. AFM and Raman spectroscopy were introduced, highlighting the strength of the latter as a hugely versatile, non-destructive technique able to

optically probe a wide range of physical and electronic 2d material properties. As covered in the last section, of particular relevance to this project, is its capability to study the progression of degradation in BP flakes, as is applied to solution-processed films in my research. In the next chapter, I will move on to discuss the most significant secondary project during my PhD - the study and development of a liquid-phase-exfoliated black phosphorus ink for use in optoelectronic applications.

Chapter 3

Solution-processing of black phosphorus for optoelectronics

Overview

As laid out in chapter 2, the thickness-dependent bandgap of black phosphorus (BP) bridges an energy window within the family of 2d materials, between that of patterned graphene and transition metal dichalcogenides. Along with its anisotropic electronic and optical properties, this affords it potential for infrared optoelectronic devices in particular. However, the large majority of devices demonstrated so far are based on flakes produced by mechanical exfoliation - a process with highly limited throughput. The chemistry of BP makes current CVD techniques unviable for its growth and as such liquid phase exfoliation is at present the only method with the capacity to produce BP in a readily scalable manner.

For the deposition of such LPE-derived dispersions during device fabrication, a range of printing techniques have been used, as demonstrated with many different 2d materials^[5]. Of these methods, inkjet printing provides arguably the most controllable and high resolution technique for precise patterned deposition of device features. However, the solvent(s) used for dispersions usually require significant rheological modification, or even to be exchanged, to render them into an ink that can be printed. In the particular case of BP, any potential formulation of such an ink, and the stability of any films printed, is further complicated by its thickness-dependent liability to photooxidise in the presence of moisture. Thus, whilst LPE production of BP had been demonstrated in multiple publications^[88,94,99,100], as of 2017, no groups had developed a method for depositing solution-phase BP flakes in thin-films for device fabrication.

Separate to my work on nanowire-based devices, a parallel project during my PhD was toward the formulation and demonstration of a stable BP ink for optoelectronic applications. In this chapter I will detail the experimental work carried out to achieve this aim, along with the presentation and discussion of results. This will begin with a short summary of the background literature on the use of inkjet printing as a means of depositing 2d materials, to help frame the following experimental work. Beyond that, my experimental research on this project will be covered, the first half of which will focus on the creation of BP dispersions. This will touch first on the LPE of BP in different solvents, determining which is the most suitable through the characterisation of the resultant dispersions by both optical and physical techniques. I will then detail my use of Raman spectroscopy as a tool to analyse the degradation of BP in the aforementioned publication before discussing my own study of BP stability using AFM measurements. The second half of the chapter concerns the process of converting the dispersion to a functional, application-ready BP ink. Within this, the first section describes the solvent-exchange process and characterisation involved to optimise the jetting and deposition of individual ink droplets. The second section moves on to discuss the optimisation of printing continuous features, the characterisation of printed films as well as the use of parylene-C as a protective, stabilising layer. In the final section, I detail devices fabricated using the ink - a photodetector and pulsed laser system - which demonstrate its viability as a low-cost, easily integrated and stable component for optoelectronic applications. This research contributed to the publication of ref. 115 in Nature Communications in 2017, in collaboration with Dr Guohua Hu. Dr Hu designed the ink and performed all steps related to its printing, while I produced the dispersions and inks, and designed and carried out all AFM and Raman spectroscopy analysis. External collaborators (authorship listed in item 1 in ‘Publications’) produced the device demonstrations.

3.1 Background: solution-phase techniques for deposition of two-dimensional materials

As discussed in chapter 2, liquid-phase exfoliation (LPE) has become established as a reliable way of mass-producing 2d material flakes in solution. Whilst in some applications, such as composites, these dispersions can be incorporated directly into another material, most devices require flakes to be deposited as thin-films. For these purposes, a variety of techniques with pre-existing industrial infrastructure have proved viable, such as inkjet, gravure and flexographic printing, as well as spin- and spray-coating^[5,69]. The choice of process depends upon its suitability for a particular application, based on considerations such as the thickness

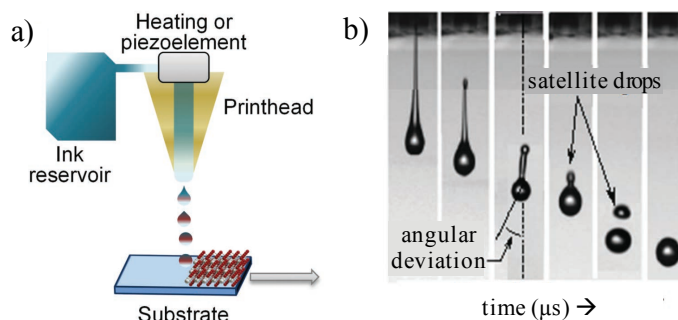


Fig. 3.1 **Inkjet printing as a 2d material deposition technique.** (a) Schematic of a drop-on-demand inkjet printing system for deposition of 2d materials. (b) In-situ imaging of the jetting process with a non-optimised ink, demonstrating two commonly seen problems; angular deviation and formation of satellite droplets. Both adapted from ref. 117.

of the film required, the substrate to be deposited on, as well as whether the film needs to be patterned and at what resolution.

Inkjet printing, the deposition technique used in this thesis, holds a number of advantages for device-based applications when using inks containing 2d material flakes. Drop-on-demand systems are commonly used in the field for the non-contact deposition of individual droplets, positioned with micrometer-scale precision^[116]. A diagram of a typical system is shown in Fig. 3.1a. Custom patterns can be printed by overlapping these droplets to form continuous features, with the thickness of the film controlled through varying the number of printing passes. Here the resolution - the line-width of the features - is clearly limited to the minimum size of the droplets, though this can be down to the order of $\sim 50 \mu\text{m}$ under suitably optimised conditions^[117].

The main challenge for inkjet printing of 2d materials - and indeed, for all of the aforementioned printing methods - is that a reliable, repeatable printing process requires the rheological properties of the ink, amongst other parameters, to be finely tuned. The solvents that are the most appropriate for dispersing flakes of a particular material with high yield at the LPE stage are *not* necessarily suited for printing, in which case they must be modified or exchanged to convert them to a 2d material ‘ink’.

The two main areas for consideration when determining a suitable ink rheology concern how it jets from the printer nozzle, and how it interacts with (and dries on) the desired substrate. In the case of the former, a dimensionless figures of merit, Z , is typically employed to assess whether the properties of a particular ink lend themselves to reliable jetting^[117]. This is the inverse of the Ohnesorge number, $Z = 1/N_{Oh}$, and is derived from the Reynolds number (N_{Re} , the ratio of inertial to viscous forces) and the Weber number (N_{We} , the ratio of

inertial forces and surface tension) as follows:

$$N_{Re} = \frac{va\rho}{\eta}; \quad N_{We} = \frac{v^2a\rho}{\gamma}; \quad Z = \frac{N_{Re}}{(N_{We})^{1/2}} = \frac{(a\rho\gamma)^{1/2}}{\eta} \quad (3.1)$$

where v is the droplet velocity (of which Z is designed to be independent), a is the nozzle diameter, and ρ , γ and η are the solvent density, surface tension and viscosity respectively^[118]. The optimal range for printing is $4 \leq Z \leq 14$, below which droplets will have long tails and above which smaller secondary droplets, known as ‘satellite’ droplets, will form^[118]; Fig. 3.1b demonstrates the jetting process and these potential issues. Whilst this forms a rough guideline when designing reliable inks, printing of 2d material inks has also been demonstrated outside of this range, with Z values as high as 24^[98]. Another consideration with respect to the jetting process is that maximum lateral flake dimensions should be roughly 1/50 of the nozzle diameter^[117], or clogging will occur over time^[119].

With respect to interactions at the substrate, the ink wettability, that is, how much it will spread on contact with the surface depends on the relative interfacial energies in the droplet-substrate system. Here, analysis can be done through measurement of the contact angle θ_c (as shown in Fig. 3.2d), which can be related to the interfacial energies between substrate, droplet and environment using Young’s law,

$$\gamma_{SV} - \gamma_{SL} - \gamma_{LV}\cos\theta_c = 0, \quad (3.2)$$

where γ_{SV} , γ_{SL} and γ_{LV} are the solid-liquid, solid-vapour and liquid-vapour surface tensions respectively^[120]. Ink droplets must be able to wet the surface sufficiently or else bulging will occur in the line^[119], but excessive spreading is also undesirable as it widens the linewidth of features or leads to random deposition of material (see Fig. 3.2a)^[98]. Another consideration here is the so-called ‘coffee-ring’ effect, whereby when the evaporation rate is higher at the droplet edges than the center, particulate matter (i.e. flakes) will flow radially outward through a capillary-type mechanism, causing a non-uniform material distribution once drying is complete, as shown in Fig. 3.2b^[121]. Balancing these factors is most commonly done by either changing or modifying the solvent, such as by using binary or co-solvents^[5], or alternatively by treating the substrate to vary its surface energy, by techniques such as O₂ plasma or HMDS treatment as used for the droplet in Fig. 3.2c^[98].

Whilst optimising ink properties will ensure successful printing of individual droplets, for continuous features with overlapping droplets, such as the channel in Fig. 3.2e, other parameters, relating to the printing system as a whole, must also be tuned. A key variable here is the droplet spacing; if this is too large, the line will have scalloped edges, whilst if too

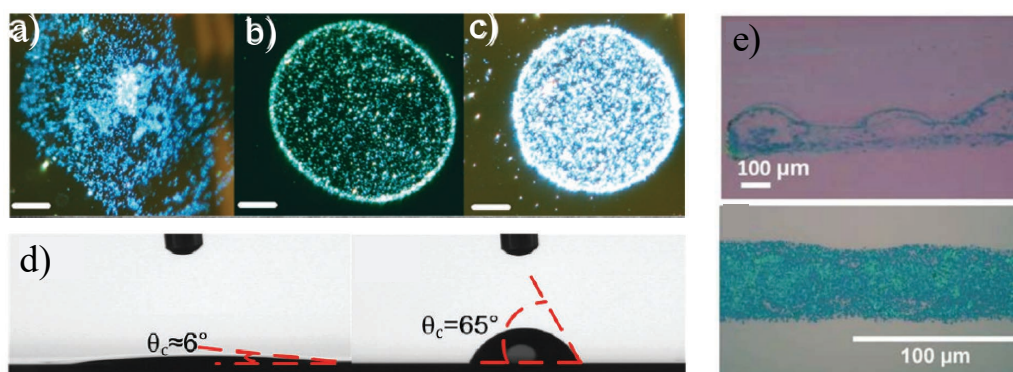


Fig. 3.2 **Imaging of 2d material inkjet printing.** Dark field optical micrographs of dried graphene ink droplets deposited on an (a) O_2 -plasma treated, (b) pristene and (c) HMDS treated $Si:SiO_2$ substrate. Scale bar is $20\ \mu m$ (d) Contact angle analysis of a water droplet on an O_2 -plasma treated (left) and HMDS-treated (right) SiO_2 surface. (e) Printed channel formed of multiple overlapping ink droplets before (top) and after (bottom) ink optimisation. a)-d) adapted from ref. 98, e) adapted from ref. 122.

small, the feature will bulge wider than the original drop diameter. Heating of the substrate can be used in order to fine-tune the droplet diameter by increasing the surface energy and thus wettability.

A general problem with most 2d material inks is that the dispersions have relatively low concentrations, typically less than $1\ g\ L^{-1}$ ^[117], meaning that multiple print passes must be used in order to deposit sufficient material. Whilst efforts are directed toward maximising concentration whilst maintaining printability, clearly rapid droplet drying is desirable in order to reduce the amount of time required between each pass, to increase throughput.

Taking these factors into account, it should be highlighted that NMP and other high boiling point solvents (such as DMF) that often obtain the highest yields at the LPE stage are not particularly well suited to inkjet printing. Aside from being toxic, NMP has low viscosity with $\eta = 1.7\ mPa\ s$, with dispersions reportedly ranging from $Z = 17 - 24$ ^[98,102], outside of the ideal jetting range, whilst its high boiling point ($\sim 202\ ^\circ C$) means that substrates must be annealed to obtain workable drying times (for example, $170\ ^\circ C$ for 5 minutes in ref. 98).

It is important to note at this stage that films deposited in these ways are disordered in nature, formed of a network of interconnected flakes^[93], and as such, whilst individual flakes can retain high quality^[103], the electronic properties of the film as a whole are significantly compromised^[98]. Carrier mobilities of graphene films produced using LPE processes are orders of magnitude lower compared to those created via CVD or micromechanical exfoliation, with optimum values in the range of $\sim 100\ cm^2V^{-1}s^{-1}$ ^[98]. However, for many applications this is no obstacle with solution-phase 2d material production and deposition

processes holding demonstrated potential for use in low-cost and flexible electronics and optoelectronics^[4,5,69]. Recently, fully inkjet printed FETs^[123], sensors^[102], capacitors^[124] and even heterostructure photodetectors^[122] have been reported.

3.2 Black phosphorus dispersions

3.2.1 Production and characterisation of dispersions

As discussed in section 2.2.3, the main underlying consideration when producing stable nanomaterial dispersions is the selection of a suitable solvent, with solubility parameters matching those of the material to be dispersed^[95,97]. Here, an empirical approach was taken by experimentally assessing the compatibility of three solvents for the LPE of BP through characterising the resultant dispersions. The solvents investigated were the high boiling point organic solvents N-Cyclohexyl-2-pyrrolidone (CHP, boiling point 284°C) and N-Methyl-2-pyrrolidone (NMP, boiling point 204°C), for which stable BP dispersion production has been demonstrated^[88]. Recognising the importance of minimising drying time at later printing stages due to BP's instability, direct exfoliation was also tested, in the low boiling point solvent, isopropanol (IPA, boiling point 82.6°C), which has been used for meta-stable exfoliation of graphene^[125].

Mixtures of bulk BP powder (Smart Elements) with anhydrous NMP, CHP and IPA (all Sigma Aldrich) were formulated, using a concentration of 1 g L⁻¹, then placed in a bath sonicator for 12 hours, at a temperature of 15°C, to facilitate exfoliation. To sediment thicker flakes or any unexfoliated material, dispersions were then centrifuged at 4000 rpm (equivalent to a force of 1500 × g) for 30 minutes, and the upper 80% siphoned off as the final dispersion, for characterisation and analysis, as well as use in the production of inks. Photographs of as-produced dispersions for the three solvents, centrifuged at different speeds, can be seen in Fig. 3.3a. For each of these processes, the tubes and phials containing the solvent-BP mixture were backfilled with N₂ and sealed, in order to create a low-O₂ environment and minimise photo-oxidation of the exfoliated flakes.

In order to estimate the concentration of the dispersions produced, and assess the relative efficacy of the solvents, UV-Vis optical absorption spectroscopy was used. To reduce the impact of scattering on these measurements, dispersions were diluted to 10% by volume of their original concentration. Plots of extinction coefficient against wavelength can be seen in figure 3.3b. Using the values for absorbance at 660 nm for each dispersion, the

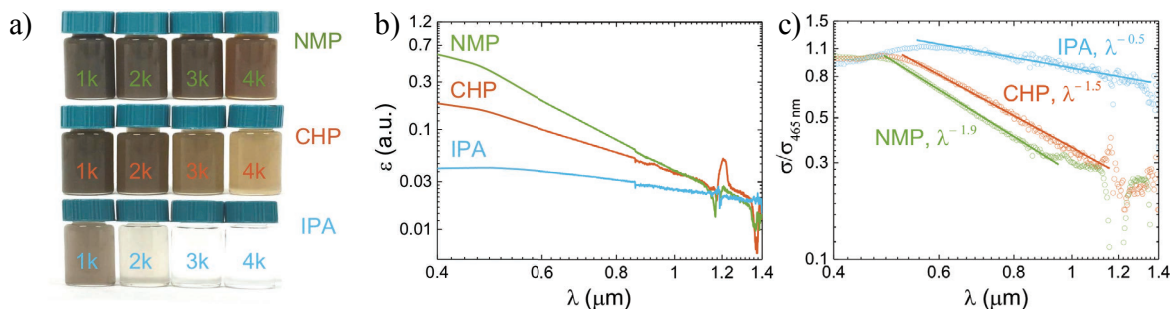


Fig. 3.3 Dispersion of black phosphorus in different solvents. (a) BP dispersions, as exfoliated *via* ultrasonication in NMP, CHP and IPA, before being centrifuged for 30 minutes at the rotational speed labelled on the bottles in $\times 10^3$ rpm. (b) Extinction coefficient for BP dispersions in the three solvents used, at varying wavelength, taken through UV-Vis optical absorption spectroscopy and plotted on a log-log scale. To avoid saturating the detector, dispersions are diluted to 10% by volume. (c) Plot of the wavelength-dependent optical scattering from flakes in the three dispersions, on a log-log scale, as normalised to the 465 nm extinction peak.

concentrations were calculated using the Beer-Lambert Law,

$$A = \alpha cl, \quad (3.3)$$

where absorbance, A , is related to the extinction coefficient, α , the concentration, c , and the optical path length, l ^[69]. A value of $\alpha = 267 \text{ Lg}^{-1}\text{m}^{-1}$ was used, as determined by ref. 126 for a wavelength of 660 nm. Thus, concentrations for NMP, CHP and IPA were estimated at 0.54 gL^{-1} , 0.32 gL^{-1} and 0.13 gL^{-1} respectively.

The optical scattering of each dispersion was then characterised to further assess the level of exfoliation by each solvent. The extinction of a dispersion has a scattering component which is proportional to λ^{-n} , where λ is the wavelength and n is the scattering exponent, for which larger values are associated with smaller, thinner flakes^[127]. The scattering characteristics for each dispersion, shown in Fig. 3.3c were obtained by measuring the absorbance spectra for each dispersion using an integrating sphere and subtracting these from the extinction. Fitting these plots gives $n \approx 1.9$, 1.5 and 0.5 for NMP, CHP and IPA respectively, suggesting that the NMP flakes are most comprehensively exfoliated.

To corroborate these results, further characterisation was carried out *via* AFM measurement (using the same equipment and operational mode as that in previous sections). Samples for AFM were prepared by repeated dropcasting of dilute (5 vol %) dispersions onto silicon chips, before drying in a desiccator under N_2 to remove residual solvent. Figure 3.4a shows a typical AFM scan of a sample area on the substrate, used to obtain size and thickness statistics for each dispersion. For reference, individual flakes, and their respective height profiles, can

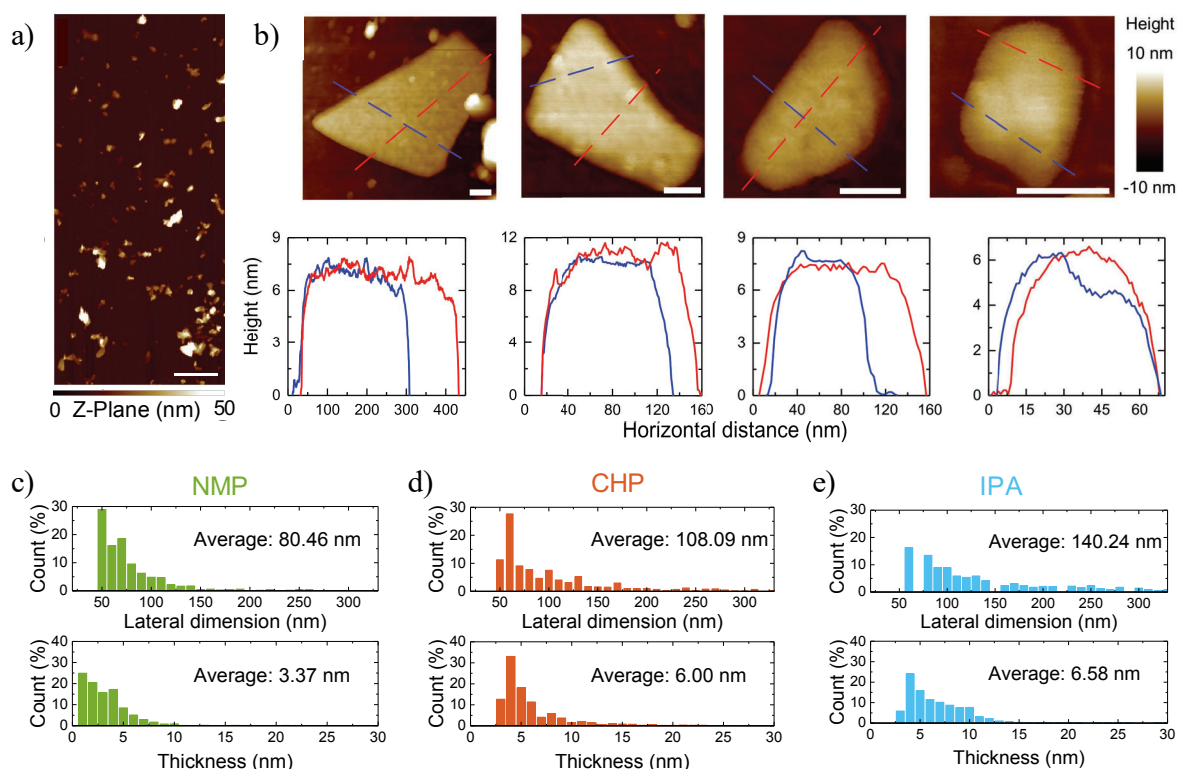


Fig. 3.4 Morphological characterisation of liquid-phase-exfoliated black phosphorus flakes. a) Section from a typical AFM scan of a drop-cast sample (from an IPA-based dispersion in this example) on Si:SiO₂ for determination of the flake thickness distribution in the dispersions. Scale bar is 1 μm. **(b)** High resolution AFM images for a sample of individual flakes with height profiles beneath, corresponding to the dashed lines in the images. Scale bars are 50 nm. **(c)-(e)** Distributions of BP flake lateral dimensions (top; taken as the major axis for each flake) and thickness (bottom) as dispersed in NMP (green), CHP (red) and IPA (blue) solvents respectively, with average values shown. Sample sizes for each dispersion are > 300 flakes.

be seen in the high resolution images in Fig. 3.4b; the even surfaces and sharp edges seen on these flakes suggest that no significant degradation (with associated phosphoric acid bubble formation) has occurred. It should be noted here that the sizes and thicknesses of these flakes are larger than average, due to the time taken to take these images, and the increased rate of degradation for thinner flakes. The lateral dimension and thickness distributions for NMP, CHP and IPA dispersions can be seen in Figs. 3.4c, d and e respectively, clearly indicating that BP dispersed in NMP was exfoliated to a greater extent, producing thinner flakes, supporting the results from the scattering spectra. Given the higher concentrations and more effective exfoliation, NMP was therefore elected as the solvent to be used going forward in the production of BP dispersions.

3.2.2 Raman spectroscopy of black phosphorus films

As discussed in the literature review, the increasing environmental instability of BP flakes with decreasing thickness is arguably the foremost challenge for realising devices with reliable performance. In this study, Raman spectroscopy was used as an analytical tool for assessing the presence and extent of any photo-oxidation of BP flakes that occurred during the dispersion processes; this was primarily inspired by its use in ref. 9 to study BP flake degradation in mechanically exfoliated samples. In ref. 9, the first of two primary signatures identified for BP degradation is a drop in the intensity of all three peaks over time, relative to that of silicon at 520 cm^{-1} . Here, A_g^2 is most commonly used as a reference, as shown plotted for a few-layer flake photooxidising under ambient conditions in Fig. 3.5a. In Figs. 3.5b and c, this metric is further used to characterise the relative rates of degradation for flakes in different conditions (passivated, vacuum, a mixture of O_2 and H_2O and ambient) as well as at different laser fluences, elucidating the dependence of oxidation on the three factors discussed in section 2.1.2: light, water and oxygen.

The second signature highlighted by Favron *et al.* is the evolution of the A_g^1/A_g^2 peak intensity ratio over time, as is demonstrated by the plot in Fig. 3.5d which they maintain to be polarisation *insensitive*, though results from polarisation-resolved Raman studies on BP contradict this claim^[113,114]. By cross-referencing the Raman data with electron-energy loss spectroscopy (EELS) and high-angle annular dark-field (HAADF) imaging, their findings suggest that pristine BP flakes typically have an $I(A_g^1)/I(A_g^2)$ ratio of between 0.4 - 0.6. As degradation progresses, this ratio gradually decreases, with values dropping to < 0.2 indicating significant levels of oxidation.

Whilst ref. 9 and many other Raman studies of BP are carried out on mechanically exfoliated flakes, refs. 88 and 99 present Raman analysis of LPE-produced samples, showing no notable or significant changes in the nature or position of peaks relative to non-solution processed samples. Yasaei *et al.* show polarisation-dependence for *individual* LPE flakes, similar to that in mechanically exfoliated flakes, and Hanlon *et al.* apply the degradation framework from ref. 9, again to *individual* LPE flakes^[88,99]. However, no work yet has carried out an extensive Raman analysis on either polarisation-dependence or degradation in solution-processed films of overlapping BP flakes, as feature in the printed devices within my research.

A Renishaw InVia microspectrometer system with an Ar^+ -ion laser was used for these measurements. For all characterisation the excitation wavelength was 514 nm and the laser power set to 0.01 mW - as low as was possible to avoid accelerating the degradation of BP flakes whilst still achieving a viable SNR. These measurements were initially carried out in ambient conditions, with an accumulation time for each data point of 10 seconds.

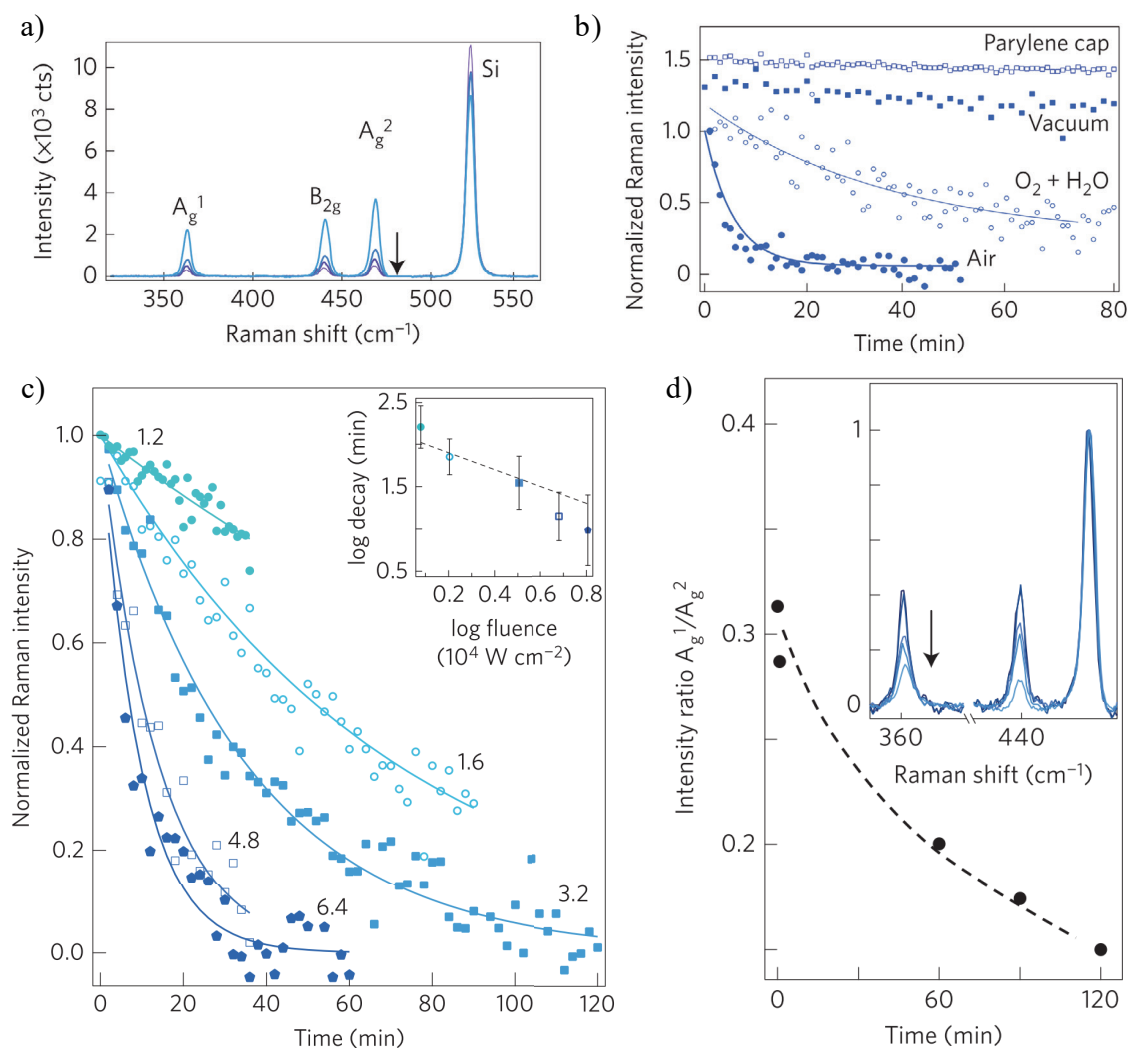


Fig. 3.5 Black phosphorus degradation as analysed by Raman spectroscopy. (a) Raman spectra measured at 532 nm, for the same ~ 5 nm thick BP flake showing a progressive decrease in all peak intensities, associated with photooxidation, when measured under ambient conditions at 24, 48, 96 and 120 minutes after exfoliation. (b) The effect of different conditions at the BP flake surface on the rate of degradation, as evidenced by evolution of the measured A_g^2 peak intensity. Showing measurements under air, a mixture of H_2O and O_2 , vacuum and under air whilst encapsulated in 300 nm parylene-C. Note the increased rate under air compared to the mixture of H_2O and O_2 is due mainly to an increased photon flux (1.7×10^4 W cm^{-2} and 1.8×10^3 W cm^{-2} respectively). Curves are shifted horizontally so as to exclude the time taken for droplet nucleation to occur, and vertically for clarity. (c) Changes in A_g^2 Raman peak intensity over time for an 8 nm thick BP flake (measured in aqueous solution, in air) illuminated under different, constant laser fluences, as annotated on the plot, all expressed in $\times 10^4$ W cm^{-2} . (d) Evolution of the A_g^1/A_g^2 intensity ratio over time for a trilayer BP flake, as it photooxidises under constant illumination from a bright lamp in air. Dashed line serves simply as a guide for the eye. All parts produced by ref. 9.

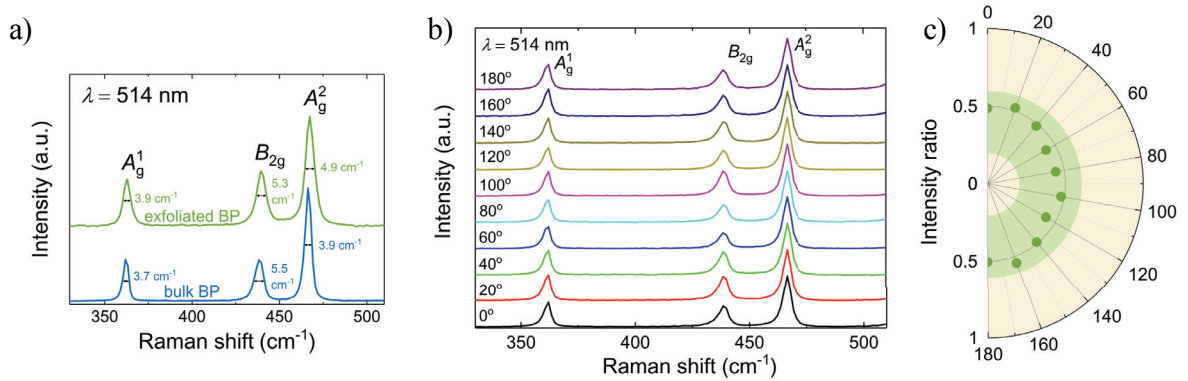


Fig. 3.6 Raman characterisation of dropcast black phosphorus dispersions. (a) Typical Raman spectra measured for BP exfoliated in NMP and dropcast onto an Si:SiO₂ substrate (blue) compared with that of a freshly mechanically-exfoliated bulk sample (black). Spectral intensities have been normalised to that of the A_g^2 peak. (b) Polarised Raman measurements for a single point on a dropcast NMP dispersion. Labelled angle represents variation in the rotation of the stage with respect to the polarisation direction of the laser probe. (c) Polar plot of the A_g^1/A_g^2 intensity ratio from the corresponding spectra in (b), with the 0.2 - 0.6 range - where flakes are not significantly degraded - highlighted in green.

For initial spectral characterisation, samples were prepared using the NMP dispersion with the same dropcast method as for AFM characterisation (on an Si:SiO₂ substrate), with measurement carried out immediately after removal from the desiccator in order to minimise exposure to air. A bulk sample was also analysed as a control, *via* mechanically exfoliating the original BP powder and measuring freshly cleaved areas. Typical Raman spectra for bulk BP and liquid-phase exfoliated flakes can be seen in figure 3.6a. The spectra observed are in corroboration with those in the literature, showing three main peaks, A_g^1 , B_{2g} and A_g^2 that correspond to the out of plane and two in-plane vibrational modes respectively^[128]. For the exfoliated flakes these lie at an average position of $A_g^1 \approx 363.0 \text{ cm}^{-1}$, $B_{2g} \approx 439.3 \text{ cm}^{-1}$ and $A_g^2 \approx 467.4 \text{ cm}^{-1}$. Peaks in the dispersion's spectra are blue-shifted by around 0.8 - 1.3 cm⁻¹ with respect to the bulk (for which peaks are positioned at $A_g^1 \approx 361.9 \text{ cm}^{-1}$, $B_{2g} \approx 438.3 \text{ cm}^{-1}$ and $A_g^2 \approx 466.4 \text{ cm}^{-1}$), which is expected due to quantisation of states in low-dimensional materials^[106]. The magnitude of the shift is smaller than that seen in the literature for flakes exfoliated to < 4 layers, suggesting that the majority of the flakes were above this thickness; this is in agreement with the findings from the AFM characterisation in the previous section.

I then looked to assess the degradation of flakes in the dropcast NMP dispersions. Introduced earlier, in the literature review, in ref. 9, the two main indicators used to assess the degradation of BP over time are the decrease in overall intensity of all peaks, and the intensity ratio between the A_g^1 and A_g^2 peaks, denoted as $I(A_g^1)/I(A_g^2)$. The latter of these was

chosen as it represents an absolute measure rather than a relative one, and thus should enable comparison of different drop cast films rather than for the same film over a period of time. As mentioned in the review section, through cross-reference of Raman data with electron-energy loss spectroscopy (EELS) and high-angle annular dark-field (HAADF) imaging, ref. 9 suggested that pristine BP flakes typically exhibit $I(A_g^1)/I(A_g^2)$ ratio of between 0.4 - 0.6, with significantly degraded flakes showing values < 0.2 . Therefore, in this study, the percentage of flakes with $I(A_g^1)/I(A_g^2)$ outside the region of 0.2 - 0.6 was used as an approximate measure of the proportion showing significant photooxidation. Throughout the investigation (in this section and later ones) analysis of how this metric varied after different stages, from exfoliation to printing, was used to capture a general picture of the extent to which flakes may have degraded.

I first sought to determine the polarisation dependence of $I(A_g^1)/I(A_g^2)$. Whilst in ref. 9 it is stated that this ratio is polarisation *insensitive*, other works have claimed that it does vary with polarisation angle, due to BP's anisotropic structure^[113,114]. Here the spectrometer's laser spot size was focused to $\sim 1 \mu\text{m}$ in diameter, while the flakes have a lateral dimension on the order of 100 nm. Therefore, the initial hypothesis was that, given the nature of the samples (a film of randomly-arranged, overlapping flakes) and the size of the laser spot relative to that of the flakes, polarisation dependence should *not* be observed. That is, even if $I(A_g^1)/I(A_g^2)$ should be polarisation sensitive for a single flake, for any one point measurement of the films, a selection of multiple, randomly orientated flakes are sampled, and as such, assuming a great enough number of flakes and orientations, this would negate any angular dependence. To assess this, the same Raman system was used, again at 514 nm, but with a rotating stage added. The same point on a dropcast NMP dispersion was measured whilst varying the rotation angle from 0° - 180° in 20° intervals, relative to a fixed polarisation direction for the laser. The spectra obtained at each angle can be seen in Fig. 3.6b, whilst a polar plot of the $I(A_g^1)/I(A_g^2)$ ratio with respect to stage rotation is shown in Fig. 3.6c. As was predicted, there was no notable dependency of the $I(A_g^1)/I(A_g^2)$ ratio on the relative angle of the sample to the polarisation direction.

A dataset was then gathered to assess the degradation after the exfoliation stage, measuring the dropcast NMP dispersions. This was done *via* Raman mapping to collect an appreciably large sample of spectra over a wide section of the film, measuring 400 points over a raster scan area of $20 \times 20 \mu\text{m}^2$. The map produced - of the $I(A_g^1)/I(A_g^2)$ for each point - can be seen in Fig. 3.7a. Typical spectra corresponding to high and low $I(A_g^1)/I(A_g^2)$ ratios, as well as null points (where SNR was too low to discern peaks) are shown in Fig.3.7b, whilst the distribution of $I(A_g^1)/I(A_g^2)$ across the map is plotted in Fig. 3.7c. Of the non-null measured spectra, 95.8 % exhibited ratios inside the 0.2 - 0.6 range, suggesting that only a

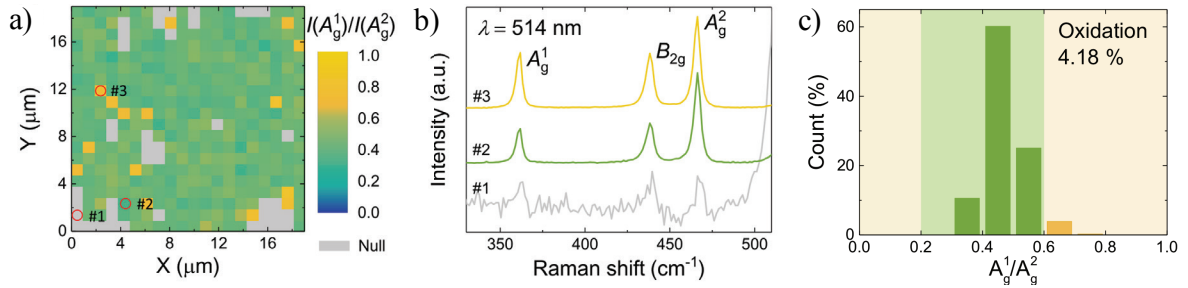


Fig. 3.7 Assessing degradation of liquid-phase-exfoliated black phosphorus through Raman spectroscopic mapping. (a) Raman mapping at 514 nm for the A_g^1/A_g^2 intensity ratio, across a $20 \times 20 \mu\text{m}$ area of dropcast BP dispersion, with a measurement grid of spacing $1 \mu\text{m}$. Raman laser focused to a spot size of $\sim 1 \mu\text{m}$ diameter. (b) Raman spectra for the correspondingly labelled points on the map in (a). (c) The distribution of A_g^1/A_g^2 ratios across the 400 points measured in the map in (a).

small portion of the flakes measured have been oxidised during the exfoliation process. A limitation here that should be noted, is that this data only represented those flakes *remaining* in the dispersion. Given that the Raman intensity of all peaks decreases with degradation, it is probable that thinner flakes have degraded entirely (either during exfoliation, after dropcasting, or during measurement) such that they do not produce an appreciable signal. Points marked as ‘null’ for instance (that have not been included in the statistics) could equally represent either areas where the BP has entirely degraded, or simply gaps in the layer, due to non-uniform flake distribution during the dropcasting. Indeed, this is also indicated by the previous AFM and Raman data on the dropcast dispersions that indicates the average flake thickness is > 4 layers thick - thinner flakes may have either completely degraded during exfoliation or flakes simply were not exfoliated to below that thickness.

3.2.3 Black phosphorus stability over time

The analysis in the previous section provides a picture of photooxidation based on the assumption from ref. 9, which is based on individual, mechanically exfoliated flakes. It is evident that a more detailed study is required on the degradation over time in collections of liquid-phase exfoliated flakes, to empirically demonstrate the validity of the $I(A_g^1)/I(A_g^2)$ metric for analysing these films. Therefore, separate to the research undertaken for ref. 115, I also began an investigation with this aim - assessing the degradation over time of the solution-processed samples. This work was planned with three channels of time-series experiments: AFM and Raman spectroscopy measurements of mechanically exfoliated BP flakes and Raman spectroscopy of drop-cast BP dispersions. Here the mechanically exfoliated samples were intended to act as a control to the liquid-phase exfoliated counterparts, to check that the

Raman results in ref. 9 could be replicated using the spectrometer available to me within a reasonable degree of accuracy. The AFM measurements were carried out in part to correlate with silicon peak intensity in the Raman analysis, as well as to independently assess the degradation rate without use of an intense laser. Furthermore, at that time, no study had carried out a detailed topographic time-series analysis of BP flakes as they degraded, over a range of flake thicknesses.

Bulk BP (sourced from hq^+ graphene) was mechanically exfoliated in a glove box under Ar atmosphere. A section of bulk material was pressed to a section of tape and removed leaving a thin layer of exfoliated material. This section of tape was then repeatedly pressed to and removed from the same area of another piece of tape, changing the orientation of the two sections each time. The tape was finally pressed onto and peeled from an Si:SiO₂ substrate, pre-patterned with a marker grid (as in previous sections for EBL) to allow for easier relocation of flakes under optical microscope. It was found that to obtain even a modest number (a selection of around 10 - 15 for a 1×1 cm² chip) of appropriately thin flakes (under 15 nm), over 15 successive peeling steps, as well as an O₂ RIE treatment (Moorfield Nanoetch system, 30 W, 120 s, 75 sccm O₂ at 3.5×10^{-3} mbar) of the SiO₂ surface were required. The chips were then mapped through an optical microscope system within the glovebox and the locations of thin flakes imaged with respect to the nearest location markers - a typical image of an exfoliated flake can be seen in Fig. 3.8a. The exfoliation and mapping processes were very low yield - even after the above optimisation of the exfoliation process, the large majority of the BP on the chip (> 99%) was still very thick, effectively 'bulk' material (yellow flakes in the image). Samples were then placed and sealed in a container whilst still in the glovebox, before removing for characterisation, such that they remained in an inert environment whilst being transported to the Raman / AFM setups. Once an initial round of spectroscopy / microscopy for a selection of flakes was complete, samples were placed in a sealed container at room temperature, illuminated from within by a typical desk lamp and shielded from outside light sources, to ensure consistent lighting conditions. Characterisation was then repeated multiple times after set periods of exposure to this ambient environment, to acquire a time-series of measurements tracking evolution of the flake degradation.

It was decided that for a rigorous study, which improved on the data already obtained within the publication, a necessary control for the Raman measurements was that they be carried out under a N₂ environment, to minimise photooxidation of flakes by the laser light during spectra collection. Therefore, spectroscopy was performed using a different system (a Horiba LabRaman Evolution, again at a wavelength of 514 nm), that allowed a sealed chamber with a glass window to be mounted to the stage, which could be purged with N₂ through a supply from an attached liquid nitrogen dewar. Unfortunately, practical

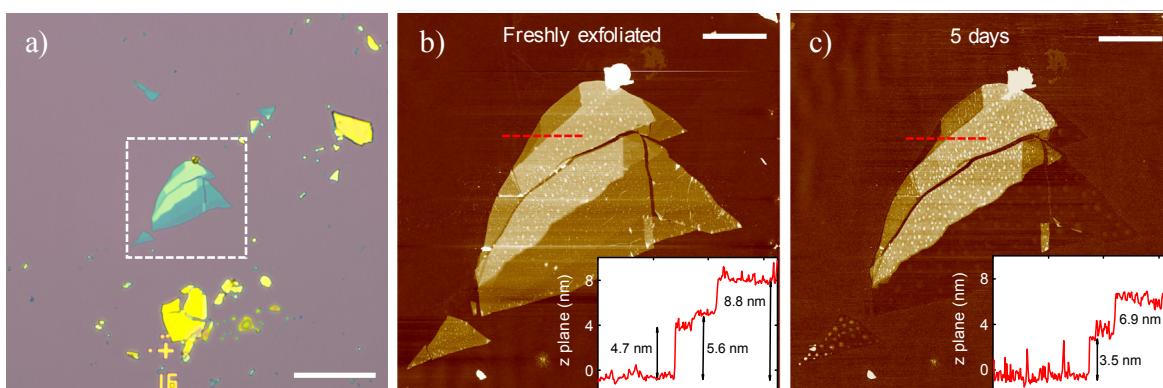


Fig. 3.8 Black phosphorus flake degradation over time. (a) Optical microscope image of BP flakes transferred onto a Si:SiO₂ substrate by mechanical exfoliation, in a glove box, under Ar atmosphere. White dashed box denotes the areas scanned by AFM in (b) and (c). Scale bar is 20 μm. (b) and (c) AFM scans of the white dashed area in (a) immediately after exfoliation and removal from the glove box, and after 5 days exposed to ambient conditions (and lighting) respectively, demonstrating degradation of the BP flake over time. Insets are height profile scans corresponding to the red dashed line in each image. Scale bars are 5 μm.

obstacles arose with this system that prevented progression of the study. Vibrations from the nitrogen supply setup as well as a gradual translational drift meant that it was impossible to accurately scan a selected area of points with a suitable level of consistency over a time series. Furthermore the N₂ chamber setup meant that a long working distance lens was required. Though magnification was at 50×, aberrations due to the glass measurement port in the chamber meant that the minimum achievable spot size was ~3 - 5 μm, making it very difficult to resolve sections of different thicknesses within individual mechanically exfoliated BP flakes (typical flake lateral dimensions were ~5 - 15 μm).

However, AFM measurements did reveal some notable findings about the nature of the degradation process in the mechanically exfoliated BP flakes. Here, the same Bruker Dimension Icon was used as in previous sections, in the PeakForce Tapping mode. The z-range of the system was reduced from 13 to 3 μm to allow for higher resolution (around 0.1 nm) in the z-dimension when measuring such small height changes. Measurements were carried out in the dark (both in the room, and with the AFM's optical microscope light turned off) to minimise photooxidation during the scans. The AFM laser provides a degree of illumination, but across flakes of the same thickness no noticeable change in degradation was observed from the start to the end of a scan (30 - 60 minutes for a high resolution, 1024 × 1024 point image), suggesting that this was a relatively negligible contribution. Clearly, the measurements would also ideally have been conducted in inert conditions, given the length of time for measurement, but such a system was not available.

Figures 3.8b and c demonstrate the degradation of a typical mechanically exfoliated BP flake (that shown in the optical image in Fig. 3.8a). The flake shown is typical of many of the mechanically exfoliated flakes, with multiple sections of different thicknesses - this is in agreement with the literature where, unlike with graphene, it is rare to find optical or AFM images of individual flakes with a uniform height plateau (*i.e.* layer number). Height profile measurement indicates three main step changes across the flake at $t = 0$, with thicknesses of 4.7 nm, 5.6 nm and 8.8 nm suggesting layer numbers of $n \approx 9$, 11 and 17 when using a value of ~ 0.53 nm per layer suggested in the literature^[129]. It should be noted as in previous sections that residues or adsorbates on the surface of the BP or Si:SiO₂, as well as inconsistencies in the interaction between AFM tip and the two different surfaces may introduce non-negligible error here when dealing with such small height differences at the limits of the system's z-plane resolution; as such these layer numbers are not certain. As can be observed, even after minimal simultaneous exposure to light and moisture, phosphoric acid bubbles have already nucleated on the surface of the freshly exfoliated flake, as is well documented in the literature. Comparing the AFM scan and height profile of the freshly exfoliated flake with that after 5 days ambient exposure and illumination demonstrates the effects of significant photooxidation. The thinnest ($n \approx 9$) section of the flake has completely degraded, with only liquid bubbles remaining on the substrate. The thicknesses of the $n \approx 11$ and $n \approx 17$ sections have reduced by 2.1 and 1.9 nm to 3.5 ($n \approx 7$) and 6.9 nm ($n \approx 13$) respectively. Heights of each section are consistent across the flake plateau (negating bubbles), corroborating the layer-by-layer nature of degradation suggested in other reports^[9].

To assess the rate of BP degradation over time, repeated scans were made of multiple sampled areas (10 to 30 μm squared) from a particular chip, themselves containing multiple flakes of different thicknesses, or individual flakes with multiple plateaus (as in Fig. 3.8). In ref. 9, Favron et al. determined a rate equation for the oxidation of BP whereby the rate increases linearly with n but also exponentially with the square of the bandgap, $E_{g,n}$. Here a simplified scenario is considered, in which the light source, and thus photonic parameters in the rate equation, is assumed to be constant, and where the rate of oxidation is directly and linearly related to the rate of thickness decrease. Theoretical calculations of the bandgap suggest that it is related to the layer number with a power law fit ($a/n^\alpha + b$) where a and b are constants and α is ~ 0.7 , depending on the methods used^[53]. Given this, in thicker flakes, where $E'_g(n)$ is low enough to be largely neglected, $n'(t)$ is simply proportional to $-n$. Therefore, it would be expected that as flakes degrade over time, n will initially decrease according to $Ae^{(-t/\tau)}$ (where A is a constant which should represent the initial flake height, and τ is a decay time constant), but as flakes become sufficiently thin, the $e^{E_{g,n}^2}$ term will begin to dominate, with the rate of degradation correspondingly rising rapidly.

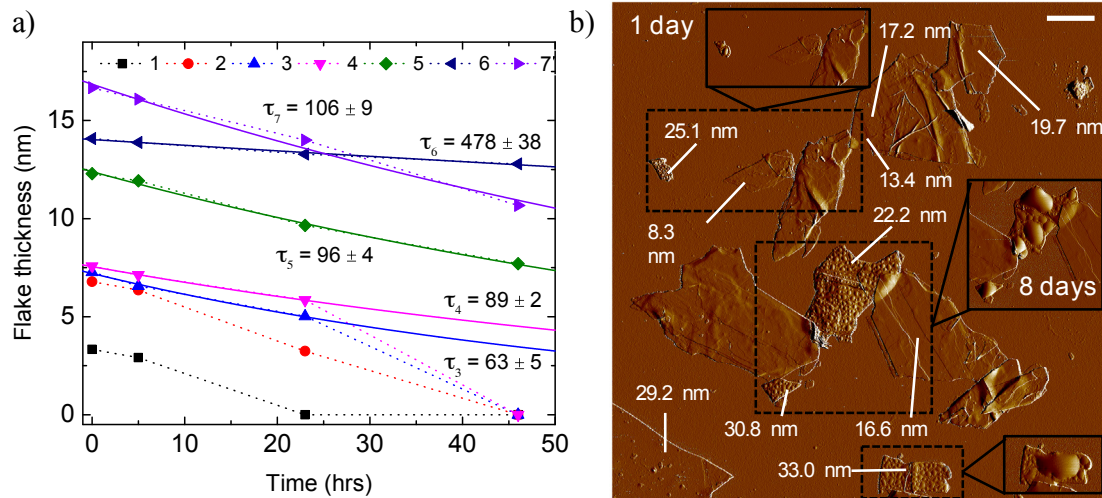


Fig. 3.9 Variation in BP flake degradation rate. (a) Plots of the thickness against the time exposed to ambient conditions (at 0, 5, 23 and 46 hours) for 7 different mechanically exfoliated BP flakes as they degrade. Solid lines are an exponential decay fit to each curve - where thickness is above 5 nm (see text for reasoning) - with time constants as annotated. (b) AFM peak force scan of a selection of BP flakes, transferred by mechanical exfoliation onto Si:SiO₂ in an inert environment, as measured $t = 1$ day after exfoliation and removal from glove box. Annotations show the initial thicknesses of each flake measured at $t = 0$ (immediately after removal from glove box) by AFM height profile scan. Inserts show the selected areas (dashed lines) a further week after. Scale bar is 2 μm ; peak force scans have been shown - rather than height profile maps - to better highlight the topography of the flakes as phosphoric acid bubbles form, given the large height of the bubbles (up to an order of magnitude higher) with respect to the flakes.

Figure 3.9a shows a plot of flake thickness for seven flakes within a typical sample area exposed to ambient conditions for $t = 0, 5, 23$ and 46 hours after removal from the glove box. Whilst with a limited number of data points, these results broadly support the above assertions; above a thickness of ~ 5 nm ($n \approx 9$) the data are well fitted by an exponential decay ($R^2 > 0.98$ for all flakes). Toward this thickness, the decay constant, τ decreases, whilst below it, the rate of degradation deviates from a simple exponential decay and accelerates significantly. For thicker flakes ($n > 15$), significant variability was observed in τ as well as in the onset of oxidation. Once bubbles had nucleated, flakes would typically degrade at around $\tau \approx 100$ hrs (an initial rate of approximately 2 nm day^{-1}), though some flakes (for example flake 6 in Fig. 3.9a) would degrade far more gradually, with initial rates as slow as 0.5 nm day^{-1} . However, as illustrated by Fig. 3.9b - within the same scan area as a selection of flakes that began to oxidise at a typical rate - some flakes (even with thicknesses as low as $n > 15$) showed no discernible evidence of bubble nucleation at all, even after ambient exposure for 8 days. In support of this, ref. 9 did observe significant delays in nucleation for flakes where $n > 20$, though does not discuss in any further detail.

To construct a detailed statistical picture a far greater number of data points would be required, especially for flakes below $n \approx 9$. This was primarily limited by the aforementioned difficulty in exfoliating a great enough number of flakes at these thicknesses. Furthermore, a limitation in the use of AFM itself was that for many flakes, as degradation progressed and the spatial density of bubbles on the flakes increased (often coalescing to form large bubbles covering most of the flake), it often became impossible to discern the true height of non-oxidised layers.

3.3 Black phosphorus inks and their application in optoelectronics

3.3.1 Conversion of dispersions to inks

The study progressed to investigate the formulation of functional, inkjet-printable inks from the dispersions produced in the last section, which at the time of publication had not yet been achieved for BP. As discussed in the literature review, due to its relatively high surface tension, NMP alone does not have the wettability required for uniform printing on low surface energy substrates such as Si:SiO₂. Further to this - and aside from the issue of its toxicity - due to its high boiling point, annealing steps or long delays are required for it to dry in between print passes. This is a particular problem considering BP's environmental instability. Therefore, a solvent exchange process was used to formulate inks and optimise them for a reliable inkjet printing process with low drying times and even material distribution. Here, a major consideration was reduction of the so-called 'coffee-ring' effect, whereby material is deposited preferentially at the edges of an ink-jetted droplet as it dries, leading to circular patterns with very low spatial uniformity in the deposited flakes. During the drying of a (single solvent) droplet, the higher surface-to-volume ratios at the edges leads to a locally increased rate of evaporation. This encourages a replenishing flow of solvent toward the edges, which carries flakes radially outward from the centre. A binary-solvent strategy was adopted to address this; this involves introduction of a secondary solvent with an appreciably different evaporation point to that of the first. As a droplet of such a mixture dries, the concentration of the lower evaporation point solvent increases in the droplet centre, creating a surface tension gradient across it^[130]. This gradient acts to produce a Marangoni-type flow radially *inward*, which can potentially counteract that directed outward, thus recirculating flakes.

For the first step of the solvent exchange, NMP-based dispersions were centrifuged at ultra-high speeds of 40,000 rpm ($275,000 \times g$) for 30 minutes - phials were again back-filled

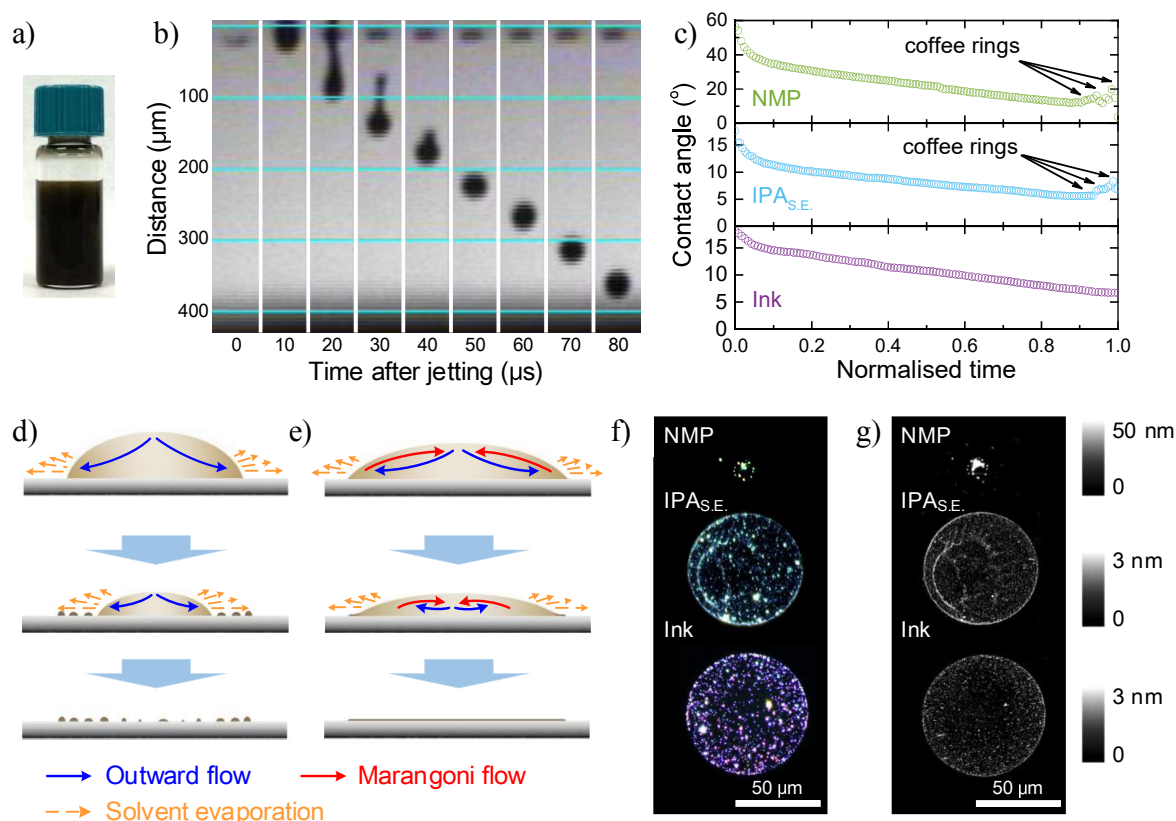


Fig. 3.10 Inkjet printing of black phosphorus inks. (a) A bottle of the final BP ink after the solvent-exchange process. (b) Time lapsed images of the jetting sequence using the BP ink taken with a stroboscopic camera (c) Evolution of the contact angle over time during the drying of a droplet of NMP dispersion, the solvent-exchanged formulation with only IPA and the binary solvent ink, as normalised to the total drying time for each droplet. (d) and (e) schematics of the droplet drying processes for a single and binary solvent ink respectively, demonstrating the effect of a surface tension gradient-induced Marangoni flow as to recirculating material during droplet evaporation. (f) and (g) Dark field optical microscope and AFM images respectively of dried dispersion or ink droplets as labelled. Scale bar is 50 μm.

with N₂ to minimise O₂ exposure. Such high forces applied for this duration caused the majority of exfoliated material to sediment at the bottom of the phial. This allowed the NMP supernatant to be removed by pipette and replaced with anhydrous IPA. IPA was added at a tenth of the previous volume of NMP, therefore affording a ten-fold increase in concentration, resulting in a loading of $\sim 5 \text{ g L}^{-1}$, as measured by optical extinction characterisation. At the date of publication, this loading was a notable advance on those previously achieved in BP dispersions, of 0.01, 0.4 and 1 g L⁻¹ by refs. 99, 100 and 88 respectively. Finally, butan-2-ol (boiling point 100°C) was added at 10 % by volume to leave the finished ink (Fig. 3.10a) - higher ratios were avoided as they caused increased droplet spreading, lowering the printing resolution. Optical scattering characteristics of the ink remained relatively unaltered with

respect to that of the NMP-based dispersion. This suggests that no significant aggregation of the flakes has occurred during the sedimentation and solvent-exchange steps. Once produced and bottled, the optical absorption of the ink changes by only 1% over the course of one week, indicating that flakes remain well dispersed, without sedimentation, as will occur in unstable 2d material inks with unsuited solvents^[87].

The ink was then studied initially in the case of inkjet-printing individual droplets, to assess their behaviour when jetting, interacting with the substrate and drying. All printing was carried out using a Fugifilm Dimatix DMP-2831 system. The rheological properties of the ink were measured and a value of $Z \approx 10$ calculated. The stable jetting suggested by this Z value was corroborated by images of the jetting sequence, shown in 3.10b, showing no angular deviation or the formation of satellite droplets.

Behaviour of the ink at the substrate were then tested against the NMP dispersion and a solvent-exchanged IPA ink, without the addition of butan-2-ol (denoted as IPA_{SE} to differentiate from the earlier IPA dispersion). Time-resolved contact angle measurements were first used to assess the drying characteristics of droplets, shown in Fig. 3.10c. When material accumulates during the formation of a coffee-ring, it pins the droplet edge preventing any further recession until tension-based forces become great enough that the droplet rapidly contracts. This can be seen in the NMP and IPA_{SE} measurements - but is absent in the ink - whereby after a gradual decrease in the contact angle, it increases again toward the end of the drying stage. This process, along with that for a binary-solvent with its recirculating Marangoni flow, are illustrated in the schematics in Figs. 3.10d and e respectively. Further evidence for the optimisation of the wetting and drying process can be seen in the optical dark field and AFM images of dried droplets on Si:SiO₂, in Figs. 3.10f and g respectively. These clearly show the relatively even distribution of material for the ink compared with the poor wetting exhibited by the NMP dispersion, and coffee rings formation in the IPA_{SE} ink droplets.

3.3.2 Printing optimisation and characterisation

Having studied and improved the jetting of and material distribution from individual droplets, the printing of extended features and patterns, formed from overlapping droplets, was optimised. Here, the inter-droplet spacing is the main system parameter that governs the morphology of the resultant line. Figure 3.11a demonstrates the spectrum of possible morphologies (when maintaining constant droplet diameter). As can be seen, these vary from excessively spread lines (with thickness far greater than that of dried individual droplets) when the droplet spacing is too narrow, to scalloped lines and, in the extreme case, individual, disconnected droplets, when the spacing is too broad. Another variable that can be adjusted

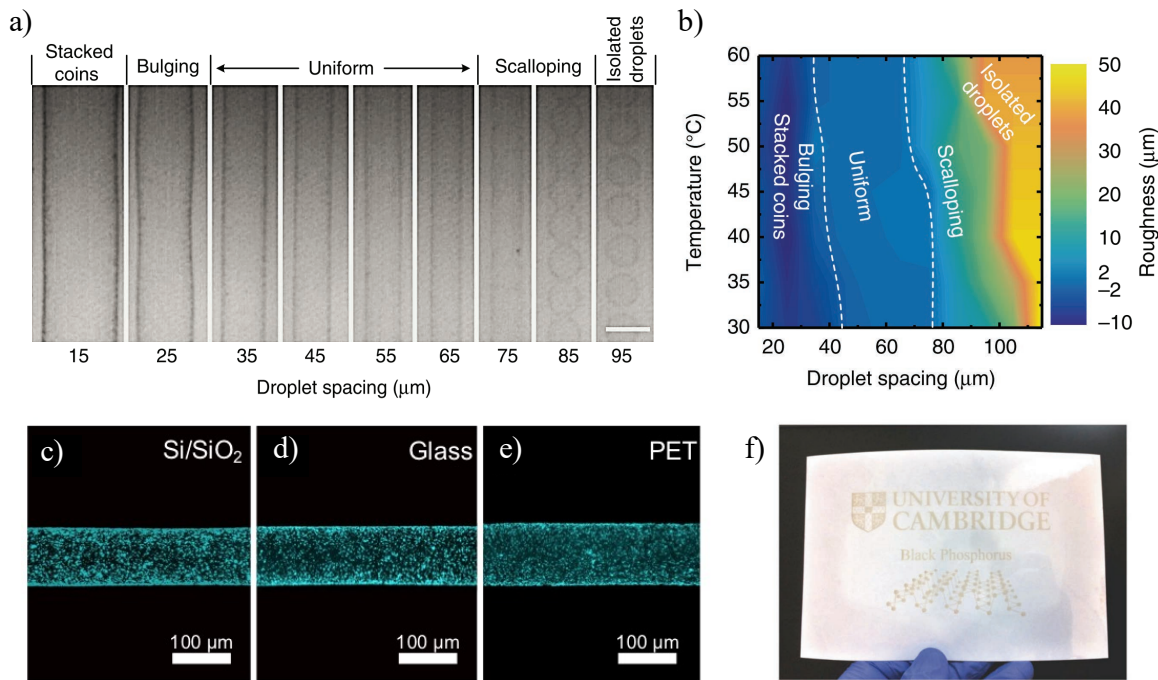


Fig. 3.11 Inkjet printing and characterisation of patterned features. (a) Optical microscope images showing the variation in the morphology of printed lines as the inter-droplet separation is varied from 15 to 95 μm . Features were printed with the BP ink on a Si:SiO₂ substrate at a temperature of 60°C; scale bar is 100 μm . (b) Plot of the line edge roughness (as defined in the text) with respect to varying temperature (and thus the droplet diameter) and inter-droplet spacing. (c)-(e) Enhanced contrast dark field optical microscope images of printed lines on Si:SiO₂, glass and PET substrates. Scale bar is 100 μm . (f) Demonstration of printing over a large area (100 × 63 mm²) on PET (a 1.5 μm layer was laminated onto photopaper to make it more robust for handling).

within the printing system is the substrate temperature; increasing this will increase its surface energy and lead to greater spreading (that is, diameter) of individual droplets, affording finer tuning of the system, as well as decreasing the drying times required. As plotted in Fig. 3.11b, the relationship of these two parameters was mapped with respect to the resultant line-edge roughness, $(L_{max} - L_{min})/2$, where L_{max} and L_{min} are the widest and narrowest points on the printed line respectively. ‘Uniform’ lines were classed as those with line-edge roughness $< \pm 2 \mu\text{m}$. Shown by the marked region on the map, uniform printing with this ink required a droplet spacing to droplet diameter (as controlled in this case by the temperature) ratio of $\sim 0.5 - 0.8$. For film printing in the rest of the study, the maximum substrate temperature of 60°C was selected, to minimise drying time and curtail BP degradation, with a droplet spacing of 35 μm to afford uniform printing. Figures 3.11c-e demonstrate that using these optimised parameters, uniform channels with relatively even material distribution across their width were achieved on three commonly used device substrates - Si:SiO₂, glass and

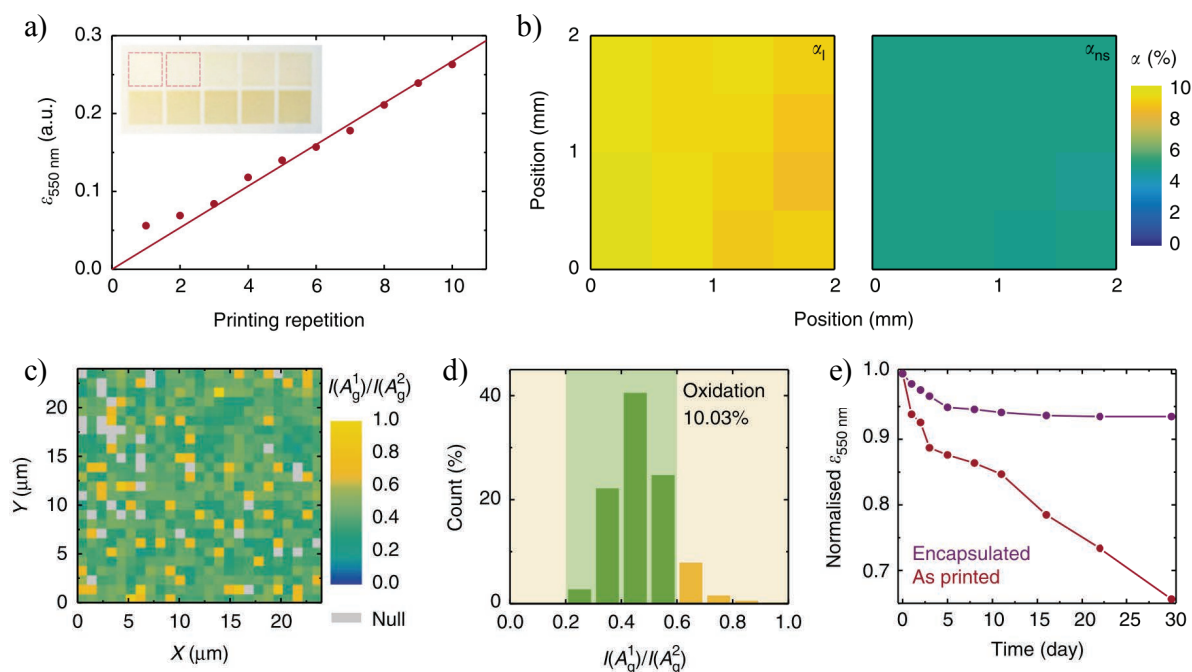


Fig. 3.12 Characterisation of printed black phosphorus films. (a) Variation in BP film optical extinction at 550 nm with respect to the number of print passes, with a linear fit. Inset shows photograph of each ($8 \times 8 \text{ mm}^2$) film used for characterisation. (b) Spatial mapping of the linear (at low intensity) and non-linear (at high intensity) absorption coefficients, α_1 and α_{ns} , measured at 1562 nm with a step of 0.5 mm (spot diameter $\sim 400 \mu\text{m}$). (c) Raman spectroscopic mapping of the $I(A_g^1)/I(A_g^2)$ ratio for an as-printed printed BP film on Si:SiO₂, carried out at 514 nm with a spatial step of $1 \mu\text{m}$. Points where the signal to noise ratio was too low for interpretation have been coloured in grey. (d) The distribution of the $I(A_g^1)/I(A_g^2)$ ratio for all non-null points in the map in (c). (e) Evolution of the optical extinction (at 550 nm) exhibited by two printed BP films exposed to ambient conditions over a 30 day period, one with and one without encapsulation by a parylene-C layer.

PET - without the need for any surface treatment. This uniformity was maintained over far larger areas ($100 \times 63 \text{ mm}^2$) without the jetting destabilising, as shown in Fig. 3.11f, demonstrating the potential for scalable applications.

After establishing conditions for optimal printing of individual lines, the optical properties of BP films formed from multiple print passes were investigated. Figure 3.12a shows the optical extinction plotted against the number of passes, as successive ink layers were deposited over the same area (allowing for drying in between). The linear relationship seen, with $< 2\%$ variation, demonstrates that the optical density of the films can be consistently and precisely controlled through varying the number of print passes. The films also show high spatial uniformity, as exhibited in the maps of linear and non-linear optical absorption (α_1 and α_{ns} respectively) in Fig. 3.12b. For these samples, $\alpha_1 = 9.19 \pm 0.31\%$ and $\alpha_{ns} = 4.99 \pm 0.09\%$ showing only $< 3.4\%$ variation across a $2 \times 2 \text{ mm}^2$ area.

Raman characterisation of printed films, as described in the previous section, also confirmed that the multiple steps in the ink formulation and printing processes did not induce any significant oxidation in the BP flakes. Figure 3.12c shows Raman mapping of a film printed using the inks carried out directly after deposition, taken over an area of $25 \times 25 \mu\text{m}^2$ (laser was again focused to a spot size $\sim 1 \mu\text{m}$ in diameter as in previous mapping). The distribution of $I(A_g^1)/I(A_g^2)$ ratio, shown in Fig. 3.12d shows only $\sim 10\%$ of material was outside the 0.2 - 0.6 range (where flakes are suggested to be not significantly degraded), representing an increase of only $\sim 6\%$ on that of the as-produced dispersion. Even after storing the ink for 2 months under nitrogen, Raman mapping of dropcast samples showed the proportion of data points outside the 0.2 - 0.6 $I(A_g^1)/I(A_g^2)$ range had only risen to $\sim 22\%$.

However, to preserve this low level of degradation clearly requires some method of protecting the BP layer from the ambient environment. To this end, parylene-C was chosen to encapsulate the BP (at a thickness of 100 nm), as it provides a pin-hole free and conformal layer, the latter of which is an important consideration given the relative roughness of a printed film formed of a collection of 2d material flakes. Figure 3.12e compares the evolution of the optical extinction exhibited by the coated and non-coated printed films. Optical extinction in the unprotected film gradually and continuously decreases over the course of 30 days as the BP flakes degrade. However, for the encapsulated film, after an initial decrease in the first 5 days (which was attributed to trapped moisture between the parylene and BP film), the extinction remained relatively stable for the 25 further days measured. Investigation of the oxidation levels of encapsulated samples by Raman spectroscopy showed an initial increase in the fraction of material with $I(A_g^1)/I(A_g^2)$ outside of the 0.2 - 0.6 range, from 10% to 23% immediately on encapsulation, which then stabilized at 34% after several days. It is however unclear whether this is actually representative of oxidation of the BP flakes, as the intensity of A_g^1 is also dependent on contact with other substances^[9].

3.3.3 Optoelectronic and photonic devices

Having demonstrated the stability of the optical properties of these films, it remained to verify the potential of these printed films for devices with a workable level of stability and performance. The BP inks were integrated as an active component in two different optoelectronic applications produced by collaborators: photodetectors and pulsed lasers. With respect to the first of these - reported in the paper - BP ink was printed onto a Si-graphene junction photodetector to act as a sensitizing layer, with the intention of expanding operation of the device to the infrared range. An Au electrode was deposited to outline a square window, $\sim 450 \times 450 \mu\text{m}^2$, on a Si:SiO₂ substrate. The oxide layer within this window was removed using lithography and a hydrofluoric acid etch, exposing the bare

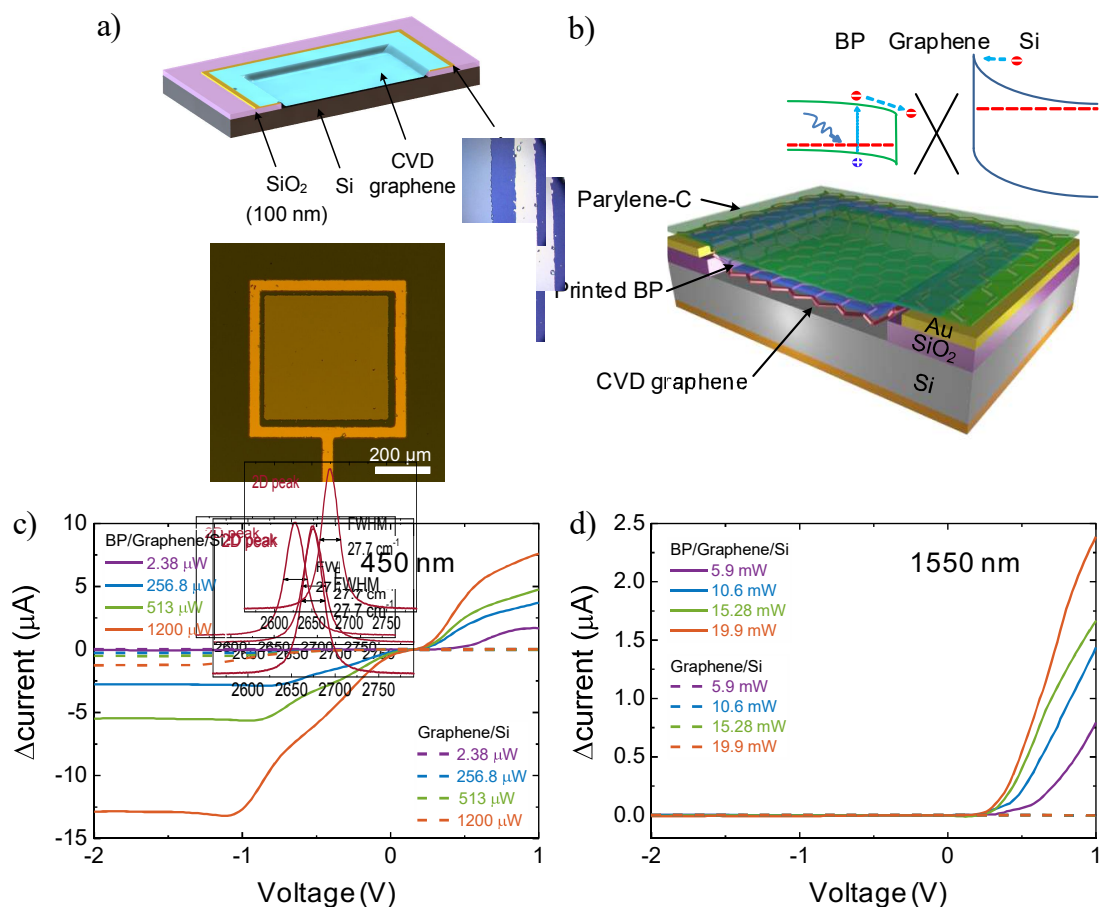


Fig. 3.13 **Demonstration of a hybrid photodetector based on a graphene-silicon junction sensitised by a printed BP film.** (a) Schematic and optical image of the graphene-Si Schottky junction photodetector prior to BP deposition. (b) Cross-sectional schematic showing the device after BP printing and encapsulation in parylene-C. The inset illustrates a possible photogating-type charge transfer mechanism that contributes to photodetection. (c) and (d) Photocurrent ($I_{light} - I_{dark}$) characteristics when the detector is under bias across the Au electrode and Si layer, and illuminated with a 450 nm and 1550 nm laser respectively, with overall power incident on the detector varying as labelled.

Si layer, before the transferring and patterning CVD graphene over the whole section, to create a Si-graphene Schottky junction (Fig. 3.13a). BP ink was then printed over the graphene-coated-Si section, before encapsulation of the whole structure in parylene-C; a schematic of the final device is shown in 3.13b.

Devices with and without the BP film were characterised through laser illumination with a bias across the Au electrode and Si substrate layer. Figures 3.13c and 3.13d show photocurrents induced in typical devices with (solid lines) and without (dashed lines) the BP layer at a wavelength of 450 nm and 1550 nm respectively. The plain Si-graphene devices showed photoresponse under negative bias and 450 nm light, as has been reported previously

in ref. 131. However, they exhibit no photocurrent at 1550 nm due to the excitation energy (~ 0.8 eV) being below that of the Si bandgap (~ 1.1 eV). The responsivity, R_λ , of these devices at a particular wavelength, λ , can be expressed as:

$$R_\lambda = \frac{I_{PC}}{P_{opt}} \quad (3.4)$$

where I_{PC} is the photocurrent, $I_{light} - I_{dark}$, and P_{opt} is the total optical power incident on the detector. Furthermore, the external quantum efficiency (EQE) at a particular wavelength - the ratio between the number of photoexcited electrons collected at the electrode, N_{el} and the number of photons incident on the detector, N_{ph} - can be calculated from the responsivity using

$$EQE = \frac{N_{el}}{N_{ph}} = \frac{R_\lambda hc}{\lambda e} \quad (3.5)$$

where h is Planck's constant, c is the speed of light and e the elementary charge. With the addition of a BP printed film, at 450 nm illumination the devices showed a significantly increased photoresponsivity at negative bias, from ~ 16 to ~ 164 mA W $^{-1}$ (corresponding to an EQE of 45%). The detector also exhibited a response under forward bias of ~ 95 mA W $^{-1}$ (EQE 26%) where previously none was measurable. More notably, at 1550 nm the device now demonstrated a low photoresponse of ~ 1.8 mA W $^{-1}$ (EQE 0.14%). Here, with respect to the physical mechanism, the increased response was attributed firstly to enhancement of the optical absorption of the device, due to BP's direct bandgap. Secondly, it was suggested that a photogating effect occurs, whereby photogeneration of electron-hole pairs in the BP film leads to a change in the Fermi energy of the graphene sheet and thus the Schottky barrier height. Such a charge transfer process is roughly illustrated in the inset of Fig. 3.13b. It was noted that thermal contributions from the increased optical absorption may also play a role in altering the Schottky barrier height.

The performance of the detectors at energies over the Si bandgap is modest in comparison to those in the literature; for instance, ref. 131 reported an EQE of $\sim 80\%$ for a Si quantum dot-sensitized graphene-Si Schottky junction. Furthermore, at the telecommunications wavelengths, whilst a response was produced, the EQE of $\sim 0.1\%$ is far below that which would be competitive with conventional CMOS detectors for these wavelength ranges. However, crucially, both the photoresponse and time response characteristics of the device remained stable, with repeatable performance when left under ambient conditions and measured 7 days apart. As such, whilst further work is clearly required to improve the device design and performance, the results are notable in showing the first integration of a BP layer into a stable, functional device, in a rapid, low-cost, controllable and scalable manner.

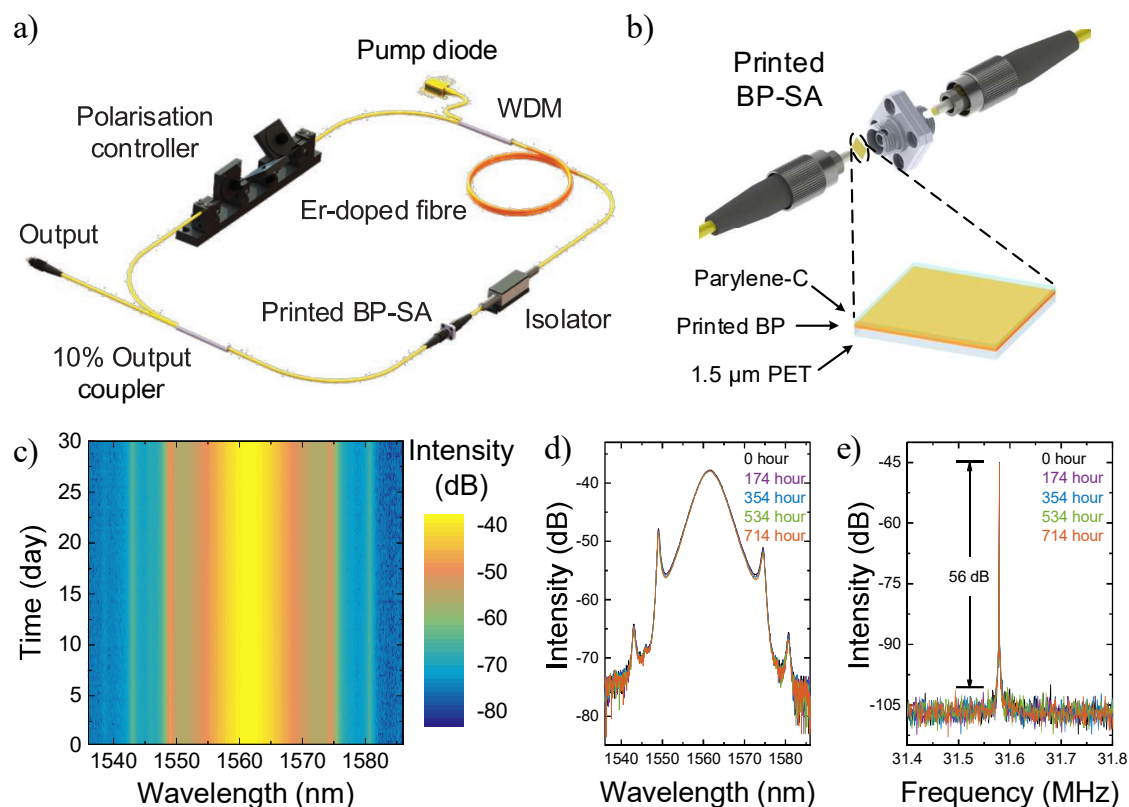


Fig. 3.14 Demonstration of an ultra-fast laser based around a black-phosphorus printed film saturable absorber. (a) Schematic illustrating the components of the fibre laser setup. (b) The printed BP saturable absorber: BP ink is printed onto an ultra-thin PET square before being encapsulated in parylene-C and coupled into the fibre cavity. (c) Output spectra of the laser measured every 6 hours over a 30 day period, with a central frequency of 1562 nm. (d) Cross sections taken from the data in (e) at the labelled time periods, demonstrating the operational stability of the system. (e) Radio frequency spectrum of the laser over time. The high intensity with respect to background, ~ 53 dB shows little variation in behaviour over the 30 day period, demonstrating the stability of the mode-locking.

As with other 2d materials, BP's non-linear optical response make it of interest for use as a saturable absorber in photonic applications such as ultra-fast pulsed lasers^[5]. In these systems, liquid-phase exfoliated 2d materials present a cheap alternative to current technology, and can be easily incorporated by blending the dispersions with polymers to create composite films which can simply be inserted into fiber-based laser setups. BP's environmental sensitivity means this strategy is less viable due to the long curing times involved, and as such the BP printing process developed here could provide a more suitable route.

The fibre laser setup (total cavity length 8.7 m) can be seen in Fig. 3.14a. A 0.7 m long erbium-doped (LIEKKI Er-8/125) fibre was used as the active amplification element, co-pumped using a 980 nm laser diode. Unidirectional propagation and polarisation states were maintained by an optical isolator and polarisation controller, respectively; measurements were taken *via* a 10:90 output coupler. BP films were inkjet printed onto an ultra-thin PET 1×1 mm layer, before being encapsulated in parylene-C at 100 nm thickness and inserted into the cavity as shown in Fig. 3.14b. Here, operating the laser at a wavelength of 1562 nm, through the action of the BP as a saturable absorber, mode-locking was achieved with a fundamental repetition frequency of 31.6 MHz. The duration of pulses was measured at 605 fs by intensity autocorrelator. Given the ultra-high intensity of radiation in the cavities of pulsed lasers (with values up to 32.7 MW cm^{-2} measured in this setup) and the direct proportionality of BP oxidation rate to the photon flux^[9], after achieving mode locking the main consideration for this system was the stability of the operation over time. Indeed, at the date of publication, the maximum duration of stable operation demonstrated in previous works based on liquid-phase exfoliated BP dispersions was 24 hours^[132]. As shown in Fig. 3.14c, the output spectra of the laser was measured every 6 hours over a period of over 30 days of continuous operation; Fig. 3.14d shows cross-sections of this plot at 0, 174, 354, 534 and 714 hours, whilst Fig. 3.14e is a spectral plot of the radio frequency at the fundamental operational frequency taken at the same time intervals. These two sets of measurements demonstrate highly stable operation and mode-locking respectively, illustrating that the printed films are not degrading even under such intense illumination, for prolonged durations. Evidently, further work is required to assess the longer term performance and viability for industrial or research applications, but these results present a promising step toward this.

Summary

In this chapter I have covered the section of my research focused on solution-phase processed BP for optoelectronic applications. A device-ready, binder-free ink, capable of printing uniform films of BP flakes on untreated substrates was developed. Through AFM and optical scattering measurements, NMP was found to exfoliate BP in solution more effectively than CHP or IPA. However, NMP is unsuitable for inkjet printing of BP due to its poor wettability and long drying times. It was shown that a BP ink can be formulated through a solvent-exchange process, replacing NMP with a mixture of IPA and butan-2-ol, with stable jetting, good wettability on glass, PET and Si:SiO₂. Furthermore the binary nature of the solvent acts to minimise the coffee-ring effect, producing a more even flake distribution within droplets. Through optimising the printing process, films with highly uniform optical properties ($< 3.4\%$

spatial variation) were deposited. It was found that the long term stability of these films (> 30 days) could be ensured by encapsulating in a parylene-C layer. Throughout this investigation, Raman spectroscopy was employed to assess the degradation of flakes, finding that despite BP's instability in contact with water, the exfoliation, formulation and printing stages did not induce significant photooxidation. The encapsulated inkjet printed films were then integrated into photodetector and pulsed laser systems, demonstrating stable operation even under intense irradiation for a period of 30 days. These results showcased the first scalable method for the deposition of solution-processed BP films and features with viable device performance and stability. The next chapter begins the component of this thesis that focuses toward my work on nanowire devices, with a review of the literature surrounding semiconductor nanowires.

Chapter 4

Semiconductor Nanowires

Overview

One of the essential requirements for the realisation of a ‘bottom-up’ approach to technological assembly, is the ability to create nanoscale components with finely-tuned, consistent electronic and optoelectronic properties. In order to achieve this, there must be control over certain crucial nanomaterial parameters, such as structure, chemical composition, size, morphology and doping; semiconductor nanowires offer arguably the most developed nanoscale system with respect to these needs^[133–135].

Nanowires are one-dimensional nanoscale structures resulting from highly anisotropic growth, with lengths usually at least two to three orders of magnitude larger than the diameter, ranging anywhere from 3 - 500 nm^[136]. It is possible to grow nanowires from a vast range of materials, including group IV, group III-V and group II-VI semiconductors, whilst holding, in many cases, the ability to control p- and n- type doping, length, diameter, growth direction and even, with some materials, cross-sectional shape^[135,137,138]. They can be produced in high yield, and integration into existing Si-based technology and other semiconductor systems is generally straightforward^[137,139]. On top of this, they are mechanically flexible and their properties remain consistent after cycles of high bending strain, whilst large surface to volume ratios afford them electronic properties that can be highly sensitive with respect to their external environment or photoexcitation^[140–143]. Furthermore, it is possible to create both radial and axial heterostructures, as well as compositionally graded wires, even at the growth stage, introducing tailored functionality without the requirement of any lithographic processes^[144–147].

Considering these characteristics together, semiconductor nanowires show great potential as a robust, tunable and scalable nanoscale component, providing a platform for a vast range of applications and devices, from horizontal, single-nanowire-based architectures, through

to vertically-aligned nanowire arrays. In the fields of (opto-)electronics and photonics, amongst other devices, a wide variety of nanowire FETs, lasers, LEDs and photodetectors have been demonstrated, whilst their geometry and controllable chemistry has seen them exploited across gas, chemical and biological sensing applications^[134,143,148–154]. For energy harvesting, nanowires have presented themselves as an interesting candidate for studies in photoelectrochemistry and artificial photosynthesis, as well as photovoltaic and thermoelectric devices^[143,146,155–159]. More exotic applications include those in nanoelectromechanical systems such as nanowire-based mechanical resonators and piezoelectronics, biological studies at the nanowire-cell interface, as well as the development of advanced epitaxial quantum devices^[143,160,161].

This chapter contains a review and discussion of the relevant literature surrounding semiconductor nanowires and, more particularly, contextualising $\text{CdS}_x\text{Se}_{1-x}$ bandgap-gradient nanowires, the central material system in my research. The chapter is divided into three sections, the first of which will concern more general background, firstly on how semiconductor nanowires can be produced across a variety of material systems, before a more detailed explanation of the vapour-liquid-solid growth mechanism - which is the basis for that used to produce the nanowires in my research - and culminating with a discussion of their electronic and optoelectronic properties. In the second section, I will explain the theory and practicalities of the techniques used in my PhD to characterise nanowire properties, as well as some not used, but of particular contemporary relevance, to provide context for discussion of the literature. Finally, the third section shall introduce compositionally-graded nanowires and the $\text{CdS}_x\text{Se}_{1-x}$ species which form the basis for the majority of the experimental work contained in this thesis. To highlight how this class of nanomaterial represents a relevant and viable nanotechnological platform, I shall first explain how established growth techniques can be adapted to produce these nanowires in a straightforward and scalable fashion, before discussing the physical and optoelectronic properties that make them of particular interest for the spectral applications developed over the course of my doctoral studies.

4.1 Synthesis and properties

4.1.1 Growth techniques

Strategies for semiconductor nanowire synthesis can broadly be categorised into two paradigms: top-down and bottom-up. *Top-down* techniques mostly involve the use of conventional, established microfabrication processes to reduce bulk materials to one dimensional structures^[139,142]. Patterning techniques such as photo- or electron-beam- lithography, used in

conjunction with appropriate anisotropic etch processes, can readily be used to create custom 1d structures or arrays with relative ease and flexibility, from any semiconductor material. However, aside from being inherently wasteful, top-down nanowire synthesis is heavily limited both by the resolution and throughput of the fabrication processes involved, as well as in the unavoidable introduction of surface defects at the etch stage. Producing nanowire structures via these methods at the ever-shrinking length scales seen in modern devices, and in a cost-effective and consistent manner, presents many challenges.

The *bottom-up* paradigm is defined by the additive construction of nanowires from raw precursor materials *via* chemical synthesis. Producing nanowires in this way can afford the tuning of a wide range of resultant parameters at the growth stage - chemical composition, length, diameter, morphology, doping - offering remarkable control in the production of near-atomically precise nanoscale building blocks. Within this paradigm, a variety of different processes have been developed to achieve the formation of 1d structures. Some less typical - and less scalable - processes centre around the self-assembly or oriented-attachment of 0d nanocrystals, where confinement within mesoscale structures or at thin-film interfaces, or the careful control of nanocrystal shape through synthetic chemistry, can be exploited to promote the additive formation of nanocrystal chains^[142,162–164]; these may prove particularly viable processes for the formation of ultra-thin nanowires such as the 1.5 nm diameter CdSe structures in ref. 165.

However, the vast majority of scalable nanowire production methods used to date are, on a fundamental level, crystallisation processes, crucially with the application of a confinement mechanism to promote highly anisotropic growth^[139]. The two primary strategies for confinement used to date broadly divide these methods into two categories: template-directed growth and metal-nanoparticle-mediated, free-standing growth^[139].

In templated-growth, a sacrificial structure is used to physically confine crystal growth to one-dimensional channels. A range of structures have been used for these purposes, such as porous polymer or anodized alumina films, relief or edge structures in solid surfaces for shadow deposition, and cylindrical micelles formed from self-assembled surfactant molecules^[142]. These methods, though readily scalable, with templates that can be fabricated to afford a wide range of nanowire diameters and lengths, carry a series of limitations. Nanowires grown in this way are often polycrystalline rather than single crystal, however the primary drawback surrounds the complete reliance on the production of a single-use template with specifically suitable properties and resolution for the process involved^[139]. Many templates may only prove viable for a limited range of materials or deposition techniques, whilst others (such as in shadow deposition techniques) present significant challenges in the removal of nanowires for further use.

Bypassing most of these challenges associated with templated-growth, by far the most extensively investigated and implemented strategy for nanowire growth has been free-standing growth employing catalytic metallic nanoparticles^[143]. Whilst reactants can also be supplied in solution (solution-liquid-solid growth), the vast majority of methods employed here are based upon the use of vapour-phase precursors, and are described by the vapour-liquid-solid (VLS) mechanism^[143]. Techniques based on VLS growth were first employed for nanowire synthesis in the early 1960s, for the relatively imprecise production of 100 nm - 200 μm silicon ‘whiskers’^[166]. However, it wasn’t until the late 1990s that this technique was revisited and expanded upon, due primarily to the work of the Lieber group in demonstrating controlled, sub-10 nm diameter growth *via* the production of Au nanoclusters through laser-ablation^[167]. Since then, the wide flexibility of this technique has been showcased in its ability to produce nanowires from almost any semiconducting material, with reported synthesis across group IV, III-V, II-VI and oxide-based semiconductors^[134,137,142,143].

4.1.2 The VLS mechanism

Represented schematically in Fig. 4.1a, VLS growth can be summarised as consisting of three main stages: alloying, nucleation and growth^[143,166]. In the first instance, a supply of *vapour*-phase precursors is introduced to a reaction chamber containing a substrate on which metallic nanoparticles have been dispersed. The growth temperature of the system is selected as that which will form a eutectic *liquid* alloy of the nanoparticle and precursor material(s). In this way, reactants are continually fed into the alloyed nanoparticle system; once this droplet becomes supersaturated, *solid* crystalline material begins to precipitate and is nucleated onto the substrate beneath. Nanowire growth thus occurs at the solid-liquid (nanowire-nanoparticle) interface, serving as a sink to afford the continued incorporation of reactants to the crystal structure. Direct observations of this process, through in-situ TEM imaging, can be seen in Fig. 4.1b.

As touched upon in the previous section, VLS growth offers an attractive degree of flexibility for the large-scale synthesis of nanowires. It is compatible with a wide range of established industrial vaporisation processes, allowing selection of those most suited to produce a particular, desired set of reactants, from molecular and chemical beam epitaxy (MBE and CBE) to pulsed laser ablation and chemical vapour deposition (CVD); the latter of which has now become the most conventionally used process^[137,139]. There is significant freedom in material choice, with the primary limitation simply being whether the reactants and metal nanoparticle can be driven to form a eutectic alloy. Phase diagrams, such as that in Fig. 4.1a, can be used to assess the stability of the relevant alloys and guide the selection of appropriate metal nanoparticles (Au in the vast majority of cases) and most suitable growth

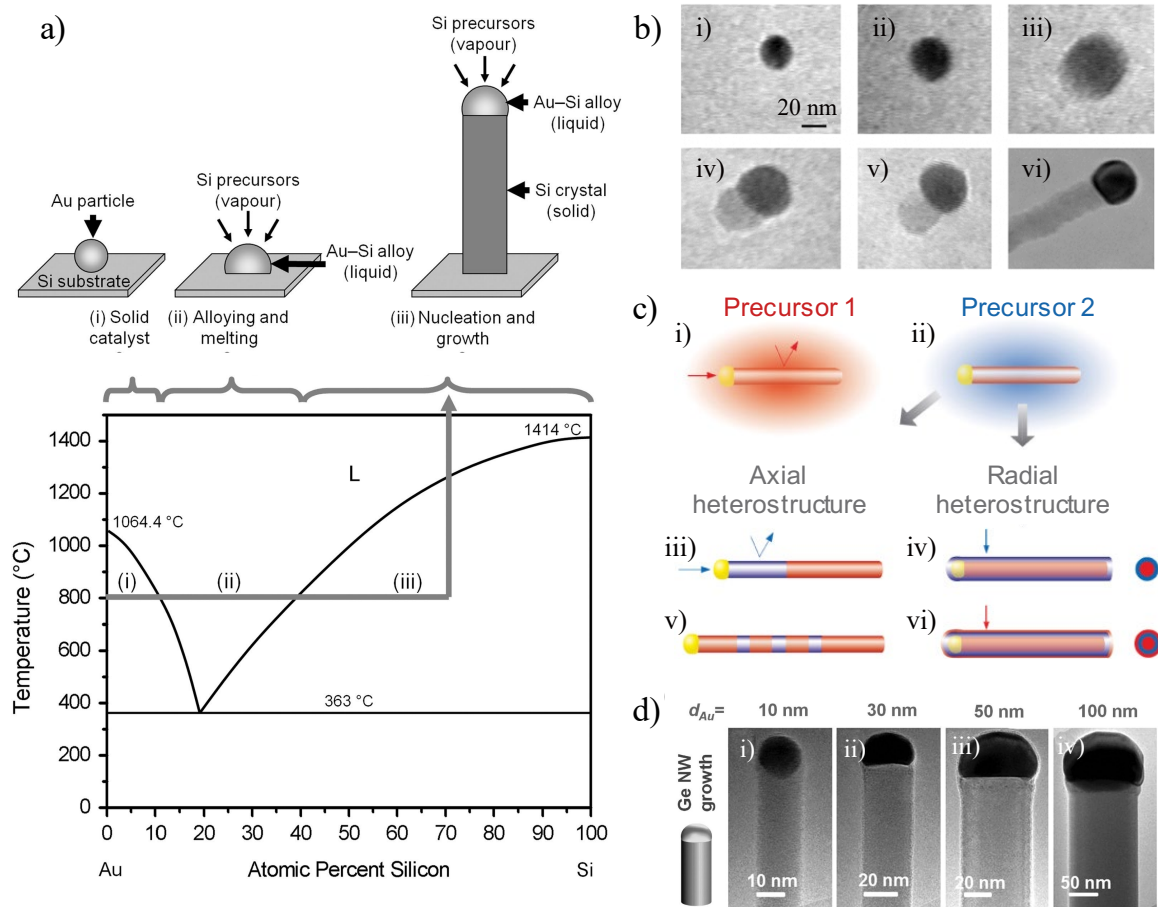


Fig. 4.1 Growth of nanowires by the vapour liquid solid method. (a) (Above) Illustration of the major steps in a typical VLS process for growth of Silicon nanowires. (Below) Binary phase diagram for the Au-Si system, labelled to show the phase corresponding to each illustrated stage i)-iii), as an increasing amount of Si is incorporated into the particle at a growth temperature of 800°C. Adapted from ref. 139. (b) Ge nanowire growth observed *via* in-situ TEM imaging, showing i) an Au nanoparticle at 500°C, ii) the solid particle as alloying begins at the 800°C growth temperature, iii) liquification of the Au-Ge droplet on increasing incorporation of Ge, iv) Ge nucleation on the substrate, v),vi) further crystallisation of Ge and the elongation of a nanowire. Adapted from ref. 168. (c) Schematic illustrating routes for axial and radial nanowire heterostructure growth. Red and blue refer to two different semiconductor precursor materials, arrows denote incorporation (straight) or rejection (reflected) of precursor vapour into the nanowire during growth. i) Axial growth through incorporation of reactant 1 preferentially at the nanoparticle rather than the wire surface, ii) source vapour switched to reactant 2, leading to iii) axial or iv) radial heterostructure formation depending on the selected reaction conditions. Repetition of these processes can create v) axial super-lattices or vi) core-multi-shell structures. Adapted from ref. 137. (d) TEM images of Ge nanowires illustrating how their diameter is constrained by that of the catalytic nanoparticle, d_{Au} , for four different sizes i)-iv). Adapted from ref. 169.

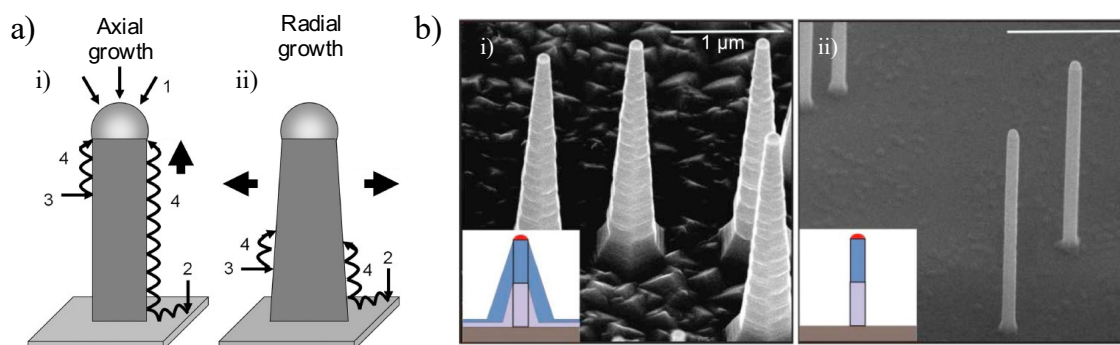


Fig. 4.2 **Nanowire growth modes.** (a) Diagram illustrating the competing axial (i) and radial (ii) growth modes, with adatom incorporation *via* 1, direct impingement at the nanoparticle, 2, adsorption to the substrate, 3, adsorption to the nanowire surface, and 4, diffusion along the nanowire concentration gradient toward the nanoparticle. Adapted from ref. 139. (b) Schematics and SEM images demonstrating how in-situ etching can be carried out to suppress the radial growth mode in the particular case of InP nanowires grown with (i) and without (ii) the addition of gaseous phase HCl. Adapted from ref. 171.

conditions^[139]. Whilst relatively straightforward for group IV elements, this can prove problematic for the creation of III-V or II-VI compound systems. The use here of more complex binary and ternary phase diagrams, is further complicated by pressure and size-dependent effects on nanoparticle melting - indeed some such processes have been shown to more likely occur *via* solid rather than liquid nanoparticle alloys, dubbed vapour-solid-solid (VSS) growth^[170].

Aside from these material allowances, the VLS process also affords integration of functionality within a single nanowire, through the creation of radial and axial heterostructures (as illustrated in Fig. 4.1c), simply by halting the initial reactant flow before the introduction of a second precursor, under the appropriate, desired growth conditions^[135,144]. Moreover, and crucially relevant to this thesis, VLS systems can be further adapted to allow synthesis of nanowires with continuous, lengthwise composition gradients, which shall be covered in greater detail later in this chapter^[147]. The controlled growth of branched structures can also readily be achieved by deposition of nanoparticles on pre-grown nanowires^[172].

However, arguably the greatest strength of the VLS mechanism is the control it affords over resultant nanowire properties. With respect to the morphology of the nanowire, length and diameter can be tuned independently; the former simply *via* growth time, whilst the latter is largely mediated by the metallic nanoparticle^[143]. Assuming growth of the nanowire occurs primarily at the liquid-solid interface, the diameter of each layer of crystal growth is mostly governed by that of the nanoparticle itself, as exemplified by the TEM image in Fig. 4.1d^[169]. The now-commercial production of metallic nanoparticles at variable sizes down to a few

nanometers has therefore enabled the production of nanowires at corresponding diameters, down to the atomic-scale, with Wu *et al.* first demonstrating growth of Si nanowires down to 3nm^[173].

In actuality, competing with the axial liquid-solid interface growth, is radial growth occurring through the direct incorporation of reactants at the vapour-solid interface, which results in the production of tapered structures, as shown in Fig. 4.2a^[139]. Here too, suppression of this growth mode has resulted in remarkable control over diameter uniformity, via the tuning of reaction conditions such as temperature, pressure, flow rates and notably the introduction of background or carrier gases, such as H₂, for routine capabilities of ~10 nm variation across length scales of over 1 μm, exemplified in Fig. 4.2b^[142,173]. Crystallographic characteristics, which have significant influence over nanowire chemical and physical properties, can also be tuned in certain systems. Varying the substrate crystal orientation, nanowire diameter and growth temperature has been shown to influence the crystallographic growth direction, whilst selectivity of crystal phase, for example between zinc-blende and wurtzite nanowires, as well as control of defect densities, has been demonstrated through adjusting impurity concentrations, precursor ratios and growth temperatures^[143,174–177]. Control of nanowire position, and the growth of regular arrays can straightforwardly be achieved *via* pre-growth lithographic patterning of the catalytic nanoclusters or films^[178].

4.1.3 Geometry-dependent properties

Clearly, when considering suitability for application, many of the electronic and optoelectronic properties for particular species of semiconductor nanowires, such as the carrier mobility and bandgap, are largely governed by the materials from which they are composed. However, nanostructures do possess common geometry-dependent characteristics - differences with respect to their bulk counterparts that arise specifically from their one-dimensional nature - which I shall discuss in this subsection. The particular properties of the central material systems in my research will be detailed in section 4.3.

A primary consideration with respect to this geometry-dependence is the nanowire diameter, and, when sufficiently small, the degree to which confinement effects must be taken into account for carriers in the system^[139]. With respect to electronic properties, confinement can lead to quantised transport in nanowires, whereby, under ideal ballistic conditions, quantum channels contribute a unit of conductance $2e^2/h$, where e is the electron charge and h is Planck's constant. This phenomena can become observable in wires with diameters near the Fermi wavelength of the material; whilst for metals this commonly requires atomic wires of width <1 nm, lengthscales are in the region of 10s of nm for semiconductors^[144,179].

Regarding optical properties, confinement effects are mainly considered with respect to how they alter the band structure, and correspondingly, the bandgap, of a system. Here, radial confinement becomes significant only when the nanowire diameter becomes comparable to that of the exciton Bohr radius for the particular semiconductor material,

$$a_B = \frac{\hbar^2 \kappa}{\mu e^2}, \quad (4.1)$$

where \hbar is the reduced planck's constant, κ is the material dielectric constant, μ is the exciton effective mass and e is the electron charge, resulting in relatively large lengthscales of concern for some commonly used compounds such as InAs (~ 35 nm)^[180–182]. Confinement results in a bandgap increase, ΔE_g and a corresponding blue-shifting of any resultant photoluminescent (PL) emission^[183]. Whilst simplified particle-in-a-box models show ΔE_g scaling according to d^{-2} , where d is the wire diameter, experimental work has shown that this is entirely material dependent, one study showing for example that in InAs nanowires, $\Delta E_g \propto d^{-\alpha}$ where $1 < \alpha < 2$ ^[144,183].

However, many, if not most, semiconductor nanowires for optoelectronic applications are produced with diameters at scales outside that of the quantum regime. Whilst this means they can be described *via* conventional semiconductor physics, their geometry and scale do nonetheless have notable and sometimes dramatic effects on their electronic and optoelectronic properties.

Crucially for their interactions with visible light, the diameters of these nanowires are comparable to minority carrier and exciton diffusion lengths (depending on the material), as well as the wavelength of the radiation^[143]. In the case of the former, diffusion lengths of several microns can be deduced from measured hole mobilities and recombination times (for example, on the order of $10,000 \text{ cm}^2\text{V}^{-1}\text{s}^{-1}$ and 1 ns, respectively, in GaAs nanowires), suggesting that electrons and holes in a particular system may even travel the entire length of a nanowire in their lifetime^[139]. This in turn bestows far greater influence to the quality of nanowire surfaces, and the presence of defects or species from the surrounding environment, on the behaviour of optical excitation and emission.

For nanowires with sub-wavelength diameters, light can be trapped in an orbit of repeated internal reflections within the structure (see Fig. 4.3a), owing to the large mismatch in dielectric properties between the nanowire and surrounding environment, and allowing waveguided axial propagation, with low losses afforded by atomically smooth sidewalls, uniform diameters, and single-crystallinity^[143,181,184].

Light can either be confined in nanowires in bound (waveguiding) modes, or "leaky" modes, which form transverse resonances at wavelengths dependent on the dimensions of the

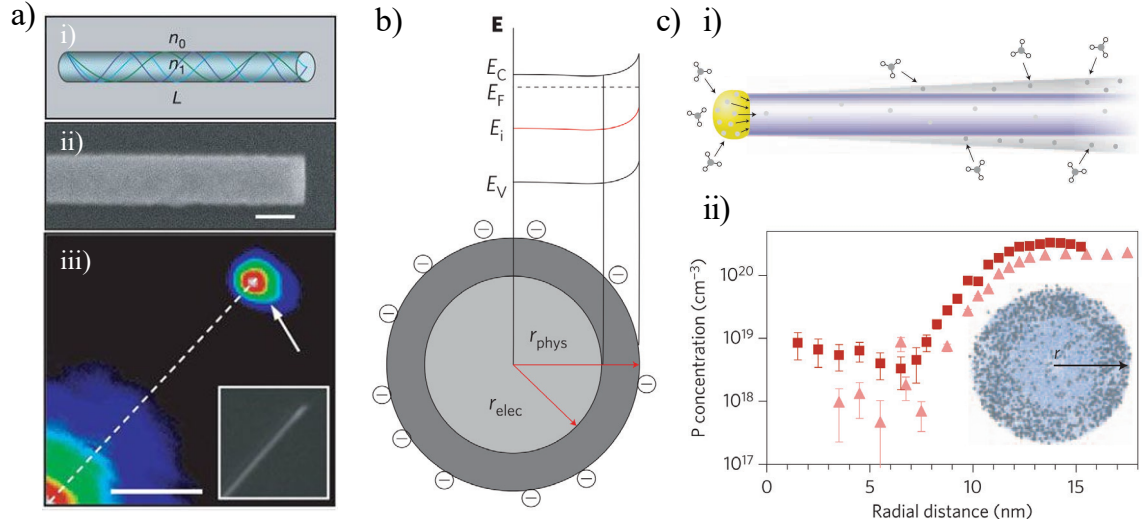


Fig. 4.3 Nanowire properties. (a) i) Schematic of a nanowire, length L , acting as a Fabry-Perot waveguide, showing a selection of modes supported within the cavity, where n_0 and n_1 are the refractive indices of the nanowire and surrounding medium respectively. ii) SEM image of a cleaved CdS nanowire with flat, regular end-face; scale bar 100 nm. iii) PL image of a CdS nanowire under localised excitation (bottom-left), demonstrating how light is waveguided along the nanowire with low loss and emitted from the end. Dashed line and arrow are the nanowire axis and end respectively. Scale bar $5 \mu\text{m}$. Inset is an optical image of the same nanowire. Adapted from ref. 185. (b) Band diagram and illustration to show the creation of a depletion zone within a nanowire through the attraction of negative charge to surface or interface states in an n-type material. E_C and E_V are the conduction and valence band-edge energies, while E_F and E_i are the Fermi and intrinsic Fermi energies respectively. r_{phys} and r_{elec} denote respectively the actual physical radius of the nanowire and the effective electronic radius where the free carrier density is such that charge can be efficiently transported. Adapted from ref. 186. (c) i) Diagram to illustrate two pathways through which donors can be incorporated during growth; through the catalyst or by decomposition at the surface. ii) Plot of the radial concentration of P dopants in a Ge nanowire, grown with $\text{PH}_3:\text{GeH}_4$ ratios of 1:1000 (triangles) and 1:500 (squares). Adapted from ref. 187.

wire; *via* both of these mechanisms, absorption can be greatly enhanced with respect to an equivalent volume section of bulk material^[143,158,184]. For single-mode optical waveguiding within a nanowire, of light with wavelength λ , a general condition is that

$$1 < \frac{\pi D}{\lambda} \sqrt{(n_1^2 - n_0^2)} < 2.4, \quad (4.2)$$

where 1 is a practical lower limit, D is the nanowire diameter, and n_1 and n_0 are the refractive indices of the nanowire and external medium respectively^[185].

Aside from the scale of nanowire diameters, a related, important geometric feature in influencing nanowire properties are their large surface-to-volume ratios. This quality makes

electronic transport through the nanowire ‘bulk’ highly sensitive to the presence and density of surface or interface states and trapped charges, which are influenced by surface defects and external species adsorbed from the surrounding environment. A key lengthscale here is the Debye length, L_D , the distance in a material over which Thomas-Fermi screening will cause an electronic potential to drop by a factor of $1/e$ in magnitude, which can be described as

$$L_D = \sqrt{\frac{\epsilon k_B T}{e^2 N_D}}, \quad (4.3)$$

where ϵ is the material’s dielectric constant, k_B is the Boltzmann constant, T the temperature, e the electron charge, and N_D the net density of either donor or acceptor dopants; broadly speaking, in nanowires with diameters on the order of the Debye length for that material, charge transport through the entire structural cross-section is influenced by surface characteristics^[143].

More specifically, the reduced screening in nanowire structures causes an increase in the ionisation energies for active impurity nuclei (normally only ~ 10 meV in bulk semiconductors and far below thermal contributions at room temperature), that is inversely dependent on the nanowire radius, and verified in ref. 186 as arising specifically from the sharp dielectric contrast between the nanowire and surrounding medium^[186,188]. In this way, trapped charges and surface states create a depletion region where ionisation energies are sufficiently high so as to deactivate the dopants present, reducing the number of free carriers in the system and defining a restricted electronic channel within the nanowire along which charge can be effectively transported, as shown in Fig. 4.3b^[186,189].

As well as the surface-state induced deactivation of dopants, when considering electronic transport through nanowires it is also important to note that spatial dopant distributions cannot necessarily be assumed to be uniform^[190]. As shown in Fig. 4.3c, during synthesis, incorporation of the active impurity precursors can generally occur not only through the catalyst droplet but also in an uncatalysed manner directly through the nanowire surface throughout the growth phase, resulting in both radial and axial dopant concentration gradients, and generally manifesting in a more heavily doped outer shell and nanowire base^[187,191,192].

Finally, with respect to physical properties, these large surface to volume ratios, and their ultra-thin nature can afford nanowires hugely increased flexibility with respect to bulk material, allowing bending radii before fracture which prove more than sufficient for flexible electronic and optoelectronic applications^[143]. Exact quantification of nanowire elastic moduli is complicated by variances based on the method of nano-mechanical characterisation employed. Whilst some systems show properties that vary as a function of nanowire size, the presence and extent of such effects depends significantly upon the particular material,

concentration of and nature of defects, crystallographic orientation and cross-sectional shape^[143,193].

4.2 Characterisation

4.2.1 Electron-mediated techniques

Though most nanowire diameters are below what can be effectively resolved by conventional optical microscopy, a wide variety of characterisation tools can be employed to analyse their physical and optoelectronic properties at the nanoscale. Here I will provide a brief summary of those techniques that are either used in my own research, or heavily referenced in relevant literature, so as to provide context for later discussion.

Scanning electron microscopy (SEM) is a form of microscopy that uses a focused beam of electrons to probe a sample, able to create topographical images of the surface, or collect information regarding its composition, at resolutions of down to ~ 1 nm. Electrons in the beam interact with the sample material to produce two main signals that are detected by the SEM. The first of these are ‘backscattered electrons’; electrons interacting with the positive atomic nuclei that undergo high-angle, elastic scattering. Images with high compositional contrast can be constructed from these signals as scattering probability is dependent on the square of the nuclei atomic number. Most widely-used for imaging, the second consists of ‘secondary electrons’; weakly bound electrons in outer atomic orbitals that are displaced by the high energy incident beam and originate primarily from close ($\sim 5 - 50$ nm) to the sample surface, thus producing the highest resolution topographical scans.

Samples to be scanned via SEM must be electrically conductive and grounded or else the incident beam will cause significant electrostatic charge to accumulate at the material surface, creating image artefacts and possible damage. Insulating samples must therefore be coated in a thin ($\sim 5 - 10$ nm) layer of a highly conductive material such as gold, via sputter coating or evaporation.

As well as secondary and backscattered electrons, X-rays can also be produced by the action of the SEM beam and utilised in energy dispersive X-ray spectroscopy (EDS or EDX) for quantitative compositional mapping. In this technique, charged particles in the beam with sufficiently high energy may eject ground-state electrons from the inner shells of atoms in the sample. Following this, an electron from the higher energy outer shells will relax into the hole left behind, emitting an X-ray in the process. The energy of this photon is equal to the difference in energy between the two shells and is thus characteristic of the particular element

involved. On detection in an energy-dispersive spectrometer, the positions and intensities of these energy signatures provide localised data on the relative elemental abundance.

Whilst SEM utilises electrons to analyse features primarily at the surface of a specimen, transmission electron microscopy (TEM) can be used to probe the internal structure of a material. Here, an electron beam is transmitted through a sample, and, after magnification and focusing, collected onto a detector on the other side. The primary condition for specimens is that they must be thin enough to allow a sufficient number of electrons to pass through; as nanomaterials are in most cases already of such low thickness, specimens are simply suspended over a micro-porous grid. Contrast in an image is mainly established by analysis of either the change in amplitude or phase of the electron signals resulting from their interaction with the sample as they pass through, enabling the mapping of atomic mass and sample thickness, as well as lattice spacing and defects.

Within a TEM, a powerful tool for elucidating the fine structures are selected area electron diffraction measurements (SAED). As the De Broglie wavelength of electrons in the beam is usually around two orders of magnitude smaller than the atomic spacing in a specimen, the crystal behaves as a diffraction grating. The diffraction patterns produced can then be used to deduce the crystallographic structure and orientation of the sample, as well as to provide further information on the nature of any defects. Through use of a beam blocking aperture, "selected areas" down to hundreds of nanometers can be isolated for analysis.

4.2.2 Photoluminescence spectroscopy

Photoluminescence (PL) spectroscopy is a non-destructive, all-optical tool often used for the characterisation of semiconducting nanomaterials, providing a direct probe of the electronic structure and transitions within a material, without requiring deposition of potentially problematic metal-to-semiconductor contacts^[106]. In this technique, laser light of a particular wavelength is focused onto a sample and the emitted light collected and passed through a grating before detection, to facilitate spectroscopic analysis. For bulk semiconductors, when excitation energy is greater than that of the bandgap, E_g , that is, where $h\nu_i \geq E_g$, where ν_i is the frequency of incident radiation, electrons in the valence band that absorb a photon are raised to energy states in the conduction band, leaving a hole in the valence band; the creation of an electron-hole pair. These are unstable, non-equilibrium states, therefore excited electrons subsequently relax back into the valence band and in doing so, emit a photon with energy equal to the difference between the initial (conduction band) and final (valence band) state.

This process can occur *via* a near-immediate radiative transmission, with corresponding emission of a photon with energy equal to that of the initial excitation, dubbed resonant

radiation. Alternatively, in crystalline semiconductors with a direct bandgap, relaxation will mostly take place through internal, non-radiative transitions prior to a radiative transition at lower energies/longer wavelengths than the excitation light (fluorescence, or, over longer timescales and through more complex processes, phosphorescence). In this way, photons with $E < E_g$ are simply not absorbed by the material, whilst the dominant pathway for those those with $E > E_g$ is to lose energy through thermalisation and the generation of phonons, followed by a transition from the edge of the higher (conduction) to that of the lower (valence) energy band, with release of a photon with $E \sim E_g$, often referred to as "near-band-edge" emission. The primary peak of an emission spectrum thus corresponds to the bandgap of the material and analysis concerning a material's bandgap is one of the central uses for PL spectroscopy^[106].

Due to quantum confinement and the quantisation of energy states in low-dimensional materials, movement from bulk material to nanostructures often results in bandgap-widening and corresponding blue-shift of photoluminescence peaks, dependent on the system size (as discussed previously); PL spectra can thus be used to analyse these confinement-based effects^[106,194,195]. However, as touched upon in section 4.1.3, for nanowires it is worth noting that quantum effects only dominate in those with widths of less than 20 nm, due to the low exciton diameters in many of the materials used, whereas the vast majority of current research concerns nanowires wider than 30 nm^[139]. For instance, the exciton bohr radii for CdS and CdSe, the primary materials used in my research, are ~ 2.8 nm and ~ 5.4 nm respectively^[196]. PL spectroscopy can however be used to investigate other physical phenomena that are important to consider for nanostructures. The width of the spectrum, as well as relative intensity variations, or the presence of unexpected secondary peaks, can be used to analyse the density of surface states or surface related transitions^[195,197,198]. These originate from impurities or defects at the surface and thus are particularly influential on the electronic states of structures with high surface to volume ratios^[139].

4.3 Bandgap-gradient nanowires in focus

4.3.1 Adapted growth strategies

Arguably the most crucial material parameter when considering semiconductors for optoelectronic applications is their bandgap. To improve the efficiency or functionality of devices such as LEDs or photovoltaics, it is important to be able to tailor their emission or absorption to particular, or multiple wavelengths. The limited, discrete range of bandgaps available when using conventional elemental or binary compound semiconductors restrict the design

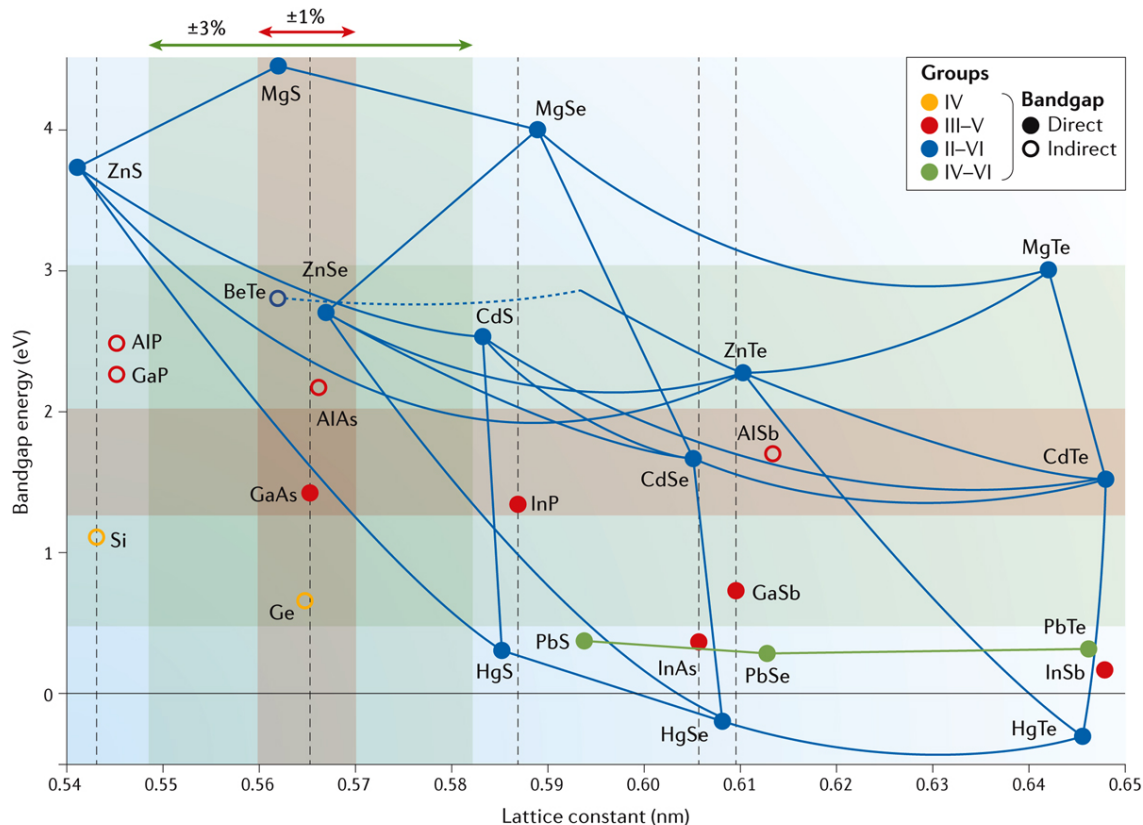


Fig. 4.4 **Tuning bandgaps through semiconductor alloying.** Plot of the bandgaps and lattice constants for typical elemental and compound semiconductors. The solid and dotted connecting lines represent direct and indirect alloys respectively. The dashed, vertical grey lines show the five most common substrate materials used in epitaxial growth, Si, GaAs, InP, InAs and GaSb. The lattice constants allowed within a 1% and 3% lattice mismatch, and the corresponding bandgap ranges, are denoted, for the specific case of GaAs, by the red and green shaded areas. Adapted from ref. 199.

flexibility and, in turn, the device performance. By alloying two or more semiconductors and varying the compositional ratio, it is possible to achieve materials of any bandgap within a continuous range between those of the two constituent materials, which will be covered in more detail in section 4.3.2^[199]. However, in practice, when growing high quality bulk single-crystals, strict requirements for lattice matching between the substrate and film will greatly constrain the range of alloys possible, as illustrated for the most commonly utilised semiconductor materials in the plot in Fig. 4.4. Here, due to the narrow cross-sections of the crystals grown, nanowires afford a far higher tolerance to lattice mismatch - as much as 7%, compared with <1% in thin films - therefore enabling a range of alloys that could not otherwise be grown, substantially improving the capacity for bandgap engineering^[199,200]. Combining this potential with the versatility of the VLS process, recent work has demon-

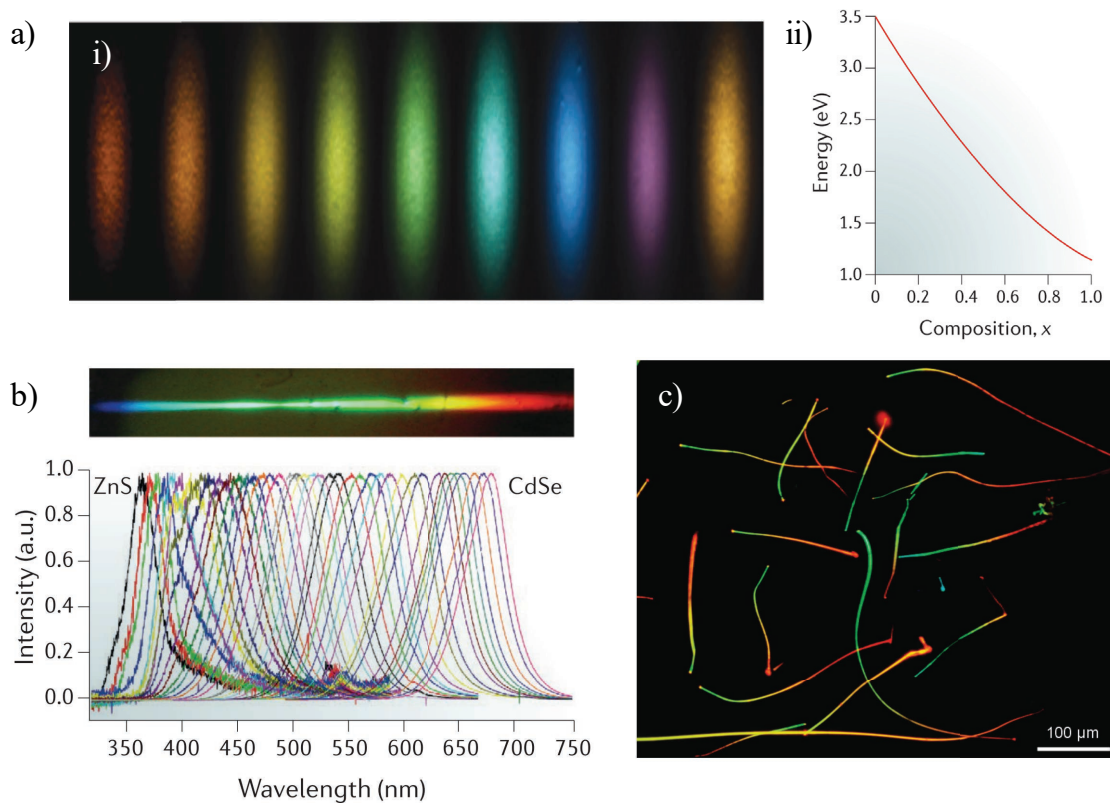


Fig. 4.5 Compositional-grading for semiconductor nanostructures. (a) i) CCD images of a $\text{In}_x\text{Ga}_{1-x}\text{N}$ nanowire growth chip under excitation, demonstrating an *on-substrate* composition gradient from $x=0.6$ (left) to $x=0$ (right). ii) Variation of bandgap with composition factor x for $\text{In}_x\text{Ga}_{1-x}\text{N}$. Adapted from ref. 201. (b) (above) Fluorescence imaging across a $\text{Zn}_{1-x}\text{Cd}_x\text{S}_{1-y}\text{Se}_y$ nanowire growth substrate with a dual composition-gradient. (below) Corresponding PL spectra showing how the bandgap, and therefore emission, gradually varies along the substrate, from ZnS to CdSe. Adapted from ref. 202. (c) Colour image under 405-nm excitation of a sample of *on-nanowire* composition-gradient, $\text{CdS}_x\text{Se}_{1-x}$ nanowires, demonstrating gradual variation in the emission colour along the nanowire. Adapted from ref. 203.

strated the capability to grow alloyed nanowires incorporating a graded range of compositions in a single growth step.

When discussing the literature around composition-graded or -gradient nanowires, otherwise known as bandgap-gradient nanowires, it is first important to make a terminological distinction between two types of gradient that appear. The majority of composition-graded nanowires reported are ternary alloy systems represented as $\text{AB}_x\text{C}_{1-x}$, whereby A is a primary material present throughout the system, B and C secondary materials, and x is an integer from 0 to 1 and defines the ratio of the two secondary elements. However, the *gradient* can refer to two different scenarios: an *on-substrate* gradient, or an *on-wire* gradient^[147].

For the former, examples of which can be seen in Fig. 4.5a and b, a growth process is engineered such that the composition of nanowires is graded - with x varying from 1 to 0 - across the growth substrate, but such that wires at any particular point on the substrate are of a homogenous nature, with fixed composition AB_xC_{1-x} along their whole structure^[202,204–206]. As shown in Fig. 4.5c, in the case of an *on-wire* gradient, the growth process is designed such that, for the whole substrate, a continuous gradient exists along the nanowires themselves, with x varying from 1 to 0 from one end of a wire to the other^[203,207,208]. There are far fewer cases of on-nanowire than on-substrate gradients reported in the literature as their growth is more challenging, but can be achieved through relatively simple adaptations to the VLS growth procedure.

Though on-nanowire gradients have been produced with other systems, such as $In_xGa_{1-x}N$, Si_xGe_{1-x} , $CsPbBr_xI_{3-x}$ and even dual graded $Zn_{1-x}Cd_xS_{1-y}Se_y$, most publications thus far have been around developing, analysing and utilising the species studied in my own research - CdS_xSe_{1-x} nanowires - in part due to their visible-range bandgap span (2.25 eV for CdS and 1.70 eV for CdSe) and corresponding attractiveness for optoelectronic applications^[201,203,207–210]. I shall therefore focus here specifically on adapted VLS processes for CdS_xSe_{1-x} growth.

Gu *et al.* first reported the growth of CdS_xSe_{1-x} with an on-wire gradient in 2011, *via* a source-moving, thermal evaporation, CVD-based method, inspired by that used by Reimers *et al.* in the late 1960s for the growth of bulk single crystal CdS_xSe_{1-x} with an along-crystal gradient^[203,211]. Note that this same method, and indeed, the same apparatus, was used to grow the nanowires that are studied in this thesis by Zongyin Yang, my chief collaborator from within the HNE group, who is also the second author in ref. 203.

A schematic of the custom-made growth system for the production of these CdS_xSe_{1-x} wires can be seen in Fig. 4.6a. A quartz tube is mounted inside a single-heating-zone furnace, with a silicon target substrate, coated in a 2 nm thick Au film, placed at the edge of the heating zone - note that during growth, at high temperature, the film will conglomerate into nanoparticles. Two alumina boats, one containing CdS and the other CdSe, are attached to a push rod in the tube, lateral movement of which is achieved via magnetic attachment to an external motor. The boats are separated at a fixed distance of around ~ 12 cm, and initially situated such that the CdS and CdSe boats are at the center of and just outside of the heating zone respectively. Throughout the process a flow of 150 sccm N_2 is maintained, to provide an inert atmosphere, and the pressure of the system maintained at 300 mbar. During growth, the temperature at the center of the tube is set to reach $830^\circ C$ at a rate of $40^\circ C \text{ min}^{-1}$. The temperature is kept here for 40 mins to allow for nucleation and growth to begin, after which the motor gradually moves the CdSe to the center of the heating zone -

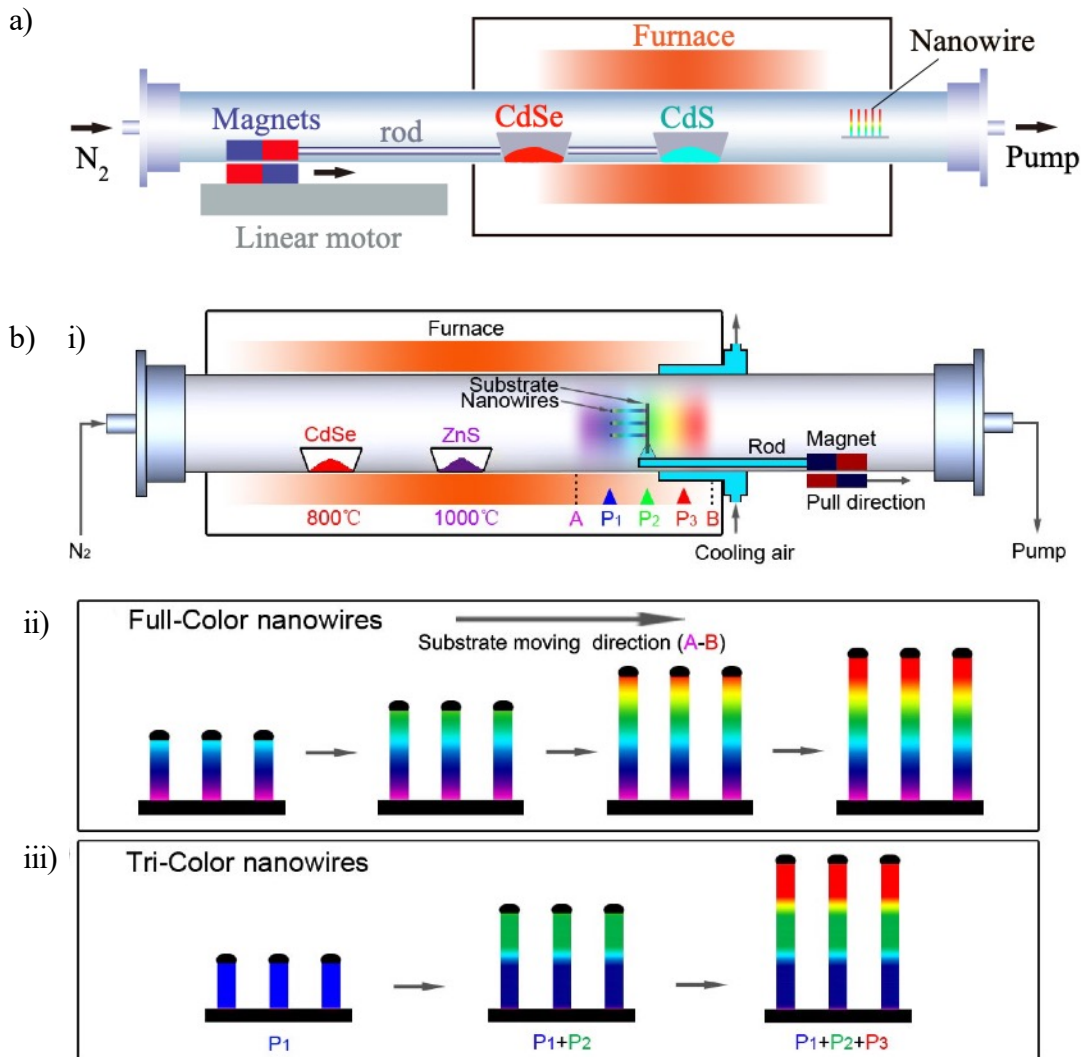


Fig. 4.6 **Apparatus for engineering on-nanowire compositional gradients.** (a) Schematic of the *moving-source* setup used for VLS growth of $\text{CdS}_x\text{Se}_{1-x}$ on-gradient nanowires. Adapted from ref. 203. (b) Schematic of the *moving-substrate* setup (i) used to grow $\text{Zn}_{1-x}\text{Cd}_x\text{S}_{1-y}\text{Se}_y$ nanowire systems and how through either continuous or intermittent substrate movement, full on-nanowire gradient (ii), or ternary heterostructure (iii) nanowires can be produced. Adapted from ref. 207.

and correspondingly, the CdS out of the heating zone - at a rate of 2.5 cm min^{-1} . Here the temperature is simultaneously reduced to 800°C at a rate of $0.5^\circ\text{C min}^{-1}$, where it remains for 1 hour, before returning to room temperature.

As each precursor boat is moved across the radial temperature gradient between the center and either edge of the furnace, they are vaporised to a greater or lesser degree depending on their position within the central heating zone. In this way, though the *substrate* remains fixed in space for the duration, the composition of vapour travelling downstream, and hence that

available to the Au nanoparticles at the surface, is varied from CdS to CdSe over the course of the process, producing nanowires with a continuous gradient between these two materials along their length.

It is worth noting that similar results can be achieved using a *substrate-moving* strategy, as demonstrated in reference 207 to produce $\text{Zn}_{1-x}\text{Cd}_x\text{S}_{1-y}\text{Se}_y$ nanowires, the setup for which is shown in Fig. 4.6b. In this case, a furnace with a radial temperature gradient is again used, but the ZnS and CdSe sources placed at *fixed* positions according to their particular vaporisation temperatures. Due to the great disparity in vaporisation/condensation temperature between the two precursors ($\sim 1000^\circ\text{C}$ for ZnS and $\sim 800^\circ\text{C}$ for CdSe), during growth a spatial composition gradient is generated in the vapour downstream of the sources, corresponding to that of the furnace's temperature gradient, gradually varying from ZnS at the hotter center to CdSe at the cooler edge. Accordingly, placing the substrate at a particular point in this gradient will cause nanowire growth corresponding to that of the vapour in the immediate surroundings. Therefore, moving a substrate across this gradient at an appropriate rate will result in nanowires with gradually varying composition. Furthermore, by fixing then subsequently relocating the substrate to another section of the gradient for suitable lengths of time, one can create an almost arbitrary number of heterojunctions along the nanowire, illustrated in Fig. 4.6b.

Combined with the versatility of the VLS process, it should be recognised here that *via* either of these two simple process adaptations, a remarkable degree of flexibility can be realised over the growth of graded and heterojunction alloy nanowires, allowing near complete control in tuning their spatial composition and hence bandgap characteristics. Whilst the work done so far has focused on a narrow set of material systems, it is evident that the processes developed here can be extended to a wide range of semiconductors in a relatively straightforward fashion, provided that they are capable of forming the requisite alloys under appropriate conditions. This factor should be kept under consideration when discussing any potential applications for $\text{CdS}_x\text{Se}_{1-x}$ nanowires, especially those that may be limited simply by the bandgap range of these particular materials.

4.3.2 Physical and optoelectronic properties

As well as their applications, to date, a significant portion of the research around composition-graded $\text{CdS}_x\text{Se}_{1-x}$ nanowires has centered around characterisation and analysis of their properties, through a variety of techniques including SEM, TEM, PL and optical-pump terahertz-probe (OPTP) spectroscopy, as well as electronic probing *via* fabrication of FETs. These investigations have often focused on confirming how composition and bandgap varies along the nanowire, and what specific optical and electronic characteristics arise from the

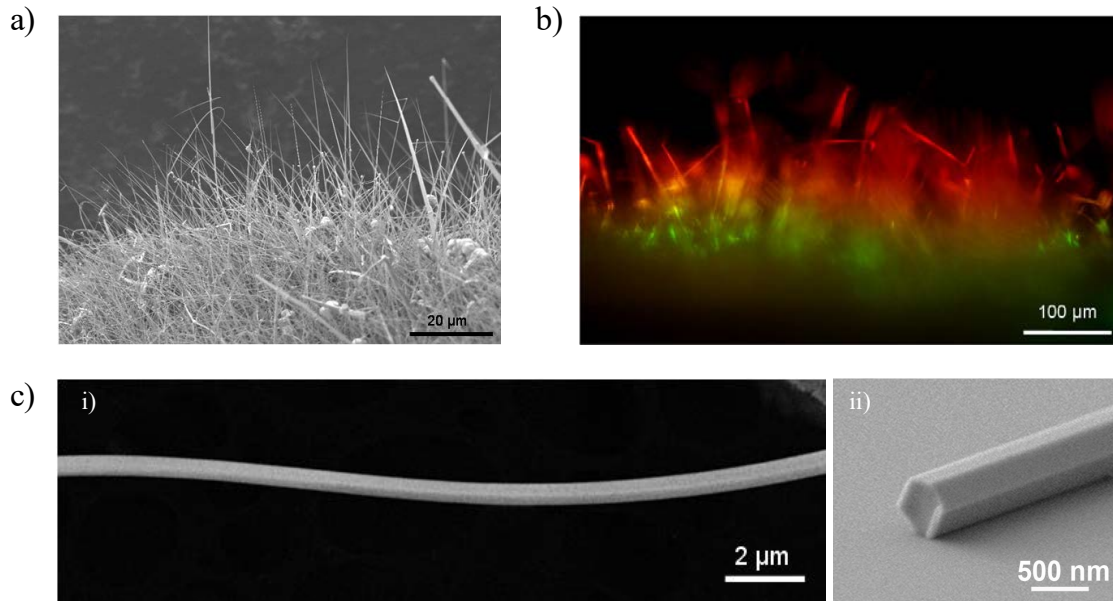


Fig. 4.7 **Imaging $\text{CdS}_x\text{Se}_{1-x}$ nanowires.** $\text{CdS}_x\text{Se}_{1-x}$ composition-gradient nanowires, grown using the source-moving method by Gu *et al.* (a) Side-view SEM image of a forest of as-grown nanowires on substrate. (b) Side-view colour image of as-grown nanowires under 405 nm excitation. (c) SEM images of i) a single nanowire, ii) a cleaved nanowire, showing the hexagonal structural cross-section. (a)-(c)i) adapted from ref. 203, (c) ii) adapted from ref. 212.

presence of such a spatial-gradient. Here it is also useful to take into account certain sections of the literature around homogeneous $\text{CdS}_x\text{Se}_{1-x}$ nanowires to learn how the alloying process itself alters nanowire properties with respect to pure CdS and CdSe wires.

Imaged in Fig. 4.7, the $\text{CdS}_x\text{Se}_{1-x}$ composition-graded samples grown by Gu *et al.*, whose method is used in the majority of works published to date, show relatively uncontrolled morphological properties, with a wide nanowire-to-nanowire variance in diameter, from 100 - 1000 nm, and typical lengths up to $500 \mu\text{m}$ ^[203]. Analysis of high-resolution TEM and selected-area electron diffraction (SAED) images shows that despite the continual variation of source vapour, the nanowires grown in this manner have a highly regular, single-crystalline, hexagonal wurtzite structure, without phase-segregations^[200,203]. SEM images show the wire cross-sections to be hexagonal (Fig. 4.7c,ii), though it should be noted that alloyed $\text{CdS}_x\text{Se}_{1-x}$ homogeneous species often exhibit nanobelt morphologies with rectangular cross-sections under similar, albeit static, growth conditions^[196,212–214]. The gradients in the wire are clarified by energy-dispersive spectrometry (EDS), displayed in Fig. 4.8a, which indicates gradual and continuous variation in the molar fraction of S along the nanowire length, complementary to that of Se. This is further evidenced by TEM images, a selection of which can be seen in Fig. 4.8b, showing that the (002) lattice spacing slowly

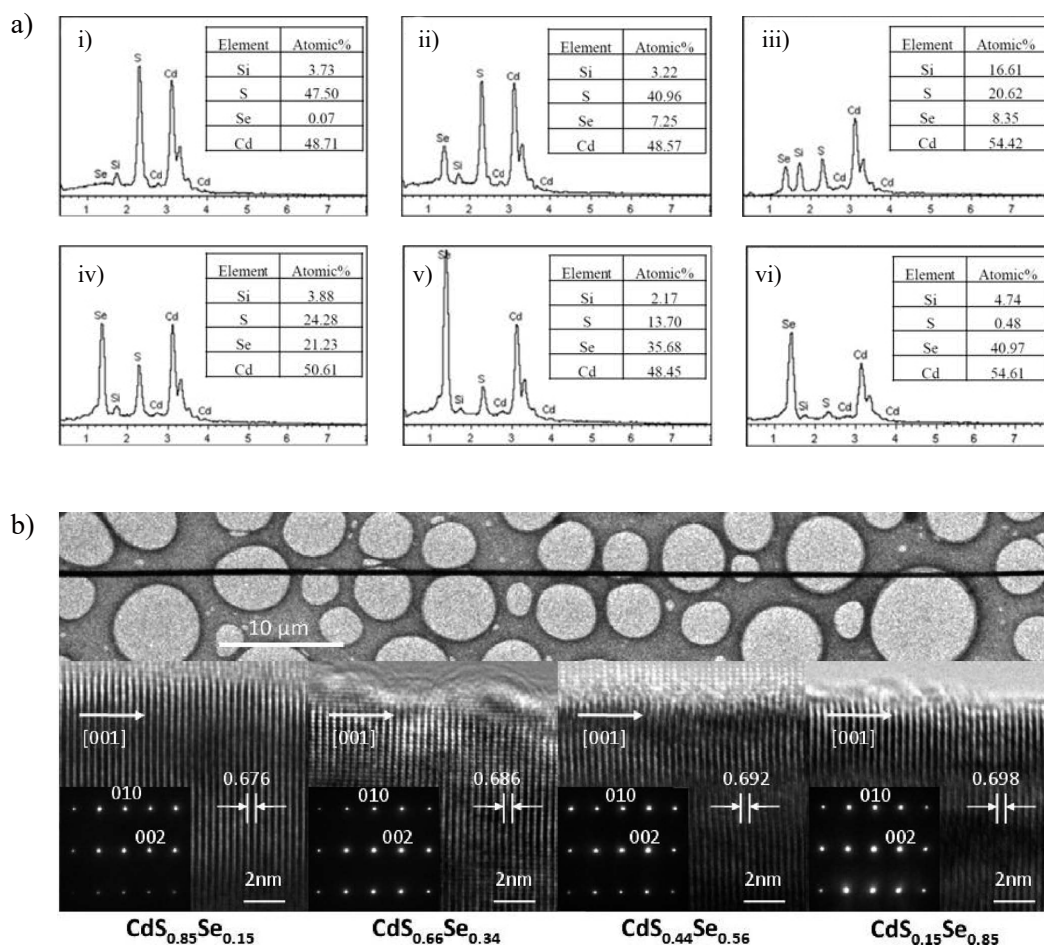


Fig. 4.8 **Spatially resolved compositional analysis of $\text{CdS}_x\text{Se}_{1-x}$ nanowires.** (a) Typical localised EDS spectra, with corresponding elemental compositions, taken at six different points along a $\text{CdS}_x\text{Se}_{1-x}$ nanowire from the CdS (i) to CdSe (vi) end. (b) (above) TEM image of a typical $\text{CdS}_x\text{Se}_{1-x}$ nanowire, with (below) high-resolution TEM and corresponding SAED images taken at four locations down the wire, with the corresponding compositional ratios labelled beneath. All adapted from ref. 203.

increases as the S content decreases and Se content rises, with a relationship that agrees well with that measured in homogeneous $\text{CdS}_x\text{Se}_{1-x}$ wires of varying compositions^[196,203]. SAED results, also shown in Fig. 4.8b, indicate crystal growth orientation is along the [002] direction^[200,203].

With respect to optoelectronic properties and applications, it is crucial to verify that this compositional variation manifests itself in a bandgap gradient along the nanowire. PL imaging and spectral analysis at successive points along a typical $\text{CdS}_x\text{Se}_{1-x}$ nanowire is shown in Figs. 4.9a-c. As can be seen the PL emission gradually varies from red to green, whilst the emission peaks gradually shift from 505 nm to 710 nm respectively, as the laser

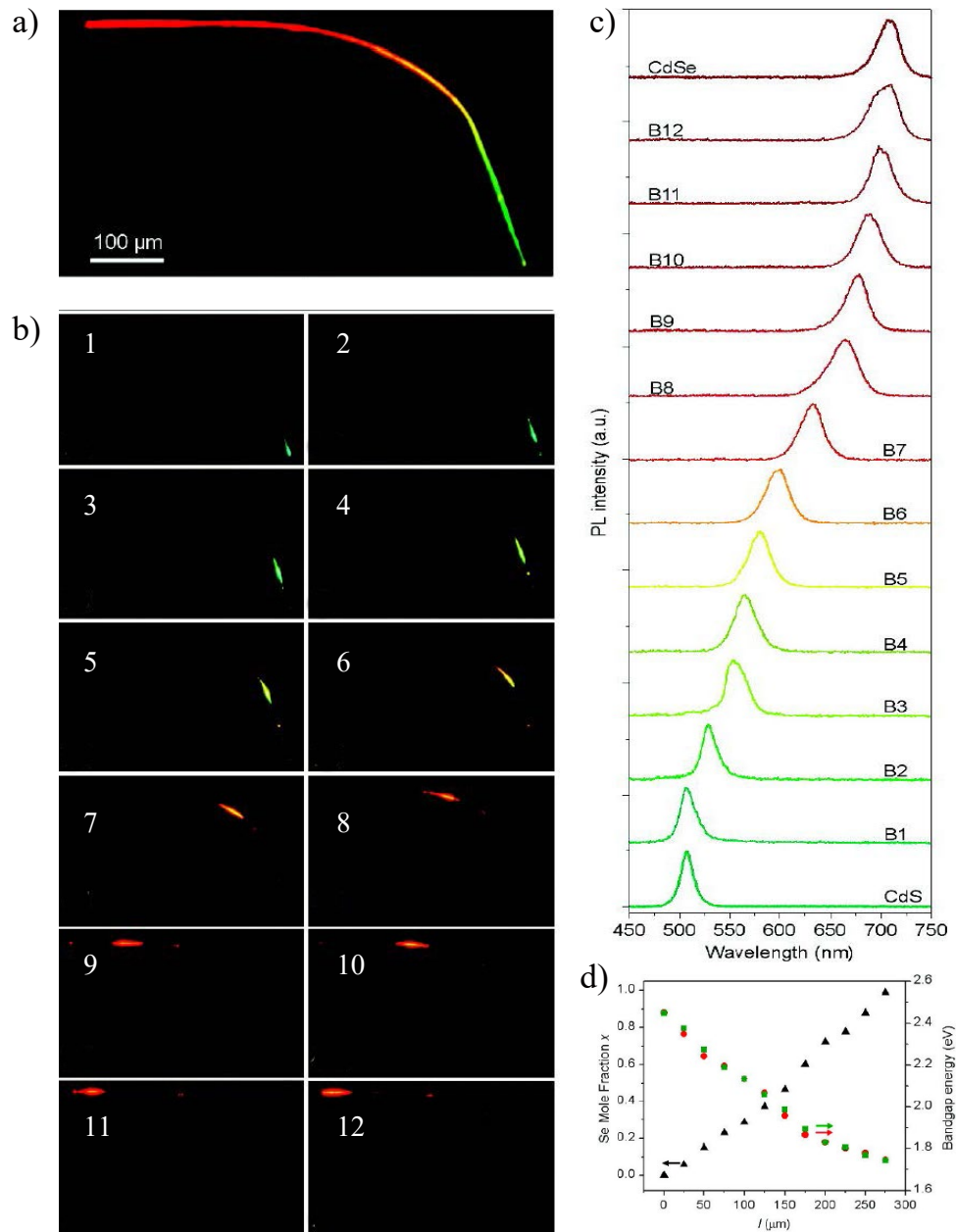


Fig. 4.9 **Photoluminescence mapping of a $\text{CdS}_x\text{Se}_{1-x}$ nanowire.** (a) A typical $\text{CdS}_x\text{Se}_{1-x}$ imaged under diffuse, 405 nm excitation. (b) 1-12 Imaging of the same nanowire with localised excitation by a focused 405 nm laser at a selection of points along the length of the wire (c) Corresponding PL spectra for excitation points b1-12, demonstrating the variation in emission along the wire. CdS and CdSe emission peaks shown for reference. (d) Plot of the variation in Se molar fraction (black triangles), the bandgap energy calculated from the PL spectra peaks (red circles), and the bandgap predicted by applying Vegard's law to EDS compositional data (green rectangles) at the same points along a typical $\text{CdS}_x\text{Se}_{1-x}$ nanowire. All adapted from ref. 203.

excitation is shifted from the CdSe to the CdS end of the nanowire^[203]. The consistent absence of any secondary, lower energy peaks across all the PL spectra indicates that the emission across the whole wire is from near-band-edge processes, rather than those involving surface or defect states which are often seen in CdS_xSe_{1-x} alloy thin films or microcrystals, again suggestive of a highly regular crystalline structure with uniform surfaces^[203,213]. As with the TEM data, these single peaks also point to a successful alloying process all along the nanowire, without the formation of any independent CdS or CdSe phases.

Further to this spectroscopic data, the expected bandgap of a ternary semiconductor alloy can also be deduced from its relative compositions using Vegard's law, which traditionally relates the lattice constant of an alloy to those of their constituent materials^[215,216]. This can be applied to the bandgap of CdS_xSe_{1-x} *via* the following quadratic equation

$$E_g^{CdS_xSe_{1-x}} = xE_g^{CdS} + (1-x)E_g^{CdSe} - bx(1-x) \quad (4.4)$$

where, $E_g^{CdS_xSe_{1-x}}$ is the alloy bandgap, $E_g^{CdS} = 2.25$ eV and $E_g^{CdSe} = 1.70$ eV are the bandgap of CdS and CdSe respectively, x is the compositional fraction, where $0 < x < 1$, and b is a bowing parameter, determining the nonlinearity and related to how affected the band structure is by disorder related to the alloying process; in the case of CdS and CdSe, a relatively small value of $b \sim 0.59$ eV has been measured experimentally across a range of homogeneous alloy nanowires with different x fractions, indicating the good miscibility of the two compounds^[214,217,218]. The variation in Se content, expected bandgaps derived from Vegard's law and the bandgaps calculated from the measured PL emission peak centers, all taken from the same selection of points along a typical CdS_xSe_{1-x} nanowire, can be seen in Fig. 4.9d. The strong concordance between predicted and measured bandgap provides further evidence that a well-alloyed structure has been formed, with near band-edge, rather than defect- or surface-related emission.

Several studies have utilised PL and OPTP spectroscopy to study the carrier dynamics in *homogeneous* CdS_xSe_{1-x} wires, revealing how phenomena in these alloys differs from that of pure CdS or CdSe nanowires. It is observed that whilst in pure CdS and CdSe nanowires the dominant recombination process is *via* surface states on a very short relaxation timescale, this mechanism is not dominant in alloyed wires. Here, the elemental replacement in the crystal lattice creates localisations of free carriers within the interior of the nanowire and as such, the main pathway for recombination is through a slower relaxation process associated with these structural, or "bulk" defects rather than surface trapping, as shown in the comparison between OPTP measurements of pure and alloyed nanowires in Fig. 4.10a^[196,219,221]. In this case, the structural-defect-associated recombination is nonradiative and the restructuring in these alloy nanowires therefore serves to actually *increase* their luminous efficiency^[219]. Liu

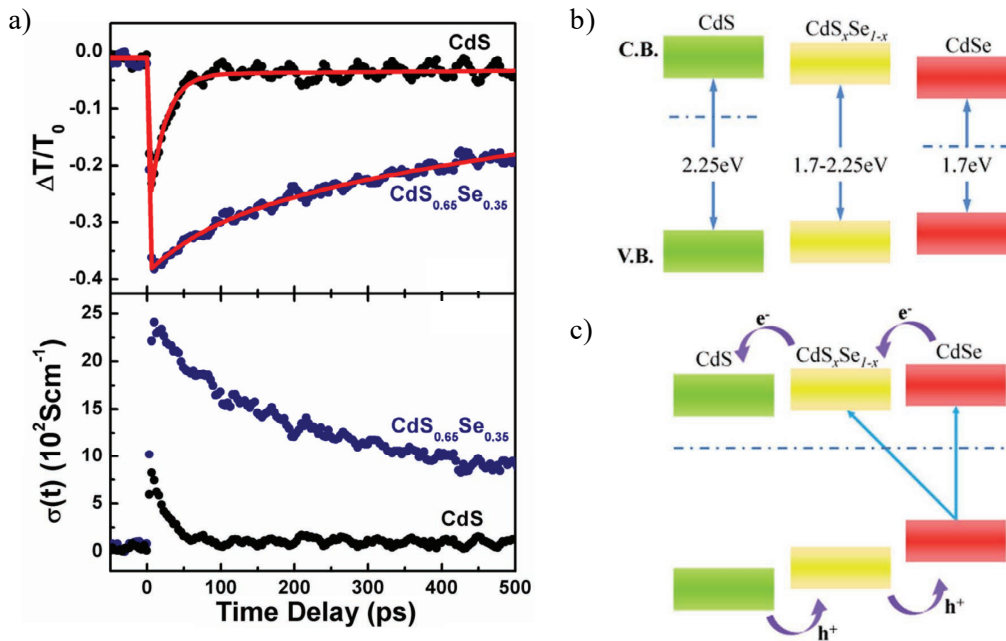


Fig. 4.10 **Photoconductive properties of CdS_xSe_{1-x}-graded compositional system.** (a) OPTP characterisation of pure CdS (black) and alloyed, homogeneous CdSSe nanobelts with (i) time-resolved THz transmission $\Delta T/T_0$ and (ii) the calculated photoexcited conductivity $\sigma(t)$, obtained under 400 nm excitation at a fluence of $40 \mu\text{J}/\text{cm}^2$. Adapted from ref. 219. (b),(c) Schematic representing the band structure along a CdS_xSe_{1-x} graded nanowire before (b) and after (c) Fermi level alignment. Purple arrows denote how such an arrangement promotes the transfer of electrons and holes. (b) and (c) adapted from ref. 220.

et al. attribute this decreased prevalence of surface trapping to the formation of a passivating, sulfur-rich outer shell during growth of the alloyed nanowires, occurring due to the difference in growth temperatures between the CdSe and CdS^[219].

Whilst these investigations were carried out using homogeneous samples with fixed x fractions, OPTP spectroscopy of CdS_xSe_{1-x} gradient nanowires, in reference 220, shows similarly restrained surface effects. This work also found that when looking solely at the structural-defect recombination pathway, the graded ternary wires show shorter decay times than uniform composition alloy CdSSe nanowires (~ 690 ps compared with >1000 ps), pointing toward yet higher relative levels of disorder in the interior structure arising from the incorporation of a gradient^[220].

The analysis in reference 220 also finds the graded CdS_xSe_{1-x} systems to exhibit the highest photoconductivity - as characterised by OPTP techniques - of any nanowire material to date. At up to $2000 \Omega^{-1}\text{cm}^{-1}$, the photoconductivity measured is significantly higher than that in ZnO ($20 \Omega^{-1}\text{cm}^{-1}$, 10K), GaAs ($10 \Omega^{-1}\text{cm}^{-1}$) or GaN ($0.5 \Omega^{-1}\text{cm}^{-1}$), though

more notably is also over twice the $900 \text{ } \Omega^{-1} \text{ cm}^{-1}$ observed in *homogeneous* $\text{CdS}_x\text{Se}_{1-x}$ nanowires. The latter comparison indicates that the gradient itself serves to greatly enhance photoconductivity.

The proposed mechanism here is that Fermi level alignment results in a relative downward and upward shifting of the band-edges in the S-rich and Se-rich sections respectively, creating a stepwise continuum of type-II band heterostructures along the nanowire, as is illustrated in Fig. 4.10b^[200,220]. This structure makes it favourable for photoexcited electrons to transfer from the higher energy conduction bands in the Se-rich end toward those of lower energy in the S-rich end. The reverse process applies to holes, which are driven in the opposite direction toward the Se-rich end, and as such, the system promotes electron-hole pair separation, correspondingly increasing the free carrier density^[220]. Here the photocarrier density can be up to two orders of magnitude higher than that measured in uniform $\text{CdS}_x\text{Se}_{1-x}$ samples, with values on the order of $\sim 10^{19} \text{ cm}^{-3}$.

Li *et al.* have also characterised the electronic properties of $\text{CdS}_x\text{Se}_{1-x}$ gradient structures by the fabrication of single nanowire FETs^[200]. Whilst the free carrier densities demonstrated in this work are far lower, on the order of $\sim 10^{17} \text{ cm}^{-3}$, the carrier mobility observed in the FET is in good agreement with that measured *via* OTP, at 1.5 and $\sim 4 \text{ cm}^2 \text{ V}^{-1} \text{ s}^{-1}$ respectively^[200,220]. The mobilities seen here are in fact around two orders of magnitude lower than the $\sim 100 \text{ cm}^2 \text{ V}^{-1} \text{ s}^{-1}$ observed *via* OTP in homogeneous samples, further evidencing the higher compositional disorder and increased density of scattering centers in the interior of the graded nanowires^[220].

A final, important and well-studied characteristic of these nanowires relates to their photonic properties, and how the bandgap gradient affects the confined propagation of light through their structure, the background for which has already been discussed with reference to general one-dimensional systems in section 4.1.3. In this case, the compositional variation along the nanowire length creates an asymmetry, with the structure behaving as a passive waveguide for light travelling from the narrow (CdSe, red) to wide (CdS, green) bandgap end of the structure, but an active one for light travelling in the other direction, illustrated by the schematic in Fig. 4.11a^[222–224]. Considering this scenario theoretically, in a nanowire of length L , the bandgap at local position l , $E_g(l)$, varies from $E_g(0)$ at one end to $E_g(L)$ at the other. For an input spectrum S_0 at position $l=0$, the spectrum after propagating a length l through the structure can be expressed as

$$S_l = S_0 e^{-\alpha(h\nu)l} \quad (4.5)$$

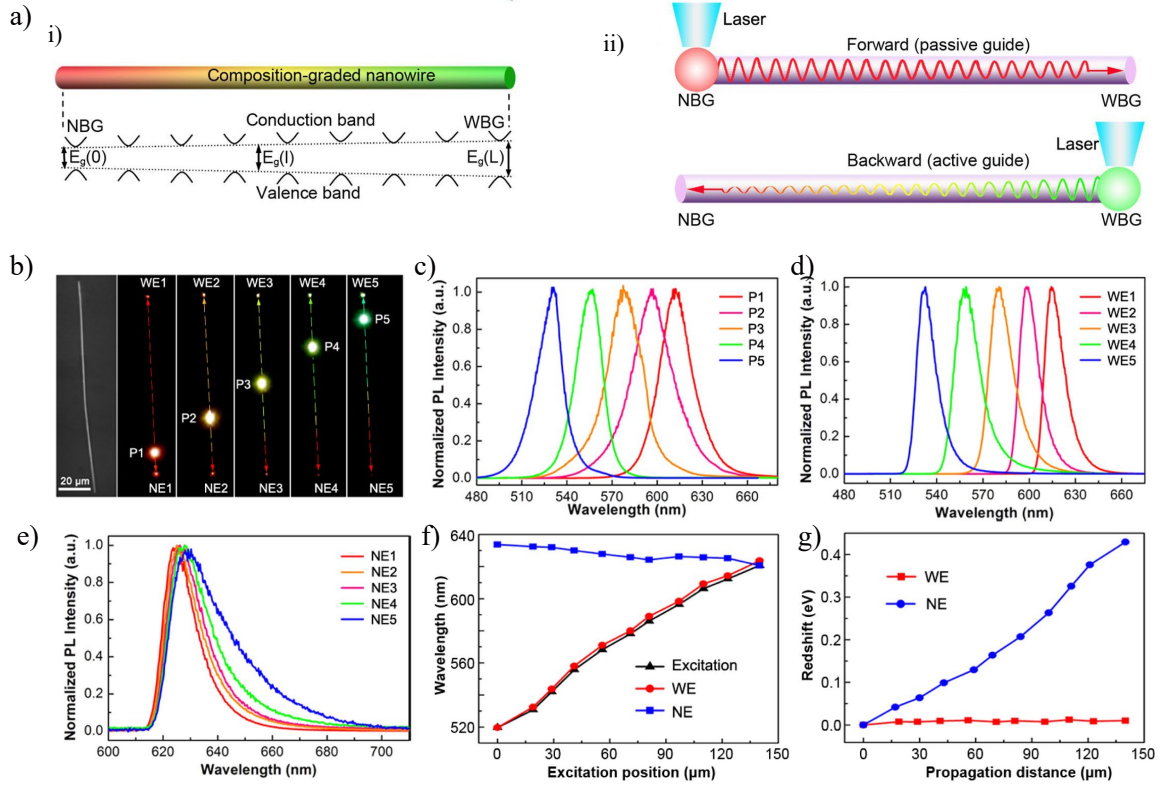


Fig. 4.11 Directionally-dependent waveguiding in compositionally graded semiconductor nanowires. (a) Schematics illustrating (i) the band structure along a $\text{CdS}_x\text{Se}_{1-x}$ gradient nanowire and (ii) the directionally-dependent waveguiding characteristics for light travelling within the wire. Adapted from ref. 222. (b) SEM image (left) and PL images of the same graded $\text{CdS}_x\text{Se}_{1-x}$ nanowire under local excitation by focused laser light at five different positions. (c)-(e) PL spectra collected at (c) the laser position, (P1-5), (d) the wide-bandgap end (WE1-5) and (e) the narrow-bandgap end (NE1-5) of the nanowire for each of the five different excitation locations. (f) Variation in PL emission peak wavelength with the location of excitation. Excitation position is measured from the wide bandgap end of the wire. (g) Redshift in the PL emission spectrum collected at the wide and narrow bandgap ends of the nanowire plotted against the distance propagated by the light. (b)-(g) adapted from ref. 223.

where $\alpha(h\nu)$ is the optical absorption coefficient, which varies depending on whether the energy of photons is above or below the local bandgap as follows

$$\text{For } E \leq E_g(l), \quad \alpha(h\nu) = A_0 \sqrt{\frac{kT}{2\sigma}} e^{[E - E_g(l) - kT/2\sigma]} \quad (4.6)$$

$$\text{For } E > E_g(l), \quad \alpha(h\nu) = A_0 \sqrt{E - E_g(l)} \quad (4.7)$$

where A_0 is a structure related constant, kT is the thermal energy, h is Planck's constant, ν is the photon frequency and σ is a dimensionless phenomenological fitting parameter which is composition-dependent^[222].

When a particular section of the wire is excited, emission from near band-edge states will have energy E equivalent to the bandgap at that location. From this emission, those photons travelling toward the wide-gap (CdS, green) end of the nanowire will have E smaller than the bandgap at any point along the rest of this section. Optical absorption is therefore governed by equation 4.6 and the light will travel as in a passive waveguide, through repeated internal reflections. However, for light travelling in the other direction, toward the narrow-gap (CdSe, red) end of the nanowire, E is *greater* than the material bandgap and therefore propagation occurs as described in equation 4.7, via repeated re-emission and re-absorption from band to band. As such, light emerging at the wide-gap end will remain at a wavelength corresponding to the bandgap at the initial point of excitation, whilst that collected at the narrow-gap end will be characteristic of the band-edge emission at that end of the wire - that is, assuming a complete wire, the red, 710 nm emission from CdSe^[222-224]. This phenomenon is demonstrated experimentally in the series of localised PL analyses in Figs. 4.11b-g.

Summary

In this chapter I have contextualised the broad class of materials that dominate the rest of this thesis: semiconductor nanowires. The most common methods for their production have been described, showing how the physical characteristics of these structures can be tuned with a remarkable degree of precision even at such tiny lengthscales. Whilst quantum effects are often not observed in these nanowires, their size and geometry lead nanowires of different material systems to have common properties, especially concerning their interactions with light. Characterisation techniques have also been introduced to illustrate how these nanowires can be studied without need for physical electronic contact. Finally, I have reviewed the literature surrounding nanowires with on-nanowire compositional gradients, including techniques for their growth as well as their distinguishing properties; these systems allow unprecedented freedom for tailored semiconductor alloying within a single nanostructure.

In the next chapter, I move on to cover how nanowires can be used in optoelectronic applications. This will address the techniques that have been used for device fabrication, before reviewing published work on nanowire photodetectors and miniaturised spectroscopy, to provide context to, and explain the physical mechanisms behind, the devices produced and studied during my PhD.

Chapter 5

Nanomaterial optoelectronic devices

Overview

As laid out in chapters 2 and 4 of this thesis, it is clear that the fundamental properties of many 1d and 2d materials are of significant interest for use in optoelectronic applications. Aside from their optical or electronic properties, as devices are driven to be ever-more compact, the physical size of these nanomaterials alone can make them attractive for ultra-miniaturised or essentially transparent components in a range of commercial and research-orientated technologies. Indeed, in many of these applications, such as smartphones, ‘internet-of-things’-connected sensors, lab-on-a-chip systems, or even wearable or implantable monitors, this factor often outweighs the need for these devices to match bulkier macroscopic technology in terms of performance.

However, also in part due to their size, realising the full potential of these nanostructures in devices, with even satisfactory performance and stability, is far from straightforward and presents a wide range of challenges in and of itself. For instance, for nanowires and 2d materials grown by bottom-up methods or produced by LPE, processes must usually be developed and optimised to transfer and ideally position them onto device-ready substrates, from their raw, as-prepared states. Though well-established top-down nanofabrication processes can be used to create electrodes and gate structures on nanomaterials, the formation of reliable electronic contact is complicated by their geometry, size-dependent effects and unpredictable surface chemistry. Furthermore, the sensitivity of these materials means that effective means of passivation must often be established if devices are to operate with the level of stability necessary for commercially viable applications.

This chapter contains a literature review providing background surrounding the fabrication, optimisation and operation of the nanomaterial optoelectronic devices that I have developed and studied in my research. Accordingly, the first section begins by addressing the

first stage of device production: the deposition of the nanomaterial components onto the device substrate. Here, I will summarise the methods used in my research to transfer nanowires and CVD-grown graphene from their growth substrates to other surfaces, as well as briefly touching on other techniques for nanowire transfer which could be made industrially scalable. In the rest of this section, I will detail common processes for patterning and depositing metallic electrodes onto nanomaterials which have been used to fabricate my own devices, as well as discussing techniques developed in the field to adapt these for thicker nanowires such as those featured in my research. It will also cover practical methods for stabilising the environmentally-sensitive properties of nanomaterial devices through passivation of their surfaces, with demonstrated results from the literature.

The second section will address the fundamental physical mechanisms behind photodetection in single nanowire devices similar to those contained in my research, such that the results reported in this thesis may be better interpreted. This will initially look at the phenomenon of photoconductivity in semiconductors, more specifically applied to the case of Ohmically contacted nanowires and summarising why nanowires in particular are good candidates for photoconductive devices. Complementary to this, I shall also address Schottky-barrier contacts in nanowire devices, covering their formation and how the mechanisms of detection differ correspondingly.

The third section will diverge to provide more focused background to the central aim of my research: the creation of a spectrometer based on a single compositionally-graded nanowire. To properly frame the impact of such a device, I will first present a general outlook on the field of miniaturised spectroscopy systems, looking initially at the most dominant technologies thus far; designs based on conventional bench-top systems, centered around gratings and interferometers. Advancing on this, I shall introduce and discuss a recently-emerged branch of microspectrometers based on computational reconstruction from broadband filter arrays, the operational principles behind which have inspired the strategy in my research. Finally, I will discuss the wavelength-selective photodetectors based on compositionally-graded nanowires reported in the literature, which represent the most structurally similar devices to those in this thesis, and thus present valuable insight into their characteristics.

5.1 Nanofabrication techniques

5.1.1 Two- and one-dimensional material transfer

As touched upon in chapter 2, it is not as of yet possible to grow 2d materials directly onto insulating surfaces with high yield^[5] and as such many methods have been developed to transfer graphene in particular from the growth foil to a desired substrate. The most commonly used method, a schematic of which can be seen in Fig. 5.1, is a wet transfer process using a polymer scaffold, which is first spin-coated onto the graphene on the (usually Cu) growth foil; a variant of this process was developed and optimised within my research, detailed in section 7.1.1. Graphene that has grown on the reverse side of the foil must then be removed by a plasma etching step. The foil is then floated onto an etchant solution and left for a length of time sufficient to completely remove the Cu foil, leaving the polymer-supported graphene film at the liquid surface. By submerging and subsequently raising a substrate from beneath the film, it can then be ‘fished’ from the etchant and placed in a deionised water bath, before this fishing is repeated using the final intended substrate. Once dried, the polymer layer is then removed using an appropriate solvent. This general framework can be adapted to almost arbitrary dimensions, from wafer-scale^[77] to roll-to-roll production of 30 inch squared sheets^[225].

There are several pitfalls with this process, and whilst these general steps feature in the great majority of reported wet transfers, a wide range of variants have been developed aimed at optimising the quality of the resultant film. The relative merits of each, in terms of minimising unwanted contamination, strain, wrinkles, physical damage and doping, whilst improving sheet resistance, are often assessed with AFM, Raman spectroscopy, or electronic characterisation, though there is little consensus on the ideal materials and techniques.

Depending on the chemical (such as FeCl_3 , Marble’s reagent (CuSO_4 , HCl and H_2O)^[226] and ammonium persulfate $[(\text{NH}_4)_2\text{S}_2\text{O}_8]$) and concentration used, the etching process can cause ionic contamination, chemical damage and the production of bubbles underneath the film, liable to cause tearing^[227]. Oxidised particulates can also remain after the etching stage. Therefore, some processes have introduced steps to clean the graphene surface by floating the film onto standardised industry wafer cleaning solutions in order to remove any organic or metallic species before fishing onto the device substrate^[228].

Probably the key challenge for these wet transfer processes concerns the polymer scaffold. Even after lengthy dissolution steps, polymer residue will remain attached at the graphene surface negatively influencing graphene transport properties^[229]. Whilst this can be removed through high temperature annealing^[229], in many cases such measures are not ideal, or even are incompatible with respect to the rest of the fabrication process. The amount of contam-

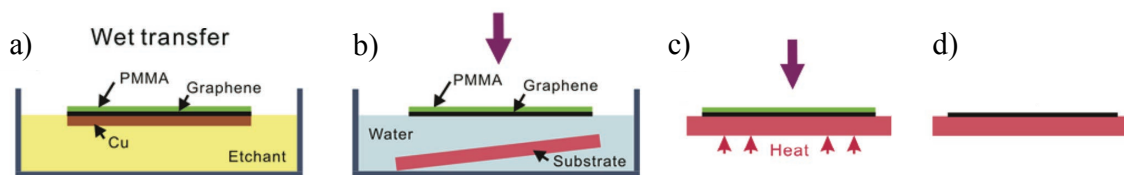


Fig. 5.1 **Wet-etch-based transfer techniques for 2d materials.** Basic stages of a typical wet transfer process for CVD grown graphene, showing (a) etching of the growth substrate, (b) transferral to a water bath followed by fishing using the target substrate, before (c) heating to improve adhesion between graphene and the surface and (d) dissolution of the polymer scaffold. All adapted from ref. 232.

ination is linked heavily to the choice of polymer, its concentration, and the removal solvents employed^[227,230]. The most commonly featured combination is PMMA (poly(methyl methacrylate)) and acetone, with one study suggesting that PC (poly(bisphenol A carbonate)) and chloroform resulted in lower relative residue density, whilst PLA (poly(lactic acid)) for instance produced far more^[227]. Others suggest that lowering the concentration of PMMA in anisole produces far cleaner films^[86,231].

Another key area for consideration is at the graphene-substrate interface. Due to the nature of the fishing process, during which water is trapped at the interface and removed as the film dries, wrinkles and folds, as well as cracks, will form in the graphene layer putting corresponding strain on the lattice^[83]. A variety of techniques have been used to address this, such as re-depositing polymer onto the film after it has dried to relax the graphene layer^[83]. Heating the film after transfer (but before dissolution) has been used to the same end, encouraging adhesion at the substrate interface^[231]. This has been shown to improve the sheet resistance of the graphene layer, though can lead to more persistent polymer contamination, and has been shown to adversely affect electronic properties beyond high enough temperatures (some works suggest above ~ 130 °C^[231]).

As with 2d materials, a key stage in nanowire device production is transfer from growth to device substrates. For vertically-orientated applications (i.e. where nanowires are perpendicular to the substrate), nanowires can be grown by VLS in regular arrays (through pre-patterning the catalytic nanocluster film) such that they can be used directly in a device without removal from the substrate^[158,235]. However, for devices where individual or multiple nanowires lie horizontally on (i.e. parallel with) a substrate, an appropriate method must be used to remove the nanowires from the growth chip and transfer them to the device substrate, ideally with control over their eventual spatial density and positioning. Indeed, if industrial scale production of horizontally-orientated devices - such as those created in this thesis - is to be

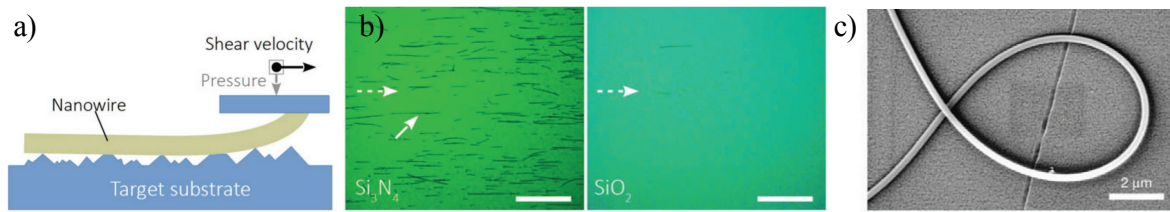


Fig. 5.2 Contact-based transfer of nanowires. (a) Schematic depicting a basic contact transfer technique for removing nanowires from a growth chip. (b) Optical microscope images of nanowires as-transferred onto Si₃N₄ and SiO₂ substrates, demonstrating the effect of differing surface energies on nanowire deposition density. Scale bar is 100 μm. (c) SEM image of a 280 nm radius amorphous silica wire drawn from a heated optical fiber, demonstrating robust physical properties under a bending radius of 2.7 μm. a) and b) adapted from ref. 233, c) adapted from ref. 234.

realised, the development of controllable, precise placement and alignment of nanowires over large length-scales is crucial.

Initial removal from the growth substrate is commonly achieved either by dry, contact-based transfer, or by submersion and gentle sonication in a suitable solvent to produce a nanowire suspension. In the case of the former (the primarily used method in this thesis) a receiving substrate is slid across the growth chip with its randomly oriented forest of nanowires, in the direction of desired alignment^[236–238]. Nanowires contacted by the target substrate become attached by van-der-Waal attractions, and the corresponding shear forces due to the surface movement bring the nanowires into alignment whilst simultaneously detaching them from the growth sample^[141,239]. This process is depicted in Fig. 5.2a and b. Chemical or plasma modification of the target surface provides a straightforward method for altering the probability of deposition and hence the density of the nanowire array^[141]. To expand upon this technique, roll-printing systems can be used for higher throughput^[239] whilst the receiver substrate can also be coated in a pre-designed resist, for production of patterned structures^[236]. Remarkable control over spatial density of deposition is possible, from packed, ~ 7 nanowires/μm high structures, to continuous columns of single nanowires^[236].

For proof-of-concept devices in research environments, where such patterned processes may not necessarily be optimised, some groups have utilised probes to manipulate or pick up and transfer individual nanowires to allow for arbitrary positioning of custom arrangements^[222,223], or even to cleave nanowires in two at specific locations^[212]. These probes are created from optical fibres that have been heated and drawn out to ultra fine tips, based on a technique established in reference 234 for the creation of free-standing silica wires down to 50 nm in diameter, shown in Fig. 5.2c. This process was used extensively in my research for the transfer and placement of nanowires, as will be detailed in section 6.1.1.

For solution-based removal, a variety of methods exist for depositing nanowires from the suspension onto a substrate in a controllable manner. Flowing suspensions through micro-fluidic channel structures patterned in poly(dimethylsiloxane) (PDMS), can achieve highly aligned deposition^[240–242], whilst surface-tension based effects can be used to align nanowires in langmuir-blodgett based techniques^[141,243]. Electric-field-directed assembly can also be achieved, exploiting the high polarizability of nanowires due to their anisotropic structures to attract and align groups of nanowires^[135,150,244] or even manoeuvre individual structures^[239].

5.1.2 Photolithography

Photolithography is the cornerstone of modern CMOS technology fabrication, as the most widely used process for wafer-patterning. The technique is based around coating of target substrates in light-sensitive polymer-based materials, known as photoresists, which can be patterned through selective exposure to UV radiation using a photomask. The stages in a typical contact-based process are detailed in Fig. 5.3. To promote adhesion of the resist, substrates are heated to minimise the adsorbed water layer, followed in some cases by treatment through an adhesion promoting chemical such as hexamethyldisilazane (HMDS). Photoresist is then applied *via* spin-coating to produce a highly uniform layer, usually with thickness in the order of 0.5 - 2.5 μm . Photomasks usually consist of a glass plate covered with a thin patterned layer of chrome, typically itself fabricated by electron-beam lithography. The mask is placed either in contact with the resist, or in close proximity, depending on the process used, before exposure to UV radiation of an appropriate wavelength, for a chosen duration, dependent on the source intensity and dose required.

Photoresists can either be positive, such as AZ 4533, whereby irradiation dissociates molecular chains in the material and makes exposed areas soluble to a photodeveloper, or negative, such as SU-8, where cross-linking of polymer in exposed areas makes them highly insoluble to the developer. Image reversal resists such as AZ 5214E also exist for which a post-exposure heating step can be used to switch the solubility of exposed areas and produce negative wall profiles desired for metal lift-off (as illustrated in Fig. 5.3b). After the resist has been patterned, a chosen process - typically an etch or deposition - is applied to the exposed areas of surface, before the removal of the resist to reveal the as-patterned substrate. Resolution in contact photolithography is typically on the micrometer scale, with minimum feature size around 1 - 2 μm .

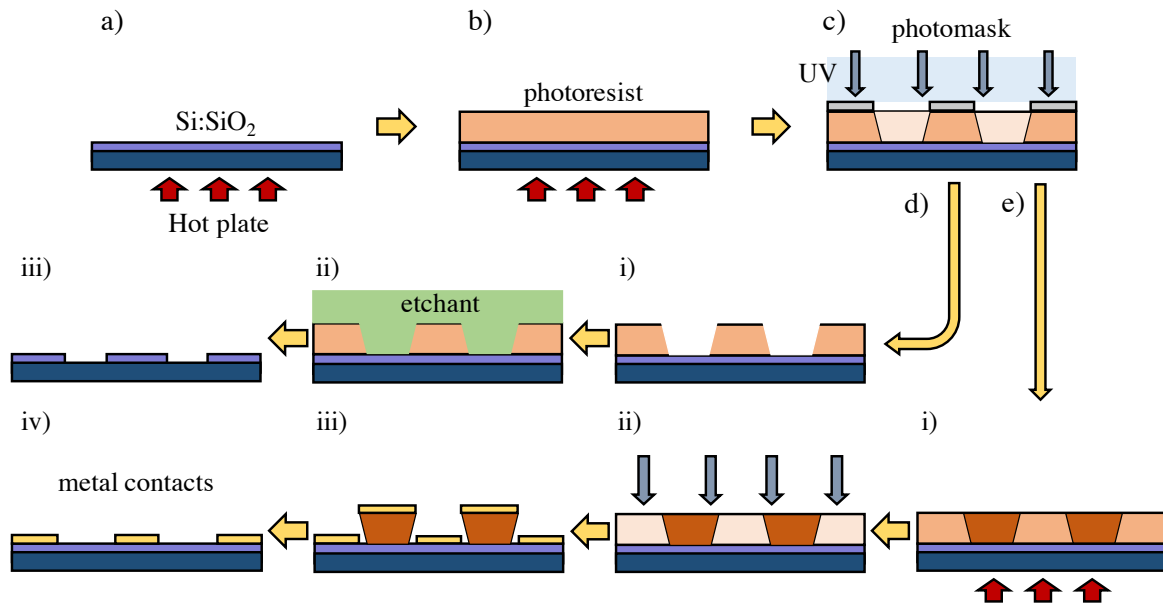


Fig. 5.3 **Photolithography for device fabrication.** Schematic of typical photolithographic patterning processes for a positive-tone photoresist with image reversal functionality. The middle path shows a procedure for producing a positive image transfer for an etch process while the bottom path details use of image reversal to obtain a negative side-wall profile in the patterned resist, to enable clean lift-off in the deposition of metallic contacts. **a)** Heating of the substrate to remove adsorbed water layer and promote resist adhesion. **b)** Resist is spin-coated onto the substrate and cured. **c)** In a contact-based process, a patterned photomask is pressed directly to the photoresist, and a dose of UV radiation delivered. Areas exposed to the UV become dissociated (lighter colour) **d)** i) Substrate is placed in photodeveloper until features have been resolved. ii) At this stage the exposed areas can be etched by a desired method. iii) Removal of the remaining photoresist in an appropriate solvent **e)** i) The sample is heated at a specific temperature to cross-link *only* those areas exposed to the UV. ii) Flood exposure with UV at a high dosage to make non-cross linked areas soluble. iii) Soluble areas removed by developer before deposition of desired metallic layer for contacts. iv) Lift-off of the metal coated resist with an appropriate solvent.

5.1.3 Electron-beam lithography

Electron beam lithography (EBL) is a maskless nanofabrication technique for the direct-writing of custom CAD patterns, capable of creating features with sub-10 nm resolution. It is limited with respect to large-scale manufacturing due to its low-throughput, however it is one of the most widely used processes for the creation of proof-of-concept, nano-scale devices, as well as in the production of high resolution photomasks. EBL is the primary tool through which $\text{CdS}_x\text{Se}_{1-x}$ nanowire-based devices have been created for this thesis.

As with photolithography, a polymer-based resist, often poly(methyl methacrylate) (PMMA), is used. Writing is carried out using a focused electron beam, often using adapted SEM setups, with ultra-precise deflection of the beam performed through electrostatic lensing.

High energy incident electrons, of between 10 - 100 keV, cause either dissociation or cross-linking of molecular chains in the resist, dependent on its positivity, before development to remove soluble areas.

As the wavelength of the electron beam is so small, the resolution of electron beam lithography is instead limited mainly by electron scattering from the resist and substrate, as well as the creation of secondary electrons, rather than diffraction. This leads to a complication known as the proximity effect, whereby areas of resist immediately around those being written also receive a dose of electrons, enlarging features. This also creates challenges for the creation of densely arranged patterns due to exposure 'spilling over' across features.

5.1.4 Electrode deposition

As discussed, once a lithographic process has been used to pattern a resist, a metal film is deposited over the whole surface, before dissolution of the resist removes all of the film except those sections exposed in the lithography; this is known as a 'lift-off' process. In the majority of nanofabrication processes, this metallisation is done by physical vapour deposition, which differs from CVD in that the deposited material is converted from a solid phase in a crucible or target, to a vapour phase, before condensing back to a solid thin-film on the target substrate, without any intended chemical modification. The rate and thickness of deposition can be monitored by a piezoelectric crystal in the chamber. This is commonly achieved using one of three processes - thermal evaporation, electron-beam evaporation or sputter deposition - all of which are used in this thesis.

In thermal evaporation, usually carried out in a low-vacuum chamber, material for deposition is situated in a crucible which is heated directly, often by an electric filament. Electron-beam evaporation differs to thermal in that the heating of the material is carried out by a focused electron-beam, under high-vacuum, affording a greater level of control over the rate of evaporation, fewer impurities in the deposited films, as well as allowing the deposition of materials with exceptionally high vaporisation points. In both of these techniques, due to the vacuums used, the path length of particles in the vapour is sufficiently long that they can be thought to travel in a straight line from the source to their point of condensation, meaning the deposition is highly anisotropic and directional. Rotation and tilt of the substrate stage is often possible in these systems to allow more uniform or conformal films, whilst stage cooling systems can be integrated to either protect the sample from high temperatures or change properties of the metal layer, such as crystal grain size.

In a sputter deposition process, rather than using heat to vaporise a material to be deposited, a target is bombarded with gaseous ions in order to physically remove and propel

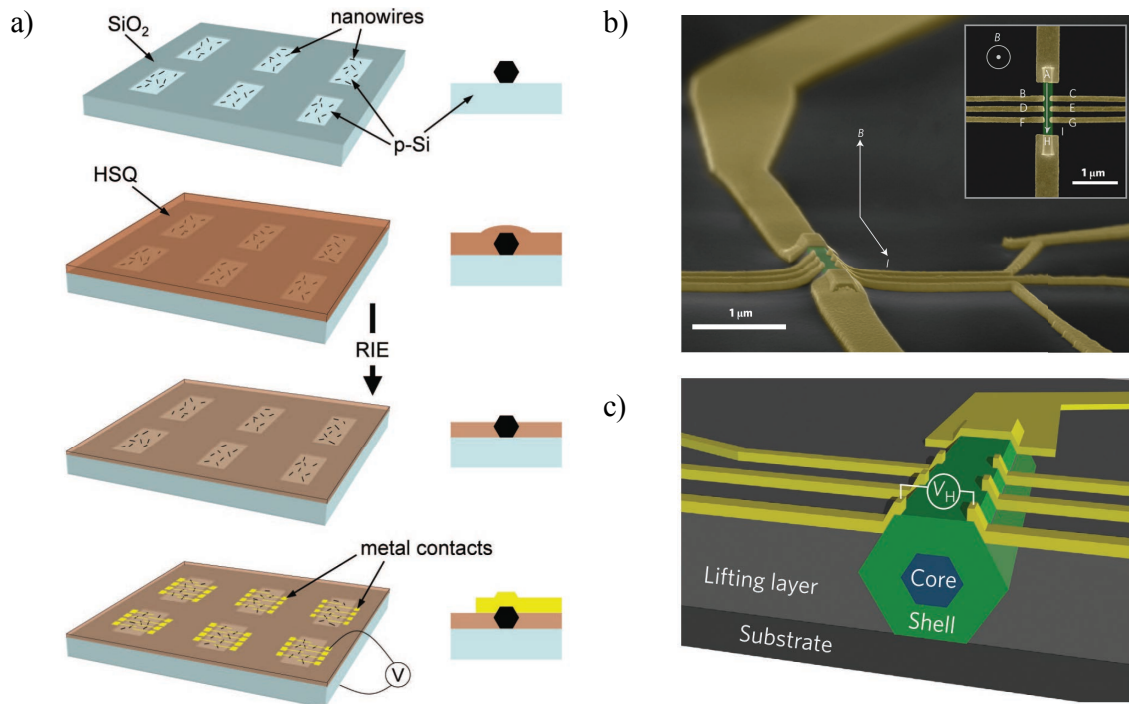


Fig. 5.4 **Embedded nanowire devices.** (a) Illustration of a typical process to produce a ‘spacer’ layer before nanowire electrode deposition. From top-to-bottom, the substrate is coated in a resist (in this case HSQ), which aligns to the top of the nanowires, before their top-surfaces are exposed using an RIE etch allowing the deposition of electrodes without risk of shadowing from the nanowire during evaporation. Adapted from ref. 245. (b) Tilted, false-colour SEM image of a hall-bar device embedded in a polymer layer using a similar process to that in a). (c) Cross-sectional schematic of the device in b). b) and c) adapted from ref. 246.

atoms into the chamber. This is often achieved with strong electronic and magnetic fields generated by a magnetron, creating a plasma from the sputtering gas (commonly Argon in magnetron-based processes) and confining it to collide with the target at high energy. Here, materials with high evaporation point materials can be sputtered with greater ease than thermal or electron-beam mediated techniques. Arguably the key variable in a sputter process is the pressure of the gas used, which can be adjusted to control the properties of the resultant film. In general, higher pressures will lead to a decreased mean free path length of sputtered particles, which in turn will lead to a more conformal coating, whilst lower pressures can be used to generate higher energy, near-ballistic motion, with greater shadowing in deposition.

For nanowires, the fabrication of metallic contacts *via* anisotropic deposition is complicated by their morphology, especially for nanowires with thicker cross-sections. In these cases, assuming a particular nanowire is not precisely above the evaporation source, its structure will ‘shadow’ incident metallic vapour, causing a discontinuity in the film adjacent

to the side of the nanowire that is facing away from the source. Clearly, this can be addressed by simply evaporating a metal layer that is thicker than the nanowire itself, but considering some nanowire dimensions may be up to hundreds of nanometres, this may require a far thicker resist to be used, increasing the difficulty of achieving high-resolution lithographic features. Alternatively, as discussed, sputtering processes can also be adapted to achieve near-isotropic deposition of highly conformal films. Whilst these will coat the side facets of thicker nanowires, they will also coat the resist side-walls, preventing solvent penetration and making lift-off problematic. This, in part, is why many works have extolled the benefits of contactless characterisation of nanowire electronic properties, through, for instance, OPTP spectroscopy^[139].

However, some groups have circumvented this problem by using a spacer or ‘lifting’ layer surrounding the nanowire to planarise the surface, decreasing the height difference between the top of the nanowire and its surroundings^[245]. Such a process is illustrated in Fig. 5.4a. In these works, after their dispersion on a substrate, a photo- or EBL-resist is spin-coated over the nanowires and baked. The top facet of the nanowires is then revealed *via* a plasma etch^[245,246], or partial exposure and development^[247] of this spacer layer. In this way, the nanowire is effectively embedded into a quasi-flat surface, on which a far thinner EBL resist can be used, allowing patterning of more complex, high-resolution structures, such as Hall bars, as shown in Figs. 5.4b and c^[246,248,249]. A variety of different methods for nanowire contact deposition, including the use of a spacer layer, are investigated in my experimental work and detailed in section 6.2.

5.1.5 Passivating one- and two-dimensional devices

As discussed in chapters 2 and 4, transport in 1d and 2d materials is highly sensitive to the external environment, due to their high - or in the case of monolayers, essentially infinite - surface to volume ratios. Electronic properties of FETs based on exposed graphene and semiconductor nanowire channels, such as the carrier mobility, on/off ratio (in nanowires) and electrostatic doping, are significantly influenced by adsorbates such as oxygen and water vapour under ambient conditions^[250–253]. In pristene samples taken from vacuum and exposed to ambient conditions or particular gaseous species, these effects show rapid onset (several minutes)^[251] and vary in magnitude with exposure time as well as both the type and concentration of gases involved^[252,253]. Furthermore, adsorbates are liable to cause hysteretic gating characteristics in both nanowire and 2d-material based devices, through capacitive coupling and charge transfer between adsorbed species and carriers in the channel or surface traps^[253–256]. This hysteresis also occurs as a result of charge traps at the nanomaterial-substrate interface, such as silanol (SiOH^-) groups where Si-SiO_2

substrates are used^[256,257]. Whilst these behaviours can be exploited in sensing applications, clearly it is undesirable for commercial electronic or optoelectronic devices which generally require operational properties that are highly stable over time, regardless of changes in their immediate environment.

As a result of this, a variety of different methods have been investigated to passivate nanomaterial surfaces and stabilise their chemistry. In nanowires this can be achieved through chemical modification, by treating the device with particular reagents to terminate surfaces with, for instance, chloride or sulfide species^[258], or organic molecules^[259], saturating any dangling bonds. These techniques are less applicable to 2d materials, where any surface modification can drastically change their chemical properties, and even in nanowires it can be difficult to control these reactions, leading to greater penetration into the ‘bulk’ of the nanowire than desired^[258].

Far more commonly in both 1d and 2d material devices is the deposition of a layer of another material to coat the channel so that it is no longer exposed to the environment. Such methods can involve organic materials, for instance through spin-coating of PMMA^[250,260] or semiconducting polymers^[261], or the application of self-assembled monolayers (SAMs)^[262]. Figure 5.5a illustrates how coating in polymer can modify the near-surface band structure of a GaAs nanowire. Likewise, the deposition of a range of different dielectric materials has been investigated^[263–265], attractive due to their compatibility with standardised CMOS processes, as well as affording the fabrication of top-gated architectures. Here, one technique demonstrated as effective for both 1d and 2d materials is the atomic layer deposition (ALD) of Al₂O₃ dielectric^[256,257,266,267], which is used for the passivation of the nanowire devices in this thesis (section 7.2). In an ALD process, a sample is placed in a heated reaction chamber which is injected sequentially with two separate gaseous precursors - in the case of Al₂O₃ these are usually trimethylaluminium (TMA) and water^[268]. When one of the precursors is introduced, a single molecular layer adsorbs to the surface in a self-limiting fashion, followed by the removal of any excess and subsequent introduction of the other precursor^[268]. Repetition of this sequence facilitates the layer-by-layer construction of a dielectric film, with near atomically-precise thickness control. Films deposited by an optimised ALD process are usually entirely conformal, regardless of surface topography^[256]. This presents an advantage for nanowires, where shadowing effects can lead to cracks in dielectric layers deposited by conventional, anisotropic evaporation processes, as discussed in the previous section with respect to metallic contacts.

The effects of such passivation processes on nanomaterial device properties are often quite dramatic, though do depend heavily on the methods and agents employed^[264]. ALD of Al₂O₃ on InAs nanowire backgated FET-type photodetectors has been demonstrated to improve

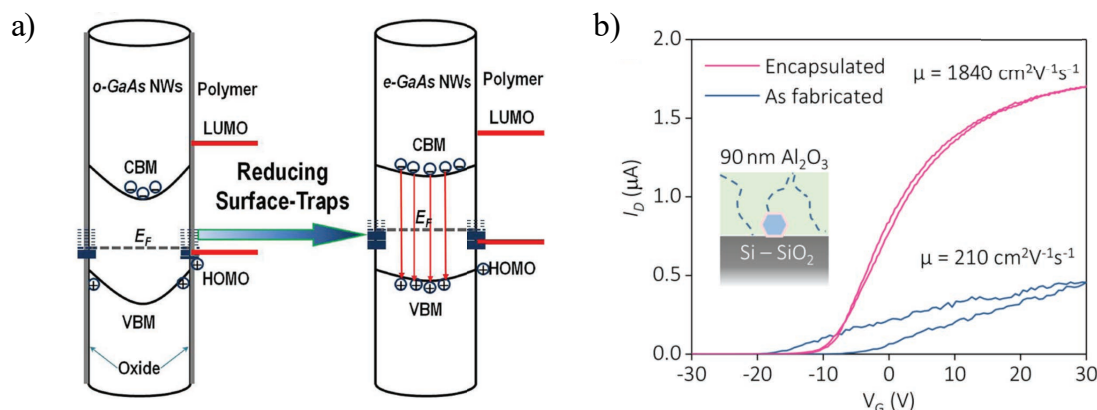


Fig. 5.5 **Passivation of nanowire and 2d material devices.** (a) Band diagram schematic illustrating surface passivation of a nanowire through removal of an oxide layer and coating with polymer. The p-doping oxide layer, and corresponding band-bending, is neutralised by the injection of electrons from the polymer, reducing the probability of surface state-mediated recombination. Adapted from ref. 261. (b) Backgated InAs FET trans-characteristics, showing the drain current whilst sweeping the gate voltage, V_G , before and after encapsulation, indicating a significant increase in carrier mobility and reduction in hysteresis. Adapted from ref. 256.

field-effect mobility by nearly an order of magnitude, whilst tripling the on-state current, and notably producing a 10 and 20 times reduction in the dark and light hysteresis respectively (see Fig. 5.5b^[256]). In ZnO nanowire FETs, deposition of a $\text{SiO}_2/\text{Si}_3\text{N}_4$ was shown to increase on/off ratios an order of magnitude, and carrier mobilities by over two orders of magnitude^[263]. With respect to photoexcitation processes, Dan *et al.* reported significant reductions in surface recombination after passivating Si nanowires with an amorphous silicon layer during the growth phase, showing a two order of magnitude increase in carrier lifetime, corresponding to a 90-fold increase in the photosensitivity when incorporated into a detector^[269].

5.2 Nanowire-based photodetection

5.2.1 Photoconductors

The large majority of single-nanowire, horizontally orientated photodetectors are simple, two-terminal, metal-semiconductor-metal structures atop a dielectric substrate. Here the primary physical mechanism that affords sensitivity to light is photoconductivity, whereby the conductivity of the nanowire will increase when illuminated (though a decrease - negative photoconductivity - is also seen in some materials such as InAs^[256,270,271]). As discussed in chapter 4, nanowires of a particular material can display significantly higher sensitivity

to light than their bulk counterparts due to their size and high surface-to-volume ratios. In ref. 272, Soci et al. provide a comprehensive explanation of this phenomenon in nanowires, starting from the fundamentals of photoconductivity in semiconductors.

For a semiconductor in the dark, its intrinsic conductivity, σ , is given by

$$\sigma = en\mu \quad (5.1)$$

where e is the electron charge, n is the charge carrier density and μ is the carrier mobility (for the latter two, considering the case for only one type of carriers). Illustrated in the schematic in Fig. 5.6, when an electric field, $F = V/l$ is applied at a bias V between two electrodes at the ends of a nanowire with length l , the current density, J is

$$J = \sigma F = env \quad (5.2)$$

where $v = \mu F$ is the carrier drift velocity. With light incident onto the nanowire, a change in either the carrier density (Δn) or mobility ($\Delta \mu$) will lead to a change in the conductivity ($\Delta \sigma$) as described by:

$$\Delta \sigma = \sigma_{light} - \sigma_{dark} = e(\mu \Delta n + n \Delta \mu) \quad (5.3)$$

and meaning that the time-dependent photocurrent, J_{PC} is

$$J_{PC}(t) = eF[\mu(t)\Delta n(t) + n(t)\Delta \mu(t)]. \quad (5.4)$$

The change in carrier density through photoexcitation far outweighs that in the mobility for most semiconductor materials and therefore equation 5.4 can be simplified to:

$$J_{PC}(t) = \Delta \sigma F = e\mu \Delta n(t)F. \quad (5.5)$$

To describe the steady-state photoconductivity, with a nanowire under constant illumination, we consider the simplest possible scenario, where an interband transition is optically excited in a continuous and linear fashion, leading to direct carrier photogeneration. The exposed area, A , of a nanowire with diameter d , length l and cross-sectional area A_0 is given by $A = 2A_0l/d$. Over the ‘bulk’ of the NW, the average optical generation rate g_d can be described by

$$g_d = \eta^* \frac{(P_{opt}/\hbar\omega)}{Vol} = 2\eta^* \frac{(P_{opt}/\hbar\omega)}{Ad} \quad (5.6)$$

where the incident optical power, $P_{opt} = I_0A$, where I_0 is the intensity of the light and $\eta^* = \eta^\dagger \eta$, where η is the quantum efficiency of the material and η^\dagger is a factor accounting

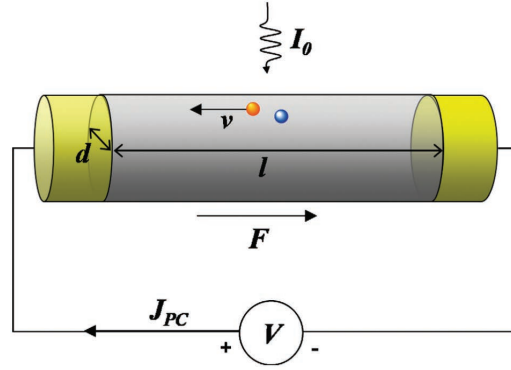


Fig. 5.6 **A nanowire photoconductor.** Diagram of a hypothetical nanowire photoconductor, under illumination intensity I_0 , with photo-separated electron (red) - hole (blue) pairs travelling at drift velocity v . Adapted from ref. 272.

for the specific phenomena in the particular architecture, such as light reflection, light scattering and the low-dimensionality of the nanowire.

The relaxation of photocarriers to the ground state occurs with a characteristic lifetime, τ . In the steady-state scenario, carrier relaxation and generation are balanced such that the shift in carrier density remains fixed over time, that is

$$\Delta n(t) = g_d \tau = \text{constant}. \quad (5.7)$$

Substituting into equation 5.3, the photoconductivity is given by

$$\Delta \sigma = g_d e (\mu \tau) \quad (5.8)$$

where $(\mu \tau)$ is a common figure of merit to describe the sensitivity of the material to excitation, known as the mobility-lifetime product. Therefore, using equations 5.5, 5.6 and 5.8, the steady-state photocurrent density in the nanowire can be expressed as,

$$J_{PC} = \Delta \sigma F = 2 \eta^* \frac{(P_{opt}/\hbar \omega)}{A d} e (\mu \tau) F \quad (5.9)$$

for a given photon energy, $\hbar \omega$. Expanding this to consider both electrons and holes, gives a photoresponse, I_{PC} , across the nanowire cross-sectional area A_0 of

$$I_{PC} = J_{PC} A_0 = \eta^* \frac{(P_{opt}/\hbar \omega)}{l} e (\mu_n \tau_n + \mu_p \tau_p) F. \quad (5.10)$$

Another useful expression for describing nanowire photoconductor sensitivity is the photoconductive gain, G . This is defined as the ratio between the number of electrons

collected at the photoconductor electrodes per second, N_{el} and the number of photons absorbed that create an electron-hole pair per second, N_{ph} :

$$G = \frac{N_{el}}{N_{ph}} = \frac{I_{PC}/e}{P_{abs}/\hbar\omega} \quad (5.11)$$

where $P_{abs} = \eta^* P_{opt}$ is the portion of power absorbed that actually results in electron-hole pair creation. Substituting equation 5.9 into equation 5.11, we can simplify the gain expression to

$$G = \frac{F\mu\tau}{l} = \frac{\tau}{\tau_t} \quad (5.12)$$

where the transit time for carriers between the two nanowire electrodes, $\tau_t = l/v = l/\mu F = l^2/\mu V$.

The expressions in equation 5.12 point toward two primary contributing factors to such high photoconductive gain in nanowires. Firstly, the high density of surface states, resulting from such large surface-to-volume ratios (as discussed in chapter 4), promotes separation of electron-hole pairs, thus *extending* the photocarrier lifetime, τ . Secondly, the small inter-electrode distances, l , and high mobility, μ , arising from their single-crystalline, low-defect structures, *reduces* the carrier transit time, τ_t . Prades *et al.* experimentally verified the latter of these contributions in ZnO nanowires^[273], demonstrating I_{PC} linearly dependent on $1/l$ (Fig. 5.7a), as well as showing greatly increased photocurrent in those structures coated in PMMA which as discussed in section 5.1.5, leads to marked increase in carrier mobility^[250,260]. In the case that $\tau > \tau_t$, photoconductive gain arises, in that a particular photogenerated free carrier can make multiple journeys through the nanowire channel before its circulation is halted only by either annihilation or trapping^[272]. This is conditional upon Ohmic contacts, such that carriers drawn off at one electrode can be freely replenished at the other^[272], which can be challenging to achieve at semiconductor-metal interfaces; the case of Schottky contacts shall be discussed later on.

Expanding upon the first contribution - the influence of surface states - this gives rise to strongly diameter-dependent photoconductive behaviour in nanowires as observed in ref. 274. As can be seen in Fig. 5.7b, near the surface of the wire, traps give rise to a depletion space charge region, which bends the conduction and valence bands upward. Therefore, in the case of an n-doped nanowire, holes are attracted to the surface whilst electrons tend to inhabit the central 'bulk' due to introduction of an energy barrier, ϕ , for surface-related recombination to occur, thus promoting charge-separation. There is therefore a critical nanowire diameter, d_{crit} , (dependent on the width of the depletion region), at which the entire wire is depleted such that transport in both dark and under illumination is space-charge limited - typical of

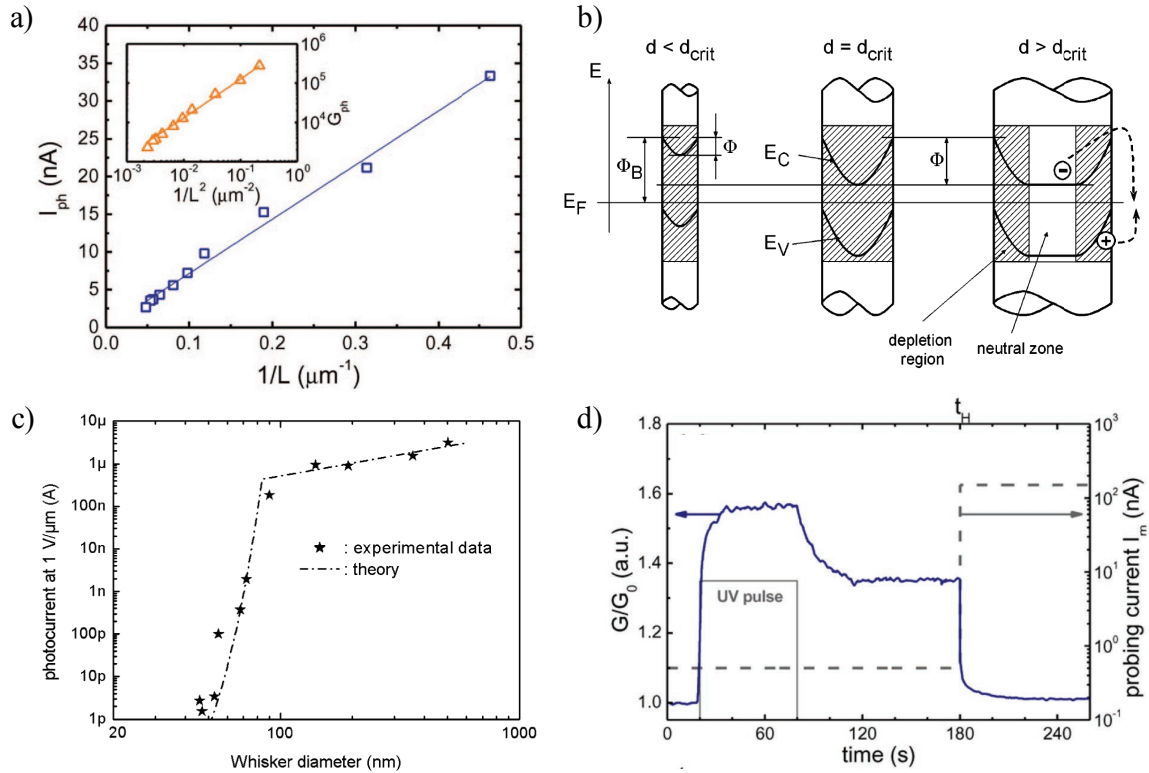


Fig. 5.7 Properties of nanowire photoconductors. (a) Plot of the photoresponse and photoconductive gain (inset) in a ZnO nanowires versus the inter-electrode distance at bias of 1 V with an excitation wavelength of 340 nm. Adapted from ref. 273. (b) Diagram of conduction (E_C) and valence (E_V) band-bending showing a recombination barrier, ϕ in the presence of a surface-associated depletion region (shaded) for nanowires with diameter below, at, and above a critical diameter d_{crit} . A surface-mediated recombination mechanism is shown in the $d > d_{crit}$ case. (c) Plot of GaN nanowire photocurrent against diameter, showing both experimental data and theoretical calculation. The kink at ~ 85 nm represents the critical diameter for this material system below and above which the photocurrent decreases exponentially and increases linearly respectively. (b) and (c) Adapted from ref. 274. (d) Demonstration of a 'persistent' photocurrent observed in ZnO nanowires seen in the conductance (G) relative to dark conductance (G_0) after a 60 s UV pulse. The persistent photocurrent stabilises before a increase in the probing current (grey dashed line) from 0.5 to 150 nA at t_H restores the conductance to G_0 . Adapted from ref. 275.

insulators^[274]. This is demonstrated experimentally in the plot in Fig. 5.7c. Below this width, ϕ decreases with the square of the diameter, leading to increased surface related recombination and therefore decreased photocurrent. Describing this mathematically, the recombination rate can be expressed as $\exp(-\phi/k_B T)$, where $k_B T$ is the thermal energy contribution, and

$$\text{for } d < d_{crit}, \quad \phi = \frac{eN_D d^2}{16\epsilon\epsilon_0} \quad (5.13a)$$

$$\text{for } d > d_{crit}, \quad \phi = \frac{eN_D d_{crit}^2}{16\epsilon\epsilon_0} \quad (5.13b)$$

where N_D is the donor concentration and $\epsilon\epsilon_0$ is the material's dielectric constant^[274].

For CdS nanowires in particular (though also observed in a range of other materials^[276]), the surface (photo-) chemistry plays a significant role in the transport and photosensitive properties under ambient conditions, due to the strong attraction of oxygen by sulfur vacancies^[277]. Oxygen will be ionised at the surface and adsorbed;



leading to the formation of a depletion shell (as discussed previously) and significantly reducing the dark conductivity of the wire, as experimentally verified by measurements under varied atmospheric conditions^[278,279]. Under illumination, photogenerated holes are drawn to combine with the ions at the surface;



acting to enhance charge-separation; in this way the oxygen behaves similarly to a photo-gating layer^[278]. Even once illumination has ceased, whilst recombination of electron-hole pairs in the center of the wire occurs rapidly through bulk-related processes, due to the oxygen-mediated charge trapping it is slowed dramatically for those near the surface^[275,280]. As seen in Fig. 5.7d, this results in a so-called 'persistent' photocurrent whereby the current will initially return only to an intermediary level, in between that of the original dark current, and the photocurrent under illumination^[274,277,280,281] unless some mechanism is employed to overcome the induced recombination barrier, such as Joule heating of the wire^[275]. Clearly, as detailed in section 5.1.5, passivation of the surface is one effective route toward stabilising such effects^[275,280].

5.2.2 Schottky barrier nanowire contacts

Whilst the discussion in the previous section assumes a nanowire contacted Ohmically by two electrodes (that is, the system obeys Ohm's law), this is not always straightforward to achieve^[282]. For an Ohmic relationship, there should be no energetic barrier (known as a Schottky barrier) impeding the supply of carriers from the metal to the semiconductor conduction band^[283], that is, the voltage drop at the contact is negligible with respect to the total drop across the two electrodes^[284]. In theory, this can be achieved by selecting a metal with a work function that is equal to or less than that of the semiconductor^[284].

However, even in bulk systems, the exact chemistry at the metal-semiconductor interface is not easily predicted^[285]. In practicality, surface treatments, such as ionic bombardment or chemical etches are often required to eliminate surface barriers or produce workable contact resistances, even when the material work functions have been matched, such as in the case of In or Ga contacts to CdS thin-films^[284,286,287]. In nanowires, this situation is further complicated by Fermi pinning from surface states, image force, field penetration and the formation of thin oxide or amorphous layers at the surface, as well as the small physical dimensions of the metal-semiconductor interface^[288,289]. This means that Ohmic contact for a particular diameter and material system must often be empirically verified.

As with bulk systems, when fabricating nanowire contacts, a surface treatment is often applied after the development stage of the lithography, immediately prior to metal deposition. For example, treatment with dilute ammonium sulfide $(\text{NH}_4)_2\text{S}_x$ has been shown to remove native oxides and contaminants in InAs^[290] and other semiconductor nanowires^[161,258], as well as terminating the nanowire surface with covalently bonded sulfur in a self-limiting process, preventing reoxidation before the contact is deposited. With CdS nanowires, Ohmic contacts have been created with Ti by using an Ar^+ ion bombardment to create sulfur vacancies, increasing the concentration of electrons in the exposed area and lowering the Schottky barrier^[291,292].

However, despite demonstration of such treatments, a significant proportion of two-terminal nanowire devices in the literature display non-linear I-V behaviour; there is often variability even across samples of devices produced with the same nanowires, contact material, and fabrication conditions^[289]. These I-V characteristics depend on both the properties of the nanowires, such as resistivity, carrier mobility, and local doping concentration, and those of the contact: the geometry, contact area, and the Schottky barrier height^[289]. Non-Ohmic devices with two symmetric terminals, where an appreciable Schottky barrier exists at both electrodes, can be thought of as back-to-back diodes (Fig. 5.8a)^[272]. A band diagram representative of this scenario can be seen in Fig. 5.8b. Some works have also sought to intentionally create nanowire (single) Schottky diodes to achieve rectifying behaviour, by treating one electrode to attain Ohmic contact whilst depositing a high work function metal such as Au or Pt at the other to introduce a Schottky barrier^[291–294].

For typical Schottky junctions, the transit of carriers over the Schottky barrier occurs by thermionic emission, in which the current, I_{TE} , is based around a saturation current, I_S , and described by the following expression:

$$I_{TE} = S I_S \left[\exp\left(\frac{eV}{k_B T}\right) - 1 \right] \quad (5.16)$$

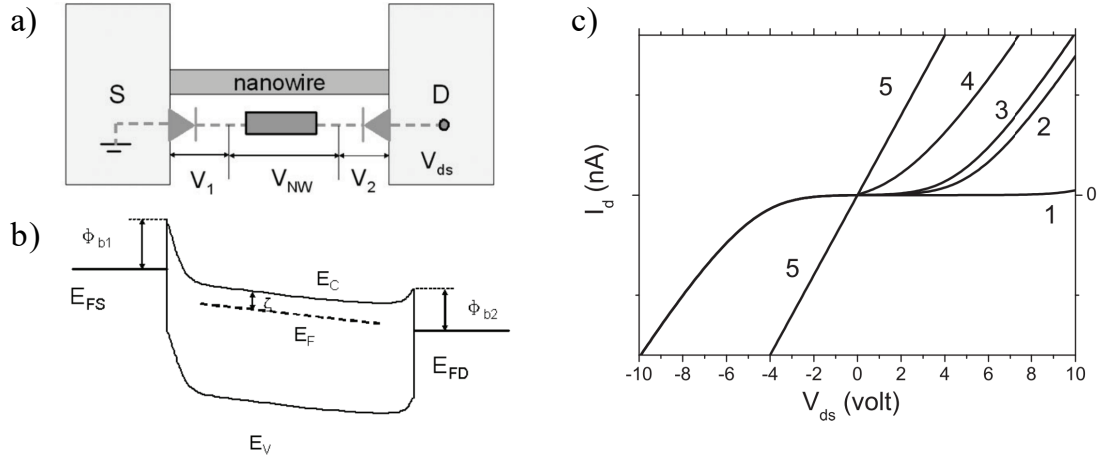


Fig. 5.8 Schottky barriers at the nanowire-electrode interface. (a) Circuit diagram for a nanowire device with a Schottky barrier at both source and drain contact, behaving as a back-to-back diode. (b) Band diagram for the system in a) when under bias, showing bending at the contacts resulting in two barriers ϕ_{b1} and ϕ_{b2} at the metal-semiconductor interface. E_C , E_V , E_F , E_{FS} and E_{FD} denote the conduction-band, valence-band and Fermi level in the wire, source and drain respectively while ζ represents the energy difference between the bottom of the conduction band and the Fermi level. (c) I-V behaviour in a two-terminal nanowire device at different combinations of Schottky barrier heights, based on the model developed in ref. 289. For curves 1-4, ϕ_{b2} is fixed at 0.4 eV whilst ϕ_{b1} is 0.6 eV, 0.43 eV, 0.4 eV and 0.35 eV respectively. In curve 5 $\phi_{b1} = \phi_{b2} = 0$. All figures adapted from ref. 289.

where S is the contact area^[295]. The saturation current is given by

$$I_S = A^* T^2 \exp\left(-\frac{e\phi_b}{k_B T}\right) \quad (5.17)$$

where the Schottky barrier height is denoted by ϕ_b and $A^* = 4\pi e m^* k_B / h^3$ is Richardson's constant, where m^* is the effective carrier mass and h is Planck's constant^[295]. Broadly speaking, deviations from ideal characteristics can be included by modifying equation 5.16 to

$$I_{TE} = S I_S \left[\exp\left(\frac{e(V - V_{th})}{nk_B T}\right) - 1 \right] \quad (5.18)$$

where V_{th} is a forward bias threshold voltage and n is an ideality factor that in nanowires can account for effects related to for instance surface states and interfacial layers^[272,289]. Whilst the above provides a broad framework for transport, another component, which can dominate under reverse bias, particularly in low-dimensional Schottky barrier systems, is the tunnelling current. In ref. 289 Zhang *et al.* provide a more detailed model including this and a range of other considerations which is able to predict a wide range of non-linear, two-terminal nanowire device characteristics, as shown for varying Schottky barriers in Fig. 5.8c.

As can be seen in equation 5.18, current passing through the barrier is highly sensitive to the Schottky barrier height, which will be affected by changes in the local electric field at the contact, through photoexcitation, adsorbed gases or otherwise^[295]. In this way, photodetection can be realised in these Schottky contacted devices where the responsivity is actually significantly higher than those based on Ohmically contacted nanowires. For example, photodetectors based on ZnO^[296] and CdS^[297] nanowires with Schottky contacts showed four and nearly two orders of magnitude higher sensitivity respectively compared to those based on the same nanowires but using Ohmic contacts. Further to this, Schottky devices also exhibit far shorter response and recovery times (in some cases by over 2 orders of magnitude), owing to the strong built-in electric fields present at the contact interface^[276,295].

5.3 Miniaturised spectroscopy

5.3.1 Conventional systems

The fundamental working principle of a conventional spectrometer is to sample radiation and introduce either a spatial or temporal separation between light of different wavelengths that can be resolved at the plane of a detector, thus constructing a spectrum of the inputted light. These systems can broadly be classified by the method used to achieve this; either using a dispersive element such as a prism or grating (spatial separation) or through interferometric optics (temporal separation)^[298]. There are different, significant challenges involved in miniaturising spectrometers based on either of these approaches due to adverse effects on performance associated with scaling their components. As such, a range of innovative designs have been employed toward developing ever more compact microspectrometers - though they invariably necessitate compromise on particular operational parameters, such as the resolution or spectral range.

Whilst prisms are generally not suited to scaling due to the long optical paths required, many reported microspectrometers center around the use of a chip-based grating to disperse light, the principle behind which is illustrated in Fig. 5.9a^[299]. Some strategies closely mirror macroscopic systems, involving complex fabrication processes to produce grating structures that both receive and scatter light out of the plane of the chip, such as those in Fig. 5.9b^[300,301]. However, most grating-based designs feature planar integrated optics (an example of which is shown in Fig. 5.9c), whereby light travels to the grating within the chip's plane, often along waveguiding channels, before being diffracted and directed to either an in- or out-of-plane detector^[302–306]. Here, a further sub-category of microspectrometers are arrayed waveguide gratings (AWGs), commonly used in wavelength division multiplexed

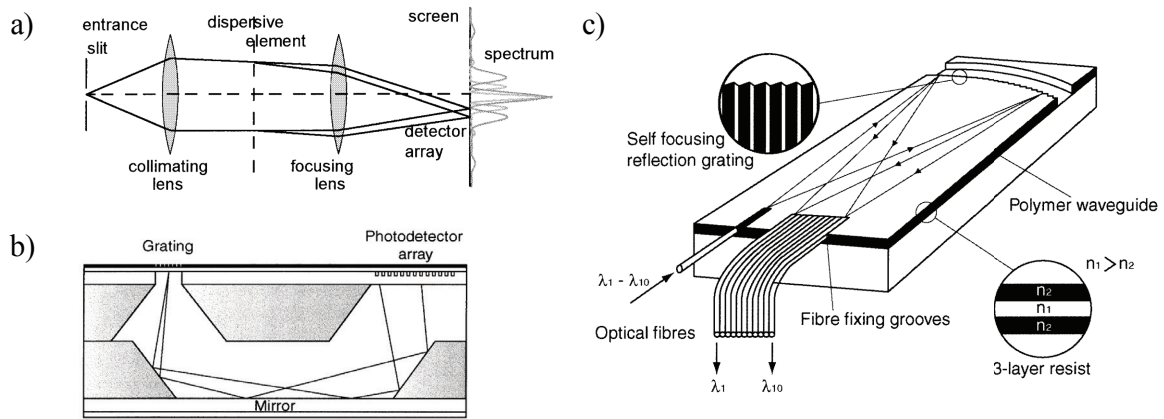


Fig. 5.9 **Microspectrometers based on miniaturised conventional systems.** (a) Operational principle behind a spectroscopy system based on the spatial separation of spectral components of incident light using a dispersive element (in this case a grating). (b) and (c) Miniaturised dispersive spectrometer systems, with (b) a micromachined, out-of-plane grating architecture (c) a planar, integrated grating system. All adapted from ref. 298.

telecoms systems, which function as an artificial prism, by guiding light into a series of channels each of incrementally longer optical paths^[307–309].

Arguably the key performance parameter when considering a spectrometer is its spectral resolution, R , which is described by

$$R = \frac{\lambda}{\Delta\lambda}, \quad (5.19)$$

where $\Delta\lambda$ is the full-width half-maximum (FWHM) for a particular wavelength, λ ^[298]. For grating-based spectrometers the resolution is equal to the number of elements in the grating, with the constraint that the optical path length must not be less than the Rayleigh distance if Fraunhofer rather than Fresnel diffraction is to occur, in the far-field optical regime^[298]. Under these conditions it can be derived that:

$$R = \frac{\sqrt{\lambda L}}{a}, \quad (5.20)$$

where L is the optical path length and a is the pitch of the grating^[298]. Clearly, miniaturising a grating-based spectrometer necessitates reduction of the path length and as such these systems are inherently limited with respect to scaling. Whilst, in accordance with this relation, improvements in the resolution can also be achieved by decreasing the pitch, retaining high quality in progressively smaller gratings and optics is complicated by the surface roughness induced during etch-based fabrication processes^[310]. As such, in order to achieve sufficient

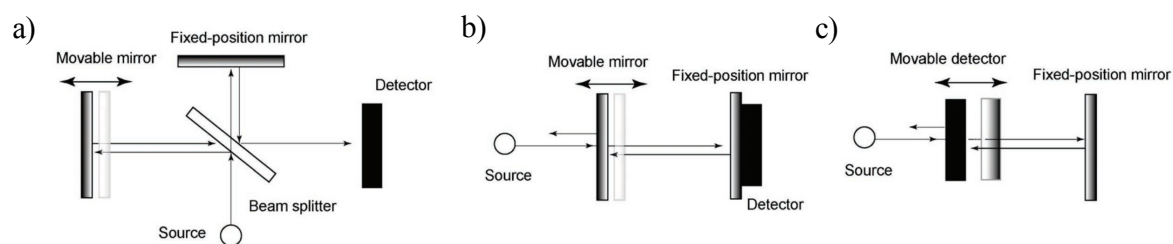


Fig. 5.10 **Interferometric microspectrometer designs.** (a) A Michelson interferometer system with a movable mirror. (b) A Fabry-Perot resonator-based interferometer with adjustable cavity length. (c) A Fourier or 'standing-wave' spectrometer with a movable detector. All adapted from ref. 299.

resolution for their desired applications, the smallest of these microspectrometers typically have a footprint in the range of 1 - 10 mm^[306,309].

Some of the more novel spatially-dispersive microspectrometer systems have utilised photonic crystals in an effort to overcome these obstacles. Momeni *et al.*, for instance, harnessed them to create superprism structures, with stronger dispersive properties than typical grating designs, allowing a more compact system^[311]. Redding *et al.* instead managed to extend the effective path length to greater than the linear dimensions of the device, by using disordered photonic crystal arrays to 'fold' paths by inducing multiple scattering events prior to detection^[312].

In interferometric spectrometer systems light is split and diverted along separate paths of different, well-defined lengths, usually using either a beam-splitter or a resonant cavity. On recombination, these paths will constructively interfere or resonate at wavelengths dependent on the difference in path length, or, more specifically in the latter case, the length of the cavity. In this way, adjusting the path length over time enables scanning across different spectral components. As such, to scale down these types of spectrometers, most approaches have employed microelectromechanical systems (MEMS) to achieve miniaturised systems with movable optics. Schematics of the three most common architectures - a Michelson interferometer, Fabry-Perot resonator and Fourier, or 'standing-wave' spectrometer - can be seen in Fig. 5.10^[299].

As with prisms, beam-splitters are a technologically challenging component to scale and though some microspectrometers have been demonstrated^[313], the majority of miniaturised interferometer-based systems fall under the latter two classifications which share similar limitations, relating to practical challenges in the fabrication of the cavity^[298,299,314]. Here, the resolution of the cavity is directly related to the mirrors' reflectivity, r , as the FWHM,

$\Delta\lambda$, at resonance is equal to the intrinsic finesse, F_{int} :

$$F_{int} = \frac{\pi\sqrt{r}}{(1-r)}. \quad (5.21)$$

[298]. However, in order to achieve a sufficient signal to noise ratio (SNR), the transmission at resonance must also be high; in metallic mirrors these two conditions cannot be satisfied simultaneously. Dielectric mirrors can offer both high reflectivity and low absorption at resonance, but they are far harder to produce using standardised industrial CMOS processes [299].

Further to this, in practical terms the effective finesse, F_{eff} , of the cavity is also limited by defects in the mirrors relating to their curvature, the roughness of their surfaces, and their non-parallelism. This can be described mathematically as:

$$\frac{1}{F_{eff}^2} = \frac{1}{F_{int}^2} + \frac{1}{F_d^2}, \quad (5.22)$$

where F_d is the defect finesse encompassing the three factors above [299,314]. As well as the resolution, the free spectral range (FSR) suffers when scaling, whilst also being inherently limited to

$$FSR = \frac{\lambda^2}{2d_{FP}}, \quad (5.23)$$

where d_{FP} is the cavity spacing, given that the shortest first-order mode wavelength cannot overlap with the longest in the subsequent second-order mode [314]. Electrostatic actuators are most commonly used in these MEMS devices, in which the practical travelling range is capped due to pull-in effects such that maximum $\Delta d_{FP}/d_{FP}$ is only around 33%, with high voltages often required to achieve this [314].

5.3.2 Filter array spectrometers

Whilst the miniaturised spectrometers listed in the previous section are primarily heavily inspired by the working principles behind conventional macroscopic designs, filter array spectrometers represent a separate paradigm designed with robust, compact systems in mind. In these devices, filters with different transmissive properties are mounted directly onto a detector array, commonly made up of multiple CCD ‘pixels’, as shown in Fig. 5.11a. A significant advantage here is that this removes the need for any focusing optics between the wavelength-selective element and the detector, enabling smaller systems, with less complex structures to fabricate than more typical spatially-dispersive designs.

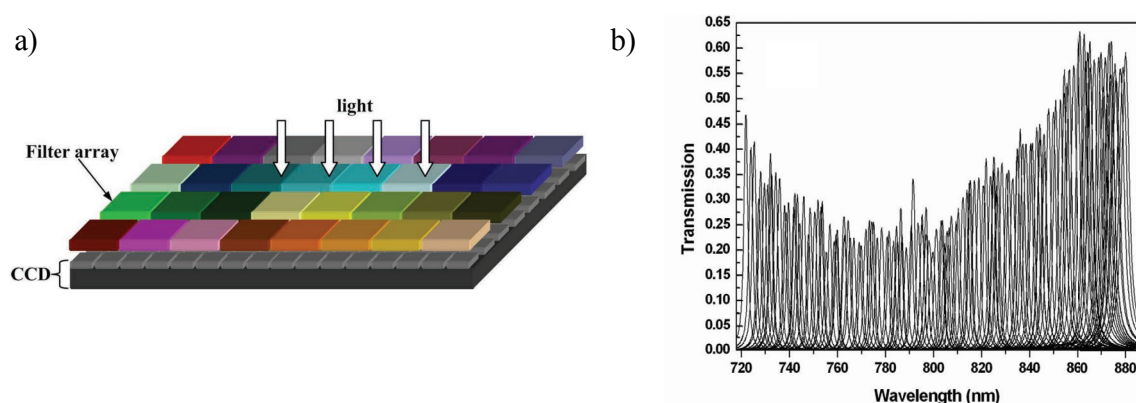


Fig. 5.11 **Filter array spectrometers.** (a) Diagram of a basic narrow-band filter-array spectrometer system. 128 monochromatic filters, fabricated from variably-etched thin-films, are integrated on top of a detector array, with total size 12×12 mm. (b) Spectral transmission of all filters from the device in a), showing the narrow-band nature of each channel. Both adapted from ref. 315.

A wide range of filter types have been used for these devices; these include Fabry-Perot^[316,317] and other resonant cavities^[318] or microinterferometers^[319], as well as photonic crystals^[320,321], quantum dots^[322], metallic plasmonic nanostructured films^[323], or more conventional variably etched thin-films^[315]. These are commonly arranged into two-dimensional arrays, though one-dimensionally arrayed designs also exist, including linear variable optical filters (LVOFs)^[324,325] - Fabry-Perot-type structures in which the cavity separation decreases along their length - and gradient grating period guided-mode resonance filters^[326]. In all of these spectrometers, a calibration process must be carried out before use to measure the spectral transmission characteristics of each filter, such that the readout from each detector can be associated to a wavelength-dependent response function. In early examples of these devices, exclusively monochromatic filters were used, each with a *narrowband* response that directly contributes an individual spectral component of the final readout, without any further signal processing, as can be seen in Fig. 5.11b^[315–318,320]. The resolution and FSR of these simple spectrometers is thus entirely dependent on the FWHM of each filter's transmission and the number of filters.

However, more recently in this area, microspectrometers based on *broadband* filters (which are far cheaper to fabricate than narrowband counterparts) have emerged^[322,323]. Most notable is the colloidal quantum dot (QD) spectrometer reported in 2015 by Bao *et al.* in ref. 322. In this work, as illustrated in Fig. 5.12, the filters are made from mixtures of CdS and CdSe QDs of different sizes, combined at varying ratios, so as to create a unique transmission spectra and response function for each array element. Due to the wavelength multiplexing principle, each detector therefore responds to multiple different wavelengths of light, to varying degrees as defined by its filter's transmission function. An algorithm

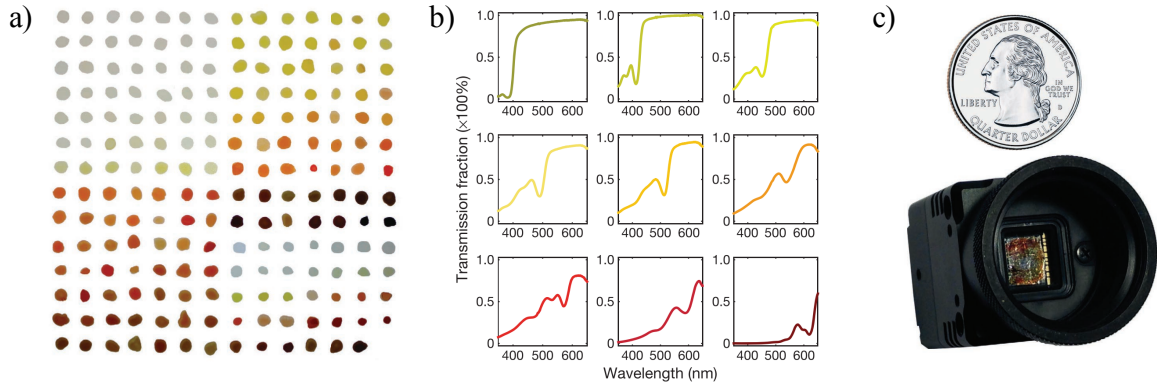


Fig. 5.12 **A colloidal quantum dot spectrometer.** The system detailed in ref. 322. (a) 195 unique filters formed from different sized CdS and CdSe quantum dots, mixed at varying ratios and embedded in a polymer film. (b) Transmission spectra corresponding to a selected sample of the filters in a). (c) The packaged spectrometer system, as compared to the size of a US quarter. All adapted from ref. 322.

is then used to computationally reconstruct a target spectrum, by cross-referencing two datasets for each of the array elements: the transmission function (as calibrated prior to measurement) and the measured intensity of the transmitted light. Figure 5.13 shows a schematic summarising and comparing this approach against conventional spectrometers and narrow-band filter systems.

The computational strategy to reconstruct incident spectra *via* the broadband array architecture is illustrated in Fig. 5.14. For an unknown incident light spectrum, $s(\lambda)$, the transmitted intensity, I_i , through filter number i (where $i = 1, 2, \dots, n_F$) with transmission function $T_i(\lambda)$, can be expressed mathematically as:

$$I_i = \sum_{\lambda} s(\lambda) T_i(\lambda), \quad i = 1, 2, \dots, n_F. \quad (5.24)$$

Evaluating in this way, $s(\lambda)$ is discretised across the spectral range into n_{λ} values of λ , corresponding to a set of n_{λ} variables, where $n_{\lambda} \leq n_F$ if equation 5.24 is to be solvable. Clearly, for a unique solution to be obtained, $n_{\lambda} = n_F$ must be satisfied to yield a set of linear equations. In practical terms however, this ideal scenario is significantly complicated by even small measurement errors in both the transmission function and the intensity collected, causing inconsistencies to arise between equations across the set. Whilst this in effect means that it is impossible to recover an exact reconstruction of $s(\lambda)$ (that is, $n_{\lambda} < n_F$), the solution can be approximated, for instance by a least-squares linear regression.

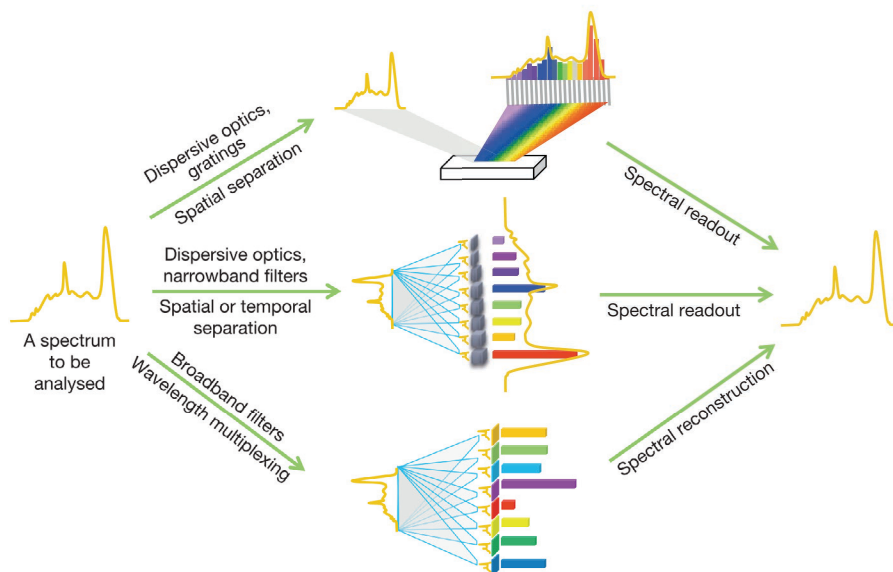


Fig. 5.13 **Different spectrometer strategies.** Schematical comparison of three different spectrometry strategies to resolve the spectra from an incident light signal. The top and middle paths show a conventional, dispersive system and a narrow-band filter array, where light is separated spatially such that the intensity of individual spectral component is measured at each detector. The bottom path illustrates the approach taken by broadband filter array spectrometers, that rely on the wavelength multiplexing principle to analyse multiple spectral components at each detector simultaneously, before computational techniques (as described in the text) are used to reconstruct the original spectrum. Adapted from ref. 322.

Considering this discrete modelling of the system, and the measurement inaccuracies and noise involved, a more detailed expression of the transformation between incident spectrum and detected signal is given by the following matrix equation^[327]

$$\mathbf{r} = \mathbf{H}\mathbf{s} + \mathbf{n} \quad (5.25)$$

where

$$\mathbf{r} = \begin{bmatrix} r_1 \\ \vdots \\ r_j \\ \vdots \\ r_N \end{bmatrix}, \mathbf{H} = \begin{bmatrix} D_1(\lambda_1) & \dots & D_1(\lambda_M) \\ \vdots & \vdots & \vdots \\ D_j(\lambda_1) & \dots & D_j(\lambda_M) \\ \vdots & \vdots & \vdots \\ D_N(\lambda_1) & \dots & D_N(\lambda_M) \end{bmatrix}, \mathbf{s} = \begin{bmatrix} s(\lambda_1) \\ s(\lambda_2) \\ \vdots \\ \vdots \\ s(\lambda_M) \end{bmatrix}, \text{ and } \mathbf{n} = \begin{bmatrix} n_1 \\ n_2 \\ \vdots \\ \vdots \\ n_N \end{bmatrix}$$

in which \mathbf{r} is a vector where the elements are the outputted signal from the j^{th} detector (where $j = 1, 2, \dots, N$), \mathbf{H} the spectral response matrix, \mathbf{s} the incident spectrum vector and \mathbf{n} a

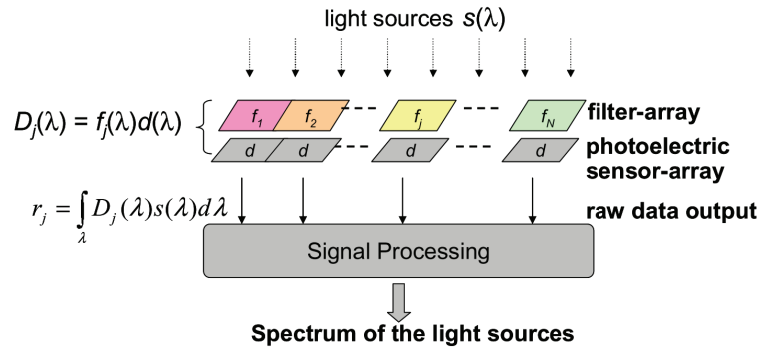


Fig. 5.14 **Computational reconstruction of an incident spectrum by a filter-detector array.** Diagram illustrating the computational spectral reconstruction process behind a broadband filter-array spectrometer with N filters. All terms are defined in the text. Adapted from ref. 327.

noise vector. Within \mathbf{H} , $D_j(\lambda) = T_j(\lambda)d(\lambda)$ is a function representing the overall spectral response for each of the N detectors, with $d(\lambda)$ representing a sensitivity function for the CCD detectors (under the assumption that all the detectors are the same). This function (and thus, the reconstructed spectrum, $s(\lambda)$) is discretised into M elements, corresponding in real terms to the resolution at which the filter calibration has been carried out.

Given the operational principles of these broadband filter array spectrometers - computational reconstruction of the entire spectrum rather than direct measurement of individual spectral bands - it should be noted that their performance metrics cannot be characterised in the same manner, or as definitively as for conventional systems. Clearly the free spectral range is governed directly by the upper and lower bounds of wavelengths for which sufficiently varied transmission information can be produced across the filters. In the case of the QDs, this is dependent on the lowest and highest bandgap crystals used respectively. However, the spectral resolution in these devices can be thought of more broadly as the accuracy of the reconstruction. This is often either characterised by the FWHM when measuring a monochromatic reference source, or by assessing the wavelength separation at which the two components of a doublet peak become indistinguishable. The reconstruction accuracy can be improved through two primary routes; by increasing the number of filters, such that M is larger for the same spectral range, or by reducing the errors in the measured intensity and pre-calibrated transmission function, for instance by improving the stability of the calibration, or the performance of the CCD detectors.

A third way to improve the spectral reconstruction process, that does not require altering the spectrometer hardware, is by using a more sophisticated algorithm to solve the inverse problem posed in equation 5.25, which can push the resolution far beyond the limit set by N . The system can either be modeled as one where the number of spectral components,

represented by M , is larger than or smaller than the number of filters N ^[328]. When $M < N$, the system is *over*-determined, that is, the number of unknowns is smaller than the number of equations. In this scenario, relatively simple approximation techniques such as non-negative least-squares algorithms are appropriate, however in practicality, even when M is much smaller than N , such methods have been shown to deliver unsatisfactory reconstructions^[327].

Far greater success has been had when modelling as an *under*-determined system, that is with $M > N$, and as such, capable of resolutions that aren't limited by the number of filters. Algorithms addressing these under-determined cases will introduce a (commonly Tikhonov-) regularisation term to stabilise the solutions, often relying on some prior knowledge of the spectrum beforehand, such as the smoothness, non-negativity, or in many cases, the sparse nature of the signals^[321,329,330]. These sparse optimization techniques usually employ L_1 -norm minimisation^[329,330] and have shown far greater success in producing accurate reconstructions, though limit the number of non-zero components allowed in the incident signal; these are known as directly-sparse spectra. More recently, dictionary/machine-learning techniques have expanded upon such algorithms to improve reconstruction of non-directly sparse signals by representing them in an alternative transform domain, or 'dictionary', in which they are sparse^[328].

5.3.3 Wavelength-selective nanowire-based optoelectronic devices

Broadband filter-array spectrometers, using algorithmic spectral reconstruction, currently present the most technologically viable route for providing the most compact, low-cost and robust microspectrometer systems possible. With respect to scaling, they supplant conventional grating or interferometric systems, in that their resolution is no longer dependent on path length, nor relies on mirror-based architectures and MEMS which require complex fabrication. The limiting factor when miniaturising their footprint is instead related to the minimum dimensions at which the filters or CCD detector can be fabricated and the number of filter-detector elements required to produce an accurate reconstruction, which together define the area of the filter array. Considering only the array, the QD spectrometer from ref. 322 has a footprint on the order of $5 \times 5 \text{ mm}^2$. It may be possible to scale this device down further; contact printing of QDs can achieve features with sub micron resolution^[331] whilst CCD pixels down to $\sim 10 \mu\text{m}$ can be made, though it is likely that fabricating the microspectrometer at such length-scales would prove technologically challenging. Miniaturisation beyond this would require a reduction in the number of filters; to achieve this whilst maintaining the same reconstruction accuracy would clearly require improvements to the algorithm, which may or may not be feasible.

Through the work contained in the rest of this thesis, I have sought to show that band-gap gradient nanowires present a plausible route toward realising spectrometers with even smaller footprints. Creating a series of electrodes along such a nanowire serves in effect to produce a one-dimensional array of wavelength-selective photodetectors, each with a different spectral response, dependent on the composition of the nanowire between the electrode pair. Such a system could function in a manner analogous to a filter array, whereby, in essence, each photodetector along the wire serves the same purpose as a filter-detector pair in a typical two-dimensional array. Assuming capability to fabricate a sufficient number of electrode pairs to provide enough spectral response information, the footprint would be limited only by size of the nanowire. However, beyond this, this strategy could hold a number of advantages over a filter array design. From a fabrication standpoint, the full bandgap range is incorporated into a single structure in one growth step, contrasting with the production, blending and printing of potentially hundreds of separate quantum dot mixtures. Likewise the simplicity of the design is attractive in that the filtering and detection of light both occur in the nanowire, requiring only a single straightforward electrode deposition, rather than the multi-step fabrication of a CCD array. With choice of the correct electrode and substrate materials, the device also could potentially be made both flexible and transparent, a far more complex task to achieve with solid-state CCD detectors. To date, only two publications have demonstrated a series of wavelength-selective devices along a single nanowire: ref. 208 in 2011 and ref. 332 in 2018, based on $\text{Si}_x\text{Ge}_{1-x}$ and $\text{CdS}_x\text{Se}_{1-x}$ gradient systems, respectively; the latter of which I shall cover in more detail below, given its use of the same material system as my own work. These are also the only works so far to produce detailed spatially-resolved optoelectronic analysis of two-terminal devices for on-nanowire composition-gradients.

In ref. 332, *Schottky* contacts were deposited on a $\text{CdS}_x\text{Se}_{1-x}$ nanowire, with x varying from 0.94 to 0.43 at the green and red end respectively; this was done using Cr-Ag electrodes, with no surface treatment. Initial characterisation of the optoelectronic properties was carried out using a simple two-terminal architecture with an electrode at either end of the nanowire as shown in Fig. 5.15a. Measurements in the dark showed symmetrical non-linear I-V characteristics (Fig. 5.15b), indicating a back-to-back diode where a Schottky barrier has formed at both contacts. Due to this strong symmetry, the assumption was made that the Schottky barrier heights at both the metal-semiconductor junctions were approximately equal due to Fermi-level pinning across the device.

Firstly, to test the relationship between illumination power, P , and photocurrent, I_{PC} , the whole device was illuminated by a diffuse 488 nm laser at different powers, revealing that $I_{PC} \propto P^k$, where $k \approx 0.93$ at bias of both +3 V and -3 V (Figs. 5.15b and c). Scanning photocurrent microscopy (SPCM) - where a focused laser excites a biased nanowire device

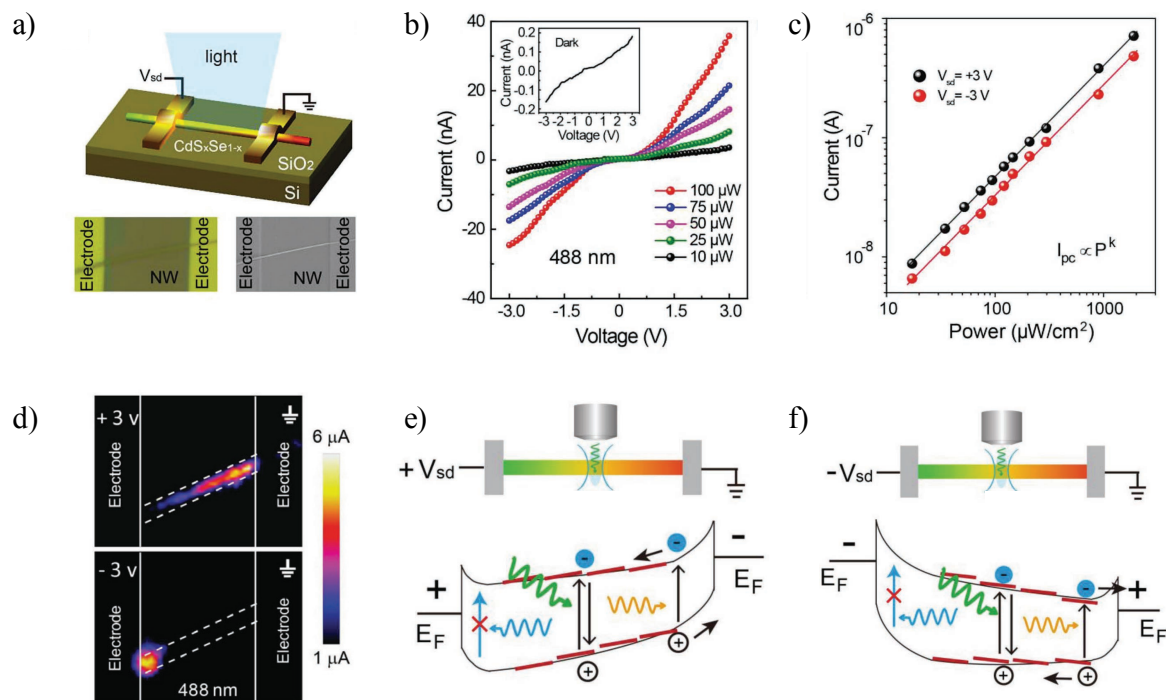


Fig. 5.15 $\text{CdS}_x\text{Se}_{1-x}$ nanowire photodetectors. (a) Optoelectronic characterisation schematic, as well as optical and SEM images, for the $\text{CdS}_x\text{Se}_{1-x}$ nanowire device with two Schottky contacts detailed in ref. 332. (b) I-V characteristics for the device in a) at varying incident light power with a wavelength of 488 nm, showing the non-linear behaviour associated with Schottky contacts. (c) The device photocurrent as a function of incident light power, plotted on a double logarithmic scale with fitted lines corresponding to a value of $k \approx 0.93$ for both reverse and forward bias. (d) Scanning photocurrent microscopy at 488 nm for the device in a) with the electrode at the CdS end biased at +3 V and -3 V as labelled. (e) and (f) Band diagrams for a photoexcitation process localised at the middle of the nanowire device in the case of a reverse-bias at the CdS- (e) and CdSe- (f) end electrode. Re-emitted photons travelling toward the CdSe side can be re-absorbed and re-emitted (orange arrow) to photoexcite material at that end, but those travelling to the CdS end are passively waveguided (blue arrow) without further absorption, as their photon energy is less than the bandgap of all material in that direction. All adapted from ref. 332.

at different locations to produce a spatial map of the photoresponse - was also used to analyse the same device, at a wavelength of 488 nm, which can be seen in Fig. 5.15d. For Schottky barrier devices based on uniform CdS nanowires, SPCM photocurrent peaks are typically strongly localised to the reverse-biased electrode^[291,292,294,333]. This suggests that only carriers within their respective diffusion length (on the order of 100 nm for holes in CdS^[291]) of the contact can be collected. That this occurs at the reverse-biased (hole-collecting) electrode in these nanowires is because hole diffusion is far less efficient (that is, electron mobility is higher) in CdS^[292]. However, notably for these gradient nanowire devices, whilst the above was true for the case when the CdS-rich end was reverse-biased,

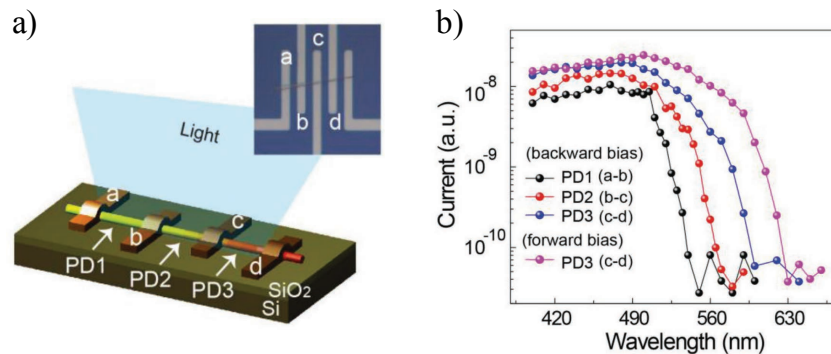


Fig. 5.16 **Wavelength-dependent nanowire photodetectors using $\text{CdS}_x\text{Se}_{1-x}$.** (a) Three wavelength-selective photodetectors fabricated on a single $\text{CdS}_x\text{Se}_{1-x}$ gradient nanowire as detailed in ref. 332, with inset showing an optical microscope image. (b) Spectral response for each photodetector as labelled in a) at reverse bias, as well as forward bias for PD3, at -3 V and $+3\text{ V}$ respectively. Both adapted from ref. 332.

when the CdSe-rich end was reverse-biased, the current was only weakly localised to that electrode, with an appreciable current measured at the forward-biased electrode (i.e. at the CdS end) also. This was explained by considering the active waveguiding that occurs due to the bandgap-gradient in these nanowires, which was previously discussed in section 4.3.2. As illustrated in the band diagram schematics in Figs. 5.15e and f, when the CdSe end is reverse biased, photons illuminating any particular point in the middle of the wire can be re-emitted (through recombination) and waveguide toward the CdSe contact to re-excite material there, as the bandgap of all material between the illumination point and that end is *lower* than the energy of the photon. Material between the illumination point and the CdS end has bandgap *higher* than the re-emitted photon energy and as such only excitation close to the contact of the CdS end can contribute to photocurrent when this is the reverse-biased side.

A multi-electrode device was then created with four electrodes (i.e. three photodetecting units) using the same conditions that produced the Schottky contacts above, a schematic of which is shown in Fig. 5.16a. Illuminating the whole device with a tunable light source at a constant power density of 0.1 mW cm^{-2} , the photocurrent as a function of wavelength for each unit is plotted in Fig. 5.16b, showing clear cut-offs around the bandgap of the material in that particular region. As can be seen for the ‘PD3’ section, the response cut-off can be extended to longer wavelengths, by varying between forward and reverse bias, so as to probe material nearer one or the other electrode for each unit, as discussed in the SPCM results. Typical device characteristics indicate I_{on}/I_{off} ratios up to 10^5 , with response and recovery times of around 3 ms. However, it is important to note that whilst these results demonstrate clear wavelength-selectivity between detector units, such a device simply functions as three

independent photodetectors, without combining the information provided by each unit to assess the relative intensities of different wavelengths of incident light, as in a spectral reconstruction spectrometer. Furthermore, the number of photodetector units is far lower than would be needed for any accurate spectral reconstruction, whilst the stability of the photoresponse has not been analysed or demonstrated in any respect as viable for such application.

Summary

In this chapter, I reviewed the literature surrounding the production and operation of nanomaterial optoelectronics relevant to the devices studied in this thesis. Wet transfer processes for CVD graphene were discussed along with some of their associated drawbacks, including polymer contamination and wrinkling. For nanowires, dry contact-based transfer and optical fiber probe-based manipulation techniques were presented.

The practicalities of nanofabrication were introduced, firstly addressing how metal electrodes can be deposited to create electronic contact to nanomaterials. I detailed the patterning techniques (photolithography and electron-beam lithography) and metal deposition processes (thermal evaporation, electron beam evaporation and sputter-coating) used in my research, with explanation of their respective capabilities and merits. Further to this, I presented methods for, and examples of, passivating nanowire and 2d material devices, to stabilise the sensitivity of their properties to environmental changes. The physical mechanisms and fundamental concepts behind the characteristics of nanowire photodetectors were summarised, addressing the central phenomenon, photoconductivity, in particular, and noting the different mechanisms involved depending on the presence of a Schottky barrier at the electronic contact.

Finally, the literature around the central device in this thesis - a nanowire-based spectrometer - was reviewed to put this device in context with the field of miniaturised spectrometers. This focused initially on microspectrometer systems based on conventional temporal- or spatially- dispersive designs, before discussing how filter arrays can be used in conjunction with computational techniques to reconstruct target spectra. Results were also assessed from one of the only two previous works to date with direct similarity to the device in this thesis; wavelength-selective photodetectors based on single, compositionally-graded nanowires. In the next chapter I move on to detailing the experimental work carried out during my doctoral research, beginning with the development and optimisation of the fabrication techniques used.

Chapter 6

Process development: nanowire transfer, characterisation and contact deposition

Overview

Chapter 6, 7 and 8 of this thesis will cover my experimental research at different stages within the central project of this thesis: developing a prototype nanowire spectrometer. This chapter will cover the processes developed to fabricate these devices, which proved to be one of the most challenging, time-consuming aspects and, in fact, the primary bottleneck for the whole project. There was highly limited prior practical experience within the HNE group of fabricating nanowire devices, and none at all of producing devices at the feature resolutions that were required, using electron-beam lithography. Furthermore, the physical characteristics of the $\text{CdS}_x\text{Se}_{1-x}$ nanowires available, as well as the highly non-uniform distribution of these properties across growth batches, presented many obstacles. As such, this required me to develop a methodology from scratch, with existing processes and conventional nanofabrication techniques adapted and optimised toward bespoke strategies that fitted this particular material system. A summary of this methodology, including process parameters, is presented in tables 7.1 and 7.2 at the end of chapter 7.

The first section of this chapter will detail the transfer processes I used to remove nanowires from the growth substrate and place them on a device substrate. Characterisation of nanowire physical and photoluminescent properties is then presented, which was used primarily to gather data for making more informed optimisations to fabrication processes. The second section will first discuss the fabrication processes themselves, highlighting key issues in the deposition of electrodes through conventional processes especially. A process

that I developed to address these issues is then detailed and discussed, involving embedding the nanowires in a polymer layer.

The compositional-gradient nanowires used in this thesis were grown by my colleague Zongyin Yang during the first year of my studies (2016), using the furnace that he and others developed under the supervision of Prof Limin Tong at Zhejiang University and using the same method as in ref. 203, detailed in section 4.3.1. Note that the setup used was dismantled shortly after, which prevented any further investigation into the growth process, or indeed the growth of any further nanowire batches. He also carried out the set of TEM measurements presented in this chapter.

6.1 Nanowire deposition and characterisation

6.1.1 Transfer from growth substrates

The $\text{CdS}_x\text{Se}_{1-x}$ compositional-gradient nanowires used in this thesis were grown *via* the source-moving VLS growth strategy published in reference 203, the specifics of which are outlined in detail in chapter 4. As grown, a ‘forest’ of randomly orientated and tangled nanowires are attached at the base to the Si growth substrate. The first step for either characterisation or device fabrication of *individual* nanowires must therefore be to remove them from this chip and isolate them onto the device/characterisation substrate. As can be seen in the SEM images in chapter 4, the nanowires at this stage are densely arranged and intertwined, which makes it almost impossible to selectively assess the quality of individual wires or to extract them using the optical fibre probe detailed later in this section. As a result of this, a contact transfer process was used to remove a selection of nanowires from the growth substrate onto an intermediary Si:SiO₂ chip, where they could be assessed for device suitability.

These intermediary chips were pre-patterned with a grid of labelled coordinate markers using electron beam lithography, to provide reference points for locations of nanowires during subsequent imaging, PL measurements or fibre-probe transfer. The chips were cleaved using a diamond scribe to a size of $\sim 3 \times 3 \text{ mm}^2$ so as to allow sampling of different areas of the growth chip, given their size of $\sim 8 \times 20 \text{ mm}^2$. Using tweezers, each intermediary chip was inverted and briefly placed SiO₂-face down onto a particular section of the growth substrate (Fig. 6.1a), before being removed and placed face-up under the microscope for initial optical assessment. Whilst contacted, some of the nanowires in the forest become sufficiently adhered to the intermediary substrate by Van der Waal’s attractions that they become detached from the growth chip when the two chips are moved apart.

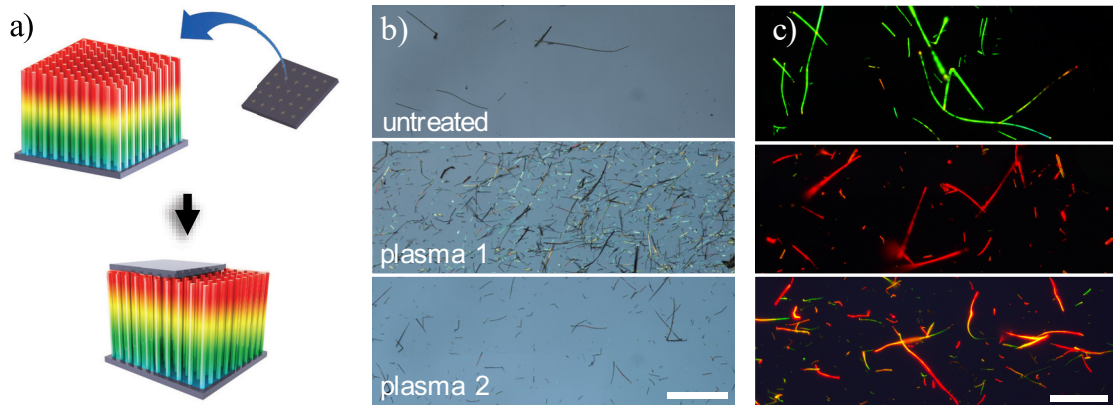


Fig. 6.1 Contact transfer of nanowires from growth to intermediary substrates. (a) Intermediary substrate is placed face-down onto the nanowire growth substrate before being removed after 5 s. (b) Optical images of three intermediary substrates after transfer, typical of those without surface treatment (top) and with an unoptimised (middle) and optimised (bottom) plasma treatment respectively. Scale bar is $50\ \mu\text{m}$. (c) Optical images taken under 390 nm UV illumination showing nanowire fluorescence from three different areas of three different growth substrates. Lack of optimisation at the growth stage to ensure spatially homogeneous properties across the growth substrate, as well as the breakage of nanowires during contact transfer, means that for some transfers mostly CdS-rich sections (top) or CdSe-rich sections are seen (middle), while only a minority contain wires with a wide-spanning gradient (bottom). Scale bar is $30\ \mu\text{m}$.

The spatial density of nanowires deposited depends on both the length of time spent in contact with the as-grown forest and the surface energy of the intermediary chip. As shown in Fig. 6.1b, untreated chips were found to take on an insufficient number of nanowires, so a mild plasma treatment (60 s, O_2 at 5 W, pressure 7.5×10^{-3} mbar ‘Moorfield Nanoetch’ reactive ion etching (RIE) system) was used on intermediary chips to increase their surface energy. Using this treatment and a growth chip contact time of 5 s produced a workable nanowire spatial density (Fig. 6.1b bottom panel). Higher plasma and contact times resulted in such dense transfers that nanowires could not be addressed individually (that is, were overlapping), or were adhered too strongly, so as to allow picking up by fibre probe (Fig. 6.1b middle panel).

As evidenced in Figs. 6.1b and c, there were highly inhomogeneous spatial distributions of nanowire morphology and compositional gradient spans across each growth chip, as well as between growth chips. Further optimisation of the growth process would evidently be required to correct this, which was not possible during the investigation. Furthermore, whilst they are highly flexible, the pressure of the intermediary chip on the as-grown forest is such that a significant proportion of nanowires are fractured as they are transferred. As the nanowires are grown with CdS ($x = 1$) at the base and CdSe ($x = 0$) at the top, one

consequence of this fracturing is that a contact transfer from a fresh growth chip will contain a significantly higher proportion of CdSe rich sections of wire, whilst subsequent transfers from the same location will produce progressively more CdS rich segments. A potential solution here would be to create liquid-phase nanowire dispersions *via* light sonication of the growth chip in an appropriate solvent; this could then be distributed onto the intermediary substrate by drop-casting.

As a result of these two issues, depending on the location sampled on the growth chip, only a very small minority of nanowires transferred onto the intermediary chips were ‘viable’ for use toward any potential spectrometer device. Here the criteria for ‘viable’ nanowire characteristics determined over the course of my research (taking into account considerations from stages of device fabrication and characterisation detailed later in this chapter and chapters 7 and 8) were, in order of priority:

1. A broad bandgap span, such that PL emission from the CdS and CdSe rich ends of the nanowire is as close as possible to 505 nm and 710 nm (corresponding to emission from pure CdS and pure CdSe), respectively.
2. An even, continuous gradient of bandgaps / PL emission along the nanowire.
3. A nanowire length, l_{nw} , between 50 - 200 μm ; $l_{nw} < 50 \mu\text{m}$ constrains the number and/or width of electrodes which can be fabricated along the structure, whilst $l_{nw} > 200$ proved problematic for optical fibre transfer.
4. The absence of any dislocations, or abnormalities such as kinks, branches, or unusually high diameter sections in the nanowire.

Each intermediary chip was therefore scanned by eye through a microscope, covering the whole substrate in a serpentine fashion (see Fig. 6.2a), to map out the locations of viable nanowires. This mapping was carried out initially under 350 nm UV light to view the fluorescence from each nanowire and roughly assess and select those with potentially suitable wavelength spans and composition gradients (criterion 1 and 2). Figures 6.2b and c show nanowires deemed unsuitable due to abrupt compositional changes (b) and limited compositional spans (c). Measurements of the nanowire length were made using the microscope software to assess criterion 3. As well as from visually assessing the nanowires under white light, criterion 4 was assessed through the waveguiding properties of the nanowires under UV illumination. Highly crystalline, intact nanowires will show strong directionally-dependent waveguiding (as introduced in chapter 4, and which can be seen in the nanowire marked with a red arrow in Fig. 6.2b) such that red/orange light is emitted (only) out of the green end - defects will result in no observable waveguiding, or

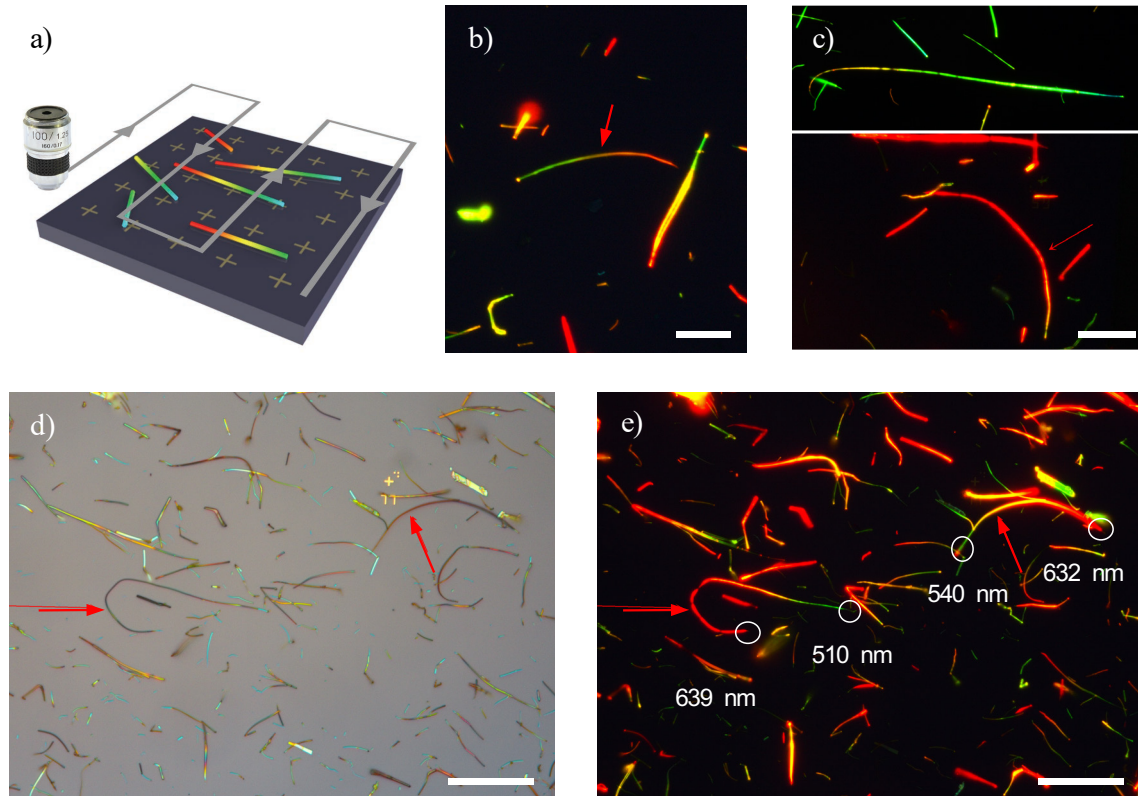


Fig. 6.2 Mapping the intermediary substrate. (a) The intermediary substrate is first scanned under microscope in a serpentine pattern to locate suitable nanowires for devices. (b)-(c) Fluorescence images, taken under 390 nm illumination of $\text{CdS}_x\text{Se}_{1-x}$ nanowires excluded from device selection due to poor compositional gradient (b) and limited bandgap spans containing majority CdS (c, top) or CdSe material (c, bottom). Scale bars are 20 μm . (d)-(e) Locations of nanowires identified as potentially suitable for devices are recorded relative to locational markers on the substrate (gold cross, d) and the PL emission peaks for each end measured by spectrometer under a focused 457 nm laser. Scale bars are 40 μm .

the escape of waveguided light at the point of notable structural anomalies or fractures. As demonstrated in Fig. 6.2d and e, after filtering the sample through these rough visual assessments, single point measurements were made of the PL emission at each end of the potentially viable nanowires (using a Renishaw InVia microspectrometer system, with an Ar^+ -ion laser filtered to a wavelength of 457 nm) to quantitatively assess the bandgap span (criterion 1); a distribution of these measurements is shown in the next section. It should be noted here that the CCD on the microscope camera was not sufficiently sensitive to capture colour variations over ~ 620 nm and as such the red ends of the nanowires all appear to be a similar colour in captured images, despite significant variation (up to and beyond 50 nm) in emission wavelength. At this stage, quantitative analysis of the composition gradient was

impractical due to the number of potential nanowires (10 - 20 per chip) and the time required for a full lengthwise mapping of each nanowire (~ 1 hour).

Nanowires in each sample with the broadest wavelength spans were then transferred to the device substrate. Optical fibre probes, similar to those detailed in chapter 5, were fashioned to achieve this, as illustrated by the schematic in Fig. 6.3a. After stripping the cladding surrounding their cores, the middle of the fibres were heated with a blowtorch flame, whilst the ends were drawn apart. Under tension the heated section thins before breaking to leave two ultra fine tips, with estimated radii < 100 nm, optical images of which are shown in Fig. 6.3b. Individual probes were then mounted on an arm, in turn attached to a travel translational stage (Thorlabs, model PT3), with manually adjustable micrometers to allow finely-controlled movement in the x- y- and z-directions. This setup was positioned next to the microscope on a vibration controlled optical table. Whilst observing through the microscope viewport, the fibre probe is moved to contact the surface near selected nanowires and manipulated such as to pry them away from the substrate, picking them up from underneath (Fig. 6.3c). The probe is then lifted away from the intermediary chip, before being brought down on to the desired location on the device substrate to deposit the nanowire by bringing it into contact with the surface (Figs. 6.3d and e).

For this latter stage, it is crucial that the surface energy of the target substrate be finely tuned, such that the nanowires will adhere preferentially to the surface rather than the probe. A standardised process to achieve this was developed and optimised; substrates were cleaned *via* sonication in IPA and acetone for 5 minutes, before a 120 s O_2 plasma exposure, at a system power of 5 W and pressure 7.5×10^{-3} mbar ('Moorfield Nanoetch' RIE system). If treated for significantly shorter (< 60 s) the nanowires will either stay attached to the fibre probe, or adhere only very loosely to the substrate, with much of the structure still not in contact with the surface. Exposures for longer than ~ 180 s result in the fibre probe becoming suddenly and sharply attracted to the surface once moved closer than a particular separation threshold, either breaking the nanowire or springing it further up the probe where it cannot be retrieved. It is also possible at this stage to make minor adjustments in the positioning or orientation of the nanowire, say, to move it away from locational markers that would short contacts.

There are multiple other practical challenges involved in the fibre probe transfer, some of which are shown in Figs. 6.3f-i. If nanowires are surrounded or overlapped by others, as is common due to the nature of the contact transfer, they must first be removed by the probe before the selected nanowire is addressed. Furthermore, the probe tip must be able to be wedge between small gaps between the nanowire and the substrate. If the whole length of a nanowire is completely adhered to the substrate, or are so thin that the probe cannot penetrate

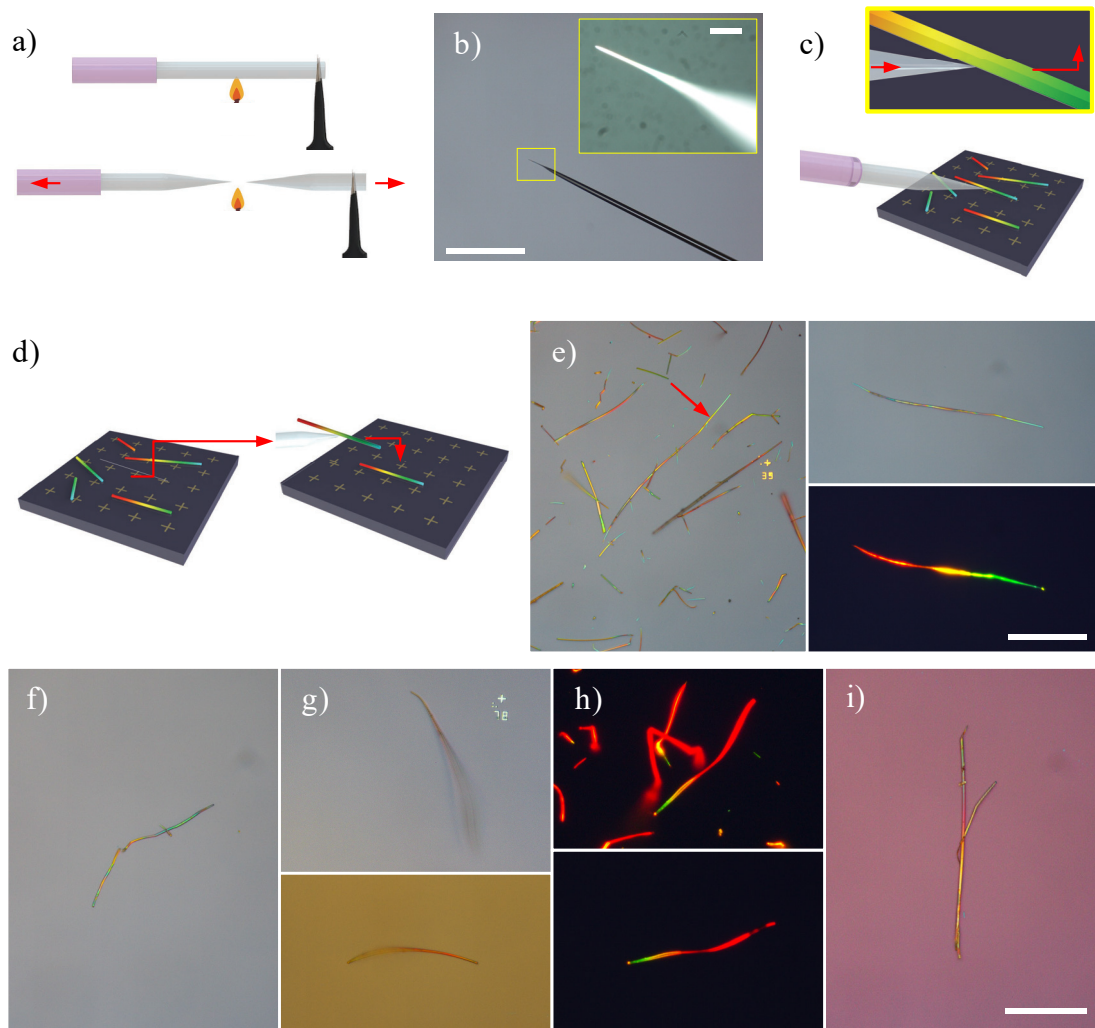


Fig. 6.3 Optical fibre probe-based nanowire transfer method. (a) Creation of a probe tip from an optical fibre probe. The cladding (purple) is stripped to reveal the fibre core, before the wire is drawn apart over a blowtorch. (b) Optical microscope images of a typical fibre probe tip. Scale bars are 500 μm and 20 μm for the main and inset images, respectively. (c)-(d) Schematic of the fibre-probe transfer process. A micrometre controlled stage is used to land the probe at the surface of the intermediary substrate, before being moved horizontally and then upward, so as to prise a nanowire away from the surface, attaching it to the probe (c). The probe is then moved to and landed on a plasma-treated device substrate where the nanowire will preferentially adhere to the surface (d). (e) Optical images of the same nanowire (marked by red arrow) on the intermediary substrates and as transferred onto the device substrate under white light (right, top) and UV illumination (right, bottom). Scale bar is 40 μm . (f)-(i) Optical and fluorescence images of nanowires exemplifying issues arising during fibre probe transfer, such as breakage by the fibre probe (f), poor adhesion to the device substrate (g), damage causing localised loss of photoluminescence (h, right-hand nanowire end) and significant overlapping on the intermediary substrate causing attachment of other nanowire fragments (i). Scale bar, shown in i) and applicable to images f) through i) is 40 μm .

underneath them, it is extremely difficult to remove them in this way. An extreme degree of care must be taken when picking up the nanowires, which is significantly complicated by vibrations of the tip due to air movement or table vibration; it is common for the nanowires to be broken in two by the probe, or for structural damage to be induced, resulting in a loss of PL in these regions. Once the nanowire is positioned on the substrate, even with optimised surface treatment, the probe must often be used to flatten it onto the surface or it can become dislodged by spin-coating processes at later fabrication stage.

6.1.2 Morphological and photoluminescence analysis

Whilst studying the physical properties of the nanowires was not a primary objective of my research in and of itself, it was necessary to characterize them to make more informed judgements and decisions relating to device fabrication. Aside from optical assessment of nanowires at the transfer stage, three main methods of analysis were used: scanning electron microscopy (SEM), atomic force microscopy (AFM) and photoluminescence (PL) measurements.

An FEI Magellan 400L XHR system was used in secondary electron detection mode to take SEM images assessing the morphology of the nanowire, primarily assessing the width and cross-sectional shape along their length. Ideally this would have been carried out on all device nanowires prior to fabrication, to allow correlation of their geometry with their optoelectronic properties. However, significant electron beam exposure is documented in the literature^[334] to affect nanowire optoelectronic properties, due to charging based effects and the creation of accumulation layers or vacancies at the nanowire surface. Instead, a sample of nanowires were imaged to provide a representative summary of the physical characteristics for the whole growth batch.

A selection of these images can be seen in Figs. 6.4a-d. To avoid the need for sputtering the nanowire and surface in Au, a low beam current of 13 pA, at acceleration voltages of 3 - 5 kV, to prevent build up of surface charge. The lack of growth optimisation is evident even in optical analysis, but elucidated further by the SEM images; the width and cross-sectional shape (Figs. 6.4a-c) were seen to vary significantly between nanowires, as well as often along each nanowire itself (Fig. 6.4d). For the majority of nanowires, variation in nanowire width was continuous and unipolar along the structure, such that the thinnest and thickest sections of nanowire were located at each end. As shown, the cross-sectional shape ranges from quasi-cylindrical, to quasi-hexagonal, to rectangular. Whilst the latter of these are often referred to in the literature as "nanobelts" or "nanoribbons", for simplicity, and considering that the rectangular cross-sections observed often transition to cylindrical or hexagonal along the length of the structure, all specimens will still be referred to in this thesis as "nanowires".

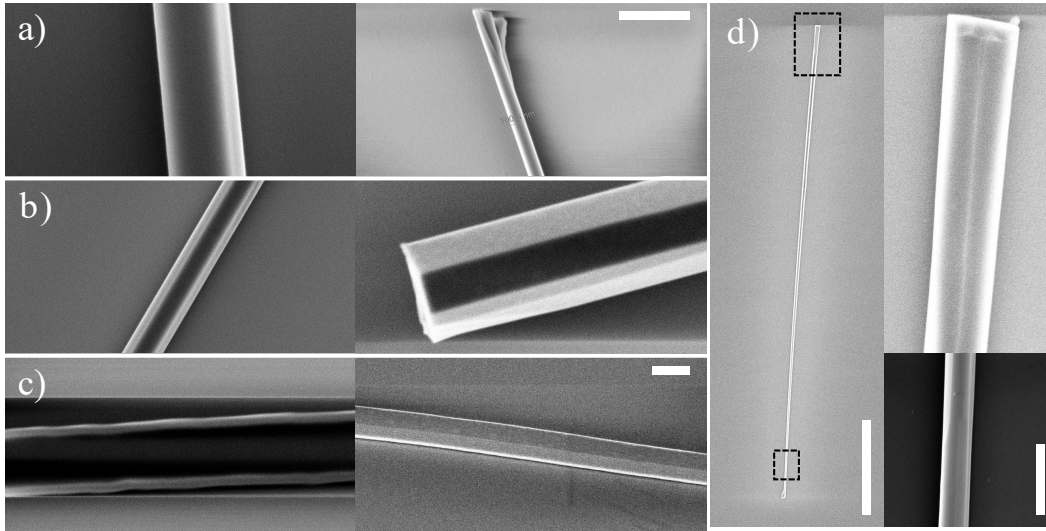


Fig. 6.4 **Morphological characterisation of $\text{CdS}_x\text{Se}_{1-x}$ nanowires.** (a)-(c) SEM images of six different nanowires showing the broad range of thicknesses (left to right) and different cross-sections - cylindrical (a), hexagonal (b) and rectangular nanobelts (c) - seen in nanowires from the same growth substrate. Scale bar in right panel of a) is 500nm, applying to all images aside from right panel of c), where scale bar is 1 μm . (d) SEM image of a whole nanowire, with insets showing magnification of black dashed boxes, demonstrating the change in morphology and thickness along the length of the wire. Scale bars are 10 μm (main image) and 500 nm (insets).

Note though that this does mean that nanowire width, w_{nw} , and nanowire height h_{nw} are *not* necessarily equal, or equivalent to nanowire diameter.

For device fabrication, due to considerations around the thickness of resists used and metal layers deposited (which will be elaborated on in the next section), it is far more important to measure h_{nw} rather than w_{nw} , which is not straightforward to assess with SEM even with a tiltable stage. Therefore, an AFM (Bruker Dimension Icon) was used for topographic imaging of the nanowires, using Bruker's proprietary "PeakForce" tapping mode. Here, even though the AFM is operated in a non-contact technique, the nanowire is liable to attract and attach to the tip, depending on how thin and how strongly adhered to the substrate it is. It was found that to lessen the chance of this occurring, the line scanning should be slow (100 mHz) and orientated as close to perpendicular as possible to the principal nanowire axis. Also with this in mind, scans of narrow sections were taken at the thickest and thinnest part of the nanowires (generally near the two ends) rather than mapping the entire length of the structure. Due to the high aspect ratio of the nanowires, even with such slow scanning the AFM system struggles to accurately track the nanowire profile when moving down from the nanowire to the substrate, resulting in an artefact called 'comet-tailing'. As such measurements of w_{nw} were often not reliable (as checked against SEM width measurements), though rough

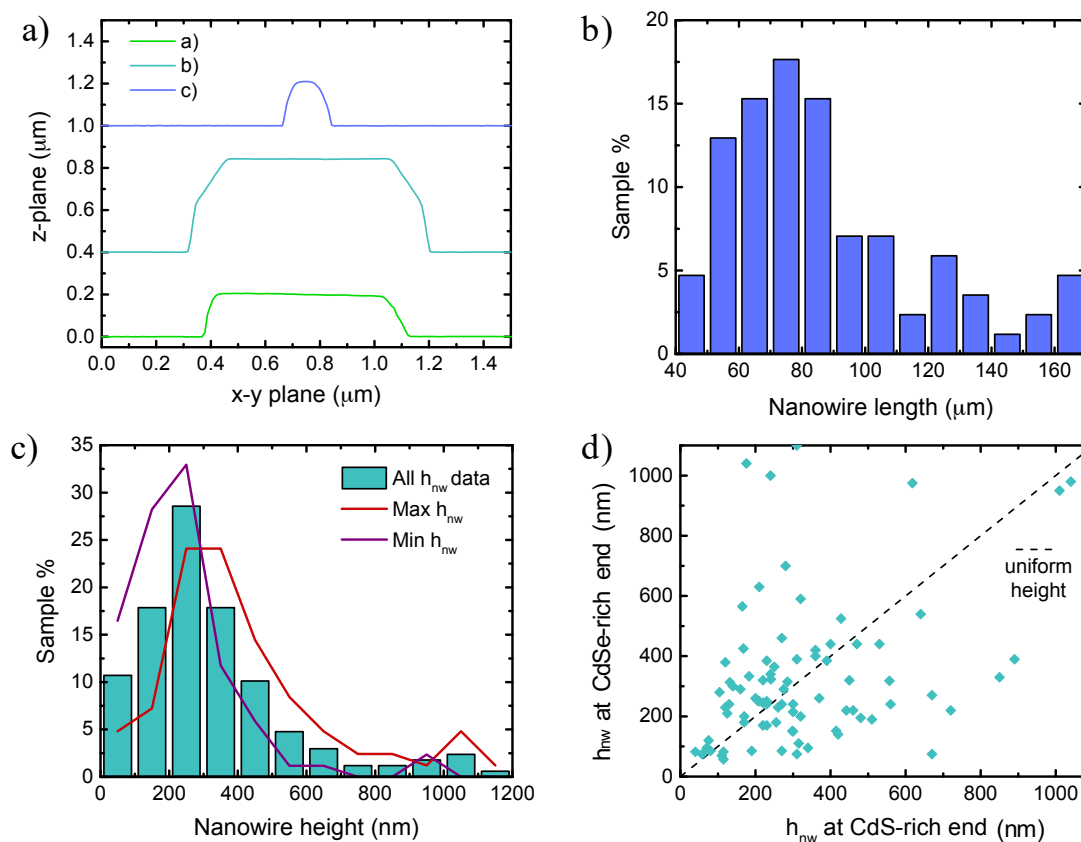


Fig. 6.5 Morphology distribution across nanowire samples. (a) AFM height profile measurements of the nanowires in the right hand panels of Fig. 6.4a, b and c, demonstrating their different cross-sections. (b) Distribution of nanowire lengths (as measured by optical microscope) across a sample ($n = 85$) of nanowires selected and transferred for device fabrication. (c) Distribution of the heights (h_{nw} , as measured by AFM) across the same sample as a), measured at either end of each nanowire. Columns show all 170 measurements, while red and purple lines are the distribution for the thicker and thinner ends of each nanowire, respectively. (d) Plot of the heights at the CdS- and CdSe-rich ends for each nanowire in the sample; dashed line represents nanowires which have uniform thickness along the length, i.e. $h_{nw}(CdS) = h_{nw}(CdSe)$.

assessment of the cross-sectional shape for larger wires is possible; nanobelt plateaus and broadly hexagonal and cylindrical shapes can be seen in Fig. 6.5a, corroborating the SEM images.

Collating the physical characteristics for 85 of the nanowires that were selected, transferred and used in devices over the duration of my studies, typical distributions of nanowire length, l_{nw} , and height, h_{nw} can be seen in Figs. 6.5b and c respectively. The mean nanowire length was $\mu_{l_{nw}} \approx 86 \mu\text{m}$ with a standard deviation of $\sigma_{l_{nw}} \approx 31 \mu\text{m}$. Note nanowires with l_{nw} outside of a 50 - 200 μm range were excluded from use in devices (criterion 3 in the previous section). As seen in the distributions of nanowire height for the CdS (h_{CdS}) and

CdSe (h_{CdSe}) rich ends, there was a broad spread of nanowire heights across the sample. For nanowire heights, taking into account all measurements (both the h_{CdS} and h_{CdSe} datasets), $\mu_{h_{nw}} \approx 334$ nm with $\sigma_{h_{nw}} \approx 254$ nm. A selection bias that should be noted here is that thinner wires ($h_{nw} < 100$ nm) were far more difficult to pick up with the fibre probe without breaking, given their relative fragility and the radii of the probe tip.

A plot of h_{CdS} against h_{CdSe} for each nanowire in the sample set is shown in Fig. 6.5d. The spread of points away from the $h_{CdS} = h_{CdSe}$ trendline indicates the non-uniformity of nanowire thickness along the wire, whilst the symmetrical nature of the scatter either side of this trendline indicates that there was little tendency for either composition end to be thicker than the other. These results again highlight the failure of the growth process to produce geometries that are either uniform along each nanowire or consistent between nanowires or batches. The changes in thickness and cross-section observed along the nanowire lengths are likely due to poorly controlled local conditions at the substrate during growth, owing to fluctuations in vapour pressure as the sources are moved through the furnace. The extent and nature of these changes is likely to be different across the length and width of each growth substrate; as the sample contains a spread of nanowires transferred from many different locations from across a growth substrate, this may explain why there is little correlation between the thickness and the material composition.

PL spectra along the length of the CdS_xSe_{1-x} nanowires were mapped using the Renishaw InVia microspectrometer system (Ar^+ -ion laser, 457 nm wavelength) at $50\times$ magnification, corresponding to a focused spot diameter of $\sim 1 - 2 \mu m$. The central wavelengths for the measured emission peaks, at measured distance d along a representative nanowire, $\lambda_c(d)$ (where $d = 0$ corresponds to the CdS-rich end and $d = l_{nw}$ corresponds to the CdSe-rich end), are plotted in 6.6a. Example PL spectra for three points can be seen in the inset; these have been normalised to the maximum peak height, though it should be noted there is significant variation along the nanowire that correlates broadly with the nanowire height (and thus, generally speaking, the volume of semiconductor) at the measurement point. No spatially resolved quantitative analysis with respect to the PL efficiency, or to elucidate physical processes was carried out, as this was not a primary objective of the project, though this, along with OPTP spectroscopy, could prove useful in future device studies. In assessing $\lambda_c(d)$, a Gaussian fit was used for each peak. The majority of peaks were well fitted by a Gaussian, though at some locations, dual-component peaks were observed, suggesting the presence of non-uniform material at that section. Remarkably, considering the variation in geometry along them, for the sample of nanowires fully mapped ($n = 15$), all show strongly linear $\lambda_c(d)$, with a continuous and even increase in emission wavelength along the nanowires, suggesting an even gradient of alloyed material, as shown in the literature

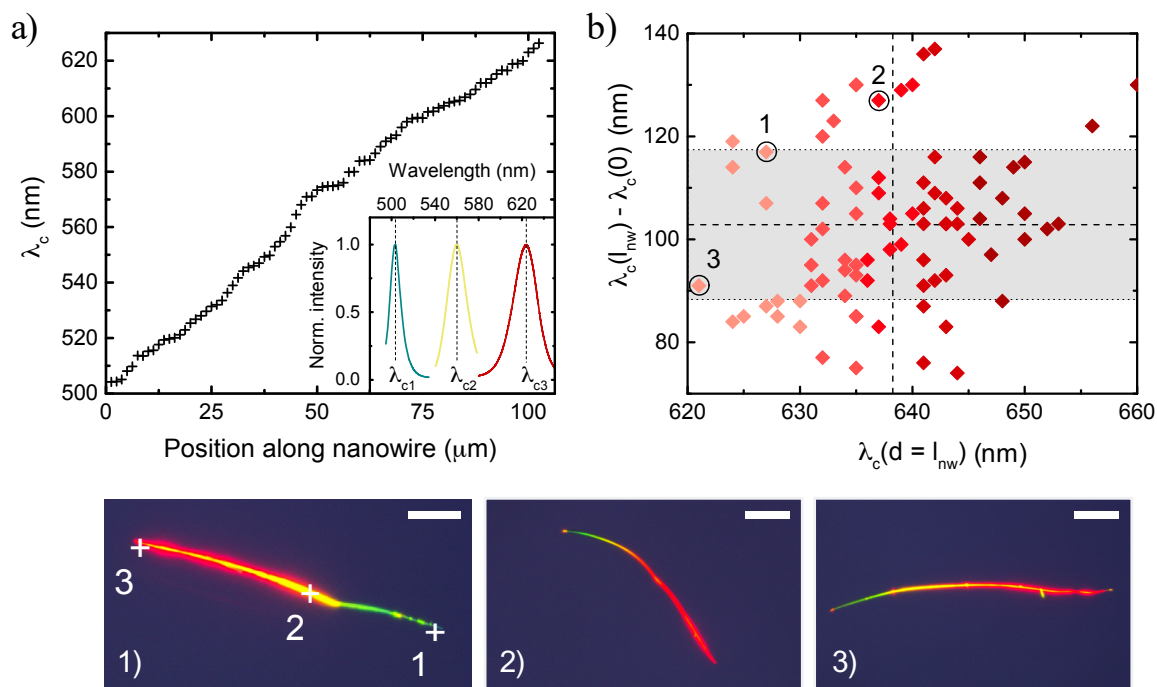


Fig. 6.6 **Photoluminescence measurements of $\text{CdS}_x\text{Se}_{1-x}$ nanowires.** (a) Central wavelength for the emission peaks of PL measurements taken at different points along the length (0 is the CdS end, $l_{nw} = 102 \mu\text{m}$ is the CdSe end) of a nanowire, shown in PL image 1 beneath and corresponding to data point 1 in part b). Inset plot shows the PL spectra for selected points as marked in the image. All measurements made using a 457 nm laser focused with $50\times$ magnification objective lens, spot size $\sim 1 - 2 \mu\text{m}$. (b) Plot showing the total emission wavelength span (that is, $\lambda_c(l_{nw}) - \lambda_c(0)$) against the emission peaks at the CdSe-rich end (position = l_{nw}) for each nanowire in a sample, $n = 85$, selected during intermediary substrate scanning after contact transfer. Dashed lines indicate the mean values for each axis, whilst grey shaded area denotes one standard deviation either side of the mean. PL images beneath are of nanowires corresponding to the numbered data points in the plot. All scale bars are $20 \mu\text{m}$.

(chapter 4). Once again the selection bias should be noted that nanowires with gradients that were obviously uneven to the naked eye were not selected for device fabrication (criterion 2 from the previous section). Distributions for $\lambda_c(0)$ and $\lambda_c(l_{nw})$ are shown in 6.6b for a wide sample of nanowires ($n = 85$) selected as passing criterion 1 - 4 under visual assessment at the intermediary substrate mapping stage, many of which were used in devices. As can be seen, even for those nanowires that have passed visual assessment, there is a wide range of bandgap spans and minimum / maximum wavelengths.

That there are *no* nanowires with $\lambda_c(l_{nw}) > 660 \text{ nm}$, when the emission for pure CdSe should be $\sim 710 \text{ nm}$, suggests that there may have been a fault during nanowire production that led to termination of the growth before this material could be incorporated. It is also

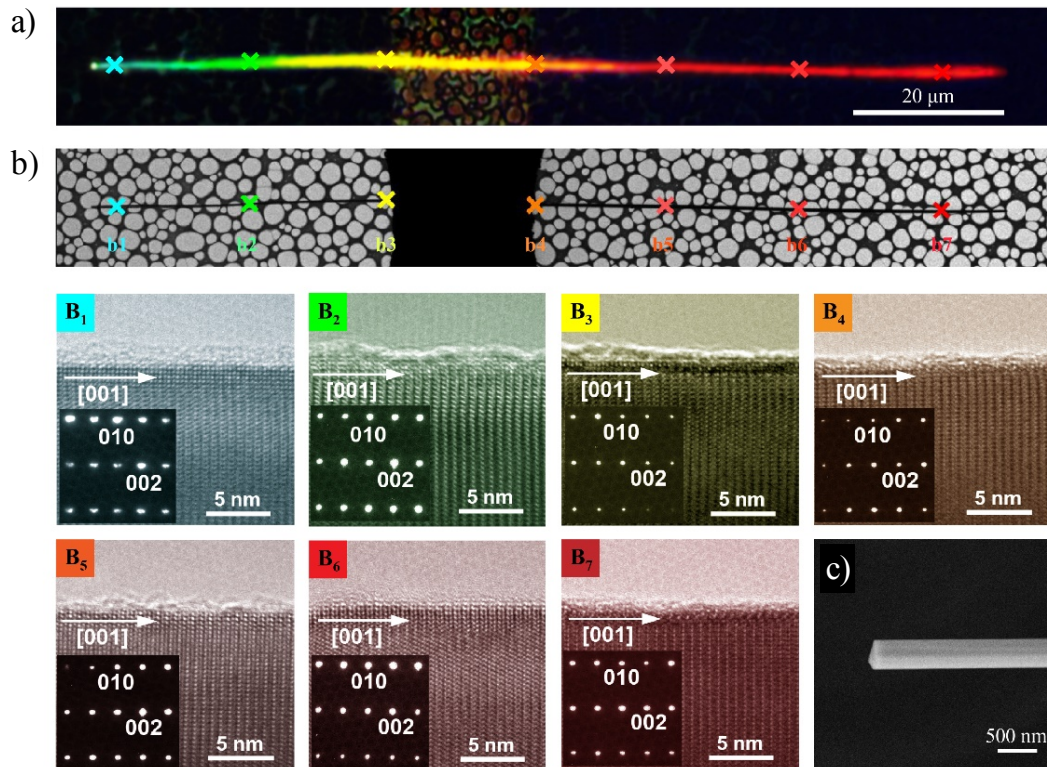


Fig. 6.7 **Spatially-resolved transmission electron microscope imaging of a $\text{CdS}_x\text{Se}_{1-x}$ nanowire.** (a) Real-color photoluminescence image of the nanowire on a Transmission electron microscope (TEM) carbon grid. (b) TEM image of the nanowire. Insets (B1-B7): High-resolution TEM images and selected-area electron diffraction patterns taken from several representative regions, as marked in b). (c) Scanning electron microscope (SEM) image of one end of the nanowire.

possible that, at the transfer stage, as the CdSe is the material at the top of the forest, these sections are being fractured off of the CdS-rich sections, as it is these ends that contact the intermediary substrate - though it seems unlikely that this would account for the whole of the 50 nm reduction in emission span. Clearly this directly limits the detectable wavelength range of photodetectors along the nanowire, however, further investigation into, and optimisation of, the growth process would be needed to rectify this that was not feasible during my study.

Transmission electron microscope (TEM) images were also captured at different locations along the length of a typical nanowire (Fig. 6.7). These results agree well with those in the literature, showing highly crystalline material at each point along the nanowire, with minimal defects and no observable dislocations, despite the alloying process.

6.2 Depositing nanowire contacts

6.2.1 Challenges surrounding electrode deposition

After transfer, for device fabrication the next stage to address was the definition and deposition of electrodes - *via* lithographic patterning - to allow electronic contact to the nanowires. Here, the variability of nanowire length presents the need to create custom lithographic patterns on a device-by-device basis, rather than being constrained by a fixed, pre-patterned mask. Furthermore, to allow the possibility of fabricating denser arrays of electrodes on the nanowires, to electronically probe them at higher spatial resolution, electrode widths and thus lithographic resolutions down to and below $\sim 1 \mu\text{m}$ are desired. Therefore, despite far lower throughput than photolithography, electron-beam lithography (EBL) was selected as evidently the more suitable patterning process. For all EBL processes detailed in this thesis, a Nanobeam Ltd. "nB1" system was used, with a beam acceleration voltage of 80 kV.

To create device substrates, doped 4" silicon wafers, with 280 nm thermally grown oxide layers, were first patterned *via* EBL with a grid of $60 \times 10 \times 10 \text{ mm}^2$ units. Each unit in this grid contains alignment markers placed in each corner (a rectangular grid of eight squares, sides: $20 \mu\text{m}$, spaced $200 \mu\text{m}$ apart) serving as reference points for calibrating the origin of the EBL write and determining the x-y-z plane of the substrate to negate any tilt. As well as this an array of markers is patterned on each unit (crosses, width: $3 \mu\text{m}$, spaced at $200 \mu\text{m}$ apart in x and y directions, simply such that four markers can be seen in the field of view at $50\times$ microscope magnification; these can be seen in nearly all nanowire or device optical images) with coordinates labelled for each to reference the locations of optical or SEM images taken of nanowires transferred to the chip at later lithographic or characterisation stages. Wafers are first cleaned through sonication in IPA and acetone (5 minutes each) before spin-coating in PMMA 950 A4 resist then baking for ten minutes at 120°C . After patterning and development, the wafer is metallized with a Ti:Au, 5:40 nm layer *via* electron-beam evaporation (Lesker PRO Line PVD 200, typical deposition pressure $\sim 5 \times 10^{-6}$ mbar), followed by lift-off through sonication in acetone then IPA for 10 minutes each. Wafers were then cleaved by diamond scribe and ruler along the borders of each unit to produce a batch of $60 \times 10 \times 10 \text{ mm}^2$ device chips. Nanowires would then be transferred after chips were further cleaned and treated with plasma to enhance adhesion (as all described in the previous section).

A number of important issues and considerations were established during fabrication of early devices during my PhD, surrounding lithographic definition and deposition of electrodes onto the $\text{CdS}_x\text{Se}_{1-x}$ nanowires. In a typical process, the pattern to be written was first designed using CAD software (Autodesk AutoCad 2017), defined relative to a

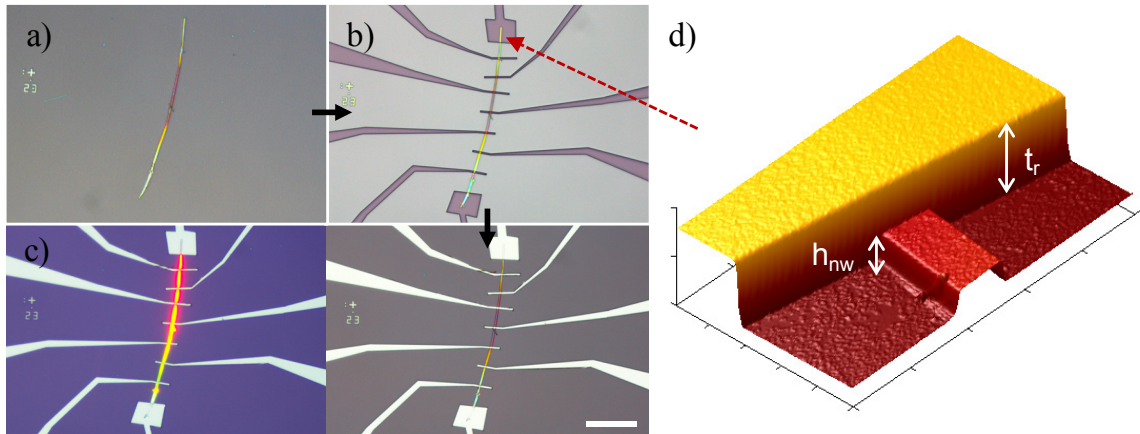


Fig. 6.8 The electrode deposition process. (a)-(c) Optical images summarising steps in the fabrication of an early nanowire test device; the nanowire is transferred to the substrate (a), before spin-coating in PMMA resist, electron-beam lithographic write of the electrode pattern and development (b) and finally metallization and lift-off, leaving the final device (c) - left and right panels under 390 nm UV illumination and white light, respectively. Scale bar is 25 μm . (d) 3-dimensional AFM image of a the region uncovered by development in b), illustrating the geometry of the resist (thickness t_r) with respect to the nanowire (height, h_{nw}). Ticks along the x- and y-axis are 5 μm apart, and 500 nm apart along the z-axis.

map of the already patterned alignment markers, coordinate grid and optical images of the as-transferred nanowire (shown in Fig. 6.8a). A chosen resist was spin-coated onto the nanowire device substrate, then the pattern written with EBL, with each features assigned particular beam doses (measured in $\mu\text{C cm}^{-2}$). For a fixed developer and development time, the choice of dose was dependent on the resist used and the thickness it is spun at, the feature size (meaning that multiple doses must be used for patterns with a large range of feature sizes), as well as the spatial density of features (due to the exposure proximity effect as detailed in chapter 5). Methods developed for ‘dose testing’ to establish appropriate doses for complex device structures will be covered later in more detail in chapter 7. Assuming dose and development time has been optimised, resist in the written areas is selectively removed (Fig. 6.8b) through soaking in the developer, exposing the substrate and nanowire beneath, an example of which is illustrated by the 3-dimensional AFM image in Fig. 6.8d. A metal layer was then deposited (Fig. 6.8c); for this, three methods were tested and used during my research - thermal evaporation, electron-beam evaporation, and sputter coating (all introduced in chapter 5), before use of a solvent to remove the resist and metal layer in those areas not exposed by the EBL writing.

At this stage, a number of general constraints were established. Firstly the resist height, t_r , must be greater than h_{nw} , or only thin sections of resist are left on top of the nanowire

which were liable to be removed at the development stage even without direct writing, due to the proximity effect. Secondly, a general, spoken rule accepted in the field for EBL is that to allow efficient lift-off, there should be a >3:1 ratio between t_r and the thickness of the metallization layer, t_m . Finally, a critically limiting factor was that exposures to acetone beyond 15 - 20 minutes were observed to dramatically reduce the PL emission intensity of the nanowires, increasing with the length of time exposed and toward negligible levels for exposures of 24 hours or longer. Figure 6.9a exemplifies this. Photocurrent in the resultant devices was correspondingly, and dramatically, reduced; further investigation would be required to establish the mechanism by which this was occurring. Long, often >12 hour soaks in lift-off solvent that are used in many nanofabrication processes were therefore not feasible here. Additionally, whilst sonication is often used to aid lift-off, this was found to both increase the resistance of final devices and often lead to removal of the nanowire from the surface. A light syringe was however effective in reducing lift-off time for all deposition methods by as much as three times, without removing the nanowire from the substrate.

In early devices a 950k A8 (molecular weight and % dilution in anisole respectively) PMMA resist, spun at 4000 rpm was used. Measured using ellipsometry as well as AFM, under these conditions, $t_r \approx 880$ nm. As the resolution of the lithography should decrease as the t_r increases (due to greater scattering of electrons while penetrating a greater volume of resist), this value was selected as a compromise, keeping t_r as low as possible whilst still larger than almost all of the thicker nanowires transferred.

Figure 6.9b shows SEM images of some typical early devices with Cr:Au electrodes deposited by thermal evaporation. These illustrate one of the main challenges when depositing contacts onto nanowires as outlined in chapter 5. Aside from affecting the required t_r , the high aspect ratios of these relatively thick nanowires (with h_{nw} of the majority of nanowires rising above ~ 300 nm) means that the nanowires can "shadow" evaporation methods where the metal vapour trajectory can be thought of as a straight line (thermal and electron-beam evaporation). As can be seen, this creates discontinuities in the film adjacent to the nanowire on the side that is facing away from the evaporation source. Further to this, depending on horizontal displacement of the source with respect to the substrate (i.e. the angle of the source vapour trajectory), metal will also be deposited on the sidewalls of the resist that are facing toward the evaporation source, resulting in the creation of a 'lip' that is liable to collapse during lift-off - see Fig. 6.9c. As the sidewalls are necessarily high due to the requirements on t_r , these lips can be large enough to short contacts that have narrow separations.

Clearly, one way to circumvent the issue of nanowire 'shadowing' is to evaporate such a thick metal layer that $t_m > h_{nw}$. However, given that h_{nw} is regularly >500 nm, aside from being time-consuming and costly, metallization of such thick layers would require a much

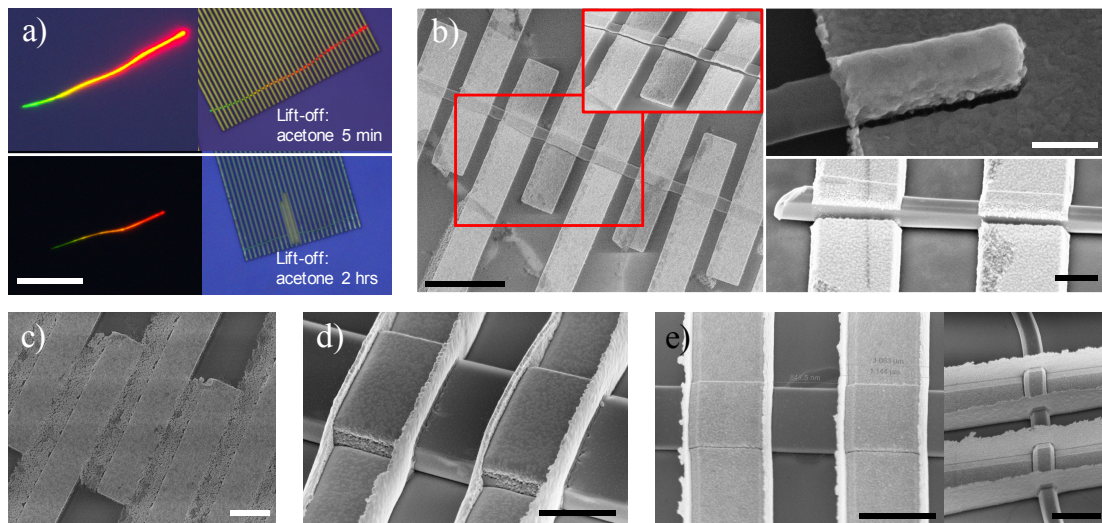


Fig. 6.9 Characterisation of, and challenges for, metallisation and lift-off. (a) Photoluminescence images comparing two nanowires before and after electrode lift-off in acetone for 5 minutes (top) and 2 hours (bottom) representative of the effects of lengthy exposures to acetone on the PL intensity. Scale bar is $20\ \mu\text{m}$. (b) SEM images of electrodes deposited by thermal evaporation, demonstrating how the nanowire ‘shadows’ the source vapour, creating discontinuities at the side-walls of the nanowire on the side facing away from the evaporation source. Inset of main image shows the highlighted area at a stage tilt of 30° . Scale bars of left, top right and bottom right images are $5\ \mu\text{m}$, $200\ \text{nm}$ and $500\ \text{nm}$, respectively. (c) Demonstration of the ‘lips’ created when metal is evaporated onto the side-walls of the resist, which can collapse and short the electrodes as shown. Scale bar is $2\ \mu\text{m}$. (d) Typical Ni electrodes deposited by sputter coating. Scale bar is $1\ \mu\text{m}$. (e) Electrodes deposited on two different nanowires by an electron-beam evaporation system using a tilted, rotating stage, so as to sequentially expose all nanowire surfaces to the source vapour evenly. Right-hand image highlights the lip structures that form as a result of deposition onto the sidewall in this method. Scale bars are $1\ \mu\text{m}$.

thicker resist than the 950 A8, limiting the resolution of the EBL and further exacerbating the issue of ‘lip’-formation, creating thick deposits on the sidewalls, significantly complicating lift-off. Sputter coating was investigated to address the problem of shadowing; as discussed in chapter 5, the mean free paths of source vapour particles is far shorter in sputter systems, resulting in a conformal film. Sputtered Ni electrodes (thickness $80\ \text{nm}$) on a nanowire can be seen in the images of an early test device shown in Fig. 6.9d. The sputter system used throughout the PhD was a magnetron-based system, produced by Precision Atomics - unless otherwise stated all sputtering was done with Ar gas, at chamber pressure $3.5 \times 10^{-3}\ \text{mbar}$, after pumping to a base pressure of $<5 \times 10^{-6}\ \text{mbar}$. The SEM and AFM analysis show that whilst the sputtering forms a continuous, conformal electrode with no cracks, it also completely coats the side-wall of the resist, producing very pronounced lip structures at the electrode edges, with heights only slightly less than t_r . For Ni, it was observed that the metal

layer was malleable enough that even despite side-wall coating, lift-off was remarkably fast ($\sim 1 - 3$ minutes depending on thickness and features). However, for other metals, such as Al, this conformality resulted in extremely challenging lift-off, as solvent cannot penetrate the resist through the sidewalls; sections of metallized resist on test devices were still attached even after a 24 hour acetone soak.

A final electrode deposition method developed was to use the electron-beam evaporation system, but with a tilted (25°), rotating (2 rpm) stage. Note that this was only done on the electron-beam evaporation system as no thermal systems had a tilted stage capability. By rotating in the plane of the tilted substrate (rather than in the horizontal-plane), all sides of each feature on the device substrate are orientated to face the evaporation source for equal time during the evaporation. Thus, a conformal coating around the nanowire sides can be achieved, as shown in the SEM images of test devices with a Ti: Au (5:120 nm) metal layer in Fig. 6.9e. As with the sputter coating, this method also coats the resist side-walls, producing 'lip' structures after lift-off. However, these are far thinner than those in the sputter-coating, given that the sidewalls are only directly facing the evaporation source for a fraction of the total deposition time, and are often removed in the lift-off process.

6.2.2 Developing a process for nanowire embedding

As detailed in chapter 5, one solution for deposition of high resolution structures onto thicker nanowires is to planarise the surface with a polymer layer, embedding the nanowire, before exposing its top surface through a plasma etch or use of a solvent^[245,246,248,249]; during my research I sought to develop such a process. In these methods, a primary requirement for the embedding layer is that it must be highly resistant to physical alteration by any further fabrication processes (for instance, solvents required for lift-off) serving as a permanent feature of the device. In test devices, parylene-C was first used, as it is highly inert, robust, and is known to form pin-hole free layers - recipes for its deposition had also already been optimised for the work on black phosphorus detailed in chapter 3. AFM imaging of a typical embedded nanowire in parylene-C are shown in Fig. 6.10a, with corresponding height profiles in Fig. 6.10b. As can be seen, the coating is almost completely conformal - that is, the thickness of the embedding layer, t_{emb} , on the top and sides of the nanowire (as determined by AFM) is equal to that on the substrate (as determined by AFM and ellipsometry), even if $t_{emb} \gg h_{nw}$. Whilst this is desirable for many applications, such a layer is not suitable for the embedded structures that were being targeted. This is because - as demonstrated in Fig. 6.10 - etching of the parylene-C layer using the RIE system available (a Diener Femto plasma system) is sufficiently directional/anisotropic that it removes material on top of the nanowire at the same rate as that around it. As such, given that the thickness on top of the nanowire

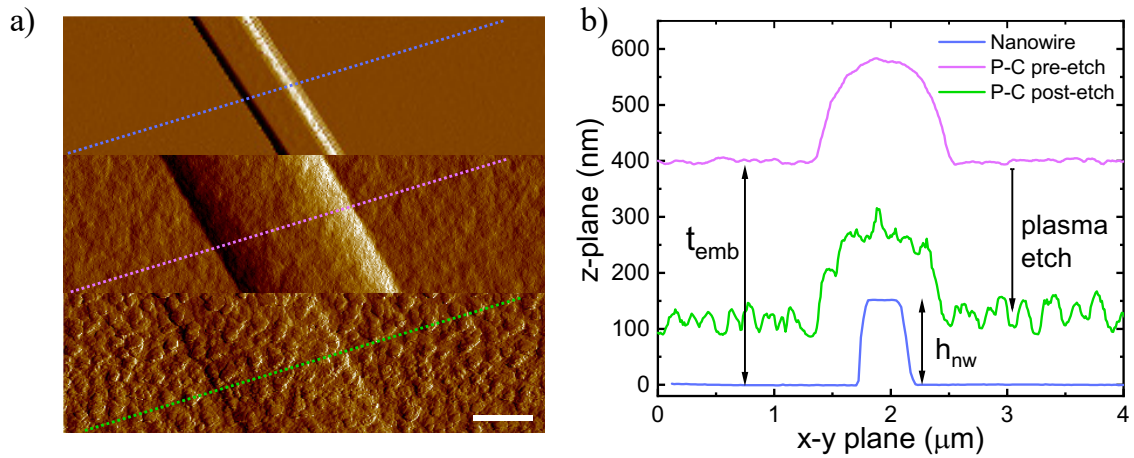


Fig. 6.10 **Unsuitability of parylene-C for nanowire embedding.** (a) AFM images (peak force mapping is shown to better highlight topography) of a nanowire before (top) and after (middle) coating in a ~ 400 nm parylene-C (P-C), and after a ~ 15 min N_2 etch (bottom). (b) Height profile measurements corresponding to the dashed lines in a).

is approximately equal to t_{emb} , the nanowire will only be revealed once *all* the material is removed. In this case it follows that if the nanowire is to be revealed, a planarising (rather than conformal) layer must be used, such that the height of material above the nanowire is as close as possible to $t_{emb} - h_{nw}$.

Embedded layers formed of SU-8 photoresist were tested in this regard. Not only is SU-8 highly resistant to any forms of chemical removal once it is cross-linked and cured, as a negative photoresist (areas exposed to UV become cross-linked), it can be lithographically patterned, allowing greater flexibility in device production, for instance in revealing sections of the substrate where the embed layer is not desired (e.g. on top of the pre-patterned EBL alignment markers). The thinnest commercially available formulation is SU-8 2000.5 (MicroChem) which can spin down to a thickness of around 500 nm. To allow a greater range of control over t_{emb} , to embed thinner wires, as well as to allow testing of layer application where $t_{emb} < h_{nw}$, dilutions were made up 50% and 25% by mixing SU-8 2000.5 and SU-8 Thinner (MicroChem) at 1:1 and 1:3 ratios, respectively, using a magnetic stirrer for 24 hours. These layers, as spin-coated onto Si:SiO₂, were measured using AFM and ellipsometry to calibrate the thickness at various spinning speeds, as shown in Fig. 6.11a. It was found that for the 50% and 25% dilutions, it was essential to spin-coat device chips within the same day as the plasma treatment for nanowire transfer, or the resist would not wet the substrate surface. In a typical process, after spin-coating the device substrate, the SU-8 layer was baked on a hot plate for 1 minute at 95 °C. Depending on the desired architecture, a flood or masked UV exposure was then administered (SUSS MicroTec MJB-4 mask aligner system,

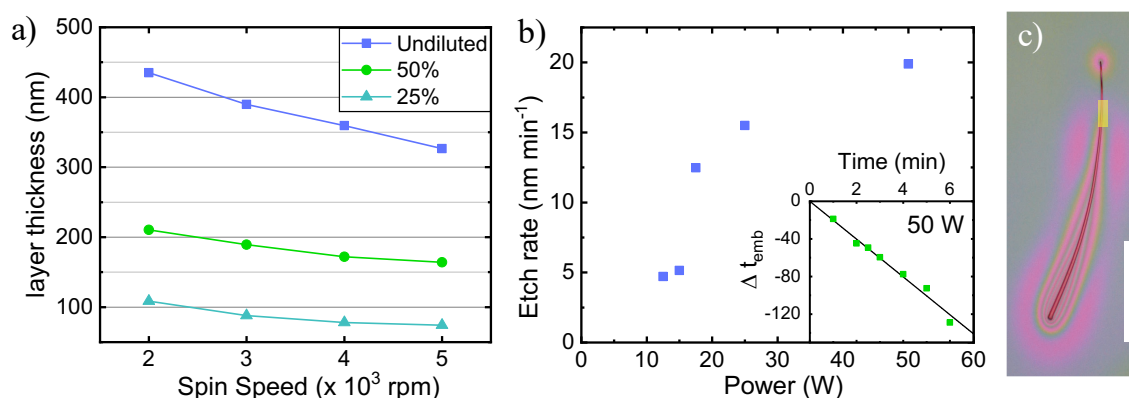


Fig. 6.11 **Nanowire embedding using SU-8 part i**. (a) Thickness of spin-coated layers on Si:SiO₂, as measured by ellipsometer, for undiluted and 50% and 25% dilutions of SU-8 2000.5 at varying angular speed. (b) Etch rate of SU-8 layers under RIE (N₂ plasma at 8×10^{-3} mbar) at varying system power. Inset shows example (for a power of 50 W) ellipsometry measurements of Δt_{emb} (the etched height of the embed layer relative to un-etched) at varying etch duration, carried out to determine the rate at each power. (c) Optical microscope image of a nanowire embedded in SU-8, showing contrast variation where film has aligned to the nanowire when $h_{nw} > t_{emb}$. Scale bar is 40 μm . Yellow highlighted section corresponds to AFM image in Fig. 6.12a.

with a Hg arc lamp) at an intensity of 10 mJ cm^{-2} for 15 s, before a second bake, of 1 minute each at 65 °C then 95 °C. If the film is being patterned (i.e. a masked exposure), development of non-exposed sections is done in PGMEA for 25 s (duration is non-critical).

To allow precise control in the process of ‘revealing’ the nanowire top surface, etch rates of the SU-8 layer under different conditions were first calibrated (plots are shown in Fig. 6.11b). This was carried out with two separate RIE systems - the Moorfield Nanoetch and a Diener Femto plasma system - over the course of my studies due to the failure of the latter during my third year. N₂ gas was used in all etches, to provide a relatively inert plasma and avoid chemically altering the nanowire surface; in this regard, O₂ plasma was found to completely extinguish any PL emission from the wires. Figure 6.11c shows an optical microscope image of a nanowire embedded in SU-8.

A typical SU-8 nanowire embedding process, including etching to reveal the surface, is demonstrated by the AFM images and measurements in Fig. 6.12, taken at each stage: before, and after, spin-coating, and after the N₂ etch. Ellipsometry was used to define the global thickness (away from the nanowire) of the embedding layer pre- and post-etch, t_{emb} and t_{emb}^* , respectively. To illustrate both scenarios where $t_{emb} < h_{nw}$ and $t_{emb} > h_{nw}$, embedding of a nanowire with a large height gradient is shown, and SU-8 spun such that $h_{nw}^- < t_{emb} < h_{nw}^+$. As can be seen, for $t_{emb} > h_{nw}$, the spin-coated surface is essentially planarised, with a small mound in the film of around 5 - 15 nm above the nanowire; the mound height was observed

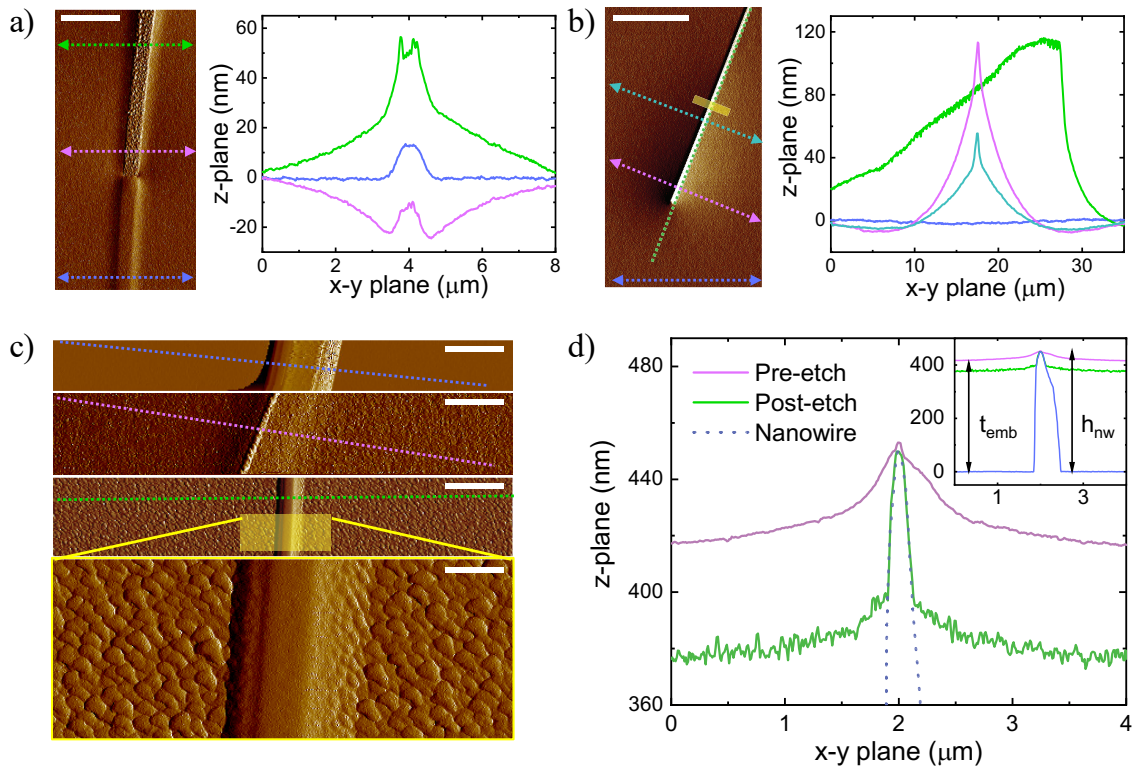


Fig. 6.12 **Nanowire embedding using SU-8 part ii).** (a) AFM image[†] (left) and height profiles (right) corresponding to like-coloured dashed lines, for the section of nanowire highlighted in Fig. 6.11c with a height gradient such that at one end $h_{nw} < t_{emb}$ (blue) and at the other $h_{nw} > t_{emb}$ (green). Scale bar is $2 \mu\text{m}$. (b) AFM image[†] (left) of the end of an embedded nanowire (different to that shown in a) and height plots (right) corresponding to the dashed lines showing profile along its length (green), at the base-line level of the SU-8 layer (blue) and perpendicularly across the nanowire at its maximum thickness (magenta) and at a thinner section (teal). Yellow highlighted section corresponds to AFM images in c). Scale bar is $10 \mu\text{m}$. (c) AFM images[†] for the highlighted section in a), of the nanowire before SU-8 embedding (top), after spin-coating (2nd top) and after a 120 s, 50 W N_2 plasma etch of the embedding layer (2nd bottom), with a magnified section of the final structure (bottom). Scale bars for top 3 images and bottom image are 500 nm and 100 nm respectively. (d) Height profile cross sections corresponding to the respectively coloured dashed lines in c). Main plot shows a zoomed section at the embedding layer surface while inset shows the whole nanowire relative to the whole structure relative to the substrate, with embed layer thickness and nanowire height labelled. [†]In all AFM images, peak force error mapping is shown to better illustrate topography, whilst cross-sections correspond to simultaneously mapped height sensor data; images have been cropped therefore arrowed dashed lines denote cross-sections that extend further than the image boundaries.

as $< 15 \text{ nm}$ regardless of the nanowire thickness or width, though where $t_{emb} \gg h_{nw}$, the mound is negligible.

More notably, for $t_{emb} < h_{nw}$, at close proximity (from $5 \mu\text{m}$ to $10\text{s of } \mu\text{m}$, depending on the magnitude of $t_{emb} - h_{nw}$) to the nanowire the SU-8 layer begins to ‘align’ itself with the

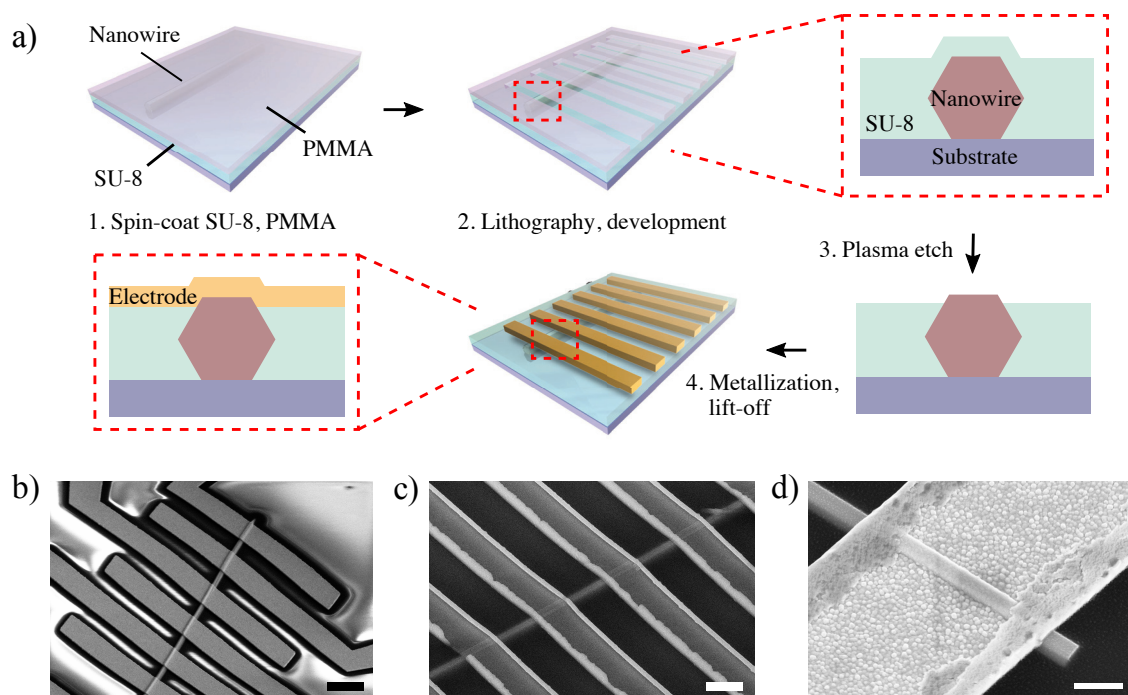


Fig. 6.13 **Embedded nanowire devices.** (a) Schematic summarising the fabrication process starting from a nanowire transferred onto a Si:SiO₂ substrate. (b)-(d) SEM images at various magnifications for a three different embedded devices with thermally evaporated (b) and sputtered contacts (c,d). The distortions observable in b) around the electrodes are due to the electron beam charging the SU-8 surface. Scale bars are 2 μm (b,c) and 500 nm (d).

top edges of the NW due to surface-tension effects, forming a slope between the nanowire and resist surface. As an aside, as can be seen, depending on the nanowire cross-section, the SU-8 will often not wet the nanowire surface well in this scenario, instead leaving small droplets of resist on the surface. This sloping surface alignment was measured (by AFM) for embedded nanowires with sections where $t_{emb} < h_{nw}$, even in scenarios where $h_{nw} - t_{emb}$ is as large as 800 nm, and regardless of the size of t_{emb} . The effects can be seen even in optical images, manifesting in interference-based variation in contrast near the nanowire (Fig. 6.11c). Therefore, by coating in SU-8 whereby $t_{emb} < h_{nw}$ along the whole nanowire length, a short etch process, removing only 15 - 20 nm of SU-8 can be used to reveal all of the nanowire surface.

In this way, the difference between the nanowire and the immediately adjacent surface is reduced from 100's of nm to around 20 nm, regardless of changes in height along the nanowire. As such, electrodes can be deposited straightforwardly without any issues of shadowing or cracking at the nanowire edges and without requiring thick metal layers. For device fabrication the etch was typically carried out after the lithography and development

step, so that channels between contacts are shielded from the plasma by the EBL resist. Figure 6.13 shows a schematic illustrating this process, as well as SEM images of some typical embedded devices, demonstrating the continuity of these electrodes near the nanowire edge, in contrast with those in the previous section deposited onto bare nanowires.

6.2.3 Embedding alumina-encased nanowires

During my studies, a notable variation developed on these embedded nanowire device structures was to first encase the nanowire in a passivating layer. The reasoning behind this was two-fold; firstly, detailed in chapter 4, nanowire properties can be highly sensitive to their interfacial chemistry. Therefore, the primary aim was that an assessment could be made to compare the effects of this pre-coating versus a direct SU-8-nanowire interface. Secondly, as can be seen with the SU-8 embedding, the top-surface of the nanowire is often not wetted properly by the resist. As such, an ALD layer encasing the nanowire would be able to shield it from later exposure to acetone during lift-off.

To achieve this, after transfer, Al_2O_3 was deposited onto the nanowire by atomic layer deposition (ALD), using a Veeco/CNT Savannah thermal atomic layer deposition system, using TMA and water precursors, at a deposition temperature of 120 °C. As introduced in chapter 5, these layers are completely conformal, and their thickness can be controlled down to atomic-level precision - the typical thickness used in these processes was ~ 20 nm as verified by ellipsometry measurements. From this point the embedding process was carried out with the same steps as for non-encased nanowires, until after EBL-writing, development and the etching of the SU-8 layer. It was verified that the ALD layer is only negligibly etched by N_2 RIE and as such a solvent-based approach was used to etch through those sections exposed by development. A TMAH-based developer, AZ726 was found to selectively etch the Al_2O_3 , without affecting the patterned PMMA resist or the SU-8 layer; ellipsometry calibration of the etch rate on test layers showed the alumina is removed at ~ 3 nm min^{-1} at room temperature. Once the ALD layer has been removed, the patterned resist would then be metallized for lift-off. A schematic illustrating the process is shown in Fig. 6.14a.

A significant issue encountered here was the isotropic nature of the TMAH etch. Whilst the Al_2O_3 on top of the nanowire was removed, TMAH would penetrate around the sides of the NW and remove the casing also, even when the etch height was carefully controlled. This was observed through AFM mapping of these structures (Fig. 6.14b-d), whereby a sharp trench can be seen in between the SU-8 surface and the nanowire top-face. SEM images of the resultant devices show that this produces a marked gap in the electrode deposited. When the metal deposition was over ~ 100 nm, current was often measured across channels, suggesting that these trenches can be bridged by the electrode. However, given these challenges, and

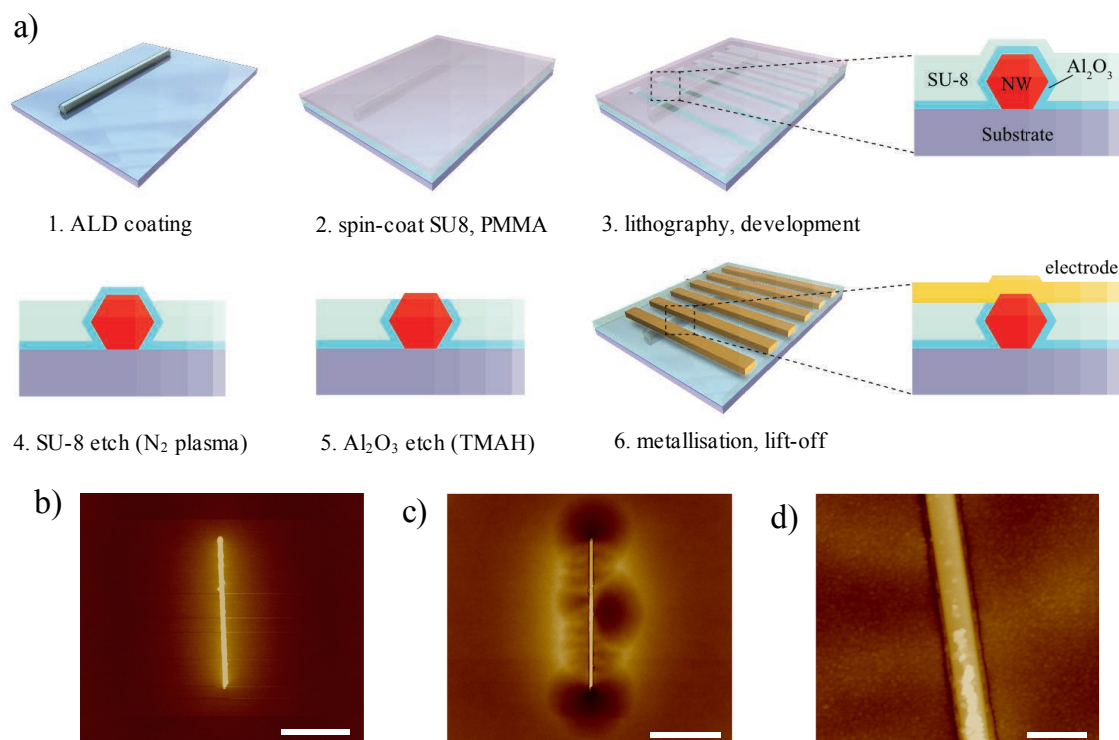


Fig. 6.14 **Embedded, alumina-encased nanowires.** (a) Schematic illustrating the different stages to create embedded structures where the nanowire is first encased in Al₂O₃. (b)-(d) AFM images showing such a structure after SU-8 etching, and after alumina etching with TMA for an InAs nanowire. These illustrate an extreme example of a drawback in this process, whereby for particularly thin nanowires, due to its isotropic nature, the second etch will penetrate beneath the SU-8 layer and undercut the Al₂O₃ layer, up to microns away from the nanowire, even when the rate of the etch is carefully controlled. Image d) is a magnified section of c), showing the trench (seen as a dark line) that has formed directly adjacent to the nanowire where the ALD-deposited layer has been removed. Scale bars are 2 μm for b) and c) and 200 nm for d).

the extra processing steps required in contrast to the relative simplicity of the SU-8-only embedding method, alumina-encasing was avoided for use in future multi-electrode devices. Further investigation should be made into anisotropic means of etching the alumina layer to increase the reliability of such a process.

Summary

Processes to transfer CdS_xSe_{1-x} nanowires, and to make electronic contact to them, have been developed. A contact transfer technique allowed nanowires to be taken from the growth substrate to an intermediary substrate; the fashioning of an ultra-fine optical fibre probe allows individual nanowire to then be picked up and transferred to a device substrate.

The inhomogeneity of nanowire PL characteristics (the nature and span of the bandgap gradient) across the growth sample significantly limited the number of nanowires available with suitable properties for device fabrication. Topological analysis further demonstrates a diverse range of nanowire morphologies and thicknesses across the sample. The magnitude and variability of nanowire heights, as well as the sensitivity of nanowires to long lift-off times, lead to the development of a bespoke process for embedding these nanowires in a polymer layer, after conventional electrode deposition processes proved problematic. These quasi-planarised structures allow straightforward deposition of electrodes using EBL at high resolution, regardless of nanowire morphology. In the next chapter, I will move on to discuss the design and characterisation of the specific spectrometer devices central to my thesis, produced utilising the techniques developed here.

Chapter 7

Nanowire-based devices

Overview

From the review of the literature surrounding filter array spectrometers (section 5.3.2), I hypothesised that it should be possible for a multi-electrode $\text{CdS}_x\text{Se}_{1-x}$ nanowire device to function in a fashion analogous to a filter-array spectrometer. By fabricating a number of parallel electrodes (adjacent electrode pairs are henceforth also referred to as ‘photodetector units’) along the nanowire, and measuring each one’s characteristic wavelength-dependent photoresponse, such a device would mirror a system of filter-detector pairs with different transmission functions. It was proposed that, in theory, it should be possible to reconstruct the spectrum of an unknown light signal illuminating the device, by cross-referencing the measured photocurrent with the pre-calibrated response function dataset, provided there is sufficient spectral information contained within the response functions for that wavelength range (again, as covered in detail in section 5.3.2). However, as also well documented in the literature, it is important that a) there be enough detector units to gather a sufficient amount of spectral information and b) that these units operate with enough stability such that errors in the measurement are not so significant that they destabilise the reconstruction.

Building on the processes developed in the previous chapter, the next stage was therefore to design and fabricate a device with a multi-electrode array architecture, that would allow the photoresponse to be probed at as many points as possible along the length of the nanowire. Top-coating embedded nanowires with graphene electrodes was first investigated in this respect, before the study turned toward the use of metallic electrodes. Beyond that, the specific conditions surrounding the fabrication were to be optimised to improve those properties of the devices that are most important with respect to spectral reconstruction, in particular the stability and the signal to noise ratio (SNR) of each photodetector unit.

The first section of this chapter will cover the development of graphene-nanowire hybrid structures, which were initially proposed as a platform on which a multi-electrode array-based device could be fabricated. This will cover the development and optimisation of a graphene transfer process, as well as electronic measurement of graphene channels on etched SU-8 (to test the viability of fabricating devices on this surface) and AFM imaging of graphene-coated embedded nanowire structures. The second section shall discuss multi-electrode nanowire devices based around metallic contacts, beginning initially with how the device architecture was devised within the constraints around measurement and fabrication. Measurement and subsequent optimisation of the devices shall then be presented, discussing the addition of extra fabrication steps such as contact treatments and surface passivation, as well as spatially resolved optoelectronic characterisation along the nanowire, including the calibration of photodetector unit spectral response functions required for spectrometer operation. Chemical vapour deposition (CVD) of graphene was carried out by Dr Phillip Braeuninger (Department of Engineering, University of Cambridge). The PCB-based control board shown in section 7.2.3 was constructed by Dr Zongyin Yang in consultation with myself.

7.1 Graphene-nanowire hybrid devices

7.1.1 Graphene transfer, optimisation and characterisation

Graphene used in this project was grown *via* CVD onto Cu foil (99.8% purity, 25 μm thick), using a cold-wall Aixtron Black Magic Pro 4' plasma-enhanced-CVD reactor. The reactor is ramped to 1065°C, and the Cu annealed in a 4:1 Ar:H₂ mixture, before injection of methane, to leave a mixture of 250:26:9 Ar:H₂:CH₄, for a 45 minute growth stage, followed by cooling under Ar. In order to deposit this graphene onto substrates for device-fabrication, a modified wet transfer technique was developed, similar in basic principle to that shown in section 5.1. Significant optimisation was necessary in order to minimise unwanted physical and electronic characteristics induced in the final film by the transfer process, notably, contamination by residual polymer, cracks or tears, wrinkles and unusually high electrostatic doping of the film. In order to assess the relative significance of different aspects of the process, a number of key variables were investigated: the type of polymer used for the support scaffold [Poly(bisphenol A carbonate) (PC) and PMMA], the composition of the Cu-etchant solution [Marbles reagent (50ml:50ml:10g H₂O:HCl:CuSO₄) and aqueous ammonium persulfate] the use of rinsing and cleaning steps in between the etch stage and final deposition, the use of surface treatment

of the target substrate (using oxygen-plasma), and heating of the polymer-graphene film after transfer (varying the temperature and duration).

In the final process that I established, PC (Sigma Aldrich) solution is prepared by dissolution in chloroform at 1.5 weight % by volume, before spin-coating onto the growth side of the Cu foil at 3000 rpm for 40 s. O₂ plasma treatment (30 seconds, 100 W, 0.6 mbar) is then used to etch the poor quality graphene from the back side of the foil, to prevent it attaching to the main graphene sheet post-removal of the Cu. The foil is then flattened and cut into sections of desired size for the target substrate, before floating onto an etchant bath of aqueous ammonium persulfate (APS) (Sigma Aldrich), concentration 1.2 weight % by volume. As soon as the Cu is completely etched - typically 7-8 hours - a glass slide is used to 'fish' the graphene-PC film from the solution, by moving it toward the film in a vertical orientation, simultaneously lifting upward out of the bath. The film is then floated onto a bath of deionised (DI) water for 10 minutes, before being fished and floated onto another DI bath a second time, to thoroughly rinse away the etchant solution.

The target substrate - Si:SiO₂ used for characterisation - is O₂-plasma-treated (Diener Femto plasma system, 10s, 100W, 0.6 mbar) to increase the wetting of the surface, which has proved essential for preventing macroscopic wrinkling of the film. However, longer treatment durations prevent the film adhering to the substrate at all. The graphene-PC film is then fished out with the substrate, before being left to dry vertically at room temperature for over 12 hours. The substrate is then heated on a hot-plate at 50°C for 10 minutes to drive off any trapped water, before raising the temperature to 200°C for 5 minutes. This second stage is included to soften the PC film, ensuring the graphene is allowed to conform to the substrate beneath. This is crucial to promoting adhesion at the SiO₂-graphene interface and significantly reduces the generation of cracks and tears in the film during removal of the polymer scaffold and in later fabrication/patterning. Finally, the polymer scaffold is removed by dissolution in chloroform for 2 hours, followed by degreasing in acetone, then isopropyl alcohol (IPA) and dried with N₂.

Optical and physical characterisation of deposited films was carried out to analyse the effects of varying different parameters in the transfer process. Optical microscopy was used for initial assessment, to examine the graphene sheet on the micrometer scale, for larger cracks, tears and wrinkles, as well as significant contamination by polymer residues. AFM was then employed for further, more detailed analysis of surface contaminants and the physical integrity of the film, able to reveal wrinkles, tears and residual polymer at dimensions and contrast that cannot be resolved using optical microscopy. This imaging was carried out using the same system and imaging mode as in previous chapters (Bruker Dimension Icon

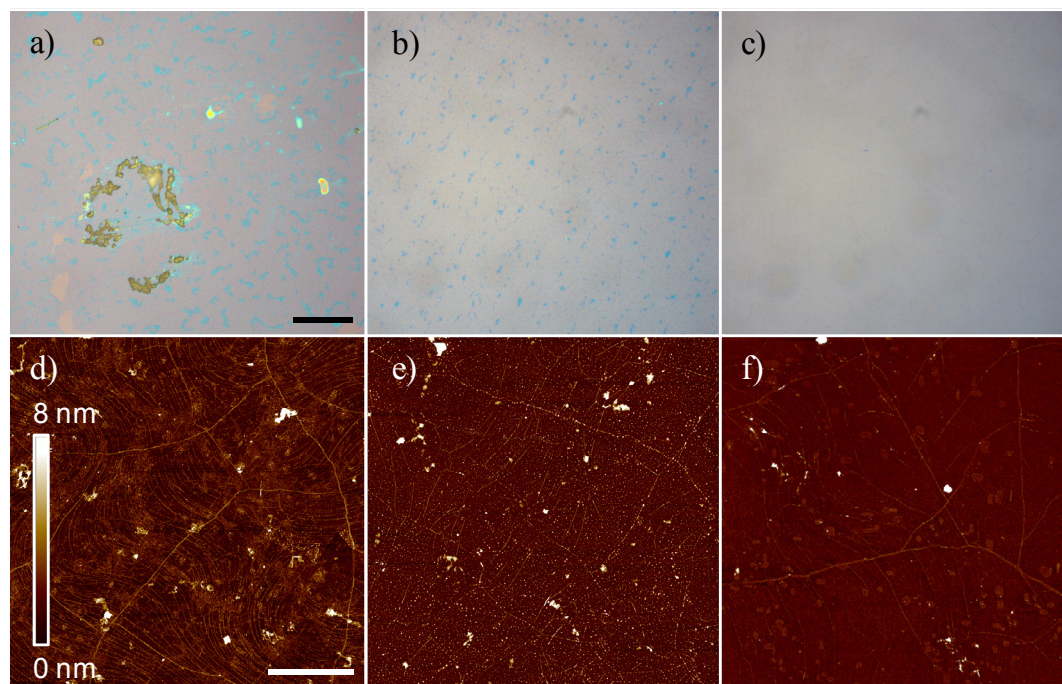


Fig. 7.1 Transferred CVD graphene characterisation. Representative optical images of CVD graphene films transferred from Cu to silicon using (a) a PC scaffold with marbles reagent etchant, showing significant ~ 10 micron-scale contamination and tears (scale bar = $40 \mu\text{m}$), (b) a PMMA scaffold and APS etchant, showing higher structural integrity, but still with dense coverage of smaller, particulate polymer residues (scale bar = $20 \mu\text{m}$) and (c) a PC scaffold and APS etchant, showing negligible contamination *via* optical scan (scale bar = $40 \mu\text{m}$). Figures (d), (e) and (f) are AFM scans corresponding to typical films transferred using the same methods as the optical scans above each respective image (though not taken from the same sample area). All AFM scale bars are $5 \mu\text{m}$.

AFM, with a silicon nitride tip, operating in ScanAsystTM mode, an automated, peak-force tapping-mode).

This analysis of the physical properties of the films can be seen in typical optical and AFM images of CVD graphene sheets, transferred using different processes, in Fig. 7.1. With respect to the presence of contaminants, in the form of residual polymer, the two most dominant factors are the etchant and polymer scaffold material used. Using marbles reagent to remove the Cu results in films with significant, micron-scale patches of residual polymer, as well as a larger quantity of cracks and tears, as can be seen in Figs. 7.1a and 7.1d, regardless of the polymer used. This would suggest that the etchant can cause chemical modification of the scaffold, making it tougher to remove. With regards to the polymer scaffold, optical and AFM analysis revealed that use of a PC layer facilitates a far cleaner transfer over PMMA, as can be seen through comparison of Figs. 7.1b and 7.1e (PMMA) with 7.1c and 7.1f (PC). The physical quality of these films, through comparison with other

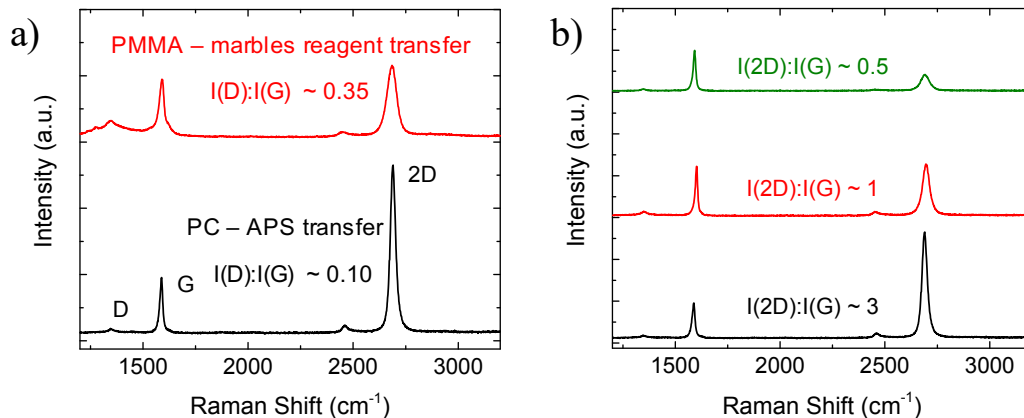


Fig. 7.2 **Raman spectroscopy of transferred CVD graphene.** (a) Raman spectra representative of a graphene film transferred using APS etchant and a PC scaffold (black) and a heavily contaminated sample, transferred using a marbles reagent etchant and PMMA scaffold (red), normalised to intensity of the G peak. (b) Raman spectra of graphene films exposed to a cleaning solution (DI-water, H₂O₂ and HCl, mixed in a ratio of 20:1:1) during transfer, showing significant electrostatic doping, with a typical (red) and extreme case (green), in comparison to that transferred without this step (black). 2D to G intensity ratios are noted for each spectrum.

AFM images in the literature^[227,231], is typical of CVD-graphene transferred using wet processes.

Finally, Raman spectroscopy was used in order to characterise transferred films with respect to the introduction of defects or any chemical modification induced in the graphene lattice during the transfer process, as well as to provide information relating to the electrostatic doping of the sample, as introduced in chapter 2, and well detailed in the literature^[108]. These measurements are carried out using a Renishaw InVia microspectrometer system, at an excitation wavelength of 514 nm from an Ar⁺-ion laser. Spectra are acquired at room temperature in a backscattering geometry, with a spot size of $\sim 1 \mu\text{m}^2$ and laser power of $\sim 0.05\text{mW}$ to avoid damaging the sample.

A comparison of representative Raman spectra for both heavily contaminated and clean graphene films transferred using initial and optimised processes respectively, can be seen in Fig. 7.2a. The spectra corresponding to the optimised transfer is typical of high quality, post-transfer CVD graphene in the literature,^[77,83] usually with a very low ($I(\text{D})/I(\text{G}) < 0.15$) or negligible D-peak; the feature which is most sensitive to defects in the graphene lattice and external contaminants^[108]. This is in contrast to typical, heavily contaminated samples, where broad D-peaks of significant intensity are observed, with $I(\text{D})/I(\text{G}) \sim 0.3$ or above.

A notable finding revealed from the Raman analysis is that the inclusion of a cleaning stage after the first DI-water rinsing step - whereby the graphene-polymer film is floated onto a bath of DI-water, hydrogen peroxide and hydrochloric acid, mixed in a ratio of 20:1:1

- has a significant impact on the electrostatic doping of the final film. The $I(2D)/I(G)$ ratio in graphene Raman spectra can be used to probe the concentration of dopants in the sheet^[108]. Neutral and lowly-doped samples typically have $I(2D)/I(G) \sim 2 - 3.3$, however heavily doped films will have ratios down between 1.5 - 0.5^[105]. This is due to suppression of the 2D peak, on filling of the conduction band at energies above that of the exciting radiation^[108]. Typical $I(2D)/I(G)$ values are between 0.5 and 1.5 for graphene transferred with an additional cleaning stage (as can be seen in the representative spectra in figure 7.2b), indicative of significant doping induced by species deriving from the HCl or H₂O₂ in the cleaning solution.

7.1.2 Graphene-top-coated embedded nanowires

As an initial step toward constructing a hybrid device system, the electronic properties of CVD graphene transferred onto etched SU-8 were first assessed. As can be seen in profiles of etched SU-8 and Parylene-C in the previous chapter, etching by RIE is inhomogeneous and causes a notable increase in the layer's surface roughness. Therefore, it was feared this would be significantly detrimental to electronic transport in the graphene layer, which is highly sensitive to the interfaces it forms with other materials, as discussed in chapter 2. It was also necessary to determine whether the graphene would adhere sufficiently to this rough SU-8 layer, or if it would become detached or torn during resist removal after the two lithographic patterning steps required (etching graphene and depositing contacts) - this is seen even on Si:SiO₂ when, for instance, unsuitable photoresists or development / lift-off solvents are used.

After transfer using the technique developed in the previous section, a mask was patterned by EBL in a PMMA resist, before development to expose the sections which are to be etched, as shown in Fig. 7.3a. A 5 μm wide channel was left covered by PMMA whilst regions for metal contact pads to be deposited are established, removing the graphene in these areas such that they do not short. The same O₂ plasma etch as used in the previous section (to remove graphene from the back-side of Cu foil) was then applied to remove the exposed graphene. A second lithography step was then carried out to pattern and deposit contacts onto the graphene channel. After development, but before metallisation, the layer was bombarded with a very low power Ar plasma (Moorfield nanoetch RIE, 0.5 W, 20 s, 7.5×10^{-3} mbar) to create defects in the graphene layer under the electrode, which has been shown to lower the contact resistance^[335]. Sputter-coating was then used to deposit Ni:Al contacts at a thickness of 15:105 nm (Fig. 7.3b), as following a recipe used in reference 336. Lift-off of these layers in acetone proved problematic and requires further optimisation, failing in cases of electrodes with narrow separations, as can be seen in the inset of Fig. 7.3b. The

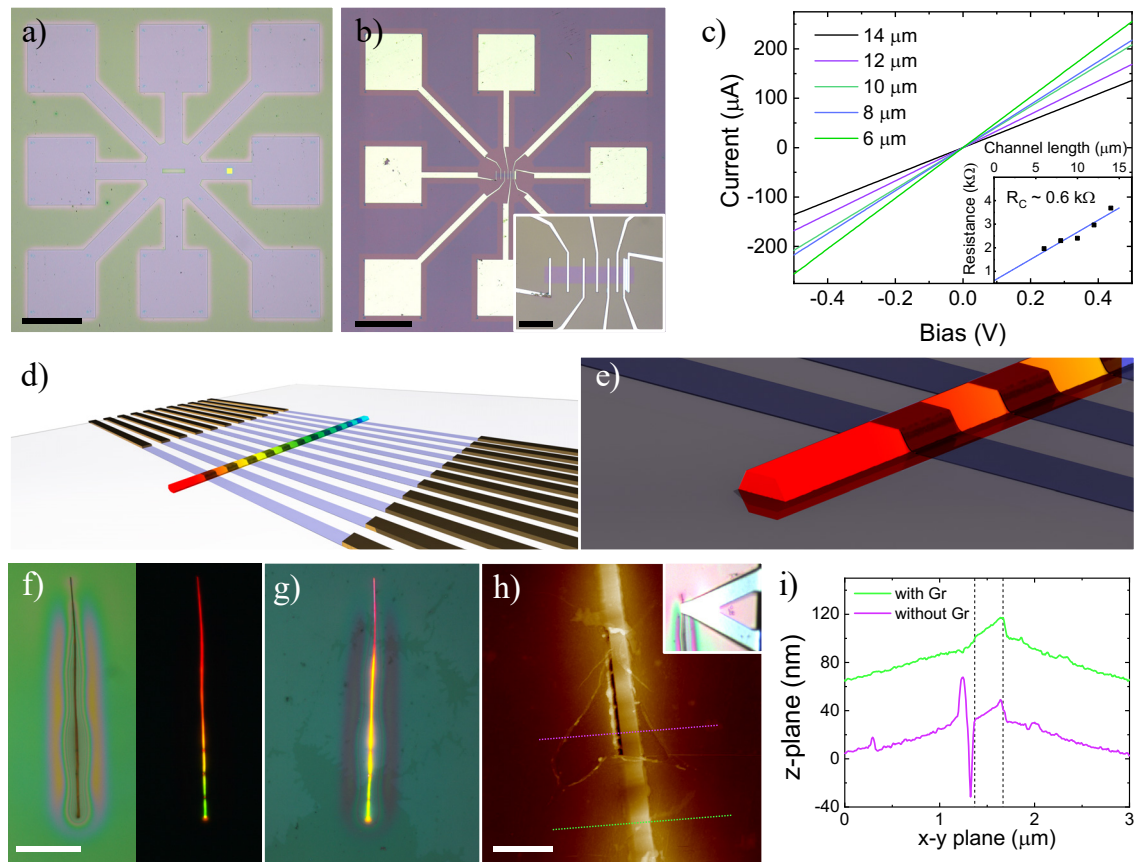


Fig. 7.3 Toward a graphene-nanowire hybrid device platform. (a)-(c) Initial electronic testing of graphene channels on etched SU-8. a) After transfer of graphene, a PMMA mask for graphene patterning is written by EBL and developed - purple area is exposed graphene on SU-8, green is PMMA. Scale bar is $200 \mu\text{m}$. (b) After plasma etching of graphene and removal of the PMMA mask, Ni:Al contacts are deposited along the graphene channel. with increasing separation. Note lift-off has failed on the last electrode pair. Inset shows a zoomed image of the graphene channel. Scale bars are $200 \mu\text{m}$ and $20 \mu\text{m}$. c) Electronic characterisation between each working electrode pair of the image in b) - inset shows measurement of the contact resistance ($R_C \approx 600 \Omega$) by the transmission line method. (d)-(e) Schematic of a potential final device with graphene channels running perpendicularly across the nanowire, so as to achieve wavelength-dependent photogating of each channel. (f)-(i) Graphene/embedded-nanowire hybrid structure, before patterning. f) Optical images under white (left) and UV (right) illumination of the initial nanowire first encased in ALD and then embedded in SU-8. g) After etching to reveal the nanowire top surface, a discontinuous graphene film is transferred, visible here under UV illumination. Scale bar in all optical images is $40 \mu\text{m}$. h) AFM height profile imaging of the graphene on nanowire structure, featuring a tear in the film so areas with and without graphene can be measured - inset shows the AFM cantilever and area of the nanowire being scanned. Scale bar is $1 \mu\text{m}$. i) Cross-sections corresponding to the like-coloured dashed lines in h).

electrodes deposited in these test devices were arranged so as to assess both the resistance of the channel as well as the resistance of the contacts, using the transmission line method

(TLM). Electrodes are positioned at increasing separation (4 to 14 μm , in increments of 2 μm) along the graphene channel, and measured using a probe-station, as shown in Fig. 7.3c. By TLM, contact resistance was read from the y-intercept at around $\sim 600 \Omega$, which is comparable with that seen for top-contacted devices in ref. 336. Resistances for the same channel lengths and widths are actually around $5\times$ lower than seen in ref. 336 ($\sim 2.3 \text{ k}\Omega$ vs 11 $\text{k}\Omega$ for a 6 μm long and 5 μm wide channel). One potential reason for this is that the graphene in the channel is of higher quality, with fewer grain boundaries than that in ref. 336. Given that the CVD processes developed by the Hofmann group are capable of grain sizes of around 50 - 100 μm , it is probable that there are no grain boundaries whatsoever in such a small channel. However, this does suggest that placement and fabrication on top of a rough SU-8 substrate does not dramatically impede charge transport. Transport characteristics, measured through back-gated FETs, would be required for a more in-depth comparison of the mobility in these films with those in the literature, or control samples, on Si:SiO₂ substrates.

Once the viability of graphene interfaced onto SU-8 was established, a design for a device was produced, a schematic of which can be seen in Figs. 7.3d and e. This involved transferring graphene onto the top-face of an embedded nanowire structure, before patterning of channels and deposition of contacts. The concept behind this design was that during illumination, the graphene channels would undergo wavelength-dependent photogating - changes in electrostatic doping of the graphene layer - depending on their location along the nanowire and corresponding to photoexcitation of carriers in the particular semiconductor material beneath. Due to graphene's sensitivity, photogating architectures can produce ultrahigh photogain, as detailed in chapter 2, and demonstrated in particular in ref. 48 - which could be far higher than simply depositing metal electrodes alone onto the nanowire.

Alumina-encased CdS_xSe_{1-x} nanowires were embedded in SU-8, as detailed in section 6.2.3. The top surfaces of the nanowires were revealed by N₂ plasma and AZ726 etches, before a layer of CVD graphene was transferred over the top, using the PC-based method detailed in the previous section. The time used for post-transfer dissolution of the PC layer in chloroform was kept to only 15 minutes, due to concern about the aforementioned sensitivity of the nanowire to solvents. However, perhaps through protection from both the embedding and graphene layers, intensity of photoluminescent emission was retained, as shown in the images of a typical structure before and after graphene transfer in Figs. 7.3f and g. As can be observed in the sample in Fig. 7.3g, a discontinuous graphene film was used for some nanowires (where growth has been terminated such that grains have not merged together), to allow comparative imaging of those areas covered by graphene or not. A scan of the graphene-nanowire hybrid structure from Figs. 7.3f and g, post-transfer but pre-patterning, is shown in Fig. 7.3h. Here, the trench adjacent to the nanowire formed from the etching of the

ALD layer (see section 6.2.3) demonstrates where the wire is covered in graphene - as can be seen from the height profile where the trench is covered and not covered. This imaging demonstrated that graphene was robust enough to reliably coat these embedded nanowire structures without tearing or structural damage at the top face of the nanowire.

The lift-off in this batch of devices failed due to an unforeseen problem with the EBL system, and due to time constraints, no further batches could be fabricated. As such, no observation of photogating in these structures was possible, though the device platform has been developed to the stage where fabrication should now be straightforward. Proposals for further work in this area are detailed in the final chapter of this thesis.

7.2 Multi-electrode CdS_xSe_{1-x} nanowire device design and development

7.2.1 Device architecture and lithography dose testing

From references 322 and 327, it was clear that for a multielectrode nanowire device to function as a spectrometer, as much varied spectral data as possible should be gathered at the response function calibration stage, that is, n , the number of electrode pairs, needs to be ‘sufficiently’ high. At the outset of the investigation, it was unknown what a ‘sufficient’ n - or in other words, the minimum number of units - would be to produce a spectral reconstruction with a viable level of accuracy for potential commercial application. As such, I sought initially to create a multielectrode device with the maximum number of photodetector units that could be fabricated and measured within the practical constraints of the methods and equipment available to us. The primary considerations in this respect were how to measure a large number of electrode units in a workable timeframe and at what resolution and thus spatial density an array could be deposited through EBL, given the issues with lift-off discussed in the previous section.

Addressing the first of these points, it was decided that if each electrode pair had to be measured using a probe-station - where contact tips must be moved and landed onto a new electrode for each measurement - the measurement time would be far too long to make efficient progress in testing the device. Therefore, a device architecture was designed to allow wire-bonding to a chip carrier for integration into a PCB-based setup (although probe station measurements were still also used for initial characterisations). After patterning of the EBL alignment and locational markers onto the device substrate (as described in the previous chapter), $0.3 \times 0.3 \text{ mm}^2$ pads (large enough to allow easier wire-bonding) were also deposited around the perimeter of the substrate, as shown in the CAD schematic in Fig.

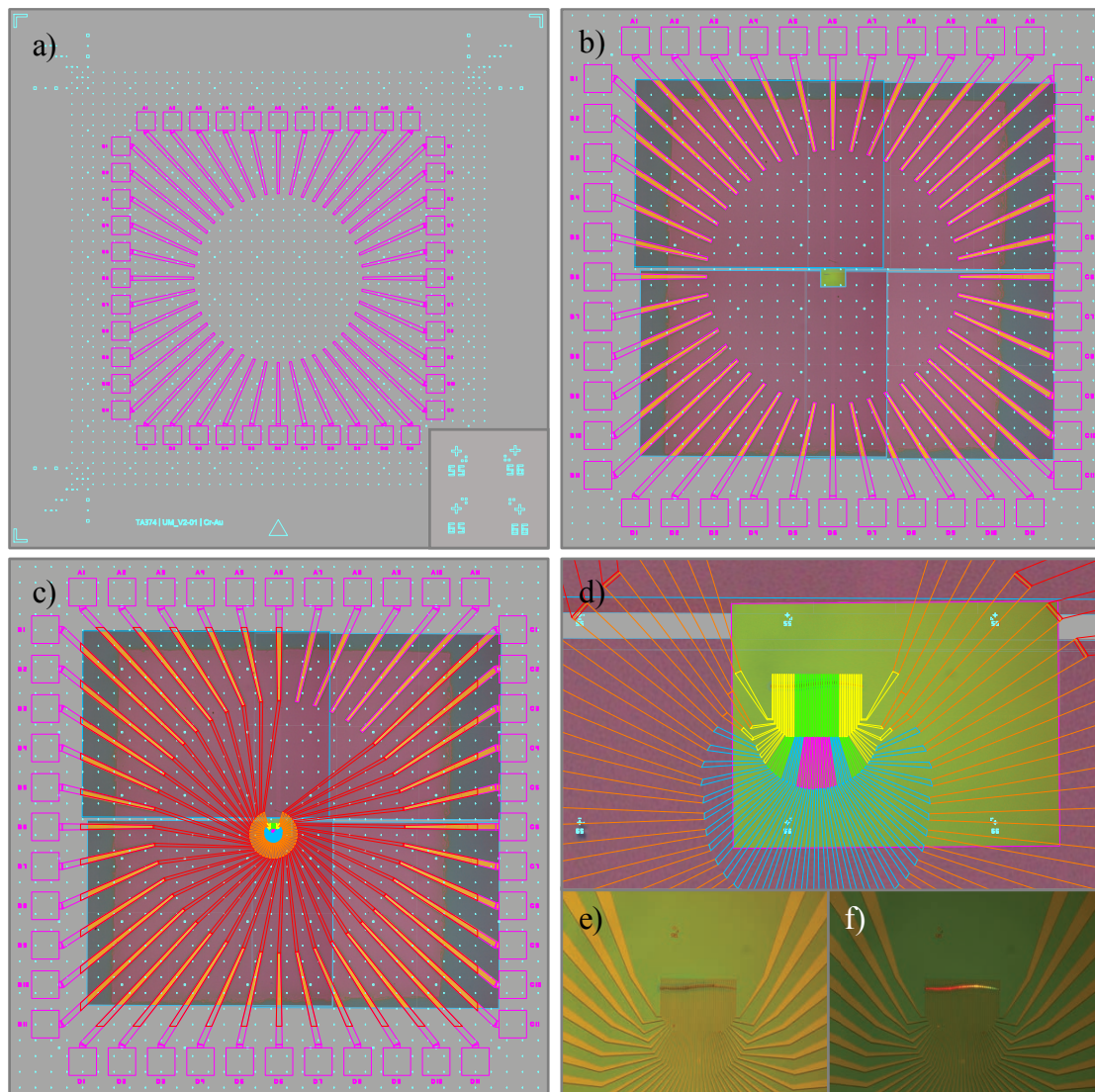


Fig. 7.4 Multielectrode device layout and fabrication stages. (a) CAD design of the initial $10 \times 10 \text{ mm}^2$ device substrate, before nanowire transfer, showing EBL alignment (corner sections) and locational (central grid) markers (blue) and pre-patterned wire-bonding pads (purple). Inset shows a zoom on four different adjacent locational markers, with the space in-between removed. (b) CAD design with overlaid optical microscope images, aligned to the locational markers, showing a substrate with a nanowire transferred to the centre, subsequently coated in SU-8 which has been patterned to a $4.5 \times 4.5 \mu\text{m}^2$ square, leaving the pads and alignment markers uncovered. (c) CAD design of EBL patterning for the device electrode deposition stage - colours show sections with different EBL doses applied. Note electrodes (red) extend over the SU-8 region so as to make contact with the wire-bonding pads (purple). (d) A zoomed in section of c), showing the fine-detail of the electrode array design as it converges to contact the nanowire. Distance between locational markers (blue) is $200 \mu\text{m}$. (e)-(f) Optical images of the final device after deposition of Cr:Au electrodes, under white-light (e) and UV (f) illumination.

7.4a. This was pre-patterned onto batches of device chips before any nanowire transfer, as the feature sizes are so large that to write them into PMMA by EBL, in the same step as the fine features at the nanowire interface, would take many hours per chip.

Ordinarily, photolithography would provide satisfactory resolution for this task. However, to avoid expenditure on production of a photolithography mask, a different EBL recipe was used, detailed in ref. 337. This process uses UV1116 (50% dilute) photoresist to allow around 20× lower exposure doses, and thus 20× faster write-time, than PMMA, enabling a batch of 15 chips to be patterned in around an hour. Ti:Au gold contacts were evaporated at a high thickness (10:180 nm), to make them more robust for wire-bonding. Here, a maximum number of 44 pads (and thus a maximum n) was dictated by the chip carriers available, which were 44 pin (11 on each side) arrangements. We did not reach the stage in this study where a greater number of electrodes warranted testing, though this would be straightforward to achieve in this respect, simply requiring a chip carrier with more pins, and possibly a larger substrate to allow more pads.

From this stage onward nanowires were transferred to the substrate as described in the previous chapter. For embedded devices, after measurement of the nanowire height (and in the case of alumina-encapsulated devices, after ALD), SU-8 was then spin-coated at a thickness less than this. The SU-8 was then patterned into a square with sides measuring ~4.5 mm (Fig. 7.4b) using the MJB-4 mask aligner (section 6.2.2), to leave the central region around the nanowire coated, but the pads and the alignment markers exposed for wire-bonding and further EBL steps respectively. A pattern was then drawn in AutoCAD and patterned by a second EBL step, to connect the pre-deposited wire-bonding pads with an electrode array on top of the nanowire (Figs. 7.4c and d) before metallization to leave the final device (Figs. 7.4e and f). Given the lengths of the nanowires (~50 - 150 μm), to fabricate up to the maximum number of electrodes allowed by the chip carriers (44) required an array pitch of ~1 - 3 μm, and thus, electrode widths and spacings down to ~500 nm. At these length-scales, it is impossible to assess the progression of development in the electrodes by optical microscope and early device fabrication attempts, using EBL dose recipes developed by others within the department of engineering, resulted in unsuccessful or very lengthy (>4 hour) lift-off. As such, methods of 'dose testing' were investigated, to ascertain the appropriate EBL doses for a particular feature size.

Initial dose testing involved assessing the resist sidewall profile for varied channel widths and separation using different resists (PMMA 495 A4 and A8, 950 A4 and A8), developers (MIBK:IPA 1:3, DI:IPA 7:3) and development conditions (at room temperature and in an ice bath). This was done by writing and developing channels in the resist across the length of a Si:SiO₂, before cleaving it perpendicular to the channels and placing it vertically at a 90°

orientation to the SEM stage. Typical SEM images of this process can be seen in Fig. 7.5a-c. For the same resist and development conditions, it can be seen that under-exposure (Fig. 7.5a) results in a positively sloped resist sidewall at the channel, whilst optimal exposure (Fig. 7.5b) produces a slightly negative sidewall (due to spreading of the electron beam as it enters the resist). The former will result in metal coating the sidewalls as well as the substrate beneath, producing a continuous metal film with no location for solvent to penetrate. In the latter case, the negative profile ensures that for anisotropic evaporation methods, metal is not deposited onto the sidewall and as such solvent can penetrate into the resist layer to enable lift-off. The case shown in Fig. 7.5c illustrates the proximity effect as these channels are brought closer together - the channels in this image were written to have equal width and spacing, but it can be seen that the spacing is far narrower. Electrons delivered to each feature are scattered to those nearby, resulting in over-exposure and thus widening of each channel. Given the photocurrent is dependent on the area of nanowire exposed, it is important to have fine control of electrode pair separation, even without consideration of the ease of lift-off.

Whilst such imaging was informative in and of itself, imaging of the sidewalls alone was not sufficient to predict the doses for which patterns would lift-off most efficiently; sidewalls with similar profiles would often produce quite different results after metallisation. Furthermore, the electron beam in the SEM would actually tend to 'melt' the resist, allowing only a relatively short window to capture images. A far more robust method of dose testing was therefore devised, whereby a dummy run of the entire electrode deposition process, including patterning and metallisation, was carried out and the final features assessed by SEM, rather than assessing the resist at an interim stage. In this method, a 5×5 grid with repeated units of the desired multi-electrode array design would be patterned on the dummy chip with an incrementally increasing exposure dose along each row of the grid in a serpentine pattern. In this way, 25 different doses are tested for the same device pattern, with a fixed resist (most commonly PMMA 950 A8), development conditions (most commonly room temperature, 1 minute, 3:7 deionised water:IPA mixture), and lift-off conditions (10 minutes, acetone, light agitation by syringe) to assess the optimal exposure dose. In the dummy chips, all other conditions are also kept the same as those intended for the actual device - for instance, the presence of an SU-8 embedding layer or the use of a plasma etch or contact treatment step - so as to control for these factors.

Optical microscope and SEM imaging of this dose testing methodology is shown in Figs. 7.5d-l. It should be noted here that another consideration is the proximity effect, which means that the features in the most densely packed regions of the array (i.e. the centre) are most liable to become over-exposed (as can be seen in Figs. 7.5f and h). As such, design of the pattern must make adjustments to compensate for this, applying different doses to those

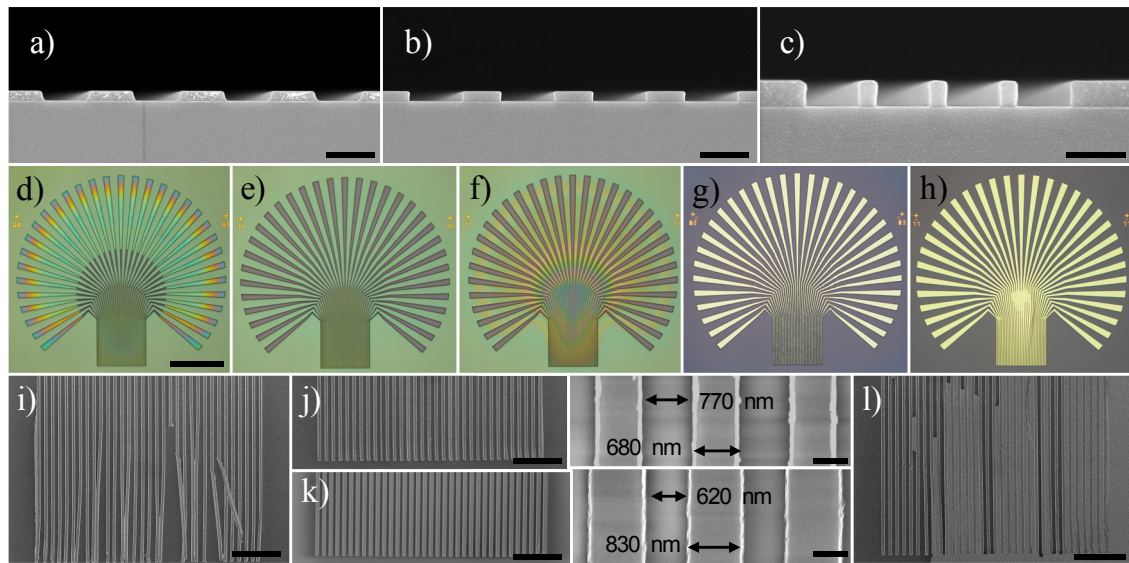


Fig. 7.5 EBL dose testing for the electrode array. (a)-(c) Cross-sectional SEM imaging of channels patterned by EBL into a 300 nm thick PMMA film demonstrating the side-wall profile in under-exposed (a) and optimally exposed channels (b), as well as the proximity effect as channels are patterned with lower separation: the channels in c) were written to be the same width as the separation. Scale bars are 1 μm (a and b) and 500 nm (c). (d)-(f) Optical microscope imaging of EBL-patterned PMMA (950 A8, spun at 4k rpm onto Si:SiO₂) films after the same development conditions (1 min, 3:7 deionised water:IPA), written with doses of 40 $\mu\text{C cm}^{-2}$ (d), 60 $\mu\text{C cm}^{-2}$ (e), 60 $\mu\text{C cm}^{-2}$ (f), resulting in under-exposure, optimal exposure and over-exposure respectively. (g)-(h) Metallisation and lift-off for the patterned films in e) and f), respectively. Scale bar for d)-h) shown in d), is 100 μm . (i)-(l) SEM imaging for metallized/lifted-off electrode arrays patterned with different exposure doses under the same resist and development conditions as in d)-h), showing those produced after under-exposure i), with optimal exposure j), slight over-exposure k), and significant over-exposure l). Right hand panels of j) and k) show magnified sections of the left-hand panels. All scale bars for all main images are 10 μm , and 500 nm for magnified images.

regions, as can be seen in the CAD schematic in Fig. 7.4d, where the colour of the region indicates the application of different doses. As a result of this dose testing process, it was possible to fabricate arrays of up to the maximum of 44 electrodes allowed by the chip carrier, with a width and spacing down to 400 nm with both thermally evaporated, electron-beam evaporated and sputtered metal layers, within the required lift-off timeframe of < 20 minutes.

7.2.2 Preliminary device measurements

Initial electronic characterisation of these multi-electrode arrays was carried out using a probe-station (Cascade Microtech coupled with an Agilent Technologies sourcemeter and analyser) equipped with three probe tips. As a rough, preliminary test of the photoresponse of these devices, measurements were made in the dark and under illumination by the probe-

station (white LED) lamp. The lamp was measured using a conventional microspectrometer and power-meter (Thorlabs) to have an intensity at the substrate of $\sim 400 \mu\text{W cm}^{-2}$, and an even emission spectrum across the nanowire response range, with a slight, broad peak in the $\sim 600 \text{ nm}$ region. Figure 7.6a shows typical results of this characterisation, as measured for electrode pairings on bare $\text{CdS}_x\text{Se}_{1-x}$ nanowires with Cr:Au contacts deposited, without any extra processing steps. The behaviour of these devices varies considerably regardless of the positioning of these electrodes along the nanowire (though the *magnitude* of the photocurrent varies, as will be discussed later). I-V curves characteristic of the formation of back-to-back Ohmic contacts, back-to-back Schottky barrier contacts, and electrode pairings Schottky-barrier contacts were all observed. The unpredictable nature of nanowire contacts is well reported in the literature, as detailed in section 5.2. Also introduced in chapter 5, treatment of the contact interface after lithography and development, immediately prior to metallisation, was investigated to try to devise a process that produced uniform characteristics across a typical sample of nanowire devices. Experimentation with the contact material was also carried out, to assess the effects of different work functions. A variety of different treatments were tested, including HCl acid etch, O_2 plasma as well as a range of electrode materials, including Ti, W, ITO (Indium tin oxide), Al and In.

Here, the most significant results were gathered through use of a N_2 plasma exposure (Moorfield nanoetch RIE, 5 W, 120 s, 7.5×10^{-3} mbar) and soaking samples in an ammonium sulfide $(\text{NH}_4)_2\text{S}$ (1:10 solution diluted in deionised water) etch for 10 minutes at 40°C , pre-contact deposition. Corresponding I-V curves are shown in Figs. 7.6b-d. These treatments, coupled with Cr:Au (similar results were also achieved using In:Au) electrodes deposited by electron-beam evaporation, produced contacts with ohmic behaviour in around 70% of photodetector units. The magnitude of photocurrent seen using the surface treatments was usually over 2 - 3 \times higher than those without, indicating a reduced contact resistance. Meanwhile, use of sputtered Ni electrodes saw more reliable production of Schottky barrier behaviour in measured I-V curves.

However, though some degree of control was attained here, fabrication of devices exhibiting a consistently predictable contact behaviour was not achieved. A far more thorough analysis, controlling for factors such as the precise nanowire composition, morphology would be required to elucidate the interfacial chemistry in a quantitative manner and inform further optimisation. Kelvin probe force microscopy (KPFM) was carried out to try and characterise the work function of the nanowire surface to match with that of the contact metal, but no conclusive results were gathered; data were inconsistent from sample to sample despite similar PL emission indicating like compositions. Due to time constraints on the project, once stable contacts with sufficiently high signal to noise ratios had been achieved using these

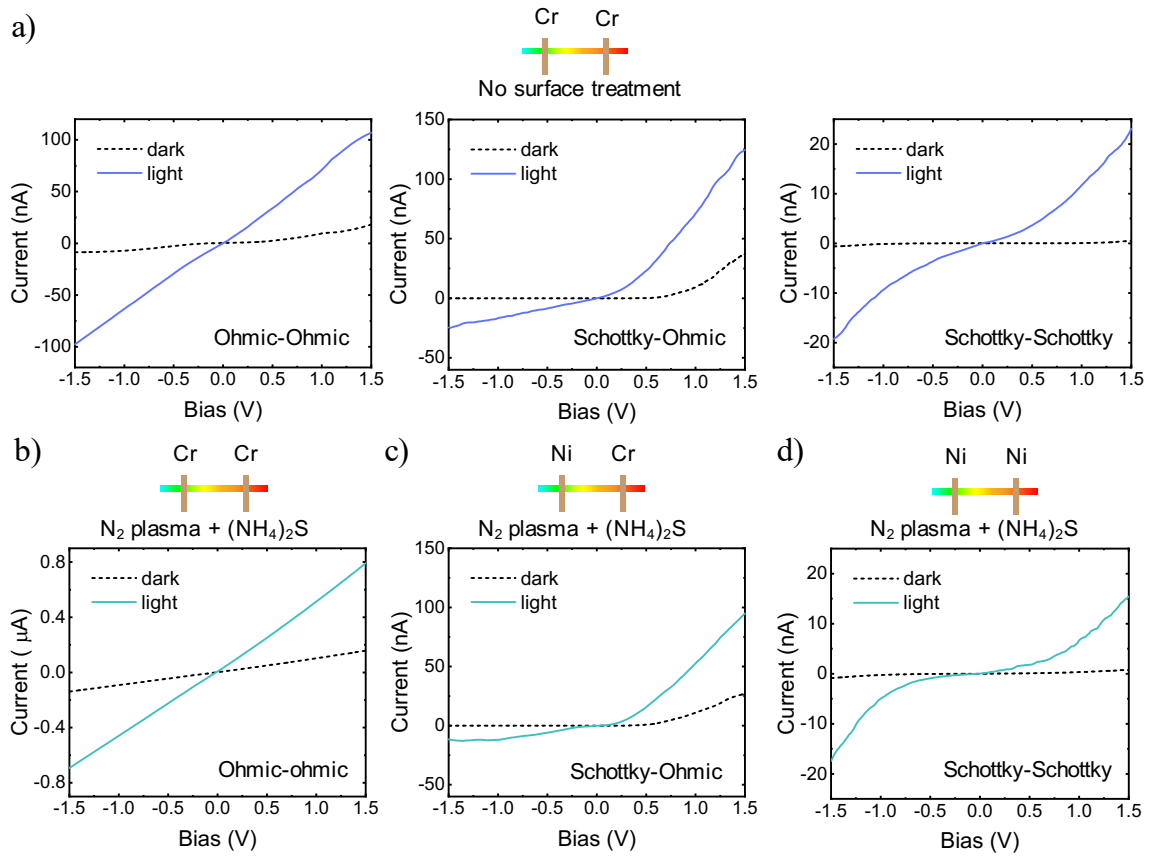


Fig. 7.6 Varying the conditions at the contact interface. I-V curves measured by probe-station, of a bias between electrode pairs deposited onto $\text{CdS}_x\text{Se}_{1-x}$ nanowires using different metals and surface treatments. Electrodes and channel widths maintained as constant. **(a)** A range of different behaviours all seen for Cr:Cr contacts without any surface treatment, representative of systems whereby two Ohmic contacts (left), one Schottky-barrier and one Ohmic (middle) and two Schottky-barrier contacts (right) have formed, respectively. **(b)-(d)** Behaviours commonly observed when depositing combinations of (sputtered) Ni and (electron-beam evaporated) Cr:Cr electrodes, immediately after treating the contact interface with nitrogen plasma and an ammonium sulfide $(\text{NH}_4)_2\text{S}$ (1:10 solution diluted in deionised water) etch for 10 minutes at 40°C .

treatments, no further optimisation was carried out with respect to controlling the contact behaviour.

Field effect measurements were also made to assess the transport characteristics for photodetector units at different positions along the length of these nanowires. This was carried out by directly contacting the Si base of the $\text{Si}:\text{SiO}_2$ substrate with a third probe tip to allow application of a backgate bias. For a fixed electrode width and spacing (typically each around $1 \mu\text{m}$), the magnitude of photocurrent measured along these nanowires was seen to increase significantly from the CdS to the CdSe end, ranging from 10s of nA, to on the order of $\sim 1 - 5 \mu\text{A}$ respectively for a source-drain bias of 500 mV, corresponding to channel

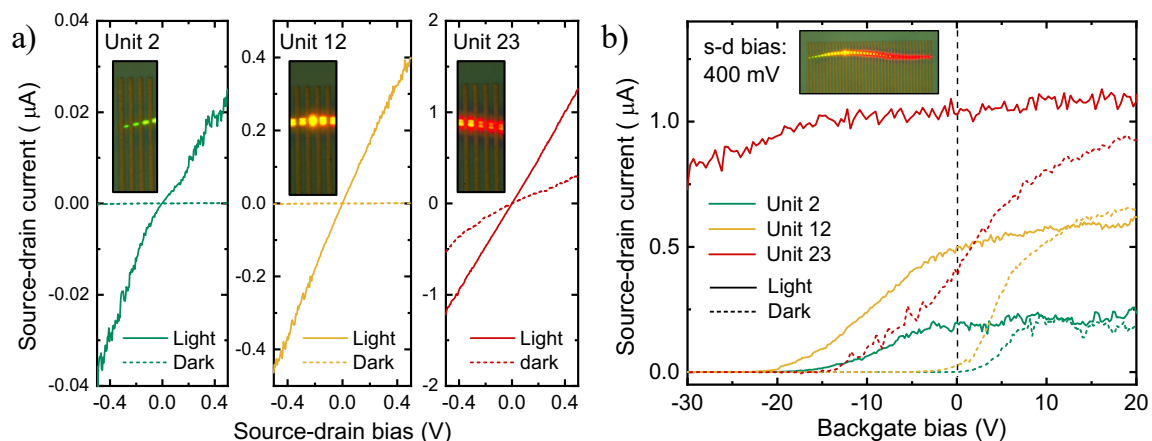


Fig. 7.7 **FET transport characteristics along the length of a $\text{CdS}_x\text{Se}_{1-x}$ nanowire.** (a) Source-drain current against bias under white (LED) light illumination (solid lines) and in the dark (dashed lines), without any backgate, for three different photodetector units positioned along the multi-electrode nanowire array shown in the inset of b); locations indicated by the inset images - numbering begins from CdS-rich end. (b) Source-drain current as a function of a back gate voltage applied to the Si substrate (300 nm SiO_2 dielectric) for the three units shown in a), under white (LED) illumination (solid lines) and in the dark (dashed lines).

resistances ranging from 50 M Ω to \sim 100 k Ω . This can be seen in the I-V curves in Fig. 7.7a, typical of quasi-Ohmic contacts onto sections with \sim 540, 580 and 600 nm PL emission (left, middle and right respectively).

Trans-characteristics, showing the source-drain current with respect to variable backgate bias can be seen in Fig. 7.7b, for the same device and units as in Fig. 7.7a. These demonstrate typical semiconductor nanowire FET characteristics for each unit, whereby the conduction of the channel can be switched from an I_{on} to an I_{off} state, by shifting the Fermi level through tuning of the backgate bias. As covered in chapter 5, illumination induces photogeneration of electron-hole pairs, increasing the free carrier density, shifting the $I - V_g$ curve in the negative direction, with a corresponding increase in conductivity. However, these results also show that the Fermi level of the channels gradually decreases along the nanowire toward the CdS-rich end, observable in a gradual negative shift of the $I - V_g$ curve, explaining the difference in the photocurrent magnitude along the wire. A possible explanation here is the stepwise band structure seen along the length of the nanowires, due to the gradual decreasing bandgap from the CdSe to CdS ends of the nanowire, as explained in the literature review in chapter 4.

The literature around filter array spectrometers (section 5.3.2) suggests that the magnitude of measurement errors is one of the key factors affecting the accuracy of spectral reconstructions. In this respect, it is crucial to have a high degree of consistency between repeated, like

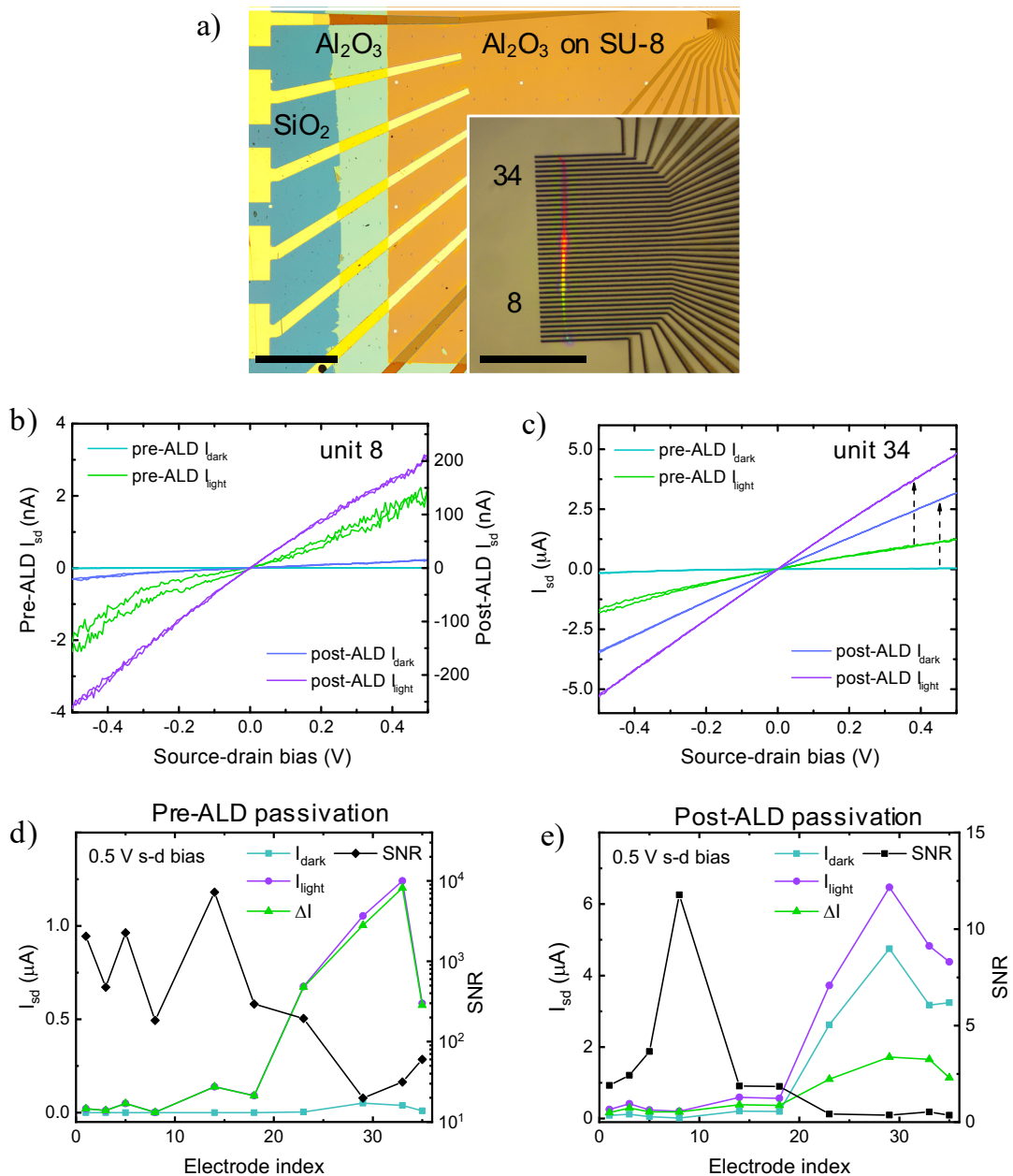


Fig. 7.8 Al_2O_3 passivation of $\text{CdS}_x\text{Se}_{1-x}$ nanowire devices. (a) Optical microscope images at $5\times$ and $50\times$ magnification of the multi-electrode device measured in this figure, showing Al_2O_3 deposited by ALD onto the whole device except the contact pads. Scale bar of main image is $500\ \mu\text{m}$, inset image $50\ \mu\text{m}$. (b)-(c) Source-drain I - V curves for photodetector unit 8 (b) and 34 (c), locations of which are labelled in a), before and after passivation by ALD, under white LED illumination and in the dark. (d)-(e) Dark (teal) and light (white LED illumination, purple) current, photocurrent (green) and signal to noise ratio (black) measured at $500\ \text{mV}$ bias for 10 different photodetectors along the length of the device in a), before (d) and after (e) coating with Al_2O_3 .

measurements (that is, with the same illumination and bias conditions) conducted on the same photodetector unit. Thus, to reduce the sensitivity of the nanowire photodetectors to their environment, passivation by atomic layer deposition (ALD) of Al_2O_3 over the device was investigated. ALD layers were patterned using photolithography such that the SU-8 and nanowire sections are coated but the contact pads were exposed, as shown in Fig. 7.8a.

Figures 7.8b and c demonstrate the effect of this passivation in the I-V characteristics of representative units at the CdS and CdSe end of the nanowire respectively. The current for the same illumination is dramatically increased by this surface passivation, by as much as two orders of magnitude for the CdS end, while more modest enhancement of around 2 to 5 \times is typically seen at the CdSe end. A potential explanation here is that without passivation, (as detailed in chapter 5 of the literature review) adsorbed gases at the bare nanowire surface create a carrier depletion region, restricting transport through the nanowire to a narrower cross-section. However, as can be seen in Figs. 7.8d and e, the signal to noise ratio, defined as $(I_{light} - I_{dark})/I_{dark}$, is dramatically reduced by the passivation - that is, the dark current is much larger relative to the photocurrent. This correlates well with results in the literature for CdS nanowire photoconductors, introduced in chapter 5, which suggest that the photogain in these devices is enhanced, or even primarily mediated through the reversible chemisorption of oxygen at the surface under illumination. The photogain is thus reduced once the devices are passivated.

The stability of the measurements, though, is significantly increased by ALD passivation, as can be observed through the coefficient of variation for photocurrent measurements (Fig. 7.9a), defined as the ratio of the standard deviation to the mean. For a series of ten repeated measurements on the same photodetector unit, the coefficient of variation is reduced from 5% before Al_2O_3 deposition, to 2% after. For the purposes of the spectrometer, the stability of measurement is a more dominant factor in determining the accuracy of spectral reconstruction as introduced in section 5.3.2. Thus this drawback - a reduction in photogain - may be offset.

Final measurements with the probe-station were directed toward assessing an appropriate bias to use for further measurement of the devices, shown in Fig. 7.9b. These demonstrated that for both non-ohmic and ohmic contacts, a bias of around 0.5 V provides a balance between attaining a high photocurrent (to increase the ratio of signal to the system noise level), whilst maintaining a stable device - above this value the coefficient of variation begins to increase significantly, potentially due to thermal effects, owing to joule heating of the channel.

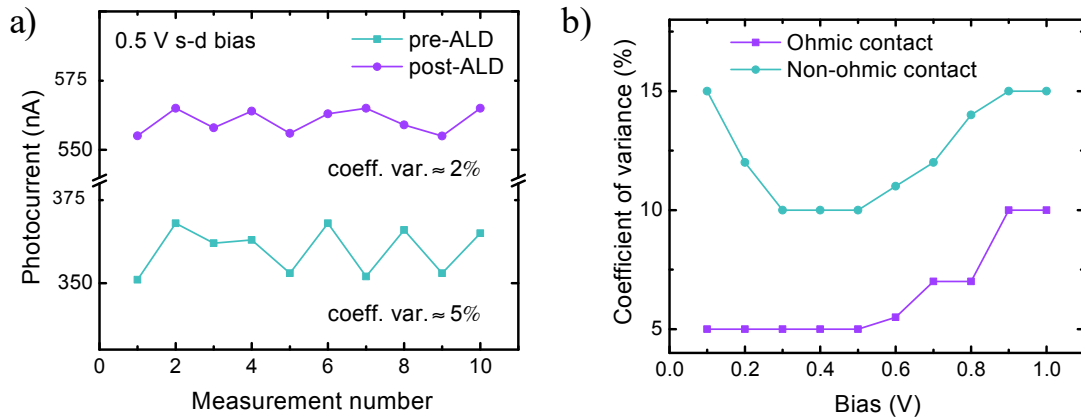


Fig. 7.9 **Effect of ALD passivation and bias on measurement stability.** (a) Photocurrent recorded for 10 repeat measurements of the same photodetector unit at 500 mV source-drain bias, before (teal) and after (purple) ALD passivation, with coefficients of variation for each set labelled. (b) The coefficient of variation seen over 10 repeated photocurrent measurements for ohmically and non-ohmically (where a Schottky barrier is observed) contacted CdS_xSe_{1-x} photodetectors without alumina passivation, denoted by the purple and teal lines respectively.

7.2.3 Optoelectronic characterisation

To carry out more thorough optoelectronic analysis of the multi-electrode devices, a custom setup was constructed to allow both wavelength- and power-dependent photoresponse measurement; this apparatus is shown in fig. 7.10. A Xe-arc lamp was used as the light source, coupled with a programmable grating, allowing wavelength tunability. As this was a lamp rather than a laser-based source, the FWHM of light produced by this setup was ~ 2 nm. An adjustable attenuator allowed variation of the intensity of light, which was focused through a lens into an optical fibre allowing direction and delivery of light to the spectrometer chip. A diffuser at the output end of the fibre ensures a uniform light distribution across the centre of the chip, whilst a motorized power meter was programmed to temporarily intercept the beam path prior to each measurement, to read the total signal power. As touched upon in section 7.2.1, to allow rapid measurement of all electrode pairings in each device, without need for adjustment of electronic connections, contact pads were wire-bonded to a packaged chip carrier. The chip carrier was then inserted into a connection interface coupled to a PCB. This control board, in turn attached to a sourcemeter (Kiethley Instruments) features a series of relays that facilitate the application of a bias, and the reading of a current across each unit, in turn, with a specified time delay. For all measurements the time delay was set as 2 ms, corresponding to the typical rise time of ohmically contacted units (discussed later in this section).

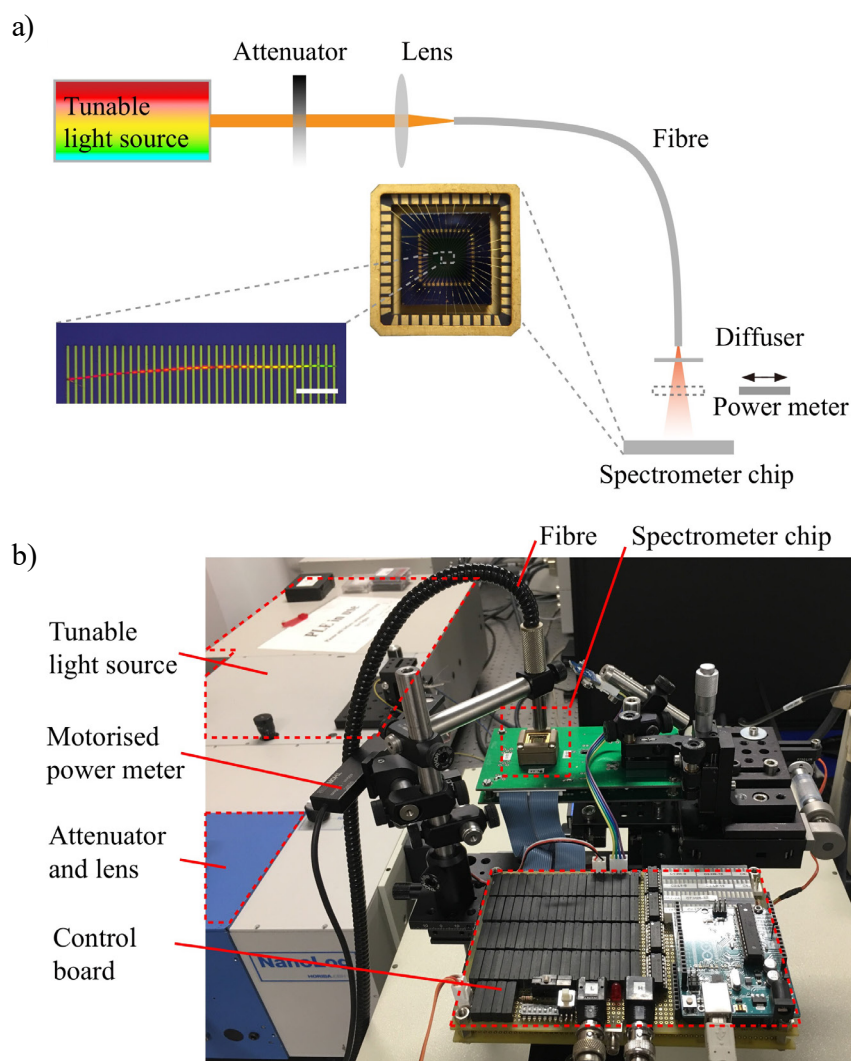


Fig. 7.10 **Multi-electrode optoelectronic characterisation setup.** (a) Schematic of the setup used for all wavelength- and power-dependent optoelectronic measurements, illustrating how light is directed onto a packaged chip to which the multi-electrode $\text{CdS}_x\text{Se}_{1-x}$ nanowire device substrate is wire-bonded. The tunable light source is based around a Xe-arc lamp. Optical microscope image shows a typical device under UV illumination, scale bar is $10\ \mu\text{m}$. The packaged chip measures $\sim 17 \times 17\ \text{mm}^2$. (b) Photograph of the setup, with key components highlighted labelled.

Figure 7.11 shows initial characterisation of two typical unit pairs (passivated by ALD), one with back-to-back Ohmic contact characteristics, and the other exhibiting back-to-back Schottky barrier behaviour, as detailed in the previous chapter. The power-dependent response of these devices was first measured, by adjusting the level of attenuation for incident 497 nm light whilst maintaining a constant source-drain bias, the I-V curves for which can be seen in Figs. 7.11a and b for Schottky barrier and Ohmic-contacted devices, respectively.

The corresponding power response for each type of contact behaviour can be seen in Figs. 7.11c and d. For Ohmic devices, a non-linear power response is observed, with a sharp increase in photocurrent at low power ($< 0.1 \text{ mW cm}^{-2}$), before flattening to a linear region between irradiances of ~ 0.3 to $\sim 1.3 \text{ mW cm}^{-2}$. This result is corroborated by findings in the literature which suggest the photocurrent, $I_{PC} \propto P^{0.8}$ for nanowire photodetectors with quasi-ohmic contacts^[338]. However, for Schottky-barrier contacted nanowires, a linear power response is seen for all irradiance levels $< 1.2 \text{ mW cm}^{-2}$. In both contact regimes, the response begins to plateau beyond irradiances of $\sim 1.3 \text{ mW cm}^{-2}$, suggesting that electronic states available for photoexcitation are becoming saturated. For the ohmically contacted sections of the nanowire, the responsivity (as defined in equation 3.4) of the detector units (at 497 nm) are consistently in the region of $\sim 10^4 \text{ A W}^{-1}$, assuming all radiation on the device is absorbed and that the total power on the device $P_{opt} = I_0 A$, where I_0 is the irradiance and A is the exposed area of the *whole* device rather than one unit, given that light may be waveguided along the wire. This corresponds to a notably high photoconductive gain, G (as defined in equation 5.11) of $\sim 3 \times 10^5$. These values are in concordance with results for similar detectors in the literature such as the CdS nanobelt devices in ref. 339, which measured (at 490 nm and 3 mW cm^{-2}) a responsivity and gain of $7 \times 10^4 \text{ A W}^{-1}$ and 2×10^5 respectively. As introduced in section 4.3.2 and 5.2.1, contributing factors to such a high gain could include the micron-scale electrode separations, light confinement within the nanowire and the high photoconductivities seen in CdS_xSe_{1-x} 1d systems, due to the band structure resulting from the compositional gradient (Fig. 4.10).

As introduced in chapter 5, as well as the previous section, it is important to minimise measurement instabilities for like measurements of the photodetector units. This means a Schottky-type contact is preferable with respect to the power-response; a steep, non-linear response implies that any variation in the incident light power at calibration will produce a greater corresponding variation in the photoresponse, increasing the measurement error level with respect to spectral reconstruction. As attempts to ‘engineer’ Schottky-contacts with reliable consistency and stability were unsuccessful (previous section), one method of circumventing this non-linearity at low power is to introduce a ‘light bias’ to Ohmically-contacted devices, in the form of an additional, low power light source (blue LED, 490 nm central peak, intensity 0.3 mW cm^{-2}) present for all measurements. This acts to provide a background level of illumination that will offset the response curve (as illustrated in 7.11d), shifting a low-power target light signal into the linear region.

Finally, the time response of these contact regimes was characterised using a pulsed LED, as shown in 7.11e and f, with rise and fall times calculated as the transition between 10% and 90% of the peak photocurrent value (treating the dark level as a baseline). The rise and fall

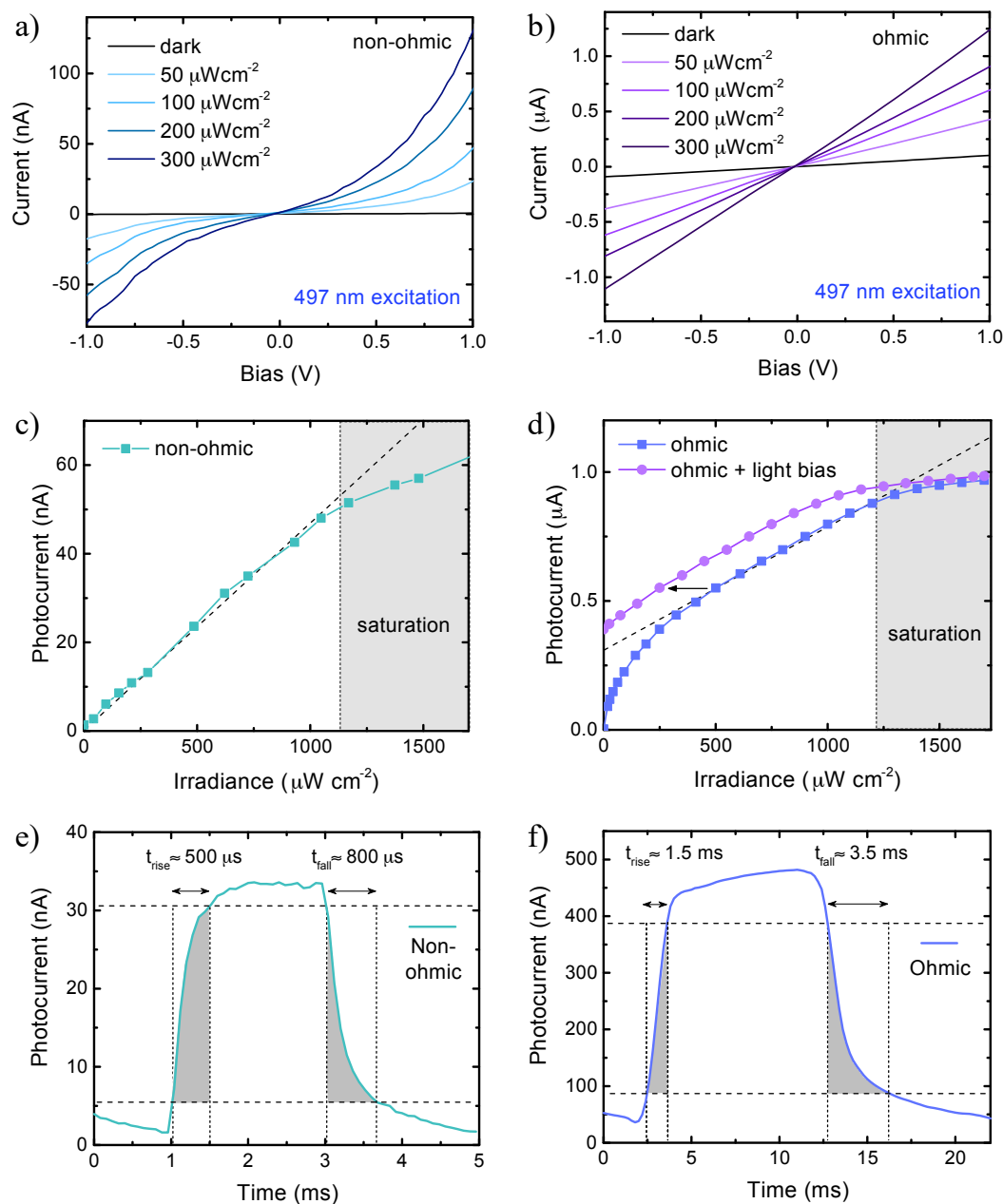


Fig. 7.11 Photodetector power and time response under different contact conditions. For a nanowire photodetector unit/electrode pair demonstrating back-to-back Schottky-barrier contact behaviour and where both display ohmic behaviour, respectively, (a),(b) the I-V characteristics under increasing irradiance of 497 nm illumination as provided by the tunable light source in Fig. 7.10, (c),(d) the photocurrent measured with respect to the incident irradiance and (e),(f) the time-dependent photoresponse measured under illumination by a blue LED pulsed at 250 Hz (e) and 50 Hz (f). The purple dataset in d) illustrates the effects of adding a $300 \mu\text{W cm}^{-2}$, 490 nm LED background source to act as 'light bias', improving the linearity for low power measurements.

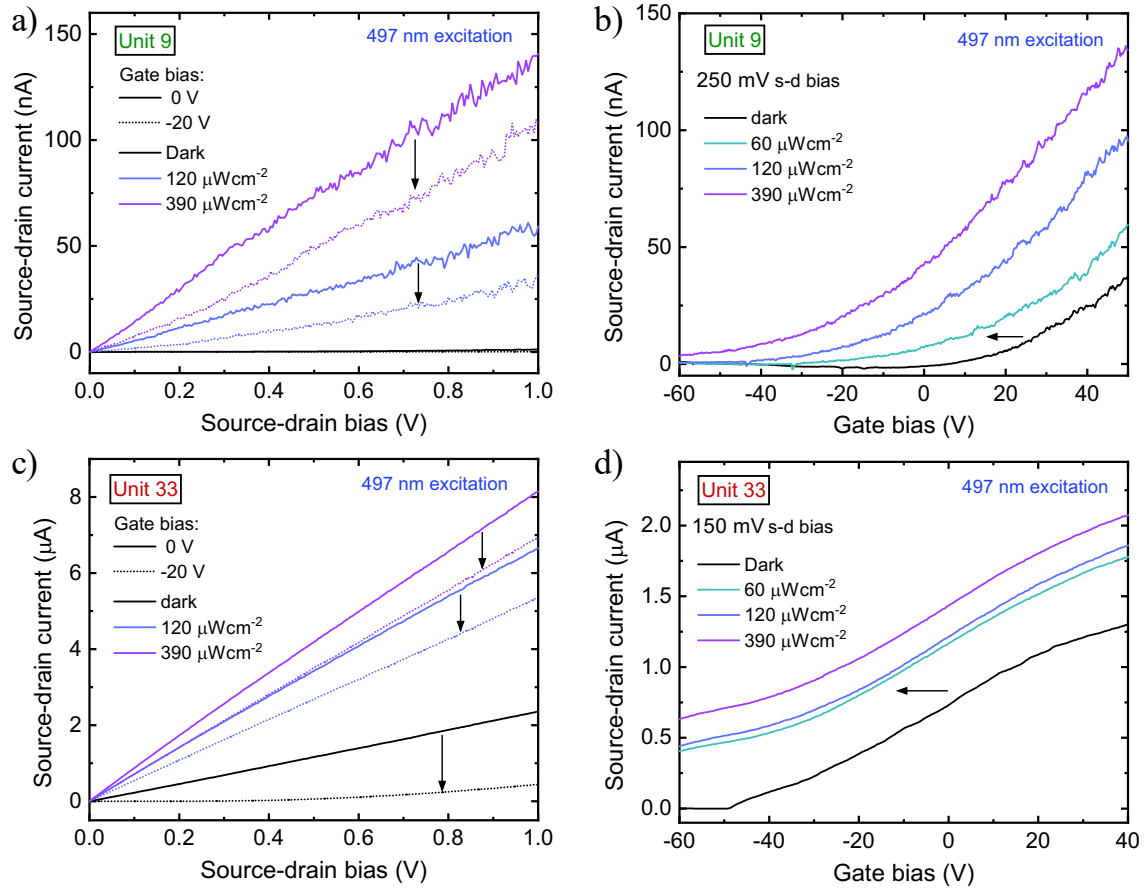


Fig. 7.12 **Backgated optoelectronic characterisation.** Power-dependent characterisation of a backgated photodetector unit in an FET architecture at the CdS (unit 9) end of a 38-unit multielectrode device, using 497 nm illumination from the setup in Fig. 7.10, showing (a) Source-drain I-V curves at varying irradiance, at zero (solid lines) and -20 V (dashed lines) backgate bias and (b) transcharacteristics for the nanowire FET at varying irradiance. (c)-(d) The same measurements as in a) and b), respectively, measured for unit 33, at the CdSe-rich end of the same nanowire photodetector array.

time for the Schottky-contacted barrier, at $\sim 500 \mu\text{s}$ and $\sim 800 \mu\text{s}$ respectively, are an order of magnitude faster than that of the ohmically contacted device, at $\sim 1.5 \text{ ms}$ and $\sim 3.5 \text{ ms}$ respectively. This agrees well with findings in the literature which suggest the strong in-built fields at the contact interface, owing to the presence of an energy barrier, lead to far higher response times in Schottky devices^[276,295].

Further to the FET measurements in the previous section, the irradiance-dependent transcharacteristics of these photodetector units were measured when subject to a varying backgate bias. The results of these measurements are shown in Fig. 7.12, for two units representative of those situated toward the green/CdS-rich (Fig. 7.12a-b) and red/CdSe-rich

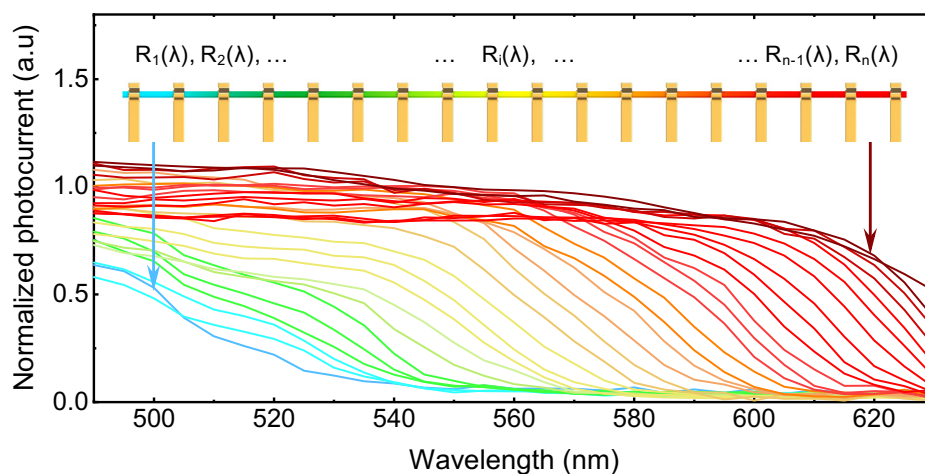


Fig. 7.13 **Spectral response calibration.** Wavelength-dependent photocurrent responses, $R_i(\lambda)$ for each unit, with index i , of a multi-electrode $\text{CdS}_x\text{Se}_{1-x}$ nanowire device (total unit number, $n = 31$, as measured using the setup shown in Fig. 7.10).

Fig. 7.12c-d ends of the nanowire - PL emission at these locations was measured as ~ 540 nm and ~ 620 nm, respectively. These provide a basic demonstration of the mechanisms occurring as different ends of the wire are photoexcited. As the fluence is increased, an increasing number of free carriers are generated through electron-hole pair creation, shifting the Fermi level of the nanowire. This positive photoconductivity manifests in the transcharacteristics ($I_{sd}(V_g)$ curve) becoming progressively more offset toward the negative polarity direction, increasing the level of conductance for a particular gate bias.

The final, most crucial optoelectronic measurements of these devices was the calibration of the wavelength-dependent photoresponse for each unit, $R_i(\lambda)$. This dataset is required as an input in a computational reconstruction, analogous to the transmission functions in filter array spectrometers. The photocurrent was therefore measured (under a bias of 500 mV) for each unit, across a wavelength range between 490 and 630 nm, corresponding to the bandgap span of the material along each wire. The emission wavelength of the tunable light source (FWHM ~ 2 nm) was varied incrementally, in steps of 3 nm over this span. This was limited by practical and time constraints surrounding the equipment available; further work would benefit from the use of, for instance, a tunable laser with a significantly narrower FWHM, and higher resolution sampling (smaller increments) over the wavelength range.

The $R_i(\lambda)$ dataset over $i = 1$ to n for a typical multi-electrode $\text{CdS}_x\text{Se}_{1-x}$ device ($n = 31$) is plotted in figure 7.13. As can be seen, the spectral responses exhibit a cut-off wavelength above which the current drops to negligible levels, as the energy of incident light is lower than the bandgap of the material. However, as can be seen, this cut-off transition is typically spread over a wavelength range of around 30 - 40 nm for each unit. A first contributing factor

to this is that the peak PL emission span across one unit (that is, a section of length around 2 - 3 μm) is typically anywhere from around 2 to 4 nm given that there is a continuous variation of material in the nanowire. Further, it may be possible that the response in a particular unit is influenced by the effects of photoexcitation and induced fields in adjacent units, effectively spreading the active detection area. Secondly, as seen in chapter 6, the PL emission, and thus, the spectral response, is broadened due to a number of possible physical factors, such as thermal energy contributions, as well as the presence of structural disorder in the wire due to the alloying process. It is further possible that, due to imperfections in the growth process, parts of the nanowires feature localised regions of irregular alloying, with higher concentrations of either S or Se than the surrounding region; this may explain, for instance the secondary peak observed for $R_1(\lambda)$ around 520 nm.

Summary

CdS_xSe_{1-x} devices have been designed toward conducting spatially resolved optoelectronic measurements along the length of the nanowire, through use of photodetector arrays. An initial approach was to use graphene channels, photogated by the nanowire as the basis for the array. CVD graphene transfer was optimised for this purpose, but whilst embedded nanowire structures coated with graphene layers were fabricated, no further measurements could be carried out due to the time constraints and the development of a different approach, using metallic electrodes. A process was optimised to fabricate device chips featuring wire-bondable contact pads and densely packed electrode arrays with high resolution at the nanowire interface, allowing the photoresponse to be probed at up to 44 points along each nanowire. A set of tables summarising and detailing the entire fabrication framework developed for embedded multi-electrode devices within this thesis is shown in Figs. 7.1 and 7.2. Initial electronic measurements of these devices demonstrated that whilst the contact behaviour was challenging to engineer with a degree of predictability, ALD passivation produced significantly more stable photoresponse. Finally, a setup was constructed to characterise the wavelength, power and time-dependent photoresponse, including calibration of the spectral responses required for potential spectral reconstruction. The next chapter shall detail demonstration of these devices when operated as computational reconstruction spectrometers.

Process Stage	Fabrication / Characterisation Step
1. Device substrate preparation	1.1 Definition of alignment markers on wafer <i>via</i> EBL
	1.2 Lift-off of alignment markers, wafer cleaving
	1.3 Definition of bonding pads on wafer <i>via</i> EBL
	1.4 Lift-off of bonding pads
	1.5 Surface treatment of substrate
2. Nanowire transfer / characterisation	2.1 Nanowires transferred from growth to intermediate substrate
	2.2 Optical and PL mapping to select suitable nanowires
	2.3 Nanowire transfer to device substrate using optical fibre probe
	2.4 AFM measurement of nanowire height
	2.5 PL mapping along length of nanowire
3. Nanowire embedding	3.1 Spin-coating in diluted SU8 embedding layer
	3.2 Photolithography to reveal bonding pads
4. Electrode deposition	4.1 Custom CAD design, definition of device contacts <i>via</i> EBL
	4.2 Plasma etch to reveal nanowire surface layer
	4.3 Surface treatment using ammonium sulfide
	4.4 Lift-off
5. Device passivation	5.1 ALD of alumina layer

Table 7.1 **Fabrication framework summary part i.** Table summarising the different stages of the device fabrication framework developed for the single nanowire spectrometers in this thesis.

Electron beam lithography				
<i>Nanobeam nb1 - beam voltage: 80 kV, current: 1 nA and 14 nA for fine and rough features, respectively</i>				
Step	Resist, spin-coating and curing	Exposure dose / C m ⁻²		Development
1.1	PMMA 950k A4, 40" 4k rpm, 10' at 120°C hot-plate (H-P)	7.5 (rough), 8.5 (fine)		IPA:DI (7:3), 20"
1.3	UV1116, 40" 3k rpm, 2' at 120°C pre and post exposure	0.6 (rough), 0.7 (fine)		MD-CD-26, 20"
4.1	PMMA 950k A8, 40" 4k rpm, 2' at 95°C H-P	4.5 (rough), 5.0 (fine)		IPA:DI (7:3), 2'30"
Metal deposition and lift-off				
<i>Lesker PRO Line PVD 200, base pressure < 10⁻⁶ mbar</i>				
Step	Layer 1	Layer 2	Lift-off	
1.2	Ti, 5 nm, 0.03 nm s ⁻¹	Au, 45 nm, 0.1 nm s ⁻¹	12 hrs sonication in acetone	
1.4	Ti, 10 nm, 0.03 nm s ⁻¹	Au, 200 nm, 0.1 nm s ⁻¹	1 hr sonication in acetone	
4.4	Cr, 5 nm, 0.03 nm s ⁻¹	Au, 60 nm, 0.1 nm s ⁻¹	~5' acetone, mild agitation with syringe	
Surface treatment and etching				
<i>Plasma system: Moorfield Nanoetch, base pressure ~ 10⁻⁷ mbar</i>				
Step	Gas / etchant	Conditions	Power	Duration
1.5	Oxygen plasma	3.5 × 10 ⁻³ mbar	30 W	120"
4.2	Nitrogen plasma	7.5 × 10 ⁻³ mbar	5 W	120"
4.3	Ammonium sulfide	40°C H-P	n/a	10'
Photolithography for nanowire embedding				
<i>SUSS MicroTec MJB-4 mask aligner</i>				
Step	Resist spin-coating, pre-bake	Exposure, cure		Development
3.2	SU8 2000.5 diluted 3:1, 40" 5k rpm, 1' 95°C H-P	20", 10 mJ cm ⁻² , 2' 95°C H-P		25" in PGMEA
Atomic layer deposition of AlO_x passivation				
<i>Savannah ALD system, base pressure ~ 10⁻² mbar</i>				
Step	Chamber conditions	Pulse 1	Pulse 2	Cycles
5.1	120°C, 20 sccm N ₂ flow	17 ms TMA	22 ms H ₂ O	550, 6" delay

Table 7.2 **Fabrication framework summary part ii.** Tables summarising the different process steps within each stage of the summary table in part i.

Chapter 8

Prototyping a single nanowire spectrometer and spectral imaging system

Overview

This chapter is the culmination of the main project of this thesis, building on and utilising the results obtained and devices designed in the previous two chapters. Here it is demonstrated that the multi-electrode devices developed around individual compositionally-engineered nanowires can indeed be an effective basis for an ultra-compact computational microspectrometer. In this platform, the previously distinct elements which separate and detect light have been combined into an individual, micrometre-scale component grown in a single bottom-up process, affording an elegantly simple spectrometer system, with a footprint 2 - 3 orders of magnitude smaller than any other reported to date.

I will begin by introducing the computational algorithm that was developed to perform spectral reconstruction, using the pre-calibrated spectral responses and the measured photocurrents from each photodetector unit along the nanowire, when illuminated by an unknown light signal. Operation of the spectrometer shall then be presented, in resolving the spectra of monochromatic and broadband light. Whilst the spectrometer developed is a proof-of-concept, there are many avenues to readily improve its performance - both in terms of the accuracy of spectral reconstruction, as well as the spectral range - which will also be discussed. The final section concerns the demonstration of spectral imaging using the device, illustrating its potential for such applications from the macroscale, down to lensless, single-cell-scale spectral mapping.

The work presented has now been accepted for publication in Science (see Publications section, item number 8). The measurements and analysis of data presented are an equal-contribution collaboration between myself and Zongyin Yang. The code for the reconstruction algorithm and simulations was developed by our collaborator Hanxiao Cui (supervised by Dr Mauro Overend, Department of Engineering), in consultation with us.

8.1 Spectrometer operation and performance

8.1.1 Principles behind spectral reconstruction

Here I shall elaborate on the computational scheme employed to reconstruct target spectra using the multi-electrode nanowire devices. The problem to be solved is essentially the same as that posed in the section in the literature review on filter array spectrometers: how can an unknown target spectrum, $F(\lambda)$, be reconstructed from a set of photocurrents measured from n photodetection units, each with different spectral responses. The strategy is illustrated schematically in Fig. 8.1.

For each i^{th} unit of the spectrometer, the measured photocurrent, I_i (also referred to as the integrated response, given the mathematical description in equation 8.1), can be expressed in terms of the unknown spectrum, $F(\lambda)$, and its pre-calibrated spectral response dataset, $R_i(\lambda)$, as follows:

$$\int_{\lambda_{min}}^{\lambda_{max}} F(\lambda)R_i(\lambda)d\lambda = I_i \quad (i = 1, 2, 3, \dots, n) \quad (8.1)$$

where λ_{max} and λ_{min} are the maximum and minimum wavelengths where varying spectral information is available for $R_i(\lambda)$ (in this case limited by the lowest and highest bandgap materials in the wire respectively).

It was decided to approximate $F(\lambda)$ as a linear combination of Gaussian basis functions. Gaussians are suited here in that they provide template functions which both match the smooth nature of most typical target spectra and are straightforwardly defined by just two parameters: the FWHM and central wavelength^[329]. This approximation can be expressed for j component functions (where $j = 1, 2, \dots, m$) as:

$$F(\lambda) \approx \hat{F}(\lambda) = \sum_{j=1}^m R_i(\lambda)\alpha_j\phi_j(\lambda) \quad (8.2)$$

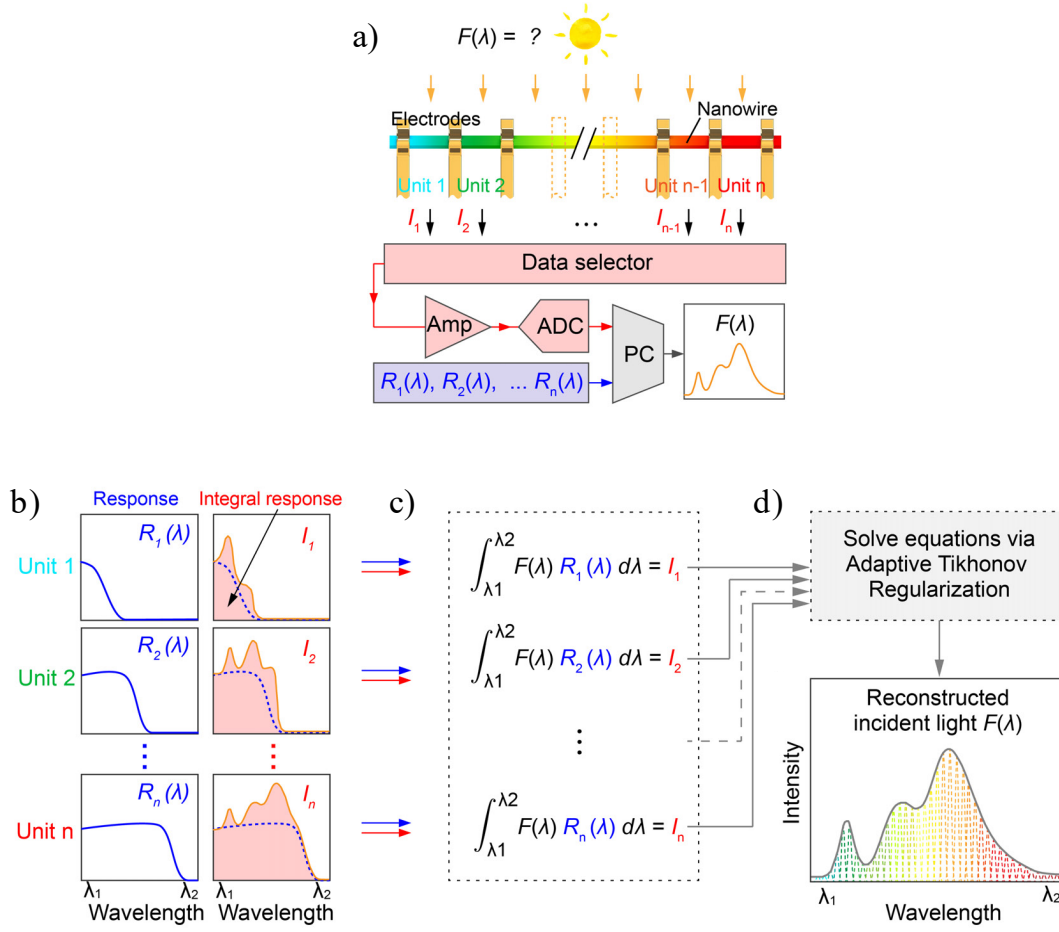


Fig. 8.1 Principles of spectral reconstruction using a nanowire spectrometer. (a) Operational schematic of the nanowire spectrometer, showing illumination by an unknown light signal with spectrum $F(\lambda)$, and measuring of the corresponding photoresponses from each photodetector unit (electrode pair), I_i . (b) Simulated spectral response, $R_i(\lambda)$, and the photocurrent I_i , which is in theory equal to the red area which indicates the integral responses to the incident light. (c) Mathematical description of the relation between $F(\lambda)$, $R_i(\lambda)$ and I_i . (d) Spectral reconstruction *via* solving the equation set, to leave the reconstructed spectrum of the simulated incident light.

where α_j is a constant coefficient for the j^{th} Gaussian function and $\phi_j(\lambda)$ is a Gaussian function whose peak is centered at $\lambda = \hat{\lambda}_j$, as described by:

$$\phi_j(\lambda) = \frac{1}{\sigma\sqrt{2\pi}} \exp\left[-\frac{1}{2}\left(\frac{\lambda - \hat{\lambda}_j}{\sigma}\right)^2\right] \quad (8.3)$$

with a constant, σ , acting as the control parameter that defines the width of the Gaussian. Here, $\sigma = (2\sqrt{\ln 2})^{-1} \delta_d \approx 0.425 \delta_d$, where δ_d is the full width at half maximum (FWHM) of the Gaussian peak. The peak positions of each Gaussian component, $\hat{\lambda}_j$ ($j = 1, 2, \dots, m$),

are simply generated such that they are distributed linearly and evenly across the wavelength range between λ_{min} and λ_{max} with equal spacing; that is:

$$\hat{\lambda}_k = \frac{\lambda_{max} - \lambda_{min}}{m - 1}(k - 1) + \lambda_{min} \quad (k = 1, 2, 3, \dots, m) \quad (8.4)$$

where, as described in equation 8.2, there are a total of m of these basis functions.

To incorporate this Gaussian approximation into the problem, equation 8.2 is substituted into equation 8.1, giving:

$$\sum_{j=1}^m \left(\int_{\lambda_{min}}^{\lambda_{max}} R_i(\lambda) \phi_j(\lambda) d\lambda \right) \alpha_j = I_i \quad (8.5)$$

As also introduced in the filter array spectrometer section of the literature review, the problem can be more elegantly represented by the matrix equation,

$$\mathbf{A}\alpha = \mathbf{c} \quad (8.6)$$

which contains two *known* variables: \mathbf{A} , an $n \times m$ matrix with elements $A_{ij} = \int R_i(\lambda) \phi_j(\lambda) d\lambda$ and $\mathbf{c} = [I_1, I_2, \dots, I_n]^T$, a $1 \times n$ vector containing the photocurrent measured by each detection unit, as well as $\alpha = [\alpha_1, \alpha_2, \dots, \alpha_m]^T$, an *unknown* $1 \times n$ vector containing the coefficients for each basis function.

Therefore, the objective of the algorithm becomes a minimization process; it seeks to return the coefficients of α which give the lowest possible residual norm, or error, $e = \{\|\mathbf{A}\alpha - \mathbf{c}\|_2\}$. This is expressed as follows:

$$\min_{\alpha} \{\|\mathbf{A}\alpha - \mathbf{c}\|_2^2\} \quad (8.7)$$

However, framing the problem as in equation 8.7 is directly equivalent to performing the inverse of the integration in equation 8.6. Even tiny errors in the measured values (photocurrents and spectral response functions) cause such a problem to become numerically unstable, leading to amplification of high-frequency noise signals. As discussed in the literature review, one way to selectively dampen noise in the produced spectrum is to use a Tikhonov regularisation scheme, where a regularisation factor, γ , is introduced into the problem. Thus, equation 8.7 becomes:

$$\hat{\alpha}_{\gamma} = \min_{\alpha} \{\|\mathbf{A}\alpha - \mathbf{c}\|_2^2 + \gamma^2 \|\alpha\|_2^2\}, \quad \gamma > 0 \quad (8.8)$$

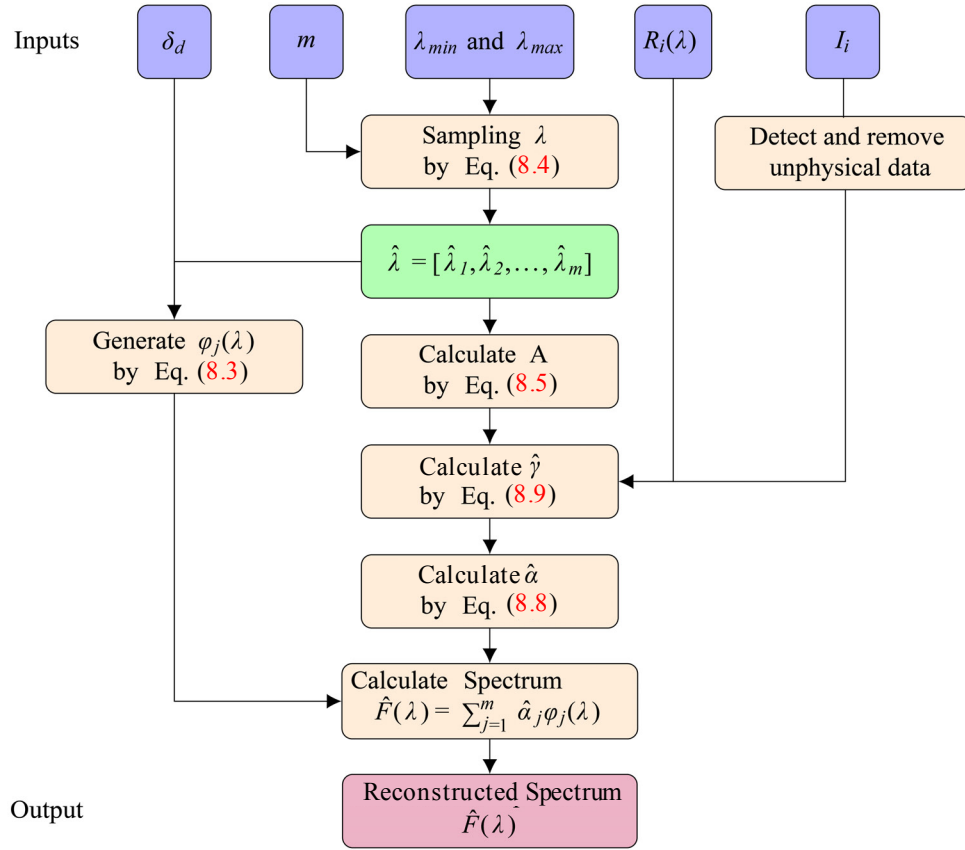


Fig. 8.2 **The reconstruction algorithm.** A flow diagram illustrating the computational process used to reconstruct spectra by adaptive regularisation. Blue boxes indicate inputs, orange for processes, green for outputted data and red for the final reconstructed spectrum.

where α is re-termed as $\hat{\alpha}_\gamma = [\hat{\alpha}_1, \hat{\alpha}_2, \dots, \hat{\alpha}_m]^T$ - the optimal coefficients for the basis functions which minimise inconsistencies in the reconstruction.

A range of different computational, parameter choice processes can be used to adaptively select the regularisation factor, γ , such as the L-curve method^[340], or Generalised Cross Validation (GCV)^[341,342]. Generally speaking, these processes find a balance between robustness and resolution, associated with high and low values of γ respectively. In the code used in the spectrometer, γ was adaptively selected using the GCV method, within which (for Tikhonov regularisation) the optimal regularisation factor, $\hat{\gamma}$, obtained from the cross-validation is described by:

$$\hat{\gamma} = \min_{\gamma} \frac{\{\|\mathbf{A}\hat{\alpha}_\gamma - \mathbf{c}\|_2^2\}}{[n - \text{trace}(\mathbf{A}(\mathbf{A}^T\mathbf{A} + \gamma^2\mathbf{I})^{-1}\mathbf{A}^T)]^2} \quad (8.9)$$

where m is the total number of basis functions and \mathbf{I} is the identity matrix. Further to optimising γ , the accuracy of the spectral reconstruction is also dependent on selecting the FWHM of the Gaussian basis functions, δ_d . This was varied incrementally for each device, to find an optimum value. Here, the optimum δ_d was seen to decrease with increasing number of units used; $\delta_d \approx 8.5$ nm and 7.0 nm for 30 unit and 38 unit device measurements respectively. A summary of the entire computational reconstruction process can be seen illustrated by the flow diagram in Fig. 8.2.

8.1.2 Characterisation of spectral reconstruction

To demonstrate the capabilities of the spectrometer, a variety of different incident light signals were measured using two different nanowire spectrometers, containing 38 and 30 photodetector units, and were compared with the same signals measured by a conventional spectrometer (Thorlabs CCS100, 0.5 nm wavelength accuracy), as displayed in Fig. 8.3. First, single peak monochromatic light signals were used to illuminate the two devices, as produced by the same tunable Xe arc lamp source as used in calibration of the spectral response. A typical set of reconstructions can be seen in Fig. 8.3a for an individual peak at 570 nm, which both agree well with the reference spectrum; peak positions are accurate to within 1 nm in this case. Given the algorithm assumes that the spectra will be constructed from a set of component Gaussian peaks, it follows intuitively that the minimum reconstructed FWHM for a monochromatic peak is equivalent to the optimal bandwidth for these basis functions, δ_d , in accordance with equation 8.3. As shown, optimal δ_d is ~ 7 and ~ 8.5 for the 30-unit and 38-unit spectrometer, respectively.

As addressed in section 5.3.2, whilst the resolution of a conventional spectrometer can simply be characterized in relation to the wavelength spacing achievable between distinct, separated spectral components, a spectral reconstruction spectrometer produces a quasi-continuous output, to which this methodology is not applicable. It is thus less trivial to decide how best to quantitatively define the ‘accuracy’ with which these spectrometers reproduce the original spectrum of light. Given the limited number of computational spectrometers in the literature, there is no established consensus here thus far. In ref. 343, the resolution is simply defined through the minimum FWHM measured from a monochromated incident signal, whilst a more statistical approach is taken in refs. 323 and 344, using the mean error or R^2 value with respect to a reference spectrum. Another method used in the literature is the measurement of spectra containing two monochromatic peaks that are shifted progressively closer together, in order to find the smallest peak separation at which the two features become indistinguishable in the reconstructed spectrum^[312,322,344]. This methodology was used to characterise the reconstruction accuracy in the nanowire spectrometers, typical results

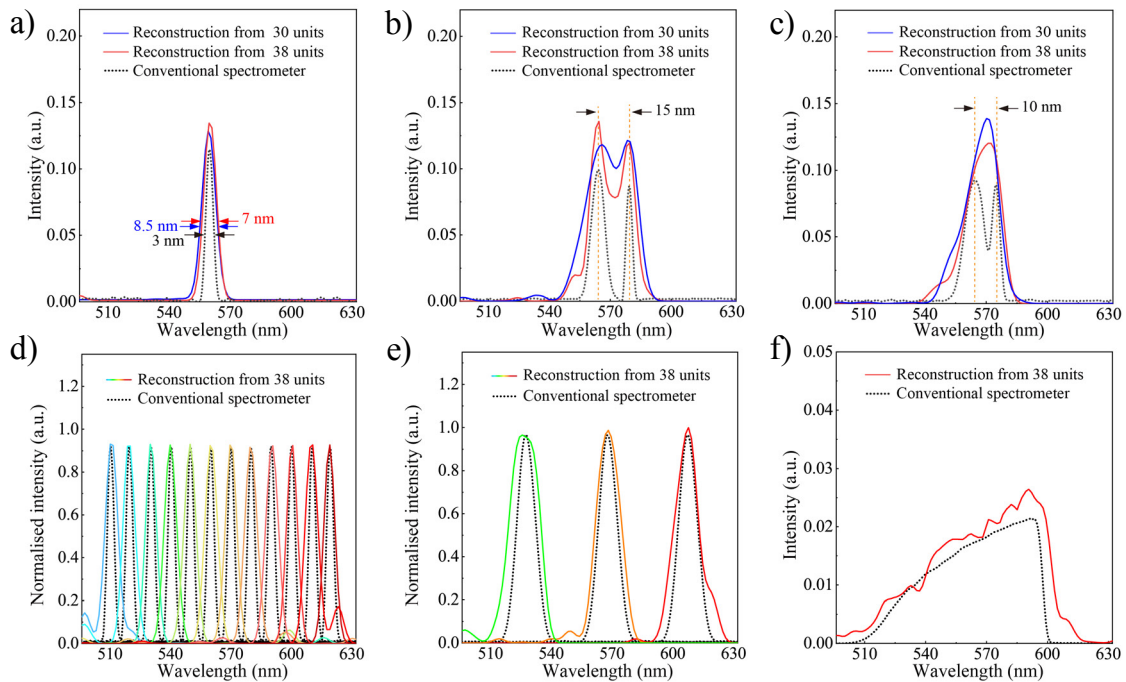


Fig. 8.3 Demonstration of spectral reconstruction by nanowire spectrometer. (a) Measurement and reconstruction of a single spectral peak at 560 nm using a 30- and 38-unit device, relative to the same signal measured by a conventional spectrometer (Thorlabs CCS100, 0.5 nm wavelength accuracy). Arrows indicate FWHM. (b) Two mixed narrow-band signals, with peaks separated by 15 nm, are resolved by the devices from A. (c) Spectral reconstruction from a 30- and 38-unit nanowire spectrometer demonstrating the separation (10 nm) at which two monochromatic peaks become indistinguishable. Reference spectrum measured by conventional spectrometer shown by dotted lines. (d) Reconstructed spectra from data measured by the 38 unit device when illuminated (separately) by monochromatic light at selected wavelengths across the spectrometer's operational range. (e) The same demonstration as in d), with broadband light signals, FWHM ~ 10 nm. (f) Spectrum of a white LED light as measured and reconstructed using the 38-unit spectrometer, demonstrating the ability to reconstruct arbitrarily shaped light signals.

for which are shown in Fig. 8.3b and c. The spectrometers were able to resolve two peaks around 570 nm separated by 15 nm, though the 38 unit spectrometer was able to more closely reconstruct the gap between these features. For both spectrometers, the two peaks became indistinguishable once the separation is decreased to ~ 10 nm.

Assessing performance across the spectral range of the 38-unit spectrometer, a sample of narrowband signals with different peak wavelengths (spread evenly across the span of cutoff wavelengths observed in the nanowire spectral responses) were measured separately, as shown in Fig. 8.3d. The operational wavelength range of the spectrometer is between 500 - 630 nm, consistent with the bandgap span of the material in the nanowire. The spectrometer cannot function outside of this range due to a lack of spectral information in the response

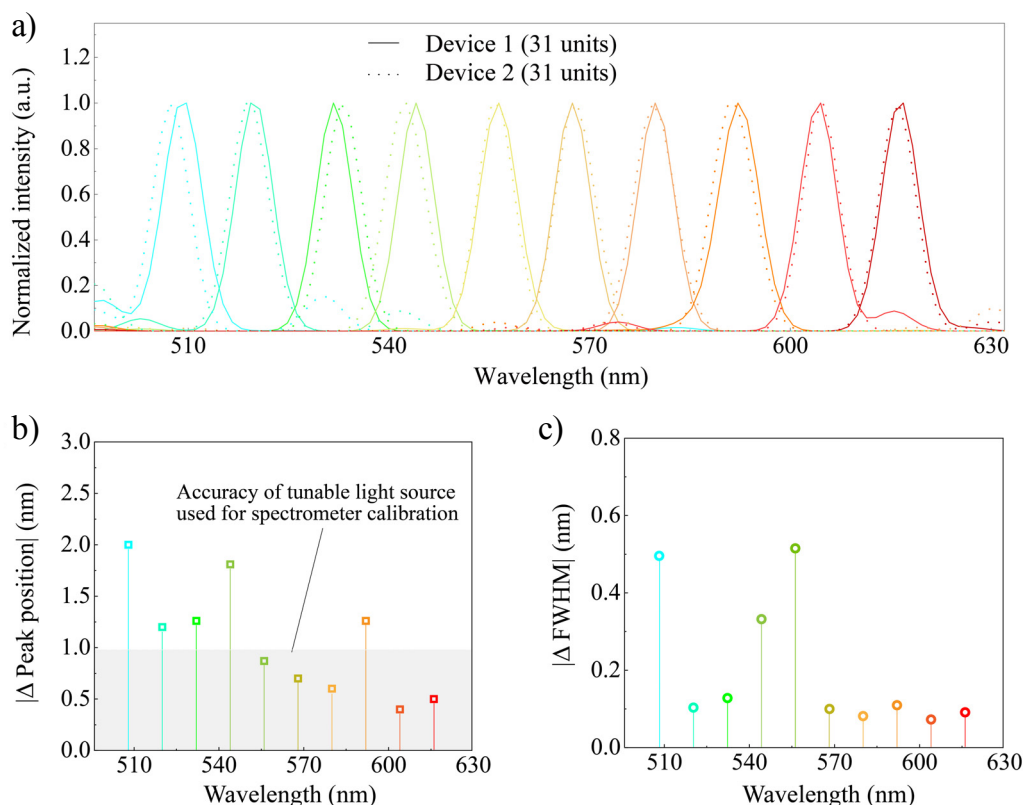


Fig. 8.4 **Device-to-device reproducibility.** (a) Measured variation for two different devices when reconstructing monochromatic light signals (from a xenon arc lamp source) across a range of wavelengths from 505 to 620 nm, using 31 photodetection units on each nanowire. (b) and (c) The differences in peak position and FWHM respectively, corresponding to the spectra in a). The grey area in b) represents the precision of the peak position produced by the light source.

functions. Further to this, separate broadband signals spread across this range were also measured, as produced again by the tunable Xe arc lamp source, with FWHM ~ 10 nm when measured by the reference spectrometer Fig. 8.3e. As can be seen, the reconstructed spectra agree well with that of the reference spectrometer, regardless of where peaks are placed within the wavelength range. Finally, a white light LED was measured with the 38 unit spectrometer to demonstrate reconstruction of an arbitrarily shaped spectrum, rather than that with distinct Gaussian peaks. As can be seen in Fig. 8.3f, whilst there are some inaccuracies in the reconstruction, the overall shape of the spectrum is consistent with that measured by the reference spectrometer.

It is important to note here that the use of a calibration process can actually be a significant advantage with respect to the reproducibility of performance on a device-to-device basis. The alternative would be to rely on one ‘master’ set of spectral responses used across all devices; in this scenario, not only must nanowires be the same length, with the same

number of units fabricated, there must be a high degree of consistency in the characteristics (responsivity, spectral response curve shape, *etc.*) of like photodetector units on different spectrometers. In practicality, this is extremely challenging to achieve with any nanomaterial system, due to uncontrollable defects in nanowire growth between or within batches, and random, even minor variation or faults in fabrication processes (nanowire transfer, lithography, metallization). Characterising a set of unique spectral responses, specific to each device can serve to negate these anomalies and inconsistencies. Whilst the nanowire length and the photodetector characteristics of unit i across two devices may be dissimilar, the overall quantity and spread of unique spectral information contained across the spectral response set should be mostly consistent (assuming that the nanowire gradients are continuous and the material compositions at each end are the same).

Therefore, it would be expected, even under different fabrication conditions, for the spectrometer reconstruction accuracy to have a good degree of consistency across two devices *with the same unit number* (and therefore, the same amount of data contained within the set of $R_i(\lambda)$). Shown in Fig. 8.4a, this was demonstrated by comparing monochromatic light reconstructions from the same two devices as in Fig. 8.3. So as to keep the number of units the same ($n = 31$) across both devices, 7 units (at equal i -spacings across $0 - n$) were removed from the 38-unit device at the data processing stage (note that one of the units in the fewer unit device later failed, which is why the characterisation in Fig. 8.3 lists it as $n = 30$). As can be seen in Fig. 8.4b, all the peak positions are consistent to within ~ 2 nm, with an average difference of ~ 1.1 nm. For reference, the tunable light source for calibration is only accurate to the nearest ~ 1 nm, which could potentially be a considerable factor in the differences between the two devices. Meanwhile, the FWHM in the reconstructed spectra differ only by an average of ~ 0.29 nm between the two devices, shown in Fig. 8.4c. Whilst, clearly, more than two spectrometers are necessary for a robust statistical analysis of the performance reproducibility, these results do suggest that through calibrating each one individually a high degree of device-to-device consistency is possible.

A potential issue relating to the device performance over time is the impact on performance should one or more units in a device fail, and how robust the system is with respect to such an occurrence. As can be seen from the comparison of the 30- and 38-unit devices in Fig. 8.3, whilst the FWHM of reconstructed monochromatic signals increases, monochromatic peak positions and the minimum distinguishable peak separation remains consistent from the lower to the higher unit device. In this respect, a reduction of one unit, let alone 8, will not dramatically affect the quality of the reconstruction. In fact, even without recalibrating the device, the failure of any particular contact is absorbed by the algorithm in a number of ways. If the contact failure leads to non-physical measurements, such as a negative or

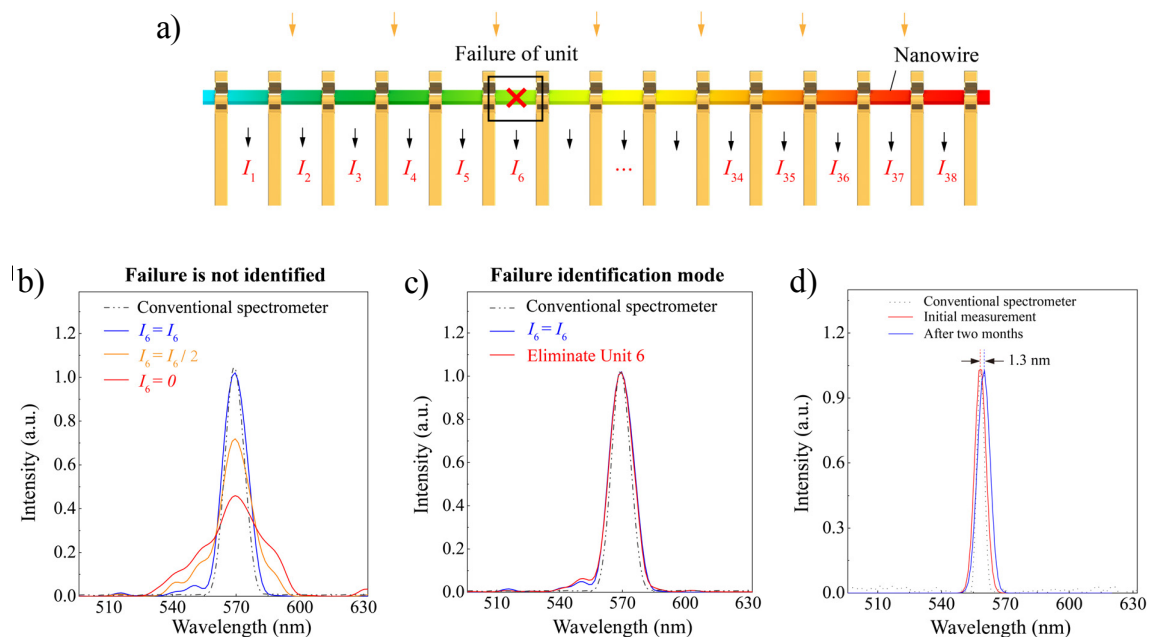


Fig. 8.5 Stability of spectral reconstruction with unit failure and over time. (a) Schematic of a nanowire spectrometer where one photodetection unit has failed. (b) Reconstruction of a narrowband peak when the signal from one unit is as measured during calibration, and when it has depreciated by half, and when it is lost completely, compared with the target spectrum as measured from a conventional spectrometer. (c) The same demonstration as in b) but where the algorithm has identified the failed unit and removed it from calculations. (d) Reconstructions of a narrowband target spectrum from a 30-unit nanowire spectrometer, as based on data measured immediately after calibration and two months after this initial measurement, relative to that measured using a conventional spectrometer.

infinitely large photocurrent, these anomalies will be identified by the algorithm and the measurements from this unit removed from the rest of calculation procedure. If the contact failure results in a noticeably higher level of measurement noise across all units, the damping coefficient γ will be re-adjusted by the parameter choice method (i.e. the GCV method in this case) to better reflect the noise level in the spectrum reconstruction process. As mentioned, generally speaking, the spectrum reconstruction becomes more robust to noise signal if the damping coefficient is increased, while more sensitive (that is, higher resolution) if the damping coefficient gets smaller. Figure 8.5 illustrates how the quality of a monochromatic peak reconstruction is affected should one of the nanowire units fail, with and without the addition of a function to detect such an event (8.5b and c respectively).

In terms of the long-term operational stability of the devices, Fig. 8.5d shows two reconstructions produced by the same device, from measurement of a single monochromatic peak at 560 nm separated by a period of two months. Whilst the two measurements are consistent within a peak position of around 1 nm, note that the long term stability of the

devices is not an area that has been extensively investigated. It may be possible, through different or more extensive passivation methods, to significantly reduce even this fairly minor deviation in performance. Furthermore, recalibration of the device sees the reconstruction accuracy return to the original level of the initial measurement.

8.1.3 Further enhancing the reconstruction accuracy

Whilst resolutions of <1 nm are now routinely achievable with benchtop scale spectrometer systems, it is important to put the performance of these nanowire spectrometers in context with other microspectrometer systems. Table 8.1 contains a comparison of the performance of the nanowire devices with respect to other microspectrometers in the literature, and the state-of-the-art in those commercially available. Clearly, the primary advantage of the platform that has been developed is the ultra-compact footprint and pixel size it allows. However, it should be noted that even without further improvements in performance, the devices are currently competitive with commercial, grating-based microspectrometers, despite a reduction in footprint of 3 - 4 orders of magnitude.

The most notable microspectrometer system to date is that reported in ref. 322 - as discussed in chapter 5, this device is based around QD-based filters that must be individually prepared and positioned on top of a millimeter-scale CCD sensor array. The spectral range in these QD devices is around 400 - 650 nm compared to that of 500 - 630 nm in the nanowire spectrometers, owing to the greater range of semiconductor materials used in the QDs. However, whilst the devices are demonstrated here with a particular nanowire material system ($\text{CdS}_x\text{Se}_{1-x}$), the spectral range can be expanded through the growth of nanowires incorporating wider or narrower bandgap materials, which has been achieved straightforwardly^[199,207]. It should also be noted that the nature of nanowire growth has a key advantage here. In QD mixtures it is possible to tune the relative intensity of different peaks in the spectral response by varying the ratio of a particular species with respect to another. However, to shift the underlying peaks and introduce more, varied spectral information, a different size or material QD must be grown in a new step and included in the mixture. This may therefore require potentially tens of separate growth steps for the same set of filters, depending on the number of different responses required. Contrastingly, through the adapted VLS growth process, a continuously varying range of material compositions can be included in one nanowire structure, in one growth step, rather than in a discrete fashion as with QDs.

In the QD device, the minimum separation for two monochromatic peaks is around 3 nm before the two features become indistinguishable, representing around a $3\times$ improvement on the current nanowire devices, where features are indistinguishable at 10 nm separation. However, it should be emphasized that the primary advantage of this work is the reduced

Type	Basis	Footprint ¹	Unit size ²	Resolution ³	Spectral range	Development	Reference
Reconstruction	Nanowire	$0.5 \times 75 \mu\text{m}^2$ ⁴	$0.5 \times 1 \mu\text{m}^2$ ⁵	10 nm	130 nm	proof-of-concept	this work
Reconstruction	Quantum dots	$8.5 \times 6.8 \text{mm}^2$	$0.5 \times 0.5 \text{mm}^2$	3.2 nm	300 nm	proof-of-concept	322
Reconstruction	Photonic crystals	$210 \times 210 \mu\text{m}^2$	$32 \times 32 \mu\text{m}^2$	- ⁶	200 nm	proof-of-concept	343
Reconstruction	Interferometer	$2.5 \times 0.6 \text{mm}^2$ ⁷	n/a	0.2 nm	20 nm ⁸	proof-of-concept	344
Conventional	Grating (planar)	$12 \times 12 \text{mm}^2$	n/a	0.15 nm	148 nm	proof-of-concept	345
Conventional	Grating (out of plane)	$21 \times 10 \text{mm}^2$	n/a	15 nm	440 nm	commercial	346

Table 8.1 Microspectrometer technology comparison. Characteristics of this work relative to current state-of-the-art microspectrometers, both based on computational reconstruction and conventional, spatially dispersive systems, from the literature as well as one that is commercially available. 1: Footprint is the area of the active dispersion element or system within the device, not including supporting systems for outputting electronic signals and otherwise. 2: The size of each individual detector within the array of the device, which defines the minimum step (that is, pixel) size within a scanning spectral imaging strategy. 3: For the spectral reconstruction spectrometers, the measured resolution is defined as the minimum separation between two indistinguishable peaks in the target spectrum, as used in Fig. 8.3c. 4: Note that the dimensions of these nanowire are variable, typically from diameters 100 - 500 nm and lengths from 50 to 100 μm . Though shorter (or longer) wires could readily be grown. 5: Use of the nanowires in reference 207, for instance, would expand spectral range to 320 nm (380 to 700 nm). 6: There is no demonstration of the minimum separation for two distinguishable peaks within this work. 7: Estimated from the scale bar in an optical image of the device. 8: Note this spectrometer operates in the telecoms wavelength range (centered at 1560 nm) rather than the visible spectrum.

footprint (and complexity) of the device, which is between 2 and 3 orders of magnitude smaller than that in the QD work, with a far smaller number of units used - 38 compared with 195. With improvements along the lines of those described in the previous section, including a greater number of units, I believe the devices presented here would match the QD spectrometer in terms of resolution, alongside the substantial reduction in footprint.

A range of readily achievable strategies have been identified for improving the spectral reconstruction accuracy further. These address what have been determined as the two primary sources for the errors arising in the computational reconstruction: 1) The (lack of) available measurement data; mathematically, since a spectrum is supposed to be a continuous curve with infinite number of points, an infinite number of measured data points to perfectly reconstruct such a curve. 2) The presence of errors in the measured data points for each unit (photoresponse and calibrated spectral response), which introduce inconsistencies into the set of equations that is to be solved.

To address the first of these points, a greater quantity of unique spectral response data should be collected at the calibration stage. This can be achieved through two routes. Firstly, the quantity of detection units on the device, n , can be increased by fabricating a greater

number of narrower electrodes (for the same nanowire length). Secondly, the resolution of the calibration process can be improved, to increase the number of data points for each unit's spectral response curve within a given range. Increases in n - by decreasing both the contact width and separation - are limited by practical constraints. As contacts become narrower, the contact resistance increases, decreasing the SNR of the photodetector unit and increasing measurement errors. This will be balanced to some degree by an increase in photocurrent due to the decreased contact separation. The minimum achievable resolution of the lithography and fabrication of electrodes is also a potential practical limitation. However, with the embedded nanowire strategy that has been developed in chapter 6, and with industry standard lithographic processes, it should be straightforward to fabricate electrodes with a width and pitch down to ~ 10 and 20 nm, respectively. Therefore, I expect that the contact resistance rather than process resolution would be the limiting factor here. In terms of the calibration resolution, given the linewidth of the tunable light source (as detailed in chapter 7) for each unit 50 data points were measured for $R_i(\lambda)$, from a wavelength of 490 to 640 nm in intervals of 3 nm. Improvements in the sampling resolution, for instance, to < 1 nm, through use of a different light source or otherwise, would allow better definition of the spectral response for each detection unit.

It is possible to reduce the effects of errors in the measured data both at the fabrication stage as well as through the computational strategy used. From a fabrication standpoint, the primary concern is reducing the coefficient of variation (CV) between repeated photocurrent measurements (that is, under the same incident light and device bias conditions) from any particular detection unit. As mentioned previously, random fluctuations here will introduce inconsistencies in both the measured photocurrent and spectral response datasets. Detailed in the previous chapter, steps have been taken to begin to address this, through Al_2O_3 passivation, as well as through the use of plasma and ammonium sulfide treatment to improve the stability and lower the contact resistance of the contacts, improving the SNR of the detector. However, further improvements are likely possible through a more extensive investigation of other surface treatments, contact conditions/metals, or passivation methods. Furthermore, the photogenerated carrier dynamics of nanowires are dependent on their intrinsic physical and geometrical properties, which can be adjusted at the growth stage; it may for instance be possible to reduce charge trapping and increase measurement stability in this way. Finally, relating to the calibration stage, as is detailed earlier in this and the previous chapter, a tunable Xe arc lamp (FWHM ~ 2 nm) was available for characterizing the spectral responses. Use of a light source with a narrower FWHM, such as a tunable laser, would allow greater accuracy here, reducing measurement error in the $R(\lambda)$ dataset.

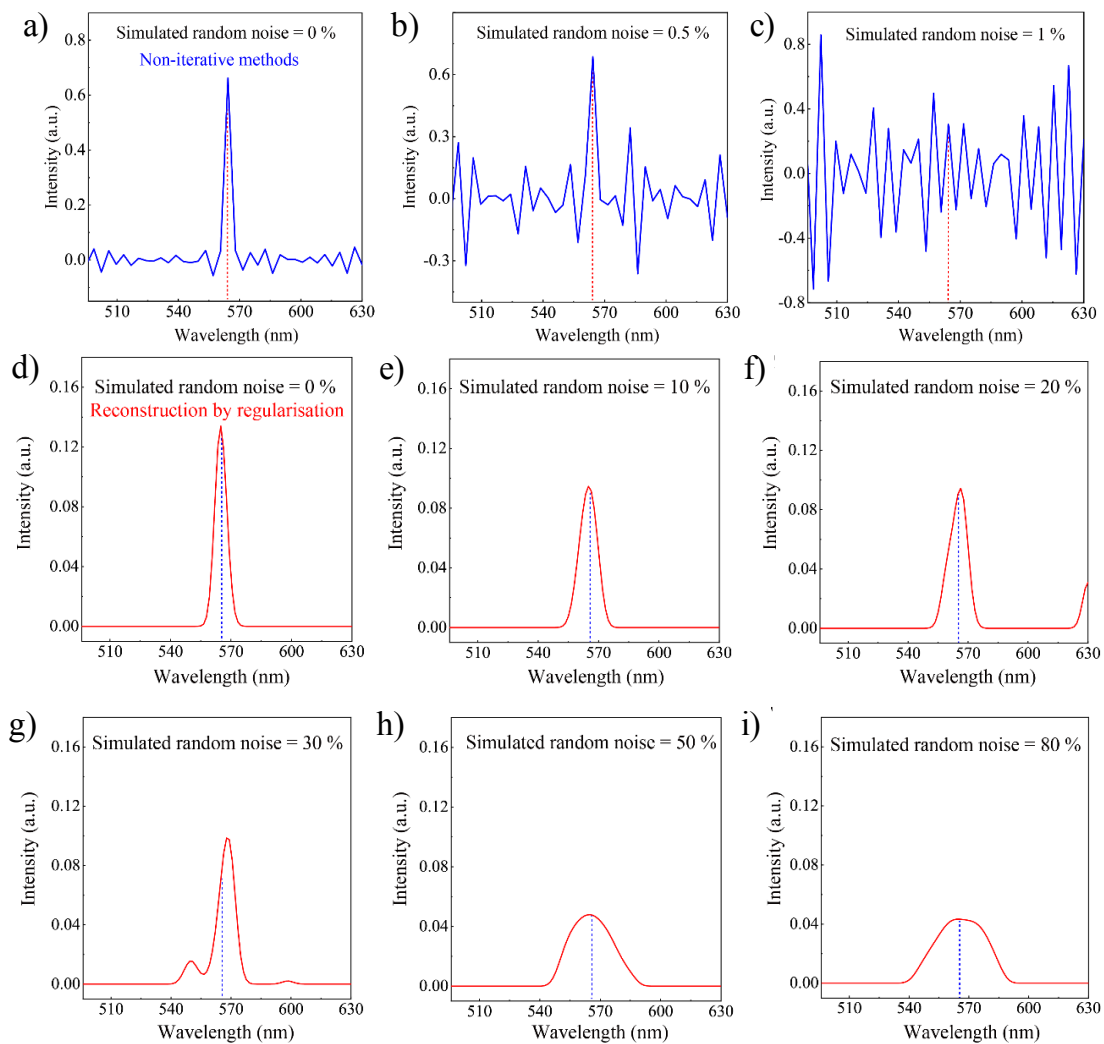


Fig. 8.6 Comparing the effects of measurement errors on non-iterative method- and adaptive regularization-based reconstructions. (a) Reconstruction of a simulated spectrum with peak wavelength of 565 nm by a non-iterative method. Unit number $n = 38$. (b) and (c) Noise of the reconstructed spectrum raises with the increase of the stimulated random error level of each photodetector unit. The spectrum is fully distorted when error is 1 %, which is below the system measurement errors (2 %). (d)-(i) Reconstructions of the same spectra as in a) by adaptive regularization, with simulated random errors of each photodetector from CV = 10 % to 80 %. Compared with the ordinary non-iterative methods, the adaptive Tikhonov regularization exhibits high error tolerance. Although the spectrum accuracy decreases, the major peak can still be observed even with an error level of 80 %.

Relating to the computational strategy, as detailed in section 8.1.1, to reconstruct the spectrum from limited and noisy measurements, a Tikhonov regularization scheme based on the GCV method is used to select the regularization parameter, which selectively dampens the noise signals. Already, the use of these techniques rather than simple, non-iterative methods makes the reconstruction significantly more robust with respect to measurement

error. This is illustrated in Fig. 8.6 through reconstructions of simulated signals with different noise levels. As introduced in chapter 5, many investigations have sought to use prior knowledge and additional information about the measured spectrum in order to improve the quality of spectral reconstruction. In this work for instance, it is assumed that the noise is white, and the spectrum of incident light can be approximated by a series of Gaussian basis functions. Several works have had success by basing reconstructions around an assumption as to the ‘sparse’ nature of the original signal, by placing limits on the number of non-zero components in the spectra (directly-sparse signals)^[321,329,330]. More recently, dictionary/machine-learning techniques have expanded upon these algorithms to improve reconstruction of non-directly sparse signals by representing them in an alternative transform domain, or ‘dictionary’ in which they are sparse^[328]. Through testing a range of other different existing reconstruction methods, or by developing new strategies for reconstruction such as in reference 328, more accurate reconstruction could be achieved even without any changes to the existing hardware.

To illustrate the potential increase in resolution, simulations have been carried out for a set of hypothetical devices with an increasing number of units, at varying levels of measurement noise as shown in Fig. 8.7. Increased unit numbers have been simulated via an interpolation of the real, measured spectral response data for one of the nanowire spectrometers, to produce an arbitrary number of simulated spectral responses at evenly separated cutoff wavelengths, within the same wavelength range (500 - 630 nm). In this instance, to simulate measurement error, a white noise component has been generated in the target spectrum that is being ‘measured’. For two simulated peaks with a 1 nm separation and no noise component, reconstruction accuracy is satisfactory (the peaks are distinguishable) at 500 units (Fig. 8.7b), but begins to break down at 400 units (Fig. 8.7c). When the peak separation is increased to 2 nm, distinguishability is maintained down to 200 units but breaks down beyond this (Figs. 8.7d-f). With the addition of a noise (simulated measurement error) component to the 1 nm separated peaks, accuracy breaks down for the 500 unit hypothetical device only once this reaches 8% (Figs. 8.7g-i). For reference, measurement error levels in the current devices is 2% (see chapter 7), though in practicality this value may increase with the fabrication of smaller electrodes necessary to increase unit number.

Note that fabricating such a number of units on, for example, a 75 μm long nanowire, would be possible with a pitch and electrode width of 150 nm and 75 nm, respectively. If the same pitch to width ratio is maintained (that is, $\sim 2:1$) the same length of nanowire should be exposed and thus the photon flux incident on the wire remains similar to the existing devices. It should be stressed that these improvements are achieved through increasing the unit number alone, and are based off of an interpolation of the existing, measured calibration curves. By

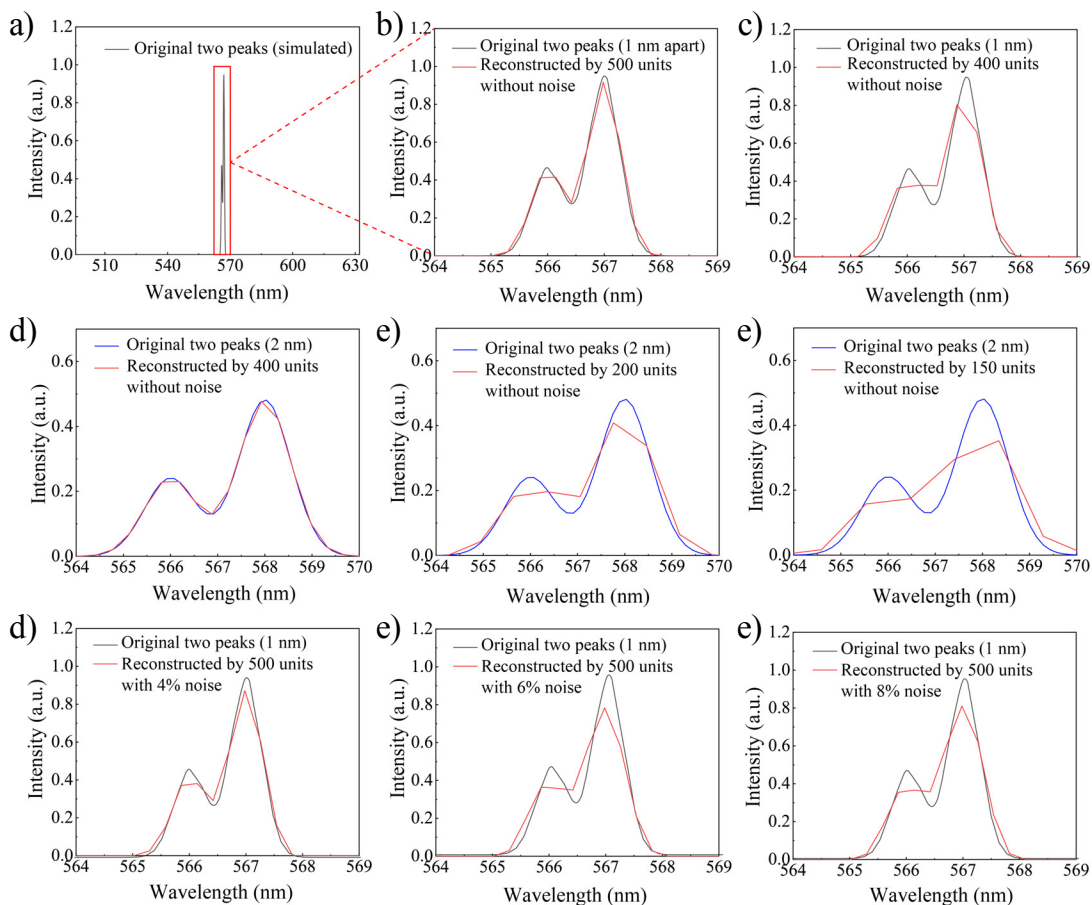


Fig. 8.7 **Simulated device performance with increased unit numbers.** (a) A simulated target spectrum with two narrowband peaks, of different intensities, at a set wavelength separation. (b),(c) Reconstructions from simulated devices of the two peaks in a) positioned at 1 nm separation, using 500 and 400 units respectively, with zero measurement noise. (d)-(f) The same reconstructions as in b), with peaks at 2 nm separation, using simulated devices with 400, 200 and 150 units respectively, and, (g)-(i), at 1 nm separation using a 500-unit device, with 4%, 6% and 8% simulated measurement noise respectively.

improving the algorithm further, reducing the noise in the measurements, increasing the resolution of the calibration, as well as increasing the number of units, it may be possible to achieve such resolution, or better, with far fewer than 500 units.

8.2 Spectral imaging

In many fields, such as astronomy^[347], precision agriculture^[348] and nanophotonics^[349], spectral imaging is in high demand to cross-analyze spectral and spatial information. Through use of a point-scanning strategy, spectral imaging was demonstrated using the 38-unit

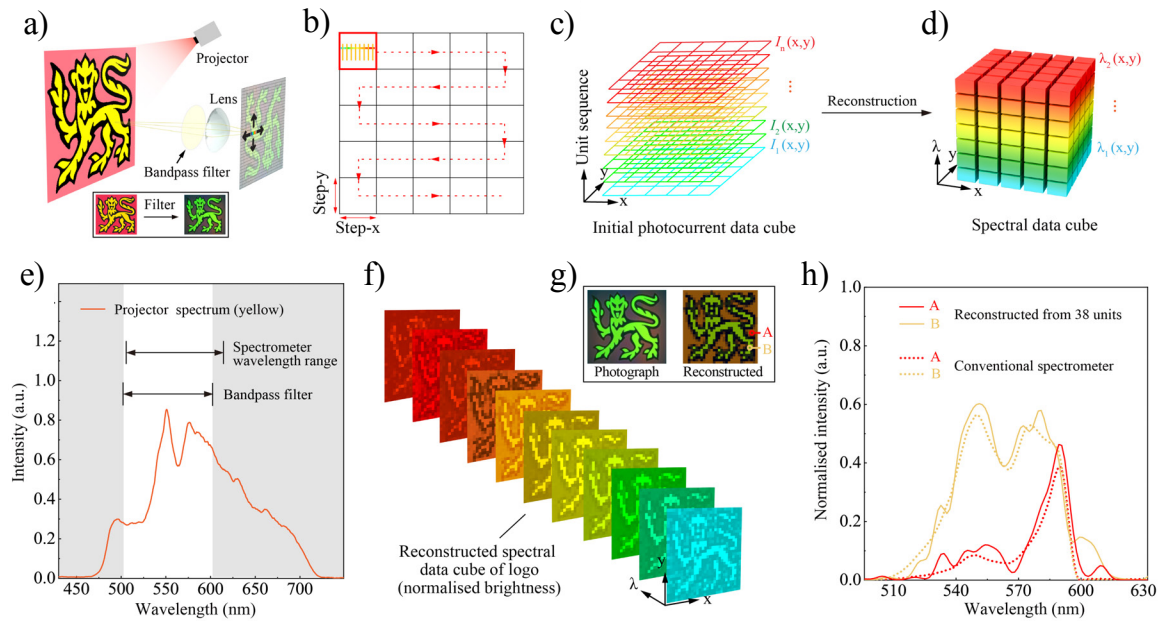


Fig. 8.8 Macroscale spectral imaging. (a) Schematic of the scanning spectral imaging scheme demonstrated using a nanowire spectrometer. Photograph of the Cambridge university logo by a CCD camera before and after filtering (bottom panel). (b) Spectral imaging is conducted by scanning the nanowire spectrometer on the imaging plane in a serpentine pattern. (c) Each pixel contains a photocurrent value of each photodetector unit and forms an initial data cube. (d) The spectral data cube is reconstructed from the initial photocurrent data cube. (e) Spectrum of yellow color from the projector. Bandpass filter and spectrometer detectable ranges are indicated in the diagram. (f) A series of reconstructed images at various wavelengths. Pixel intensity range of these images is normalized. (g) Left panel: Original photograph of the image. Right panel: Pseudo-coloured spectral image converted from the spectra according to CIE color matching functions. (h) Spectra of A and B points in g), measured by the nanowire spectrometer and a conventional spectrometer.

nanowire spectrometer. As shown in Fig. 8.8a, an image was focused by a lens onto the device, which was then translated across the focal plane on centimetre scales using an electronically controlled scanning stage, in a serpentine pattern - Fig. 8.8b. In this scheme, the resolution is defined by the mapping step used, which can be equal to or larger than the device footprint; here a step-size of 0.3 mm has been used. Photocurrents measured at each mapping step are recorded in a 3D (x, y, I_i) data cube (Fig. 8.8c). This initial cube was then converted to a spectral data cube (x, y, λ) by the reconstruction algorithm (Fig. 8.8d). A bandpass filter was used to remove wavelengths outside the operational span of the device Fig. 8.8e.

Cross sections of the spectral data cube in the x - y plane are equivalent to single-wavelength spatial mapping (Fig. 8.8f). Applying standardized (International Commission on Illumination) color matching functions to the spectral cube produces a pseudo-coloured

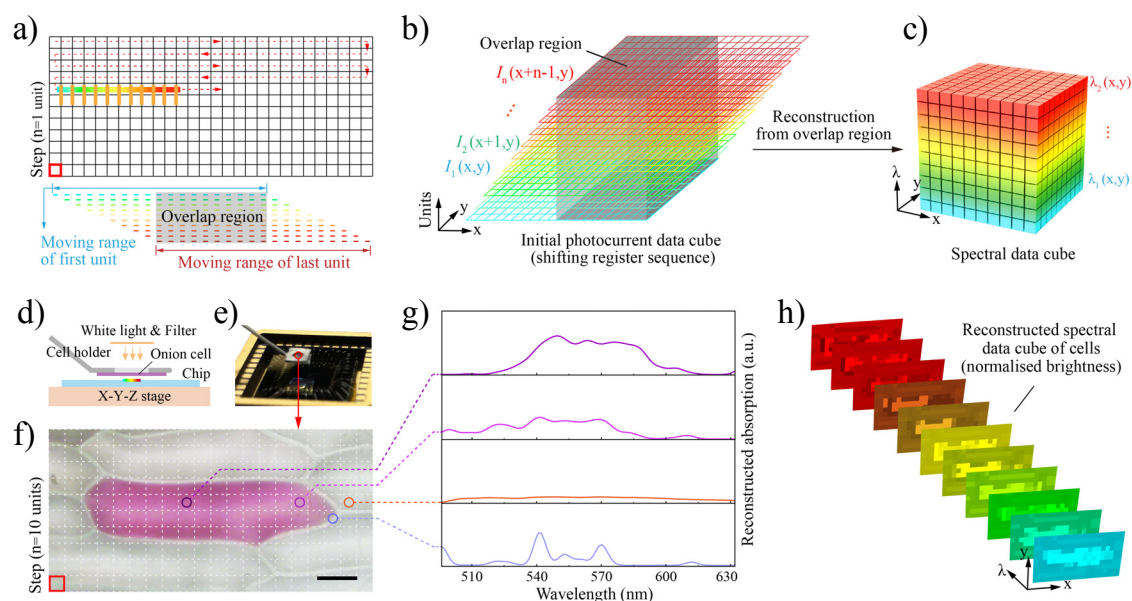


Fig. 8.9 **Spectral imaging at the micrometre scale.** (a) Schematic of spectral imaging at microscale by nanowire spectrometer. (b) Initial photocurrent data cube, where each layer is shifted because of the different location of the photodetector units. (c) Spectral data cube reconstructed from the photocurrent overlap region. (d) Schematic of the operation of cell mapping. (e) Photograph of the cell mapping apparatus. (f) Micrograph of a naturally pigmented red onion cell surrounded by transparent cells. Scale bar: $50 \mu\text{m}$. (g) Reconstructed absorption spectra from different parts of the red onion cells. (h) Absorption spectral images of onion cells at various wavelengths. Pixel intensity range of these images is normalized.

image which is consistent with the original photograph (Fig. 8.8g). In addition, the reconstructed spectra are in good agreement with conventional spectrometer measurements of the same points (Fig. 8.8h).

Furthermore, in-situ, micrometer-scale spectral imaging was demonstrated using the nanowire spectrometers, which has long been a great challenge across fields such as cytobiology and biomedicine^[350,351]. Given the typical footprint of the spectrometers is between $50 - 100 \mu\text{m}$, the scanning method above must be adapted to achieve these resolutions. A shift register strategy was adopted, which sequences the measured photocurrent data with the measurement location for each unit (Fig. 8.9a). The spectral image data cube is reconstructed from the overlapping register region of the initial photocurrent data cube (Fig. 8.9b and c). The scanning step can be any integer multiple of the electrode array's pitch, meaning the maximum resolution is limited by the width of one unit ($\sim 1 \mu\text{m}$ for current devices).

A red onion cell membrane, featuring naturally coloured cells surrounded by transparent cells, was mounted onto the holder and positioned over the nanowire spectrometer with a gap of several μm (Fig. 8.9d and e). During imaging, the nanowire spectrometer scans

across the x-y plane beneath the membrane surface, under illumination by white light through the aperture, with a fixed mapping step (Fig. 8.9f). In this case, a step size of 10 units was chosen to shorten imaging time and avoid the cell membrane drying out during the measurement. Constrained by the stage setup, imaging time is currently limited by the movement and adjustment between points, which results in a total measurement timeframe of around 1 - 2 minutes for each pixel. More sophisticated scanning or imaging technologies would allow higher resolution scans within the same timeframe. High-speed measurement could also be achieved through the development of a snapshot spectral imaging system based on a two-dimensional spectrometer array (see next chapter). The intensity maps at fixed wavelengths and reconstructed absorption spectra for different points on the onion cells (Figs. 8.9g) illustrate the potential of these spectrometers to obtain spectral images at the cellular level.

Summary

The use of individual compositionally-engineered nanowires enables an entire spectroscopy system to be miniaturized down to a scale of tens of micrometers, which could open new opportunities for almost any miniaturized spectroscopic application, including lab-on-a-chip systems, drones, implants, and wearable devices. The proof of concept demonstrated here presents a simple, versatile and ultra-compact platform that can be expanded upon through a number of avenues by altering either the hardware or software of the system. This study also offers a practical step forward for other light sensitive nanomaterials to be directly exploited for customized design of ultra-miniaturized spectroscopy systems. The next chapter shall conclude this thesis, summarising the achievements of my research, before addressing possible avenues for future investigation that can be derived from my work.

Chapter 9

Conclusion

9.1 Avenues for further research

9.1.1 Liquid-phase-exfoliated black phosphorus

Extension of the work on solution-processed black phosphorus (BP) in this thesis should initially focus on the completion of the study on the environmental stability of films produced by liquid-phase-exfoliation (LPE), which was curtailed by practical limitations, as discussed in chapter 3. A stage setup should be engineered for a Raman spectroscopy system that allows repeatable, high spatial resolution (spot size $<2 \mu\text{m}$) mapping measurements of drop cast LPE BP films, within an inert environment. The exposure of these films to pseudo-ambient environments should be carried out at increments on the order of only 30 minutes, with careful control maintained over conditions such as the temperature, light intensity and spectral characteristics. A statistically significant sample size of films must be studied so as to effectively analyse the evolution of each BP Raman peak over time. Factors such as the film thickness and the dispersion carrier solvent should also be assessed. In this way, it may be possible to develop a simple and non-contact technique for analysing the stability of these BP films; this would represent a vital characterisation tool to help, for instance, analyse the effects of different device processing steps on this sensitive material platform.

9.1.2 Advancing the single nanowire spectrometer

As illustrated by the experimental work in chapter 6, the rate-determining step in the production of these devices, and perhaps the key bottleneck for the entire nanowire spectrometer project, was the lack of available nanowires with suitable properties for device production. For any one batch of devices, the most time-consuming aspect of fabrication was the location

of potentially viable nanowires for transfer. Even then, a number of obstacles exist between transfer and the final device, that meant that only a very small fraction of these nanowires produced fully operational devices with > 30 functioning, stable units, possessing a sufficient spread of spectral information across them. These include for instance, nanowire breakage or damage during fibre-probe manipulation, extinguishing of PL emission during lift-off or an insufficient number of working, stable contacts. This dramatically limited the number of devices that could be investigated during my research, negating the possibility of any meaningful or rigorous statistical analysis that would have provided insight as to how best to further optimise these devices. Further to this, an even smaller fraction of nanowires had wavelength ranges that stretched to 650 nm, with none stretching above 660 nm, correspondingly limiting the spectral range of the final devices. Considerable inconsistency of morphological properties both between nanowires but also within nanowire structures meant also that it was impossible to control for these factors when trying to assess the influence of certain fabrication processes on, for example, the stability of electronic contact.

As such, it is evident that the area to address for the highest impact on the study as a whole is the nanowire growth and transfer stage. Growth of compositionally-graded nanowires is a far more complex challenge than those of a single material due to continually varying vapour compositions and pressures. However, if even $\sim 20\%$ of each growth batch were comprised of viable nanowires, the number of chips that could be transferred in the same period of time would increase by an estimated factor of 10 or more. An in-depth study of the effect of varying different growth parameters should be carried out, including the growth temperature range and its gradient across the furnace, the flow and type of carrier gases and the rate of movement (and thus evaporation) of pre-cursors through the chamber. The primary aim of this investigation should be to minimise variation in nanowire properties both across the growth substrate and within each nanowire structure. At the extreme, this would seek to produce nanowires with entirely homogeneous cross-sections, thicknesses and lengths. Furthermore, the gradient span of these nanowires should be from pure CdS at one end, to pure CdSe at the other, with as even as possible a gradient of bandgaps, that is, $dE_g/ds \approx \text{constant}$, where s is the distance along the wire.

The optoelectronic properties of the nanowire should also be optimised at the growth stage. Analysis by PL or OPTP spectroscopy of as-grown samples could be correlated with their growth conditions to further tailor and optimise nanowire production to produce for example, nanowires with enhanced photoluminescent efficiency and thus, higher photoconductivity. Incorporating different concentrations of dopants into the nanowire during growth could also be investigated to produce more stable electronic contact.

Even without uniform nanowire properties, a larger number of nanowires would allow a more rigorous study, with a statistically significant sample size ($n > 100$) to ascertain optimal device parameters, such as contact metal, surface treatments, and electrode widths. Such a study would also benefit from correlating all electronic measurements with the material at that section, either through PL measurements or, for instance, electron energy loss spectroscopy, as well as the nanowire width and height, as measured through AFM and SEM.

Beyond this, there are many other routes toward advancing the performance of the spectrometer, which have been discussed in more detail in section 8.1.3. At ~ 10 nm, the current resolution of the spectrometer is already sufficient for certain basic spectral imaging applications; for instance, the requirements in remote agricultural analysis can often simply be detection of the presence of very broad spectral features, with FWHM > 40 nm^[348]. However, for more detailed analyses, in for instance biological or medical hyperspectral imaging, where narrow spectral features separated by nanometres in wavelength may need to be distinguished, resolution down to the order of ~ 1 nm or below is desirable^[352]. An initial investigation should aim toward increasing the number of photodetector units, n , and experimentally studying the effect of this on reconstruction accuracy; a starting point would be to assess the minimum contact size viable for the electrode array. There are multiple considerations here including: the minimum electrode width and array pitch that can be fabricated whilst maintaining ease of lift-off, the dependence of the contact resistance and barrier behaviour as the nanowire-electrode interface is decreased and how the impingement of light on the system is affected as the pitch of the array is decreased to near- and sub-wavelength scales. Furthermore, a setup should be constructed that allows expansion of the number of contacts to upward of 100 electrodes. It should also be assessed whether it is possible to introduce new spectral responses into the system through measuring different permutations of multiple electrodes in parallel. This in theory does not introduce new spectral information to the set, as the combined response is a convolution of the individual responses, though in practicality this may not prove the case, and could allow a greater number of $R_i(\lambda)$, without actually increasing the number of physical units. Aiming further afield, toward more dramatic expansion of the system, there are a variety of areas which warrant bespoke investigations in their own right. These include: methods to deposit precisely arranged arrays of nanowires, with a view toward creating arrays of spectrometers for snapshot spectral imaging, conducting the entire device development using different material systems to expand the spectral range, and the development of machine learning-based algorithms to provide more robust and accurate reconstruction capabilities.

With respect to spectral imaging, to overcome the need for a stage scanning system with moving parts, a snapshot image sensor, in which each pixel consists of an electronically



Fig. 9.1 **Potential design for a nanowire-array-based snapshot spectral imaging device.** An array is constructed whereby each ‘pixel’ contains its own spectrometer system. Furthermore, each spectrometer system may consist of multiple nanowires operating in tandem, covering different wavelength ranges, from the mid infrared to ultraviolet.

addressed nanowire spectrometer should be developed, such as exemplified in Fig. 9.1. Furthermore, a device could be designed whereby each spectroscopic-super-pixel in this snapshot imager has multiple nanowires integrated per pixel, each covering a different waveband; from UV-VIS to near-to-midwave IR (NIR-MWIR). Current snapshot imagers are limited to mosaics of spectrally distinct bandpass filters atop image sensors providing the spatial-spectral disclination; known as multispectral filter arrays (MSFAs)^[353–355]. In MSFAs there is an inherent trade-off between spectral and spatial resolution, that is: the higher the number of spectral bands, the lower the spatial resolution, and vice versa^[355]. Our devices have potential to develop into snapshot systems operating with high spectral and spatial resolution with short acquisition time, covering broad wavebands, which has long been considered a primary target in the field of spectral imaging^[352].

9.1.3 Devices based on bandgap-gradient nanowires

As introduced in chapter 7, the embedding techniques developed in this investigation show evident potential for creating horizontally aligned graphene-coated nanowire hybrid photodetectors; such devices have not yet been reported in the literature. Clearly, a study here would lead directly on from - and complete - the work detailed in section 7.1.2, by fabricating and characterising graphene channels on top of $\text{CdS}_x\text{Se}_{1-x}$ nanowires. Particular areas to be analysed would be the photosensitivity and wavelength-dependency of graphene channels in this architecture, as well as the effect of varying the width of the graphene channels. The results in ref. 48 suggest that far higher photogain may be possible through such a system than using metallic electrodes. Backgating of this device in an FET architecture should be

investigated to assess whether this can be used to afford a greater level of control over the device properties, or enhance the stability in some way. For instance, it may be possible, by applying a different backgate voltage for each photodetector measurement, to avoid the variations in photosensitivity seen in the metal electrode devices. Photocurrent mapping would elucidate the mechanisms occurring in these devices and determine the effects of directionally-dependent waveguiding of light along the nanowire. Given the sensitivity of both of these nanomaterial components to their surrounding environment, a key element to device development would be identification of the most effective means of passivating these devices to afford long-term stability. This should begin with assessing ALD of Al_2O_3 , but could also look to other surface coatings, such as parylene-C, ALD of alternative materials, or even encapsulation in other 2d materials such as *h*-BN. Particularly considering graphene's interfacial sensitivity, effects on the device performance and stability of using different etch parameters (varying, for instance, the systems, gases and powers used) for exposing the nanowire top-surface is another area that could be investigated.

Once these initial investigations have been completed and the stability of the devices maximised, the next step would be to assess whether these hybrid devices could be used in the same way as the metal multielectrode structures, to function as a spectrometer. The same setup as used in the investigation in this thesis could be used for this purpose, without any necessary modifications. Here, the algorithm and the measurement parameters would need to be tailored appropriately, after initial measurements determine the most limiting factors for the spectral reconstruction when replacing the metal electrode architecture with this hybrid system.

Further investigation beyond this could center around assessing new device structures and mechanisms, rather than the top-gated / photogating system proposed in chapter 7. The most straightforward step in this direction, using existing techniques, and still based on a photogating mechanism, would be to instead place nanowires on top of graphene channels that have been transferred and patterned on Si:SiO₂. This avoids embedding, and may offer more stable photogating given the cleaner, flatter interface with silicon rather than the rough, etched SU-8 surfaces. More complex device designs could however look toward different basis mechanisms, for example by attempting to form direct junctions *between* the nanowire and the graphene, rather than relying on electrostatic doping by proximity. Direct transfer of charge perpendicular to the graphene plane is far less efficient than at the graphene edge, though it may be possible to address this by introducing physical damage to the graphene at the nanowire junction, through, for instance, bombardment with Ar ions. Finally, an advantage of using graphene over metallic electrodes is their transparency and flexibility, properties shared by the other components in this system - SU-8 and the nanowires. As such,

a study should be conducted where the silicon substrate is replaced with a platform such as PET, to probe the potential for flexible, transparent wavelength-dependent photodetectors, or even spectrometers.

9.2 Concluding summary

The results contained within this thesis demonstrate first and foremost that compositionally-engineered nanowires can form the basis for a new paradigm of ultra-compact spectrometers, with footprints two to three orders of magnitude below those previously reported. In order to achieve this, first, a comprehensive device fabrication framework has been developed for the creation of photodetector arrays on $\text{CdS}_x\text{Se}_{1-x}$ nanowires. This framework draws on the literature, as well as initial experimental findings to address a series of challenges posed by the material system in general, but more specifically the particular samples of as-grown nanowires available for the investigation. Included within this, a series of processes have been devised to identify, transfer and characterise nanowires that are most likely to be viable for functioning devices. Nanowire embedding techniques have been developed to allow reliable fabrication of electrode arrays at the high resolutions required. This embedding technique has also been applied to allow the hybridisation of graphene and embedded-nanowire structures for the first time. Furthermore, processes have been established to tailor the electronic behaviour at the contact through surface treatment, as well as to dramatically improve the repeatability of photoresponse measurements *via* ALD-mediated passivation.

Alongside the creation of a custom-built characterisation setup, multi-electrode nanowire devices have been designed to allow for spatially resolved measurements at between 30 and 44 points along each nanowire, including calibration of the spectral response of each photodetector unit in these arrays. Crucially, under illumination by an unknown optical signal, it has been shown that by cross-referencing these calibrated responses with the measured photocurrent for each unit, the spectrum of the incident light can be computationally reconstructed by a bespoke algorithm. Characterisation of the reconstruction accuracy in these single-nanowire spectrometers reveals competitive resolution with existing microspectrometer technology, despite the dramatic reduction in the device footprint. Furthermore a range of strategies for further enhancing the performance have been identified, through altering either the device fabrication or through changing the computational techniques used, many of which could be straightforward to achieve. The potential of these devices for spectral imaging, from the macroscopic down to the single-cellular scale, has also been illustrated, using a custom-designed point-scanning apparatus. The strategy that has been developed

could be applied to virtually any compositionally-engineered nanomaterial system, allowing great versatility in the operational wavelength range.

Further to this, the most significant, secondary findings of this thesis relate to the production of inkjet-printable black phosphorus (BP) inks for optoelectronic applications. In developing this platform, high concentration black phosphorus dispersions have been produced and characterised, with minimal degradation to the flakes. A solvent-exchange method has been devised to allow the conversion of these dispersions into inks, based on a binder-free mixture of IPA and butan-2-ol that can be reliably printed to produce highly uniform black phosphorus films, with ultra fast drying times. Raman spectroscopic analysis of deposited flakes suggests that despite multiple processing steps flakes are not significantly degraded over the course of this entire process. Parylene-C encapsulation of these films ensures their long-term stability (> 30 days), and allows their integration and use in photodetectors and lasers, under intense irradiation, without any observed drop in performance over time. These results have showcased the first scalable method for the deposition of solution-processed BP films and features with viable device performance and stability.

References

- [1] A. K. Geim, and K. S. Novoselov. “The rise of graphene.” *Nature Materials* **6**, 183 (2007).
- [2] A. K. Geim. “Graphene: status and prospects.” *Science* **324**, 1530 (2009).
- [3] K. S. Novoselov, A. K. Geim, S. V. Morozov, D. Jiang, Y. Zhang, *et al.* “Electric field effect in atomically thin carbon films.” *Science* **306**, 666 (2004).
- [4] K. S. Novoselov, V. I. Falko, L. Colombo, P. R. Gellert, M. G. Schwab, *et al.* “A roadmap for graphene.” *Nature* **490**, 192 (2012).
- [5] A. C. Ferrari, F. Bonaccorso, V. Falko, K. S. Novoselov, S. Roche, *et al.* “Science and technology roadmap for graphene, related two-dimensional crystals, and hybrid systems.” *Nanoscale* **7**, 4598 (2015).
- [6] F. Schwierz. “Graphene transistors.” *Nature Nanotechnology* **5**, 487 (2010).
- [7] R. R. Nair, P. Blake, A. N. Grigorenko, K. S. Novoselov, T. J. Booth, *et al.* “Fine Structure Constant Defines Visual Transparency of Graphene.” *Science* **320**, 2008 (2008).
- [8] H. O. H. Churchill, and P. Jarillo-Herrero. “Two-dimensional crystals: phosphorus joins the family.” *Nature Nanotechnology* **9**, 330 (2014).
- [9] A. Favron, E. Gaufrès, F. Fossard, A.-L. Phaneuf-L’Heureux, N. Y.-W. Tang, *et al.* “Photooxidation and quantum confinement effects in exfoliated black phosphorus.” *Nature Materials* **14**, 826 (2015).
- [10] N. O. Weiss, H. Zhou, L. Liao, Y. Liu, S. Jiang, *et al.* “Graphene: An emerging electronic material.” *Advanced Materials* **24**, 5782 (2012).
- [11] A. H. Castro Neto, N. M. R. Peres, K. S. Novoselov, A. K. Geim, and F. Guinea. “The electronic properties of graphene.” *Reviews of Modern Physics* **81**, 109 (2009).
- [12] E. V. Castro, H. Ochoa, M. I. Katsnelson, R. V. Gorbachev, D. C. Elias, *et al.* “Limits on electron quality in suspended graphene due to flexural phonons.” *Physical Review Letters* **105**, 266601 (2010).
- [13] J. Baringhaus, M. Ruan, F. Edler, A. Tejada, M. Sicot, *et al.* “Exceptional ballistic transport in epitaxial graphene nanoribbons.” *Nature* **506**, 349 (2014).

- [14] D. G. Purdie, N. M. Pugno, T. Taniguchi, K. Watanabe, A. C. Ferrari, *et al.* “Cleaning Interfaces in Layered Materials Heterostructures.” *Nature Communications* 1–12 (2018).
- [15] R. R. Nair, P. Blake, A. N. Grigorenko, K. S. Novoselov, T. J. Booth, *et al.* “Universal Dynamic Conductivity and Quantized Visible Opacity of Suspended Graphene.” *Science* **320**, 1308 (2008).
- [16] T. Mueller, F. Xia, and P. Avouris. “Graphene photodetectors for high-speed optical communications.” *Nature Photonics* **4**, 297 (2010).
- [17] P. A. George, J. Strait, J. Dawlaty, S. Shivaraman, M. Chandrashekar, *et al.* “Spectroscopy of the Carrier Relaxation Epitaxial Graphene.” *Nano Letters* **8**, 17 (2008).
- [18] D. Brida, A. Tomadin, C. Manzoni, Y. J. Kim, A. Lombardo, *et al.* “Ultrafast collinear scattering and carrier multiplication in graphene.” *Nature Communications* **4**, 1987 (2013).
- [19] A. A. Balandin. “Thermal properties of graphene and nanostructured carbon materials.” *Nat. Mater.* **10**, 569 (2011).
- [20] C. Lee, X. Wei, J. W. Kysar, and J. Hone. “Measurement of the elastic properties and intrinsic strength of monolayer graphene.” *Science* **321**, 385 (2008).
- [21] Y. Lin, C. Dimitrakopoulos, K. A. Jenkins, D. B. Farmer, H. Chiu, *et al.* “100-GHz Transistors from Wafer-Scale Epitaxial Graphene.” *Science* **327**, 100 (2010).
- [22] L. Liao, Y.-C. Lin, M. Bao, R. Cheng, J. Bai, *et al.* “High-speed graphene transistors with a self-aligned nanowire gate.” *Nature* **467**, 305 (2010).
- [23] L. Liao, and X. Duan. “Graphene for radio frequency electronics.” *Materials Today* **15**, 328 (2012).
- [24] S. A. Wolf, D. D. Awschalom, R. A. Buhrman, J. M. Daughton, and S. V. Molna. “Spintronics : A Spin-Based Electronics Vision for the Future.” *Science* **294**, 1488 (2001).
- [25] M. Zhou, Y. Zhai, and S. Dong. “Electrochemical Sensing and Biosensing Platform Based on Chemically Reduced Graphene Oxide Supporting Information (SI).” *Analytical chemistry* **81**, 5603 (2009).
- [26] Y. Wang, Z. Shi, Y. Huang, Y. Ma, C. Wang, *et al.* “Supercapacitor Devices Based on Graphene Materials.” *The Journal of Physical Chemistry C* **113**, 13103 (2009).
- [27] J. R. Miller, R. A. Outlaw, and B. C. Holloway. “Graphene double-layer capacitor with ac line-filtering performance.” *Science* **329**, 1637 (2010).
- [28] M. F. El-Kady, and R. B. Kaner. “Scalable fabrication of high-power graphene micro-supercapacitors for flexible and on-chip energy storage.” *Nature communications* **4**, 1475 (2013).
- [29] T. Liu, M. Leskes, W. Yu, A. J. Moore, L. Zhou, *et al.* “Cycling Li-O₂ batteries via LiOH formation and decomposition.” *Science* **350**, 530 (2015).

- [30] O. Y. Loh, and H. D. Espinosa. “Nanoelectromechanical contact switches.” *Nature Nanotechnology* **7**, 283 (2012).
- [31] S. J. Heerema, and C. Dekker. “Graphene nanodevices for DNA sequencing.” *Nature Nanotechnology* **11**, 127 (2016).
- [32] F. H. L. Koppens, T. Mueller, P. Avouris, A. C. Ferrari, M. S. Vitiello, *et al.* “Photodetectors based on graphene, other two-dimensional materials and hybrid systems.” *Nature Nanotechnology* **9**, 780 (2014).
- [33] A. N. Grigorenko, M. Polini, and K. S. Novoselov. “Graphene plasmonics.” *Nature Photonics* **6**, 749 (2012).
- [34] F. J. G. de Abajo. “Graphene Nanophotonics.” *Science* **339**, 917 (2013).
- [35] P. Alonso-González, A. Y. Nikitin, F. Golmar, A. Centeno, A. Pesquera, *et al.* “Controlling graphene plasmons with resonant metal antennas and spatial conductivity patterns.” *Science* **344**, 1369 (2014).
- [36] Z. Q. Li, E. A. Henriksen, Z. Jiang, Z. Hao, M. C. Martin, *et al.* “Dirac charge dynamics in graphene by infrared spectroscopy.” *Nature Physics* **4**, 6 (2008).
- [37] D. Popa, Z. Sun, F. Torrisi, T. Hasan, F. Wang, *et al.* “Sub 200 fs pulse generation from a graphene mode-locked fiber laser.” *Applied Physics Letters* **97**, 203106 (2010).
- [38] Z. Sun, T. Hasan, F. Torrisi, D. Popa, G. Privitera, *et al.* “Graphene mode-locked ultrafast laser.” *ACS Nano* **4**, 803 (2010).
- [39] A. Kumar, and C. Zhou. “The race to replace tin-doped indium oxide: Which material will win?” *ACS Nano* **4**, 11 (2010).
- [40] X. Huang, Z. Zeng, Z. Fan, J. Liu, and H. Zhang. “Graphene-based electrodes.” *Advanced Materials* **24**, 5979 (2012).
- [41] J.-H. Ahn, and B. H. Hong. “Graphene for displays that bend.” *Nature Nanotechnology* **9**, 737 (2014).
- [42] K. I. Bolotin, K. J. Sikes, Z. Jiang, M. Klima, G. Fudenberg, *et al.* “Ultrahigh electron mobility in suspended graphene.” *Solid State Communications* **146**, 351 (2008).
- [43] Y. C. Lin, C. C. Lu, C. H. Yeh, C. Jin, K. Suenaga, *et al.* “Graphene annealing: How clean can it be?” *Nano Letters* **12**, 414 (2012).
- [44] N. Mohanty, and V. Berry. “Graphene-based single-bacterium resolution biodevice and DNA transistor: Interfacing graphene derivatives with nanoscale and microscale biocomponents.” *Nano Letters* **8**, 4469 (2008).
- [45] Y. Ohno, K. Maehashi, Y. Yamashiro, and K. Matsumoto. “Electrolyte-gated graphene field-effect transistors for detecting pH and protein adsorption.” *Nano Letters* **9**, 3318 (2009).
- [46] M. Steenackers, A. M. Gigler, N. Zhang, F. Deubel, M. Seifert, *et al.* “Polymer brushes on graphene.” *Journal of the American Chemical Society* **133**, 10490 (2011).

- [47] K. Kostarelos, and K. S. Novoselov. “Exploring the Interface of Graphene and Biology.” *Science* **344**, 261 (2014).
- [48] G. Konstantatos, M. Badioli, L. Gaudreau, J. Osmond, M. Bernechea, *et al.* “Hybrid graphene–quantum dot phototransistors with ultrahigh gain.” *Nature Nanotechnology* **7**, 363 (2012).
- [49] S. Huang, and X. Ling. “Black Phosphorus: Optical Characterization, Properties and Applications.” *Small* **13**, 1700823 (2017).
- [50] L. Li, Y. Yu, G. J. Ye, Q. Ge, X. Ou, *et al.* “Black phosphorus field-effect transistors.” *Nature Nanotechnology* **9**, 372 (2014).
- [51] A. Castellanos-Gomez, L. Vicarelli, E. Prada, J. O. Island, K. L. Narasimha-Acharya, *et al.* “Isolation and characterization of few-layer black phosphorus.” *2D Materials* **1**, 025001 (2014).
- [52] T. Low, A. S. Rodin, A. Carvalho, Y. Jiang, H. Wang, *et al.* “Tunable optical properties of multilayer black phosphorus thin films.” *Physical Review B - Condensed Matter and Materials Physics* **90**, 3 (2014).
- [53] V. Tran, R. Soklaski, Y. Liang, and L. Yang. “Layer-controlled band gap and anisotropic excitons in few-layer black phosphorus.” *Physical Review B* **89**, 235319 (2014).
- [54] A. Carvalho, M. Wang, X. Zhu, A. S. Rodin, H. Su, *et al.* “Phosphorene: from theory to applications.” *Nature Reviews Materials* **1** (2016).
- [55] H. Liu, A. Neal, Z. Zhen, Z. Luo, X. Xu, *et al.* “Phosphorene : An Unexplored 2D Semiconductor with a High Hole Mobility.” *ACS Nano* **8**, 4033 (2014).
- [56] F. Xia, H. Wang, and Y. Jia. “Rediscovering black phosphorus as an anisotropic layered material for optoelectronics and electronics.” *Nature Communications* **5**, 4458 (2014).
- [57] J. Qiao, X. Kong, Z.-X. Hu, F. Yang, and W. Ji. “High-mobility transport anisotropy and linear dichroism in few-layer black phosphorus.” *Nature Communications* **5**, 4475 (2014).
- [58] F. Xia, H. Wang, D. Xiao, M. Dubey, and A. Ramasubramaniam. “Two-dimensional material nanophotonics.” *Nature Photonics* **8**, 899 (2014).
- [59] B. Radisavljevic, A. Radenovic, J. Brivio, V. Giacometti, and A. Kis. “Single-layer MoS2 transistors.” *Nature nanotechnology* **6**, 147 (2011).
- [60] H. Yuan, X. Liu, F. Afshinmanesh, W. Li, G. Xu, *et al.* “Polarization-sensitive broadband photodetector using a black phosphorus vertical p-n junction.” *Nature Nanotechnology* **10**, 1 (2015).
- [61] X. Wang, A. M. Jones, K. L. Seyler, V. Tran, Y. Jia, *et al.* “Highly anisotropic and robust excitons in monolayer black phosphorus.” *Nature Nanotechnology* **10**, 517 (2015).

- [62] R. Fei, A. Faghaninia, R. Soklaski, J.-A. Yan, C. Lo, *et al.* “Enhanced Thermoelectric Efficiency via Orthogonal Electrical and Thermal Conductances in Phosphorene.” *Nano Letters* **14**, 6393 (2014).
- [63] S. Sonde, L. Tao, N. Lu, and D. Akinwande. “Flexible Black Phosphorus Ambipolar Transistors, Circuits and AM Demodulator.” *Nano Letters* **15**, 1883 (2015).
- [64] J. O. Island, G. A. Steele, H. S. J. van der Zant, and A. Castellanos-Gomez. “Environmental instability of few-layer black phosphorus.” *2D Materials* **2**, 011002 (2015).
- [65] V. Tayari, N. Hemsworth, I. Fakih, A. Favron, E. Gaufrès, *et al.* “Two-Dimensional Magnetotransport in a Black Phosphorus Naked Quantum Well.” *Nature Communications* **6**, 1 (2014).
- [66] R. Gusmao, Z. Sofer, and M. Pumera. “Black Phosphorus Rediscovered : From Bulk Material to Monolayers.” *Angewandte Chemie International Edition* **56**, 8052 (2017).
- [67] J. D. Wood, S. A. Wells, D. Jariwala, K.-S. Chen, E. Cho, *et al.* “Effective passivation of exfoliated black phosphorus transistors against ambient degradation.” *Nano Letters* **14**, 6964 (2014).
- [68] X. Chen, Y. Wu, Z. Wu, Y. Han, S. Xu, *et al.* “High-quality sandwiched black phosphorus heterostructure and its quantum oscillations.” *Nature Communications* **6**, 7315 (2015).
- [69] F. Bonaccorso, A. Lombardo, T. Hasan, Z. Sun, L. Colombo, *et al.* “Production and processing of graphene and 2d crystals.” *Materials Today* **15**, 564 (2012).
- [70] W. Kern, and G. L. Schnable. “Low-Pressure Chemical Vapor Deposition for Very Large-Scale Integration Processing - A Review.” *IEEE Trans Electron Devices* **26**, 647 (1979).
- [71] X. Li, W. Cai, L. Colombo, and R. S. Ruoff. “Evolution of graphene growth on Ni and Cu by carbon isotope labeling.” *Nano letters* **9**, 4268 (2009).
- [72] A. Reina, X. Jia, J. Ho, D. Nezich, H. Son, *et al.* “Large area, few-layer graphene films on arbitrary substrates by chemical vapor deposition.” *Nano letters* **9**, 30 (2009).
- [73] R. S. Weatherup, B. Dlubak, and S. Hofmann. “Kinetic Control of Catalytic CVD for High-Quality Graphene at Low Temperatures.” *ACS nano* **6**, 9996 (2012).
- [74] R. S. Weatherup, B. C. Bayer, R. Blume, C. Baetz, P. R. Kidambi, *et al.* “On the mechanisms of Ni-catalysed graphene chemical vapour deposition.” *Chemphyschem : a European journal of chemical physics and physical chemistry* **13**, 2544 (2012).
- [75] X. Li, W. Cai, J. An, S. Kim, J. Nah, *et al.* “Large-area synthesis of high-quality and uniform graphene films on copper foils.” *Science* **324**, 1312 (2009).
- [76] N. Petrone, C. R. Dean, I. Meric, A. M. van der Zande, P. Y. Huang, *et al.* “Chemical vapor deposition-derived graphene with electrical performance of exfoliated graphene.” *Nano letters* **12**, 2751 (2012).

- [77] Y. Lee, S. Bae, H. Jang, S. Jang, S.-E. Zhu, *et al.* “Wafer-scale synthesis and transfer of graphene films.” *Nano Letters* **10**, 490 (2010).
- [78] O. V. Yazyev, and S. G. Louie. “Electronic transport in polycrystalline graphene.” *Nature materials* **9**, 806 (2010).
- [79] P. Y. Huang, C. S. Ruiz-Vargas, A. M. van der Zande, W. S. Whitney, M. P. Levendorf, *et al.* “Grains and grain boundaries in single-layer graphene atomic patchwork quilts.” *Nature* **469**, 389 (2011).
- [80] D. L. Duong, G. H. Han, S. M. Lee, F. Gunes, E. S. Kim, *et al.* “Probing graphene grain boundaries with optical microscopy.” *Nature* **490**, 235 (2012).
- [81] Z. Fei, A. S. Rodin, W. Gannett, S. Dai, W. Regan, *et al.* “Electronic and plasmonic phenomena at graphene grain boundaries.” *Nature Nanotechnology* **8**, 821 (2013).
- [82] Q. Yu, L. a. Jauregui, W. Wu, R. Colby, J. Tian, *et al.* “Control and characterization of individual grains and grain boundaries in graphene grown by chemical vapour deposition.” *Nature materials* **10**, 443 (2011).
- [83] X. Li, Y. Zhu, W. Cai, M. Borysiak, B. Han, *et al.* “Transfer of large-area graphene films for high-performance transparent conductive electrodes.” *Nano Letters* **9**, 4359 (2009).
- [84] C. Neumann, S. Reichardt, P. Venezuela, M. Drögeler, L. Banszerus, *et al.* “Raman spectroscopy as probe of nanometre-scale strain variations in graphene.” *Nature Communications* **6**, 8429 (2015).
- [85] H. Li, J. Wu, X. Huang, Z. Yin, J. Liu, *et al.* “A universal, rapid method for clean transfer of nanostructures onto various substrates.” *ACS Nano* **8**, 6563 (2014).
- [86] J. W. Suk, W. H. Lee, J. Lee, H. Chou, R. D. Piner, *et al.* “Enhancement of the electrical properties of graphene grown by chemical vapor deposition via controlling the effects of polymer residue.” *Nano Letters* **13**, 1462 (2013).
- [87] V. Nicolosi, M. Chhowalla, M. G. Kanatzidis, M. S. Strano, and J. N. Coleman. “Liquid Exfoliation of Layered Materials.” *Science* **340**, 1226419 (2013).
- [88] D. Hanlon, C. Backes, E. Doherty, C. S. Cucinotta, N. C. Berner, *et al.* “Liquid exfoliation of solvent-stabilized few-layer black phosphorus for applications beyond electronics.” *Nature Communications* **6**, 8563 (2015).
- [89] Y. Hernandez, V. Nicolosi, M. Lotya, F. M. Blighe, Z. Sun, *et al.* “High-yield production of graphene by liquid-phase exfoliation of graphite.” *Nature Nanotechnology* **3**, 563 (2008).
- [90] M. Lotya, Y. Hernandez, P. J. King, R. J. Smith, V. Nicolosi, *et al.* “Liquid Phase Production of Graphene by Exfoliation of Graphite in Surfactant / Water Solutions.” *Journal of the American Chemical Society* **131**, 3611 (2009).
- [91] G. Eda, G. Fanchini, and M. Chhowalla. “Large-area ultrathin films of reduced graphene oxide as a transparent and flexible electronic material.” *Nature Nanotechnology* **3**, 270 (2008).

- [92] M. Li, R. B. Bhiladvala, T. J. Morrow, J. A. Sioss, K.-K. Lew, *et al.* “Bottom-up assembly of large-area nanowire resonator arrays.” *Nature Nanotechnology* **3**, 88 (2008).
- [93] A. A. Green, and M. C. Hersam. “Solution phase production of graphene with controlled thickness via density differentiation.” *Nano Letters* **9**, 4031 (2009).
- [94] J. R. Brent, N. Savjani, E. A. Lewis, S. J. Haigh, D. J. Lewis, *et al.* “Production of few-layer phosphorene by liquid exfoliation of black phosphorus.” *Chemical Communications* **50**, 13338 (2014).
- [95] Y. Hernandez, M. Lotya, D. Rickard, S. D. Bergin, and J. N. Coleman. “Measurement of multicomponent solubility parameters for graphene facilitates solvent discovery.” *Langmuir* **26**, 3208 (2010).
- [96] G. Cunningham, M. Lotya, C. S. Cucinotta, S. Sanvito, S. D. Bergin, *et al.* “Solvent Exfoliation of Transition Metal Dichalcogenides : Dispersability of Exfoliated Nanosheets Varies Only Weakly Between Compounds.” *ACS Nano* **6**, 3468 (2012).
- [97] J. M. Hughes, D. Aherne, and J. N. Coleman. “Generalizing solubility parameter theory to apply to one- and two-dimensional solutes and to incorporate dipolar interactions.” *Journal of Applied Polymer Science* **127**, 4483 (2013).
- [98] F. Torrisci, T. Hasan, W. Wu, Z. Sun, A. Lombardo, *et al.* “Inkjet-printed graphene electronics.” *ACS Nano* **6**, 2992 (2012).
- [99] P. Yasaei, B. Kumar, T. Foroozan, C. Wang, M. Asadi, *et al.* “High-Quality Black Phosphorus Atomic Layers by Liquid-Phase Exfoliation.” *Advanced Materials* **27**, 1887 (2015).
- [100] J. Kang, J. D. Wood, S. A. Wells, J. H. Lee, X. Liu, *et al.* “Solvent exfoliation of electronic-grade, two-dimensional black phosphorus.” *ACS Nano* **9**, 3596 (2015).
- [101] J. N. Coleman, M. Lotya, A. O’Neill, S. D. Bergin, P. J. King, *et al.* “Two-Dimensional Nanosheets Produced by Liquid Exfoliation of Layered Materials.” *Science* **331**, 568 (2011).
- [102] D. J. Finn, M. Lotya, G. Cunningham, R. J. Smith, D. McCloskey, *et al.* “Inkjet deposition of liquid-exfoliated graphene and MoS₂ nanosheets for printed device applications.” *Journal of Materials Chemistry C* **2**, 925 (2014).
- [103] K. Lee, H. Y. Kim, M. Lotya, J. N. Coleman, G. T. Kim, *et al.* “Electrical characteristics of molybdenum disulfide flakes produced by liquid exfoliation.” *Advanced Materials* **23**, 4178 (2011).
- [104] L. M. Malard, M. A. Pimenta, G. Dresselhaus, and M. S. Dresselhaus. “Raman spectroscopy in graphene.” *Physics Reports* **473**, 51 (2009).
- [105] A. Das, S. Pisana, B. Chakraborty, S. Piscanec, S. K. Saha, *et al.* “Monitoring dopants by Raman scattering in an electrochemically top-gated graphene transistor.” *Nature Nanotechnology* **3**, 210 (2008).

- [106] A. Singha, P. Dhar, and A. Roy. “A nondestructive tool for nanomaterials: Raman and photoluminescence spectroscopy.” *American Journal of Physics* **73**, 224 (2005).
- [107] A. C. Ferrari, J. C. Meyer, V. Scardaci, C. Casiraghi, M. Lazzeri, *et al.* “Raman Spectrum of Graphene and Graphene Layers.” *Physical Review Letters* **97**, 187401 (2006).
- [108] A. C. Ferrari, and D. M. Basko. “Raman spectroscopy as a versatile tool for studying the properties of graphene.” *Nature Nanotechnology* **8**, 235 (2013).
- [109] R. F. Begley. “Coherent anti-Stokes Raman spectroscopy.” *Applied Physics Letters* **25**, 387 (1974).
- [110] A. C. Ferrari. “Raman spectroscopy of graphene and graphite: Disorder, electron–phonon coupling, doping and nonadiabatic effects.” *Solid State Communications* **143**, 47 (2007).
- [111] L. G. Cançado, A. Jorio, E. H. M. Ferreira, F. Stavale, C. a. Achete, *et al.* “Quantifying defects in graphene via Raman spectroscopy at different excitation energies.” *Nano Letters* **11**, 3190 (2011).
- [112] H. B. Ribeiro, M. A. Pimenta, and C. J. S. D. Matos. “Raman spectroscopy in black phosphorus.” *Journal of Raman Spectroscopy* **49**, 76 (2018).
- [113] A. L. Phaneuf-L’Heureux, A. Favron, J. F. Germain, P. Lavoie, P. Desjardins, *et al.* “Polarization-Resolved Raman Study of Bulk-like and Davydov-Induced Vibrational Modes of Exfoliated Black Phosphorus.” *Nano Letters* **16**, 7761 (2016).
- [114] J. Kim, J. U. Lee, J. Lee, H. J. Park, Z. Lee, *et al.* “Anomalous polarization dependence of Raman scattering and crystallographic orientation of black phosphorus.” *Nanoscale* **7**, 18708 (2015).
- [115] G. Hu, T. Albrow-Owen, X. Jin, A. Ali, Y. Hu, *et al.* “Black phosphorus ink formulation for inkjet printing of optoelectronics and photonics.” *Nature Communications* **8**, 278 (2017).
- [116] H. Sirringhaus, T. Kawase, R. H. Friend, and T. Shimoda. “High-Resolution Inkjet Printing of All-Polymer Transistor Circuits.” *Science* **290**, 2123 (2000).
- [117] F. Bonaccorso, A. Bartolotta, J. N. Coleman, and C. Backes. “2D-Crystal-Based Functional Inks.” *Advanced Materials* 6136–6166 (2016).
- [118] D. Jang, D. Kim, and J. Moon. “Influence of Fluid Physical Properties on Ink-Jet Printability.” *Langmuir* **25**, 2629 (2009).
- [119] T. H. J. van Osch, J. Perelaer, A. W. M. de Laat, and U. S. Schubert. “Inkjet Printing of Narrow Conductive Tracks on Untreated Polymeric Substrates.” *Advanced Materials* **20**, 343 (2008).
- [120] P. G. D. Gennes. “Wetting: statics and dynamics.” *Reviews of Modern Physics* **57**, 827 (1985).

- [121] R. D. Deegan, O. Bakajin, T. F. Dupont, G. Huber, S. R. Nagel, *et al.* “Capillary flow as the cause of ring stains from dried liquid drops.” *Nature* **389**, 827 (1997).
- [122] D. McManus, S. Vranic, F. Withers, V. Sanchez-Romaguera, M. Macucci, *et al.* “Water-based and biocompatible 2D crystal inks for all-inkjet-printed heterostructures.” *Nature Nanotechnology* (2017).
- [123] T. Carey, S. Cacovich, G. Divitini, J. Ren, A. Mansouri, *et al.* “Fully inkjet-printed two-dimensional material field-effect heterojunctions for wearable and textile electronics.” *Nature Communications* **8** (2017).
- [124] A. G. Kelly, D. Finn, A. Harvey, T. Hallam, and J. N. Coleman. “All-printed capacitors from graphene-BN-graphene nanosheet heterostructures.” *Applied Physics Letters* **109**, 1 (2016).
- [125] A. O’Neill, U. Khan, P. N. Nirmalraj, J. Boland, and J. N. Coleman. “Graphene dispersion and exfoliation in low boiling point solvents.” *Journal of Physical Chemistry C* **115**, 5422 (2011).
- [126] J. Kang, J. D. Wood, S. A. Wells, J. H. Lee, X. Liu, *et al.* “Solvent exfoliation of electronic-grade, two-dimensional black phosphorus.” *ACS Nano* **9**, 3596 (2015).
- [127] C. Backes, R. J. Smith, N. McEvoy, N. C. Berner, D. McCloskey, *et al.* “Edge and confinement effects allow in situ measurement of size and thickness of liquid-exfoliated nanosheets.” *Nature Communications* **5**, 1 (2014).
- [128] Z. Guo, H. Zhang, S. Lu, Z. Wang, S. Tang, *et al.* “From Black Phosphorus to Phosphorene: Basic Solvent Exfoliation, Evolution of Raman Scattering, and Applications to Ultrafast Photonics.” *Advanced Functional Materials* 6996–7002 (2015).
- [129] R. Hultgren, N. S. Gingrich, and B. E. Warren. “The atomic distribution in red and black phosphorus and the crystal structure of black phosphorus.” *The Journal of Chemical Physics* **3**, 351 (1935).
- [130] H. Hu, and R. G. Larson. “Marangoni effect reverses coffee-ring depositions.” *Journal of Physical Chemistry B* **110**, 7090 (2006).
- [131] T. Yu, F. Wang, Y. Xu, L. Ma, X. Pi, *et al.* “Graphene Coupled with Silicon Quantum Dots for High-Performance Bulk-Silicon-Based Schottky-Junction Photodetectors.” *Advanced Materials* 4912–4919 (2016).
- [132] Y. Chen, S. Chen, J. Liu, Y. Gao, and W. Zhang. “Sub-300 femtosecond soliton tunable fiber laser with all-anomalous dispersion passively mode locked by black phosphorus.” *Optics Express* **24**, 13316 (2016).
- [133] C. M. Lieber. “Nanoscale Science and Technology: Building a Big Future from Small Things.” *MRS Bulletin* **28**, 486 (2003).
- [134] W. Lu, and C. M. Lieber. “Nanoelectronics from the bottom up.” *Nature Materials* **6**, 841 (2007).
- [135] C. M. Lieber, and Z. L. Wang. “Functional Nanowires.” *MRS Bulletin* **32**, 99 (2007).

- [136] C. M. Lieber. “Semiconductor nanowires: A platform for nanoscience and nanotechnology.” In “Materials Research Society Fall Meeting,” , vol. 361052–1063 (2012).
- [137] W. Lu, and C. M. Lieber. “Semiconductor nanowires.” *Journal of Physics D-Applied Physics* **39**, R387 (2006).
- [138] Y. Li, F. Qian, J. Xiang, and C. M. Lieber. “Nanowire electronic and optoelectronic devices.” *Materials Today* **9**, 18 (2006).
- [139] H. J. Joyce, Q. Gao, H. Hoe Tan, C. Jagadish, Y. Kim, *et al.* “III–V semiconductor nanowires for optoelectronic device applications.” *Progress in Quantum Electronics* **35**, 23 (2011).
- [140] T. Q. Trung, and N. E. Lee. “Materials and devices for transparent stretchable electronics.” *Journal of Materials Chemistry C* **5**, 2202 (2017).
- [141] X. Liu, Y. Z. Long, L. Liao, X. Duan, and Z. Fan. “Large-scale integration of semiconductor nanowires for high-performance flexible electronics.” *ACS Nano* **6**, 1888 (2012).
- [142] Y. Xia, P. Yang, Y. Sun, Y. Wu, B. Mayers, *et al.* “One-dimensional nanostructures synthesis characterization and applications.” *Advanced Materials* 353–389 (2003).
- [143] N. P. Dasgupta, J. Sun, C. Liu, S. Brittman, S. C. Andrews, *et al.* “25th anniversary article: Semiconductor nanowires - Synthesis, characterization, and applications.” *Advanced Materials* **26**, 2137 (2014).
- [144] M. Law, J. Goldberger, and P. Yang. “Semiconductor Nanowires and Nanotubes.” *Annual Review of Materials Research* **34**, 83 (2004).
- [145] O. Hayden, R. Agarwal, and W. Lu. “Semiconductor nanowire devices.” *Nano Today* **3**, 12 (2008).
- [146] B. Tian, T. J. Kempa, and C. M. Lieber. “Single nanowire photovoltaics.” *Chemical Society Reviews* **38**, 165 (2009).
- [147] X. Zhuang, C. Z. Ning, and A. Pan. “Composition and Bandgap-Graded Semiconductor Alloy Nanowires.” *Advanced Materials* **24**, 13 (2012).
- [148] C. Couteau, A. Larrue, C. Wilhelm, and C. Soci. “Nanowire lasers.” *Nanophotonics* **4**, 90 (2015).
- [149] S. W. Eaton, A. Fu, A. B. Wong, C.-Z. Ning, and P. Yang. “Semiconductor Nanowire Lasers.” *Nature Reviews Materials* **1**, 455 (2016).
- [150] X. Duan, Y. Huang, Y. Cui, J. Wang, and C. M. Lieber. “Indium phosphide nanowires as building blocks for nanoscale electronic and optoelectronic devices.” *Nature* **409**, 66 (2001).
- [151] F. X. Liang, J. Z. Wang, Z. P. Li, and L. B. Luo. “Near-Infrared-Light Photodetectors Based on One-Dimensional Inorganic Semiconductor Nanostructures.” *Advanced Optical Materials* **5**, 1 (2017).

- [152] Y. Zou, Y. Zhang, Y. Hu, and H. Gu. “Ultraviolet detectors based on wide bandgap semiconductor nanowire: A review.” *Sensors* **18**, 1 (2018).
- [153] P. Feng, F. Shao, Y. Shi, and Q. Wan. “Gas sensors based on semiconducting nanowire field-effect transistors.” *Sensors* **14**, 17406 (2014).
- [154] W. Zhou, X. Dai, and C. M. Lieber. “Advances in nanowire bioelectronics.” *Reports on Progress in Physics* **80** (2017).
- [155] Y. Su, C. Liu, S. Brittman, J. Tang, A. Fu, *et al.* “Single-nanowire photoelectrochemistry.” *Nature Nanotechnology* **11**, 609 (2016).
- [156] C. Liu, N. P. Dasgupta, and P. Yang. “Semiconductor nanowires for artificial photosynthesis.” *Chemistry of Materials* **26**, 415 (2014).
- [157] P. Yu, J. Wu, S. Liu, J. Xiong, C. Jagadish, *et al.* “Design and fabrication of silicon nanowires towards efficient solar cells.” *Nano Today* **11**, 704 (2016).
- [158] P. Krogstrup, H. I. Jørgensen, M. Heiss, O. Demichel, J. V. Holm, *et al.* “Single-nanowire solar cells beyond the Shockley–Queisser limit.” *Nature Photonics* **7**, 306 (2013).
- [159] A. Ali, Y. Chen, V. Vasiraju, and S. Vaddiraju. “Nanowire-based thermoelectrics.” *Nanotechnology* **28** (2017).
- [160] C. N. Prinz. “Interactions between semiconductor nanowires and living cells.” *Journal of Physics Condensed Matter* **27** (2015).
- [161] S. Gazibegovic, D. Car, H. Zhang, S. C. Balk, J. A. Logan, *et al.* “Epitaxy of advanced nanowire quantum devices.” *Nature* **548**, 434 (2017).
- [162] T. Reuter, O. Vidoni, V. Torma, G. Schmid, L. Nan, *et al.* “Two-Dimensional Networks via Quasi One-Dimensional Arrangements of Gold Clusters.” *Nano Letters* **2**, 709 (2002).
- [163] K.-S. Cho, D. V. Talapin, W. Gaschler, and C. B. Murray. “Designing PbSe nanowires and nanorings through oriented attachment of nanoparticles.” *Journal of the American Chemical Society* **127**, 7140 (2005).
- [164] Z. Tang, N. A. Kotov, and M. Giersig. “Spontaneous Organization of Single CdTe Nanoparticles into Luminescent Nanowires.” *Science* **297**, 237 (2002).
- [165] N. Pradhan, H. Xu, and X. Peng. “Colloidal CdSe quantum wires by oriented attachment.” *Nano Letters* **6**, 720 (2006).
- [166] R. S. Wagner, and W. C. Ellis. “Vapor-Liquid-Solid Mechanism of Single Crystal Growth.” *Applied Physics Letters* **4**, 89 (1964).
- [167] A. M. Morales, and C. M. Lieber. “A Laser Ablation Method for the Synthesis of Crystalline Semiconductor Nanowires.” *Science* **279**, 208 (1998).
- [168] Y. Wu, and P. Yang. “Direct observation of vapor-liquid-solid nanowire growth.” *Journal of the American Chemical Society* **123**, 3165 (2001).

- [169] S. A. Dayeh, N. H. MacK, J. Y. Huang, and S. T. Picraux. “Advanced core/multishell germanium/silicon nanowire heterostructures: The Au-diffusion bottleneck.” *Applied Physics Letters* **99**, 11 (2011).
- [170] K. A. Dick, K. Deppert, L. S. Karlsson, L. R. Wallenberg, L. Samuelson, *et al.* “A New Understanding of Au-Assisted Growth of III-V Semiconductor Nanowires.” *Advanced Functional Materials* **15**, 1603 (2005).
- [171] M. T. Borgström, J. Wallentin, J. Trägårdh, P. Ramvall, M. Ek, *et al.* “In situ etching for total control over axial and radial nanowire growth.” *Nano Research* **3**, 264 (2010).
- [172] K. A. Dick, K. Deppert, M. W. Larsson, T. Mårtensson, W. Seifert, *et al.* “Synthesis of branched ‘nanotrees’ by controlled seeding of multiple branching events.” *Nature Materials* **3**, 1 (2004).
- [173] Y. Wu, Y. Cui, L. Huynh, C. J. Barrelet, D. C. Bell, *et al.* “Controlled Growth and Structures of Molecular-Scale Silicon Nanowires.” *Nano Letters* **4**, 433 (2004).
- [174] R. E. Algra, M. A. Verheijen, M. T. Borgstro, E. Vlieg, and E. P. A. M. Bakkers. “Twinning superlattices in indium phosphide nanowires.” *Nature* **456**, 369 (2008).
- [175] H. J. Joyce, Q. Gao, H. H. Tan, C. Jagadish, and Y. Kim. “Twin-Free Uniform Epitaxial GaAs Nanowires Grown by a Two-Temperature Process.” *Nano Letters* **7**, 921 (2007).
- [176] H. J. Joyce, J. Wong-leung, Q. Gao, H. H. Tan, and C. Jagadish. “Phase Perfection in Zinc Blende and Wurtzite III - V Nanowires Using Basic Growth Parameters.” *Nano Letters* **10**, 908 (2010).
- [177] B. Mandl, K. A. Dick, D. Kriegner, M. Keplinger, G. Bauer, *et al.* “Crystal structure control in Au-free self-seeded InSb wire growth.” *Nanotechnology* **22** (2011).
- [178] T. Martensson, M. Borgstrom, W. Seifert, B. J. Ohlsson, and L. Samuelson. “Fabrication of individually seeded nanowire arrays by vapour – liquid – solid.” *Nanotechnology* **14**, 1255 (2003).
- [179] A. I. Yanson, G. R. Bollinger, H. E. van den Brom, N. Agrait, and J. M. V. Ruitenbeek. “Formation and manipulation of a metallic wire of single gold atoms.” *Nature* **395**, 783 (1998).
- [180] A. L. Efros, and M. Rosen. “The electronic structure of semiconductor nanocrystals.” *Annual Review of Materials Science* **30**, 475 (2000).
- [181] R. Agarwal, and C. M. Lieber. “Semiconductor nanowires: Optics and optoelectronics.” *Applied Physics A: Materials Science and Processing* **85**, 209 (2006).
- [182] S. Kan, T. Mokari, E. Rothenberg, and U. Banin. “Synthesis and size-dependent properties of zinc-blende semiconductor quantum rods.” *Nature Materials* **2**, 155 (2003).
- [183] F. Wang, H. Yu, S. Jeong, J. M. Pietryga, J. A. Hollingsworth, *et al.* “The Scaling of the Effective Band Gaps in Indium Arsenide Quantum Dots and Wires.” *ACS Nano* **2**, 1903 (2008).

- [184] L. Cao, J. S. White, J. S. Park, J. A. Schuller, B. M. Clemens, *et al.* “Engineering light absorption in semiconductor nanowire devices.” *Nature Materials* **8**, 643 (2009).
- [185] X. Duan, Y. Huang, R. Agarwal, and C. M. Lieber. “Single-nanowire electrically driven Lasers.” *Nature* **421**, 241 (2003).
- [186] M. T. Björk, H. Schmid, J. Knoch, H. Riel, and W. Riess. “Donor deactivation in silicon nanostructures.” *Nature Nanotechnology* **4**, 103 (2009).
- [187] D. E. Perea, E. R. Hemesath, E. J. Schwalbach, J. L. Lensch-Falk, P. W. Voorhees, *et al.* “Direct measurement of dopant distribution in an individual vapour-liquid-solid nanowire.” *Nature Nanotechnology* **4**, 315 (2009).
- [188] M. Diarra, Y. M. Niquet, C. Delerue, and G. Allan. “Ionization energy of donor and acceptor impurities in semiconductor nanowires: Importance of dielectric confinement.” *Physical Review B - Condensed Matter and Materials Physics* **75**, 1 (2007).
- [189] L. C. L. Hollenberg, H. Ryu, D. L. Thompson, A. Fuhrer, W. C. T. Lee, *et al.* “Ohm’s Law Survives to the Atomic Scale.” *Science* **335**, 64 (2012).
- [190] S. A. Dayeh, R. Chen, Y. G. Ro, and J. Sim. “Progress in doping semiconductor nanowires during growth.” *Materials Science in Semiconductor Processing* **62**, 135 (2017).
- [191] G. Imamura, T. Kawashima, M. Fujii, C. Nishimura, T. Saitoh, *et al.* “Distribution of Active Impurities in Single Silicon Nanowires 2008.” *Nano Letters* **8**, 2620 (2008).
- [192] E. C. Garnett, Y. C. Tseng, D. R. Khanal, J. Wu, J. Bokor, *et al.* “Dopant profiling and surface analysis of silicon nanowires using capacitance-voltage measurements.” *Nature Nanotechnology* **4**, 311 (2009).
- [193] A. Heidelberg, L. T. Ngo, B. Wu, M. A. Phillips, S. Sharma, *et al.* “A generalized description of the elastic properties of nanowires.” *Nano Letters* **6**, 1101 (2006).
- [194] P. Moriarty. “Nanostructured materials.” *Reports on Progress in Physics* **64**, 297 (2001).
- [195] S. Okamoto, and Y. Kanemitsu. “Photoluminescence properties of surface-oxidized Ge nanocrystals: Surface localization of excitons.” *Physical Review B* **54**, 16421 (1996).
- [196] H. W. Liu, J. P. Lu, H. M. Fan, C. H. Sow, S. H. Tang, *et al.* “Temperature and composition dependence of photoluminescence dynamics in CdS_xSe_{1-x} nanobelts.” *Journal of Applied Physics* **111**, 073112 (2012).
- [197] T. S. Kim, S. D. Lester, and B. G. Streetman. “Observation of radiative surface states on InP.” *Journal of Applied Physics* **61**, 2072 (1987).
- [198] X. Y. Wang, L. H. Qu, J. Y. Zhang, X. G. Peng, and M. Xiao. “Surface-Related Emission in Highly Luminescent CdSe Quantum Dots.” *Nano Letters* **3**, 1103 (2003).

- [199] C.-Z. Ning, L. Dou, and P. Yang. “Bandgap engineering in semiconductor alloy nanomaterials with widely tunable compositions.” *Nature Reviews Materials* **2**, 1 (2017).
- [200] L. Li, H. Lu, Z. Yang, L. Tong, Y. Bando, *et al.* “Bandgap-Graded CdS x Se 1-x Nanowires for High-Performance Field-Effect Transistors and Solar Cells.” *Advanced Materials* **25**, 1109 (2013).
- [201] T. Kuykendall, P. Ulrich, S. Aloni, and P. Yang. “Complete composition tunability of InGa_N nanowires using a combinatorial approach.” *Nature Materials* **6**, 951 (2007).
- [202] A. Pan, R. Liu, M. Sun, and C.-Z. Ning. “Spatial Composition Grading of Quaternary ZnCdSSe Alloy Nanowires with Tunable Light Emission between 350 and 710 nm on a Single Substrate.” *ACS Nano* **4**, 671 (2010).
- [203] F. Gu, Z. Yang, H. Yu, J. Xu, P. Wang, *et al.* “Spatial bandgap engineering along single alloy nanowires.” *Journal of the American Chemical Society* **133**, 2037 (2011).
- [204] A. Pan, W. Zhou, E. S. P. Leong, R. Liu, A. H. Chin, *et al.* “Continuous alloy-composition spatial grading and superbroad wavelength-tunable nanowire lasers on a single chip.” *Nano Letters* **9**, 784 (2009).
- [205] D. Caselli, Z. Liu, D. Shelhammer, and C. Z. Ning. “Composition-graded nanowire solar cells fabricated in a single process for spectrum-splitting photovoltaic systems.” *Nano Letters* **14**, 5772 (2014).
- [206] S. Guo, Z. Li, G. Song, B. Zou, X. Wang, *et al.* “Large-area photodetector with high-sensitivity and broadband spectral response based on composition-graded CdSSe nanowire-chip.” *Journal of Alloys and Compounds* **649**, 793 (2015).
- [207] Z. Yang, J. Xu, P. Wang, X. Zhuang, A. Pan, *et al.* “On-nanowire spatial band gap design for white light emission.” *Nano Letters* **11**, 5085 (2011).
- [208] C.-J. Kim, H.-S. Lee, Y.-J. Cho, J.-E. Yang, R. R. Lee, *et al.* “On-Nanowire Band-Graded Si:Ge Photodetectors.” *Advanced Materials* **23**, 1025 (2011).
- [209] W. Guo, M. Zhang, A. Banerjee, and P. Bhattacharya. “Catalyst-free InGa_N/Ga_N nanowire light emitting diodes grown on (001) silicon by molecular beam epitaxy.” *Nano Letters* **10**, 3356 (2010).
- [210] L. Huang, Q. Gao, L. D. Sun, H. Dong, S. Shi, *et al.* “Composition-Graded Cesium Lead Halide Perovskite Nanowires with Tunable Dual-Color Lasing Performance.” *Advanced Materials* **30**, 1 (2018).
- [211] P. Reimers. “The Preparation of Graded-Band-Gap Single Crystals of II-VI Compounds.” *Physica Status Solidi (B)* **35**, 707 (1969).
- [212] Z. Yang, D. Wang, C. Meng, Z. Wu, Y. Wang, *et al.* “Broadly Defining Lasing Wavelengths in Single Bandgap-Graded Semiconductor Nanowires.” *Nano Letters* **14**, 3153 (2014).

- [213] A. Pan, H. Yang, R. Liu, R. Yu, B. Zou, *et al.* “Color-tunable photoluminescence of alloyed CdS_xSe_{1-x} nanobelts.” *Journal of the American Chemical Society* **127**, 15692 (2005).
- [214] J. Lu, S. Cheng, Z. Minrui, N. Mathews, L. Hongwei, *et al.* “Facile one-step synthesis of CdS_xSe_{1-x} nanobelts with uniform and controllable stoichiometry.” *Journal of Physical Chemistry C* **115**, 19538 (2011).
- [215] N. W. Ashcroft, and A. R. Denton. “Vegard’s Law.” *Physical Review A* **43**, 3161 (1991).
- [216] S. J. Kwon, Y.-J. Choi, J.-H. Park, I.-S. Hwang, and J.-G. Park. “Structural and optical properties of CdSSe nanowires.” *Physical Review B* **72**, 205312 (2005).
- [217] M. Gratzel. “Photoelectrochemical Cells.” *Nature* **414**, 338 (2001).
- [218] J. Pan, M. I. B. Utama, Q. Zhang, X. Liu, B. Peng, *et al.* “Composition-tunable vertically aligned CdS_xSe_{1-x} nanowire arrays via van der Waals epitaxy: Investigation of optical properties and photocatalytic behavior.” *Advanced Materials* **24**, 4151 (2012).
- [219] H. Liu, J. Lu, H. F. Teoh, D. Li, Y. P. Feng, *et al.* “Defect engineering in CdS_xSe_{1-x} nanobelts: An insight into carrier relaxation dynamics via optical pump-terahertz probe spectroscopy.” *Journal of Physical Chemistry C* **116**, 26036 (2012).
- [220] H. Liu, J. Lu, Z. Yang, J. Teng, L. Ke, *et al.* “Ultrahigh photoconductivity of bandgap-graded CdS_xSe_{1-x} nanowires probed by THz spectroscopy.” *Scientific Reports* **4**–6 (2016).
- [221] J. Lu, H. Liu, S. X. Lim, S. H. Tang, C. H. Sow, *et al.* “Transient photoconductivity of ternary CDSSE nanobelts as measured by time-resolved terahertz spectroscopy.” *Journal of Physical Chemistry C* **117**, 12379 (2013).
- [222] J. Xu, X. Zhuang, P. Guo, W. Huang, W. Hu, *et al.* “Asymmetric light propagation in composition-graded semiconductor nanowires.” *Scientific Reports* **2**, 820 (2012).
- [223] J. Xu, X. Zhuang, P. Guo, Q. Zhang, W. Huang, *et al.* “Wavelength-converted/selective waveguiding based on composition-graded semiconductor nanowires.” *Nano Letters* **12**, 5003 (2012).
- [224] P. Guo, X. Zhuang, J. Xu, Q. Zhang, W. Hu, *et al.* “Low-threshold nanowire laser based on composition-symmetric semiconductor nanowires.” *Nano Letters* **13**, 1251 (2013).
- [225] S. Bae, H. Kim, Y. Lee, X. Xu, J. S. Park, *et al.* “Roll-to-roll production of 30-inch graphene films for transparent electrodes.” *Nature Nanotechnology* **5**, 574 (2010).
- [226] Z. Z. Sun, Z. Yan, J. Yao, E. Beitler, Y. Zhu, *et al.* “Supplementary Information: Growth of graphene from solid carbon sources.” *Nature* **468**, 549 (2010).
- [227] J. D. Wood, G. P. Doidge, E. A. Carrion, J. C. Koepke, J. A. Kaitz, *et al.* “Annealing free, clean graphene transfer using alternative polymer scaffolds.” *Nanotechnology* **26**, 055302 (2015).

- [228] X. Liang, B. a. Sperling, I. Calizo, G. Cheng, C. A. Hacker, *et al.* “Toward clean and crackless transfer of graphene.” *ACS Nano* **5**, 9144 (2011).
- [229] A. Pirkle, J. Chan, A. Venugopal, D. Hinojos, C. W. Magnuson, *et al.* “The effect of chemical residues on the physical and electrical properties of chemical vapor deposited graphene transferred to SiO₂.” *Applied Physics Letters* **99**, 122108 (2011).
- [230] M. Her, R. Beams, and L. Novotny. “Graphene transfer with reduced residue.” *Physics Letters, Section A: General, Atomic and Solid State Physics* **377**, 1455 (2013).
- [231] G. Borin Barin, Y. Song, I. de Fátima Gimenez, A. G. Souza Filho, L. S. Barreto, *et al.* “Optimized graphene transfer: Influence of polymethylmethacrylate (PMMA) layer concentration and baking time on graphene final performance.” *Carbon* **84**, 82 (2015).
- [232] J. W. Suk, A. Kitt, C. W. Magnuson, Y. Hao, S. Ahmed, *et al.* “Transfer of CVD-grown monolayer graphene onto arbitrary substrates.” *ACS Nano* **5**, 6916 (2011).
- [233] D. Roskopf, and S. Strehle. “Surface-controlled contact printing for nanowire device fabrication on a large scale.” *Nanotechnology* **27** (2016).
- [234] L. Tong, R. R. Gattass, I. Maxwell, J. Lou, M. Shen, *et al.* “Subwavelength-diameter silica wires for low-loss optical wave guiding.” *Nature* **426**, 816 (2003).
- [235] J. Wallentin, N. Anttu, D. Asoli, M. Huffman, I. Åberg, *et al.* “InP Nanowire Array Solar Cells Achieving 13.8% Efficiency by Exceeding the Ray Optics Limit.” *Science* 1–5 (2013).
- [236] Z. Fan, J. C. Ho, Z. A. Jacobson, R. Yerushalmi, R. L. Alley, *et al.* “Wafer-Scale Assembly of Semiconductor Nanowire Arrays by Contact Printing.” *Electrical Engineering* 1–14 (2008).
- [237] Z. Fan, J. C. Ho, Z. A. Jacobson, H. Razavi, and A. Javey. “Large-scale, heterogeneous integration of nanowire arrays for image sensor circuitry.” *Proceedings of the National Academy of Sciences of the United States of America* **105**, 11066 (2008).
- [238] R. Yerushalmi, Z. A. Jacobson, J. C. Ho, Z. Fan, and A. Javey. “Large scale, highly ordered assembly of nanowire parallel arrays by differential roll printing.” *Applied Physics Letters* **91**, 2007 (2007).
- [239] Y.-Z. Long, M. Yu, B. Sun, C.-Z. Gu, and Z. Fan. “Recent advances in large-scale assembly of semiconducting inorganic nanowires and nanofibers for electronics, sensors and photovoltaics.” *Chemical Society Reviews* **41**, 4560 (2012).
- [240] Y. Huang, X. Duan, Q. Wei, and C. M. Lieber. “Directed assembly of one-dimensional nanostructures into functional networks.” *Science* **291**, 630 (2001).
- [241] Y. Huang, X. Duan, Y. Cui, L. J. Lauhon, K. H. Kim, *et al.* “Logic gates and computation from assembled nanowire building blocks.” *Science* **294**, 1313 (2001).
- [242] Y. Huang, X. Duan, and C. Lieber. “Nanowires for Integrated Multicolor Nanophotonics.” *Small* **1**, 142 (2004).

- [243] D. Whang, S. Jin, Y. Wu, and C. M. Lieber. “Large-scale hierarchical organization of nanowire arrays for integrated nanosystems.” *Nano Letters* **3**, 1255 (2003).
- [244] P. A. Smith, C. D. Nordquist, T. N. Jackson, T. S. Mayer, B. R. Martin, *et al.* “Electric-field assisted assembly and alignment of metallic nanowires.” *Applied Physics Letters* **77**, 1399 (2000).
- [245] M. A. Zimmler, D. Stichtenoth, C. Ronning, W. Yi, V. Narayanamurti, *et al.* “Scalable fabrication of nanowire photonic and electronic circuits using spin-on glass.” *Nano Letters* **8**, 1695 (2008).
- [246] K. Storm, F. Halvardsson, M. Heurlin, D. Lindgren, A. Gustafsson, *et al.* “Spatially resolved Hall effect measurement in a single semiconductor nanowire.” *Nature nanotechnology* **7**, 718 (2012).
- [247] P. Tchoulfian, F. Donatini, F. Levy, B. Amstatt, A. Dussaigne, *et al.* “Thermoelectric and micro-Raman measurements of carrier density and mobility in heavily Si-doped GaN wires.” *Applied Physics Letters* **103** (2013).
- [248] Z. Cui, R. Perumal, T. Ishikura, K. Konishi, K. Yoh, *et al.* “Characterizing the electron transport properties of a single 110 InAs nanowire.” *Applied Physics Express* **7**, 85001 (2014).
- [249] O. Hultin, G. Otnes, M. T. Borgström, M. Björk, L. Samuelson, *et al.* “Comparing Hall Effect and Field Effect Measurements on the Same Single Nanowire.” *Nano Letters* **16**, 205 (2016).
- [250] S. Song, W. K. Hong, S. S. Kwon, and T. Lee. “Passivation effects on ZnO nanowire field effect transistors under oxygen, ambient, and vacuum environments.” *Applied Physics Letters* **92**, 2006 (2008).
- [251] Y. Yang, K. Brenner, and R. Murali. “The influence of atmosphere on electrical transport in graphene.” *Carbon* **50**, 1727 (2012).
- [252] V. Panchal, C. E. Giusca, A. Lartsev, N. A. Martin, N. Cassidy, *et al.* “Atmospheric doping effects in epitaxial graphene: correlation of local and global electrical studies.” *2D Materials* **3**, 015006 (2016).
- [253] A. R. Ullah, H. J. Joyce, H. H. Tan, C. Jagadish, and A. P. Micolich. “The influence of atmosphere on the performance of pure-phase WZ and ZB InAs nanowire transistors.” *Nanotechnology* **28**, 1 (2017).
- [254] A. Veligura, P. J. Zomer, I. J. Vera-Marun, C. Józsa, P. I. Gordiichuk, *et al.* “Relating hysteresis and electrochemistry in graphene field effect transistors.” *Journal of Applied Physics* **110** (2011).
- [255] H. J. Hwang, S. Seo, C. G. Kang, B. H. Lee, R. Choi, *et al.* “Fast transient charging at the graphene/SiO₂ interface causing hysteretic device characteristics.” *Applied Physics Letters* **98**, 183508 (2011).

- [256] J. A. Alexander-Webber, C. K. Groschner, A. A. Sagade, G. Tainter, M. F. Gonzalez-Zalba, *et al.* “Engineering the Photoresponse of InAs Nanowires.” *ACS Applied Materials and Interfaces* **9**, 43993 (2017).
- [257] J. A. Alexander-Webber, A. Cabrero-Vilatela, A. A. Sagade, R. Wang, J. Sui, *et al.* “Encapsulation of graphene transistors and vertical device integration by interface engineering with atomic layer deposited oxide.” *2D Materials* **4**, 011008 (2016).
- [258] T. Hanrath, and B. A. Korgel. “Chemical surface passivation of Ge nanowires.” *Journal of the American Chemical Society* **126**, 15466 (2004).
- [259] Y. Cui, Z. Zhong, D. Wang, W. U. Wang, and C. M. Lieber. “High performance silicon nanowire field effect transistors.” *Nano Letters* **3**, 149 (2003).
- [260] W. K. Hong, B. J. Kim, T. W. Kim, G. Jo, S. Song, *et al.* “Electrical properties of ZnO nanowire field effect transistors by surface passivation.” *Colloids and Surfaces A: Physicochemical and Engineering Aspects* **313-314**, 378 (2008).
- [261] C. K. Yong, K. Noori, Q. Gao, H. J. Joyce, H. H. Tan, *et al.* “Strong carrier lifetime enhancement in GaAs nanowires coated with semiconducting polymer.” *Nano Letters* **12**, 6293 (2012).
- [262] M. H. Sun, H. J. Joyce, Q. Gao, H. H. Tan, C. Jagadish, *et al.* “Removal of surface states and recovery of band-edge emission in InAs nanowires through surface passivation.” *Nano Letters* **12**, 3378 (2012).
- [263] P.-C. Chang, Z. Fan, C.-J. Chien, D. Stichtenoth, C. Ronning, *et al.* “High performance ZnO nanowire field effect transistor.” *Applied Physics Letters* **2005**, 217 (2005).
- [264] J. A. Robinson, T. Daniels, M. Fanton, K. A. Trumbull, M. LaBella, *et al.* “Epitaxial Graphene Materials Integration: Effects of Dielectric Overlayers on Structural and Electronic Properties.” *ACS Nano* **4**, 2667 (2010).
- [265] A. Konar, T. Fang, and D. Jena. “Effect of high- κ gate dielectrics on charge transport in graphene-based field effect transistors.” *Physical Review B - Condensed Matter and Materials Physics* **82**, 1 (2010).
- [266] M. L. Huang, Y. C. Chang, C. H. Chang, Y. J. Lee, P. Chang, *et al.* “Surface passivation of III-V compound semiconductors using atomic-layer-deposition-grown Al₂O₃.” *Applied Physics Letters* **87**, 1 (2005).
- [267] S. Kim, E. Tutuc, L. Colombo, J. Nah, D. Shahrjerdi, *et al.* “Realization of a high mobility dual-gated graphene field-effect transistor with Al₂O₃ dielectric.” *Applied Physics Letters* **94**, 062107 (2009).
- [268] A. I. Aria, K. Nakanishi, L. Xiao, P. Braeuninger-Weimer, A. A. Sagade, *et al.* “Parameter Space of Atomic Layer Deposition of Ultrathin Oxides on Graphene.” *ACS Applied Materials and Interfaces* **8**, 30564 (2016).
- [269] Y. Dan, K. Seo, K. Takei, J. H. Meza, A. Javey, *et al.* “Dramatic reduction of surface recombination by in situ surface passivation of silicon nanowires.” *Nano Letters* **11**, 2527 (2011).

- [270] N. Guo, W. Hu, L. Liao, S. P. Yip, J. C. Ho, *et al.* “Anomalous and highly efficient InAs nanowire phototransistors based on majority carrier transport at room temperature.” *Advanced Materials* **26**, 8203 (2014).
- [271] J. Li, X. Yan, F. Sun, X. Zhang, and X. Ren. “Anomalous photoconductive behavior of a single InAs nanowire photodetector.” *Applied Physics Letters* **107** (2015).
- [272] C. Soci, A. Zhang, X.-Y. Bao, H. Kim, Y. Lo, *et al.* “Nanowire Photodetectors.” *Journal of Nanoscience and Nanotechnology* **10**, 1430 (2010).
- [273] J. D. Prades, R. Jimenez-Diaz, F. Hernandez-Ramirez, L. Fernandez-Romero, T. Andreu, *et al.* “Toward a systematic understanding of photodetectors based on individual metal oxide nanowires.” *Journal of Physical Chemistry C* **112**, 14639 (2008).
- [274] R. Calarco, M. Marso, T. Richter, A. I. Aykanat, R. Meijers, *et al.* “Size-dependent photoconductivity in MBE-grown GaN - Nanowires.” *Nano Letters* **5**, 981 (2005).
- [275] J. D. Prades, F. Hernandez-Ramirez, R. Jimenez-Diaz, M. Manzanares, T. Andreu, *et al.* “The effects of electron-hole separation on the photoconductivity of individual metal oxide nanowires.” *Nanotechnology* **19** (2008).
- [276] K. Deng, and L. Li. “CdS nanoscale photodetectors.” *Advanced Materials* **26**, 2619 (2014).
- [277] J. S. Jie, W. J. Zhang, Y. Jiang, X. M. Meng, Y. Q. Li, *et al.* “Photoconductive characteristics of single-crystal CdS nanoribbons.” *Nano Letters* **6**, 1887 (2006).
- [278] T. Gao, Q. H. Li, and T. H. Wang. “CdS nanobelts as photoconductors.” *Applied Physics Letters* **86**, 1 (2005).
- [279] Y. Gu, and L. J. Lauhon. “Space-charge-limited current in nanowires depleted by oxygen adsorption.” *Applied Physics Letters* **89**, 2 (2006).
- [280] C. Soci, D. P. R. Aplin, J. Park, Y. H. Lo, X. Y. Bao, *et al.* “ZnO Nanowire UV Photodetectors with High Internal Gain.” *Nano Letters* **7**, 1003 (2007).
- [281] L. M. Mansfield, K. A. Bertness, P. T. Blanchard, T. E. Harvey, A. W. Sanders, *et al.* “GaN nanowire carrier concentration calculated from light and dark resistance measurements.” *Journal of Electronic Materials* **38**, 495 (2009).
- [282] L. Vj, J. Oh, A. P. Nayak, A. M. Katzenmeyer, K. H. Gilchrist, *et al.* “A perspective on nanowire photodetectors: Current status, future challenges, and opportunities.” (2011).
- [283] A. M. Cowley, and S. M. Sze. “Surface states and barrier height of metal-semiconductor systems.” *Journal of Applied Physics* **36**, 3212 (1965).
- [284] F. A. Kröger, G. Diemer, and H. A. Klasens. “Nature of an ohmic metal-semiconductor contact.” *Physical Review* **103**, 279 (1956).
- [285] R. T. Tung. “The physics and chemistry of the Schottky barrier height.” *Applied Physics Reviews* **1** (2014).

- [286] M. J. Thompson, and M. G. Cornwall. "Low Resistance Ohmic Contacts To Photoconductive CdS." *Solid-State Electronics* **15**, 861 (1972).
- [287] D. D. M. Allan, A. J. Hay, and M. A. Reid. "Ohmic contacts to cadmium sulphide films." *Solid-State Electronics* **16**, 951 (1973).
- [288] Z. Y. Zhang, C. H. Jin, X. L. Liang, Q. Chen, and L. M. Peng. "Current-voltage characteristics and parameter retrieval of semiconducting nanowires." *Applied Physics Letters* **88**, 1 (2006).
- [289] Z. Zhang, K. Yao, Y. Liu, C. Jin, X. Liang, *et al.* "Quantitative analysis of current-voltage characteristics of semiconducting nanowires: Decoupling of contact effects." *Advanced Functional Materials* **17**, 2478 (2007).
- [290] D. B. Suyatin, C. Thelander, M. T. Björk, I. Maximov, and L. Samuelson. "Sulfur passivation for ohmic contact formation to InAs nanowires." *Nanotechnology* **18**, 105307 (2007).
- [291] Y. Gu, J. P. Romankiewicz, J. K. David, J. L. Lensch, and L. J. Lauhon. "Quantitative measurement of the electron and hole mobility-lifetime products in semiconductor nanowires." *Nano Letters* **6**, 948 (2006).
- [292] Y. Gu, J. P. Romankiewicz, J. K. David, J. L. Lensch, L. J. Lauhon, *et al.* "Local photocurrent mapping as a probe of contact effects and charge carrier transport in semiconductor nanowire devices." *Journal of Vacuum Science & Technology B: Microelectronics and Nanometer Structures* **24**, 2172 (2006).
- [293] Y. W. Heo, L. C. Tien, D. P. Norton, S. J. Pearton, B. S. Kang, *et al.* "Pt/ZnO nanowire Schottky diodes." *Applied Physics Letters* **85**, 3107 (2004).
- [294] T. Dufaux, M. Burghard, and K. Kern. "Efficient charge extraction out of nanoscale schottky contacts to CdS nanowires." *Nano Letters* **12**, 2705 (2012).
- [295] Y. Hu, J. Zhou, P. H. Yeh, Z. Li, T. Y. Wei, *et al.* "Supersensitive, fast-response nanowire sensors by using schottky contacts." *Advanced Materials* **22**, 3327 (2010).
- [296] J. Zhou, Y. Gu, Y. Hu, W. Mai, P. H. Yeh, *et al.* "Gigantic enhancement in response and reset time of ZnO UV nanosensor by utilizing Schottky contact and surface functionalization." *Applied Physics Letters* **94**, 1 (2009).
- [297] T. Y. Wei, C. T. Huang, B. J. Hansen, Y. F. Lin, L. J. Chen, *et al.* "Large enhancement in photon detection sensitivity via Schottky-gated CdS nanowire nanosensors." *Applied Physics Letters* **96** (2010).
- [298] R. F. Wolffenbuttel. "State-of-the-art in integrated optical microspectrometers." *IEEE Transactions on Instrumentation and Measurement* **53**, 197 (2004).
- [299] R. F. Wolffenbuttel. "MEMS-based optical mini- and microspectrometers for the visible and infrared spectral range." *Journal of Micromechanics and Microengineering* **15** (2005).

- [300] T. A. Kwa, and R. F. Wolffenbuttel. "Integrated grating/detector array fabricated in silicon using micromachining techniques." *Sensors and Actuators: A. Physical* **31**, 259 (1992).
- [301] S. H. Kong, D. D. Wijngaards, and R. F. Wolffenbuttel. "Infrared micro-spectrometer based on a diffraction grating." *Sensors and Actuators, A: Physical* **92**, 88 (2001).
- [302] D. Sander, and J. Müller. "Selffocussing phase transmission grating for an integrated optical microspectrometer." *Sensors and Actuators, A: Physical* **88**, 1 (2001).
- [303] K. Chaganti, I. Salakhutdinov, I. Avrutsky, and G. W. Auner. "A simple miniature optical spectrometer with a planar waveguide grating coupler in combination with a plano-convex lens." *Optics Express* **14**, 4064 (2006).
- [304] I. Avrutsky, K. Chaganti, I. Salakhutdinov, and G. Auner. "Concept of a miniature optical spectrometer using integrated optical and micro-optical components." *Applied Optics* **45**, 7811 (2006).
- [305] S. Grabarnik, R. Wolffenbuttel, A. Emadi, M. Loktev, E. Sokolova, *et al.* "Planar double-grating microspectrometer." *Optics Express* **15**, 1031 (2007).
- [306] B. B. C. Kyotoku, L. Chen, and M. Lipson. "Sub-nm resolution cavity enhanced microspectrometer." *Optics Express* **18**, 102 (2009).
- [307] P. Cheben, I. Powell, S. Janz, and D.-X. Xu. "Wavelength-dispersive device based on a Fourier-transform Michelson-type arrayed waveguide grating." *Optics Letters* **30**, 1824 (2005).
- [308] P. Cheben, J. H. Schmid, A. Delâge, A. Densmore, S. Janz, *et al.* "A high-resolution silicon-on-insulator arrayed waveguide grating microspectrometer with sub-micrometer aperture waveguides." *Optics Express* **15**, 2299 (2007).
- [309] Z. Hu, A. Glidle, C. N. Ironside, M. Sorel, M. J. Strain, *et al.* "Integrated microspectrometer for fluorescence based analysis in a microfluidic format." *Lab on a Chip* **12**, 2850 (2012).
- [310] J. P. Carmo, R. P. Rocha, M. Bartek, G. De Graaf, R. F. Wolffenbuttel, *et al.* "A review of visible-range Fabry-Perot microspectrometers in silicon for the industry." *Optics and Laser Technology* **44**, 2312 (2012).
- [311] B. Momeni, E. S. Hosseini, and A. Adibi. "Planar photonic crystal microspectrometers in silicon-nitride for the visible range." *Optics Express* **17**, 17060 (2009).
- [312] B. Redding, S. F. Liew, R. Sarma, and H. Cao. "Compact spectrometer based on a disordered photonic chip." *Nature Photonics* **7**, 746 (2013).
- [313] F. Han, W. Wang, X. Zhang, and H. Xie. "Miniature Fourier transform spectrometer with a dual closed-loop controlled electrothermal micromirror." *Optics Express* **24**, 22650 (2016).
- [314] L. P. Schuler, J. S. Milne, J. M. Dell, and L. Faraone. "MEMS-based microspectrometer technologies for NIR and MIR wavelengths." *Journal of Physics D: Applied Physics* **42** (2009).

- [315] S.-W. Wang, X. Chen, W. Lu, M. Li, C. Xia, *et al.* “Concept of a high-resolution miniature spectrometer using an integrated filter array.” *Optics Letters* **32**, 632 (2007).
- [316] J. H. Correia, M. Bartek, and R. F. Wolffenbuttel. “High-selectivity single-chip spectrometer in silicon for operation at visible part of the spectrum.” *IEEE Transactions on Electron Devices* **47**, 553 (2000).
- [317] J. H. Correia, G. De Graaf, S. H. Kong, M. Bartek, and R. F. Wolffenbuttel. “Single-chip CMOS optical microspectrometer.” *Sensors and Actuators, A: Physical* **82**, 191 (2000).
- [318] G. Schweiger, R. Nett, and T. Weigel. “Microresonator array for high-resolution spectroscopy.” *Optics Letters* **32**, 2644 (2007).
- [319] T. Yang, C. Li, Z. Wang, and H. Ho. “An ultra compact spectrometer based on the optical transmission through a micro interferometer array.” *Optik* **124**, 1377 (2013).
- [320] X. Gan, N. Pervez, I. Kymissis, F. Hatami, and D. Englund. “A high-resolution spectrometer based on a compact planar two dimensional photonic crystal cavity array.” *Applied Physics Letters* **100** (2012).
- [321] K. M. Bryan, Z. Jia, M. J. Gazes, M. P. Cox, N. K. Pervez, *et al.* “Inexpensive photonic crystal spectrometer for colorimetric sensing applications.” *Optics Express* **21**, 4411 (2013).
- [322] J. Bao, and M. G. Bawendi. “A Colloidal Quantum Dot Spectrometer.” *Nature* **523**, 67 (2015).
- [323] U. Kurokawa, B. I. Choi, and C. C. Chang. “Filter-based miniature spectrometers: Spectrum reconstruction using adaptive regularization.” *IEEE Sensors Journal* **11**, 1556 (2011).
- [324] A. Emadi, H. Wu, G. de Graaf, and R. Wolffenbuttel. “Design and implementation of a sub-nm resolution microspectrometer based on a Linear-Variable Optical Filter.” *Optics Express* **20**, 489 (2011).
- [325] A. Emadi, H. Wu, G. de Graaf, P. Enoksson, J. H. Correia, *et al.* “Linear variable optical filter-based ultraviolet microspectrometer.” *Applied Optics* **51**, 4308 (2012).
- [326] H.-A. Lin, H.-Y. Hsu, C.-W. Chang, and C.-S. Huang. “Compact spectrometer system based on a gradient grating period guided-mode resonance filter.” *Optics Express* **24**, 10972 (2016).
- [327] C.-C. Chang, and H.-N. Lee. “On the estimation of target spectrum for filter-array based spectrometers.” *Optics Express* **16**, 1056 (2008).
- [328] S. Zhang, Y. Dong, H. Fu, S. L. Huang, and L. Zhang. “A spectral reconstruction algorithm of miniature spectrometer based on sparse optimization and dictionary learning.” *Sensors* **18** (2018).
- [329] C.-C. Chang, N.-T. Lin, U. Kurokawa, and B. I. Choi. “Spectrum reconstruction for filter-array spectrum sensor from sparse template selection.” *Optical Engineering* **50**, 114402 (2011).

- [330] J. Oliver, W. Lee, S. Park, and H.-N. Lee. “Improving resolution of miniature spectrometers by exploiting sparse nature of signals.” *Optics Express* **20**, 2613 (2012).
- [331] T. H. Kim, K. S. Cho, E. K. Lee, S. J. Lee, J. Chae, *et al.* “Full-colour quantum dot displays fabricated by transfer printing.” *Nature Photonics* **5**, 176 (2011).
- [332] X. Hu, H. Liu, X. Wang, X. Zhang, Z. Shan, *et al.* “Wavelength Selective Photodetectors Integrated on a Single Composition-Graded Semiconductor Nanowire.” *Advanced Optical Materials* **6**, 1 (2018).
- [333] Y. Gu, E. S. Kwak, J. L. Lensch, J. E. Allen, T. W. Odom, *et al.* “Near-field scanning photocurrent microscopy of a nanowire photodetector.” *Applied Physics Letters* **87**, 1 (2005).
- [334] C. Blömers, T. Grap, M. I. Lepsa, J. Moers, S. Trellenkamp, *et al.* “Hall effect measurements on InAs nanowires.” *Applied Physics Letters* **101** (2012).
- [335] M. S. Choi, S. H. Lee, and W. J. Yoo. “Plasma treatments to improve metal contacts in graphene field effect transistor.” *Journal of Applied Physics* **110** (2011).
- [336] M. Shaygan, M. Otto, A. A. Sagade, C. A. Chavarin, G. Bacher, *et al.* “Low Resistive Edge Contacts to CVD-Grown Graphene Using a CMOS Compatible Metal.” *Annalen der Physik* **529**, 1 (2017).
- [337] C. Williams, R. Bartholomew, G. Rughoobur, G. S. D. Gordon, A. J. Flewitt, *et al.* “Fabrication of nanostructured transmissive optical devices on ITO-glass with UV1116 photoresist using high-energy electron beam lithography.” *Nanotechnology* **27**, 485301 (2016).
- [338] P. Yang, B. Messer, M. Law, H. Yan, and H. Kind. “Nanowire Ultraviolet Photodetectors and Optical Switches.” *Advanced Materials* **14**, 158 (2002).
- [339] L. Li, P. Wu, X. Fang, T. Zhai, L. Dai, *et al.* “Single-Crystalline CdS Nanobelts for Excellent Field-Emitters and Ultrahigh Quantum-Efficiency Photodetectors.” *Advanced Materials* **22**, 3161 (2010).
- [340] P. C. Hansen. “Analysis of Discrete Ill-Posed Problems by Means of the L-Curve.” *SIAM Review* **34**, 561 (1992).
- [341] G. Wahba. “Practical Approximate Solutions to Linear Operator Equations when the Data are Noisy.” *SIAM Journal on Numerical Analysis* **14**, 651 (1977).
- [342] G. H. Golub, M. Heath, and G. Wahba. “Generalized cross-validation as a method for choosing a good ridge parameter.” *Technometrics* **21**, 215 (1979).
- [343] Z. Wang, S. Yi, A. Chen, M. Zhou, T. S. Luk, *et al.* “Single-shot on-chip spectral sensors based on photonic crystal slabs.” *Nature Communications* **10**, 3 (2019).
- [344] D. M. Kita, B. Miranda, J. Hu, H. Lin, D. Favela, *et al.* “High-performance and scalable on-chip digital Fourier transform spectroscopy.” *Nature Communications* **9**, 1 (2018).

- [345] G. Calafiore, A. Koshelev, S. Dhuey, A. Goltsov, P. Sasorov, *et al.* “Holographic planar lightwave circuit for on-chip spectroscopy.” *Light: Science and Applications* **3** (2014).
- [346] *Hamamatsu, C12666MA microspectrometer. Details viewable online (at the time of writing) at www.hamamatsu.com/eu/en/product/type/C12666MA/index.html .*
- [347] N. Blind, E. Le Coarer, P. Kern, and S. Gousset. “Spectrographs for astrophotonics.” *Optics Express* **25**, 27341 (2017).
- [348] D. J. Mulla. “Twenty five years of remote sensing in precision agriculture: Key advances and remaining knowledge gaps.” *Biosystems Engineering* **114**, 358 (2013).
- [349] J.-S. Bouillard, S. Vilain, W. Dickson, and A. V. Zayats. “Hyperspectral imaging with scanning near-field optical microscopy: applications in plasmonics.” *Optics Express* **18**, 16513 (2010).
- [350] A. S. Stender, K. Marchuk, C. Liu, S. Sander, M. W. Meyer, *et al.* “Single cell optical imaging and spectroscopy.” *Chemical Reviews* **113**, 2469 (2013).
- [351] A. T. Harris. “Spectral Mapping Tools from the Earth Sciences Applied to Spectral Microscopy Data.” *Cytometry Part A* **69A**, 872 (2006).
- [352] G. Lu, and B. Fei. “Medical hyperspectral imaging: a review.” *Journal of Biomedical Optics* **19**, 010901 (2014).
- [353] P. J. Lapray, X. Wang, J. B. Thomas, and P. Gouton. “Multispectral filter arrays: Recent advances and practical implementation.” *Sensors* **14**, 21626 (2014).
- [354] B. Geelen, N. Tack, and A. Lambrechts. “A compact snapshot multispectral imager with a monolithically integrated per-pixel filter mosaic.” *Advanced Fabrication Technologies for Micro/Nano Optics and Photonics VII* **8974**, 89740L (2014).
- [355] N. Hagen, and M. W. Kudenov. “Review of snapshot spectral imaging technologies.” *Optical Engineering* **52**, 090901 (2013).